Bioenergetic Studies on the Quinone Electron Acceptors of Photosystem II

Imperial College London

Sven De Causmaecker

Thesis submitted for the degree of Doctor of Philosophy of Imperial College London

Department of Life Sciences

Division of Molecular Biosciences

2017

Declaration of Originality

I hereby declare that this thesis, submitted in fulfilment of the requirements for the degree of Doctor of Philosophy of the Imperial College London, represents my own work and has not previously submitted to this or any other institute for any degree, diploma or other qualification. All other work has been appropriately referenced.

Sven De Causmaecker

Abstract

Photosystem II (PSII) is a membrane-bound protein complex found in plants, algae and cyanobacteria that converts light into chemical energy. Despite extensive research, many energetic and mechanistic questions of PSII remain unresolved. Here the energetics and kinetics of the electron-acceptor side of PSII from *Thermosynechococcus elongatus* were investigated using biophysical approaches.

Based on data from electron paramagnetic resonance and thermoluminescence measurements, the two midpoint potentials of the terminal electron acceptor, Q_B, were measured ($E_m(Q_B/Q_B^{\bullet-})$ = 92 mV; $E_m(Q_B^{\bullet-}/Q_BH_2)$ = 43 mV). It was found that i) $Q_B^{\bullet-}$ is significantly stabilized, contradicting the recent literature, ii) the energy-gap between Q_A and Q_B is larger than previously assumed (235 mV instead of ≈80 mV), contradicting the older literature, and iii) the release of Q_BH_2 into the pool is thermodynamically favourable, (≈50 meV). No significant shift of the Q_B midpoint potentials in response to the loss of the Mn_4O_5Ca cluster was found. These findings allow for a better understanding of charge separation and the energetics of PSII.

Isolated PSII from *T. elongatus* is used in many structural and functional studies but the electron acceptor side kinetics of this organism are poorly defined. Using absorption spectroscopy, the kinetics which were previously treated as a single "fast phase", were resolved as follows: $Q_A^{\bullet-} \rightarrow Fe^{3+}$ ($t_{1/2}$ = 50 µs); $Q_A^{\bullet-} \rightarrow Q_B$ ($t_{1/2}$ = 350 µs); $Q_A^{\bullet-} \rightarrow Q_B^{\bullet-}$ ($t_{1/2}$ = 1.3 ms). Furthermore, the kinetic data analysis developed in this work allowed the proportions of these reactions to be determined under a range of conditions. It was found that in long dark-adapted samples up to 50% of the non-heme iron was oxidized and this oxidation was inhibited when bicarbonate was present. These data will be useful for future research on PSII and help understanding the mechanism of electron transfer on the acceptor side.

Acknowledgements

I would like to sincerely thank my supervisor Bill Rutherford for his support and guidance throughout my project.
I would like to thank Wolfgang Nitschke for his tireless enthusiasm, energy and ability to drive us home without crashing after multiple consecutive all-night shifts.
I appreciate the help and support I received from my colleagues; Jeffrey Douglass, Andrea Fantuzzi, Tanai Cardona and Dennis Nürnberg.
I thank Angus Morrison for introducing me to Inventor and Matlab, as well as the climbing and sauna sessions. Thanks also go to Susan Parker for her useful input to TL electronics design and to the ICAH for a £500 project boost grant.
I would like to thank Imperial College London for providing me with financial support and a challenging work environment. In addition I thank all those who supported my work where Imperial could not, in particular Fabrice Rappaport, Alain Boussac, Fraser Macmillan and Petra Fromme and her group.
I would also like to thank the current and former members of the 7^{th} floor for the inspiring discussions and comradeship.

Most importantly, I thank Sarah Wieners and my parents Luc and Sybille De Causmaecker for their patience, love and support over all the years.

Contents

List of Figures

List of Tables

List of Acronyms

10-PQ Decylplastoquinone

ATP Adenosine triphosphate

β-DDM n-dodecyl-β-D-maltoside

BA Benzamidine

BSA Bovine serum albumin

Chl Chlorophyll

CV Column volume

DAD Diaminodurol

DCBQ 2,6-Dichloro-p-Benzoquinone

DCMU 3-(3,4-Dichlorophenyl)-1,1-Dimenthylurea

DCPIP 2,6-Dichlorophenolindophenol

DNase I Deoxyribonuclease I

EDTA Ethylene-Diamine-Tetraacetic Acid

EPR Electron paramagnetic resonance

ET Electron transfer

FeCN Ferricyanide ($K_3Fe(CN)_6$)

FNR Ferredoxin-$NADP^+$ reductase

FWHM Full-width-half-maximum

HEPES 4-(2-hydroxyethyl)-1-piperazineethanesulfonic acid

HOMO Highest occupied molecular orbital

ITS Potassium indigotetrasulfonate

LHCII Light harvesting complex II

LUMO Lowest unoccupied molecular orbital

MES 2-(N-Morpholino)Ethane-sulphonic acid

MOPS 3-(N-Morpholino)Propane-sulphonic acid

MWCO Molecular weight cut-off

Nd:YAG Neodymium:Yttrium-Aluminum-Garnet

NADPH Nicotinamide adenine dinucleotide phosphate

OD Optical density

OEC Oxygen-evolving cluster

OPO Optical Parametric Oscillator

P_{680} P_{680}, primary donor of PSII with an absorption maximum at 680 nm.

PC Plastocyanin

PES Phenazine ethosulphate

PMS Phenazine methosulphate

PSI Photosystem I

PSII Photosystem II

PT Proton transfer

PQ Plastoquinone

Q_A Primary quinone acceptor

Q_B Secondary quinone acceptor

QM/MM Quantum mechanics/molecular mechanics

RC Reaction centre

T. elongatus *Thermosynechococcus elongatus*

TMPD *N,N,N',N'*-Tetramethyl-p-phenylenediamine dihydrochloride

1 Introduction

Photosynthesis is nature's way of transforming solar energy into energy stored in chemical bonds. It is the process that, directly or indirectly, provides the energy for almost all life on earth. Understanding the process and its boundaries therefore offers insights into the energetics underpinning terrestrial life. The work presented in this thesis, aims at a better understanding of Photosystem II (PSII), which is one of the key enzyme complexes within photosynthesis. This is deemed worthwhile because it is fun, a challenge for the experimenter and the discovery of new knowledge is recognized as *per se* valuable without the need for any, in reality highly speculative, economical benefit calculations.

In this chapter, a brief introduction into photosynthesis in general will be followed by an overview of the mechanism of PSII. Before summarizing the aims of the thesis, the energetics of the reactions occurring on the "acceptor side" of PSII will be described in more detail to provide the theoretical background for this work.

1.1 Introduction to Photosystem II

1.1.1 PSII in the photosynthetic membrane

Oxygenic photosynthesis is the light driven production of oxygen and organic compounds from carbon-dioxide and water. This process, occurring in plants, algae and cyanobacteria, can be separated into two main stages. In the first, light-dependent stage, energy from the sun is captured and stored in ATP and NADPH. In the second, light-independent stage, ATP and NADPH are then used to capture and

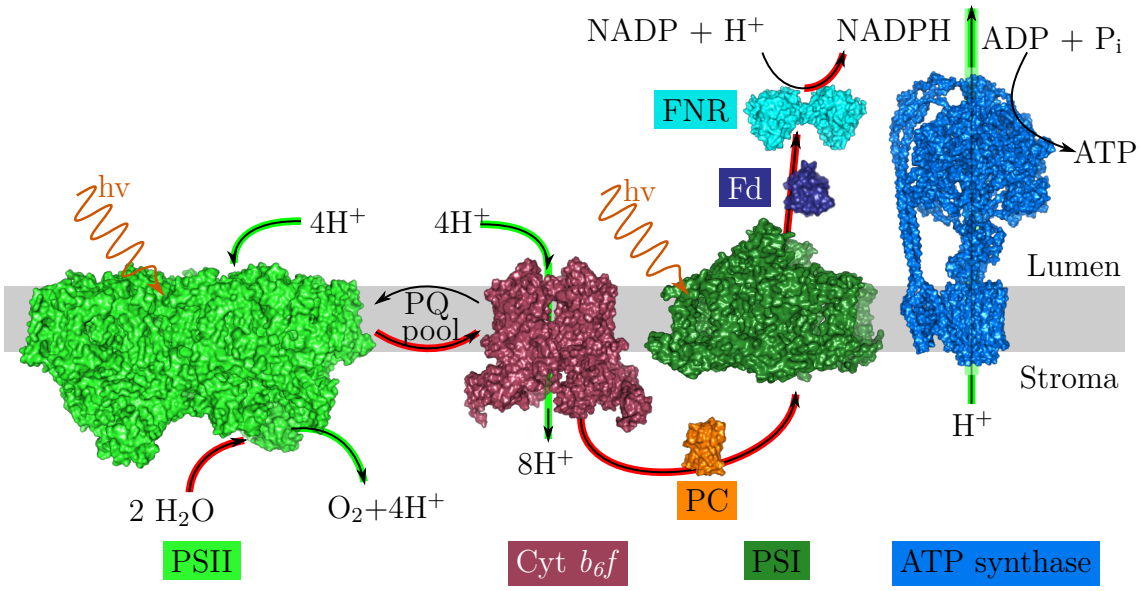

Figure 1.1: Schematic overview of the electron transport chain of the photosynthetic light reactions. Arrows with red underlay indicate the transport of electrons through the membrane, Arrows with green underlay indicate reactions that transport protons across the membrane. Image created using the following resources: ATP synthase (PDB ID: 5540, Sobti et al., 2016), Cyt b_6f (PDB ID: 4H44, Hasan et al., 2013), Ferredoxin (PDB ID: 1OFF, Van Den Heuvel et al., 2003), FNR (PDB ID: 2B5O), PC (PDB ID: 1JXD, Bertini et al., 2001), PSI (PDB ID: 1JBO, Jordan et al., 2001), PSII (PDB ID: 3WU2, Umena et al., 2011).

reduce carbon dioxide. This process, the reductive pentose-phosphate cycle[1], yields the carbohydrates and sugars that become the building blocks for all organic matter. Although of fundamental importance for photosynthesis, the second stage is not further described, as it is not of direct relevance for the here presented work.

Considering the light dependent reactions, while there are some differences between plants, algae, and cyanobacteria (cell architecture, antennas, regulation etc.) the

[1]The reductive pentose-phosphate cycle is also known as the Calvin–Benson–Bassham cycle. In this work however, more value is placed on recognizing the dialectic nature of the scientific process, than on nurturing the vanities of men. Therefore, descriptive naming schemes are preferred over historical attributions.

overall process is conserved across all organisms. Figure 1.1 shows a graphical representation of the light-dependent reactions in cyanobacteria. The complexes catalysing the light-dependent reactions are localized in the membranes of specialized photosynthetic compartments, called thylakoids. Thylakoids from cyanobacteria contain Photosystem I (PSI), PSII and the cytochrome b_6f complex as well as quinone electron carriers. Soluble phycobilisome antennae complexes are attached to PSI/PSII (Bald et al., 1996; Watanabe et al., 2014). In eukaryotic thylakoids the soluble antennae is replaced by LHCII (Dekker and Boekema, 2005) in the thylakoid membrane. Dynamic re-arrangement of the antenna systems balances excitation between PSI and PSII (Allen and Pfannschmidt, 2000). Furthermore elaborate quenching mechanisms can manipulate the excitation flux towards the reaction centres. Due to the difference in antenna systems, these have evolved separately and differ from each other in plants (Ruban, 2016) and cyanobacteria (Kirilovsky, 2007). The association of the membrane-bound complexes into larger photosynthesis super complexes is highly dynamical and an ongoing field of study (Liu, 2016; Yadav et al., 2017).

Photosystem II, the water-plastoquinone photo-oxidoreductase, plays a key role in the light reactions as it is the place where light energy is used to oxidise water and reduce plastoquinone according to Equations 1.1 and 1.2.

$$2H_2O \xrightarrow{\text{light}} O_2 + 4H^+ + 4e^- \tag{1.1}$$

$$PQ + 2e^- + 2H^+ \longrightarrow PQH_2 \tag{1.2}$$

Reduced quinol passes through the membrane to the Cytochrome b_6f complex were it is reoxidized. The Cytochrome b_6f complex passes the two electrons sequentially on to Plastocyanine, a soluble one-electron carrier protein in the thylakoid lumen, whilst pumping four protons across the membrane. Plastocyanine is the substrate of PSI, which upon excitation re-energizes the electron, which ultimately leads to the reduction of $NADP^+$ by the FNR. The proton gradient, built by PSII and Cytochrome b_6f, is used by the ATP-Synthase to make ATP, completing the light

reactions (Meier et al., 2011; Kühlbrandt and Davies, 2016).

It should be noted that anoxygenic photosynthesis using other reductants than water, such as hydrogen or hydrogensulfide, is found in nature as well. However in terms of primary production this contributes very little ($<< 1\%$, Overmann, 1997).

1.1.2 Photosystem II from thermophyllic cyanobacteria

Throughout this work, detergent-solubilized PSII particles, prepared from the thermophyllic organism *Thermosynechococcus elongatus* (*T. elongatus*), have been used. PSII preparations from this organism and the close relative *Thermosynechococcus vulcanus*, are used due to two main reasons. Firstly, the possibility of crystallizing PSII from this organism, allows for the determination of the structure of PSII by x-ray diffraction methods. Secondly, the improved stability of PSII from the thermophile over other preparations allows for functional studies on isolated complexes. In this section, a structural overview of PSII from *T. elongatus* is given.

PSII is the archetype of type II reaction centres, which are characterised by their two electron quinone chemistry.[2] This motif was studied extensively in reaction centres from purple bacteria, using numerous biochemical and biophysical techniques including X-ray crystallography (Deisenhofer et al., 1985) and EPR (Nitschke et al., 1990). Due to the close similarity between bacterial reaction centres and PSII reaction centres, many suggestions on structure and function could be made before the advent of crystallographic data on PSII.

Crystallisation of PSII became possible, once the thermophyllic cyanobacterium *T. elongatus* was used for PSII purifications. Due to its thermophyllic nature, PSII preparations from this organism retain the manganese cluster and the lumenal extrinsic polypeptides, resulting in more homogeneous samples that allow for the crystallisation of PSII.

First low resolution crystal structures were reported by Zouni et al. (2001) and Ferreira et al. (2004). Since then structures with improved resolution have been published, with the so far highest resolution being 1.9 Å (Umena et al., 2011).

[2]The Type I reaction centres, including Photosystem I, only deal with one-electron chemistry.

PSII, depicted in Fig. 1.2, is made up of at least 20 subunits, which bind 35 Chlorophylls (Chls), two pheophytins, two hemes, one non-heme iron, at least two plastoquinones, one Mn_4O_5Ca cluster, two chloride ions, twelve carotenoids and 25 lipids (Umena et al., 2011).

The majority of subunits (17 subunits) incorporate membrane spanning α-helices. Two of these subunits, PsbA (also called D1) and PsbD (also called D2), each comprising five transmembrane helices, form the reaction centre of PSII.

T. elongatus harbours three genes coding for isoforms of the D1 (*psbA1-3*) and two genes coding for isoforms of the D2 subunit (*psbD1* and *psbD2*). Under normal conditions *psbA1* is transcribed. *psbA3* has been connected to high-light conditions,*psbA2* to microaerobic conditions (Sugiura and Boussac, 2014). In this work, only conditions resulting in the expression of *psbA1* were used.

The reaction centre contains four chlorophyll *a* molecules P_{D1} and P_{D2}, Chl_{D1} and Chl_{D2} and the two Pheophytin *a* molecules, $Pheo_{D1}$ and $Pheo_{D2}$ that are responsible for the primary light absorption and charge separation. It furthermore contains the two plastoquinones, Q_A and Q_B, and in-between those, a non-heme iron, to which a bicarbonate anion is ligated. On the "electron donor side" it binds two redox active tyrosines Tyr_D and Tyr_Z. Tyr_Z connects P_{D1} and P_{D2} to the bound Mn_4O_5Ca-cluster, responsible for the water oxidation. On its periphery the RC binds two more Chl*a*-molecules, Chlz_{D1} and Chlz_{D2}.

The exact composition of lipids within PSII varies within the different available crystal structures and is likely dependent on the specific strain used, the culturing conditions and the methods of PSII isolation and crystallisation used by the different groups. A remarkable structural feature is a cluster of eight lipid molecules, which forms a shallow isolated bilayer within PSII, encircled by protein subunits D1, CP43, PsbE, PsbF, PsbJ and PsbK, most likely forming a PQ-PQH2 exchange cavity (Guskov et al., 2009).

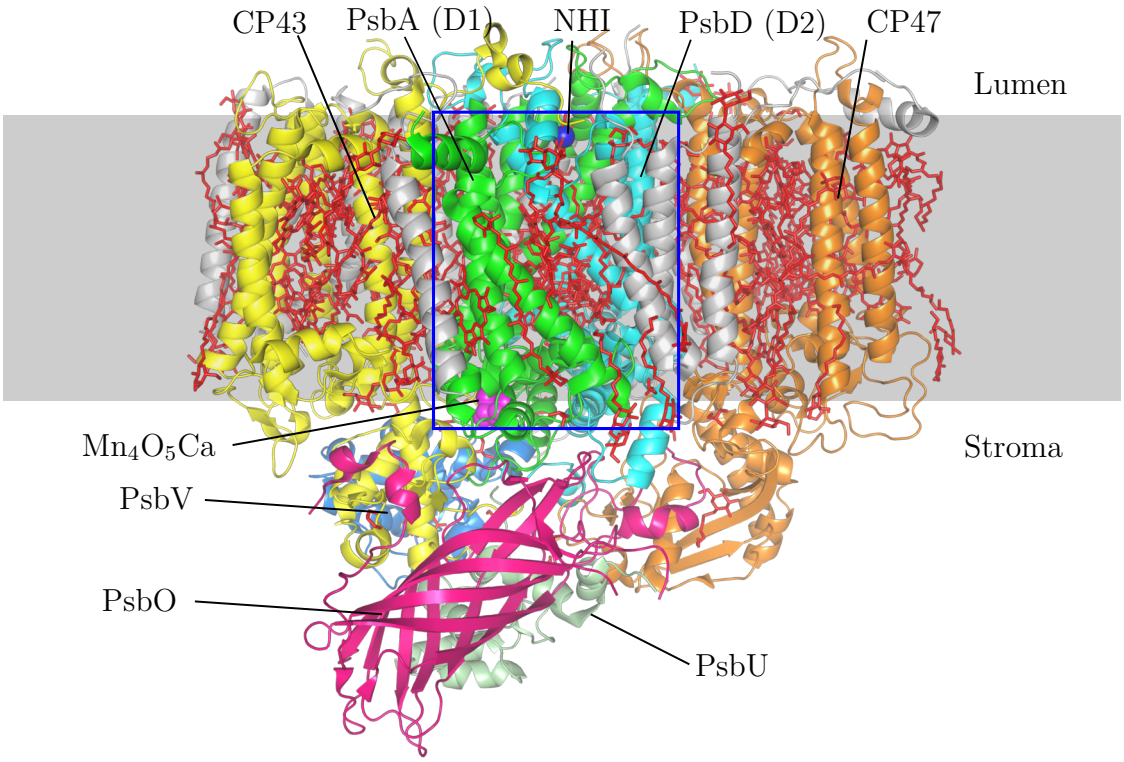

Figure 1.2: Side view of the structure of the cyanobacterial PSII monomer. Lipids and cofactors are shown in red, the position of the thylakoid membrane is indicated by the grey shading. The Mn_4O_5Ca cluster is shown in purple and the non-heme iron is blue. The blue rectangle indicates the section of the complex that is shown in Figure 1.3 (generated using the Umena et al. (2011) structure; PDB ID: 3WU2).

1.2 Mechanism of Photosystem II

In this section the mechanism of PSII, to the extent necessary for understanding the experiments in this thesis, will be introduced.

As described earlier, PSII is the light-driven water-plastoquinone oxidoreductase. Water is a very stable molecule and its oxidation, according to Equation 1.1, requires the availability of a strong oxidant, capable of removing four electrons, at a potential of 810 mV, from two water molecules. In PSII, this is accomplished by the successive conversion of four photons into electrochemical energy. Each absorbed photon promotes an electron from the ground state (HOMO) to the first excited state (LUMO) of a redox-active chlorophyll molecule. This, now high potential, electron is a strong reductant, capable of reducing a nearby acceptor. The resulting charge-separated state is further stabilized by successive electron transfer steps, each increasing the distance between the anion and the cation. The remaining chlorophyll cation is highly oxidizing. In order to oxidise water the equivalent of four chlorophyll cations is stored by oxidizing the Mn_4O_5Ca-cluster. This cluster can cycle through five different oxidation states ($S_0 - S_4$) with each absorbed photon advancing the S-state by one increment. Upon S_4 formation, an oxygen molecule is produced, and the S_0-state regenerated (Joliot et al., 1969; Kok et al., 1970). Figure 1.3 shows the sequence of events happening within PSII upon the absorption of a photon. The initial charge separation events (1 and 2 in Figure 1.3) leading to the $P^+Q_A^-$ state will be described in Section 1.2.1. The "donor side" reactions and the S-state model of the Mn_4O_5Ca cluster (3 and 4 in Figure 1.3) will be described in Section 1.2.2. The acceptor side and the quinone electron transfer (5 in Figure 1.3) will be described in more detail in Section 1.2.3.

1.2.1 Stabilisation of charge separation

After the absorption of a photon to yield an exited state chlorophyll molecule and excitation transfer to the reaction centre chlorophylls, charge separation is a central step in the energy conversion from solar to chemical energy and a basic understanding

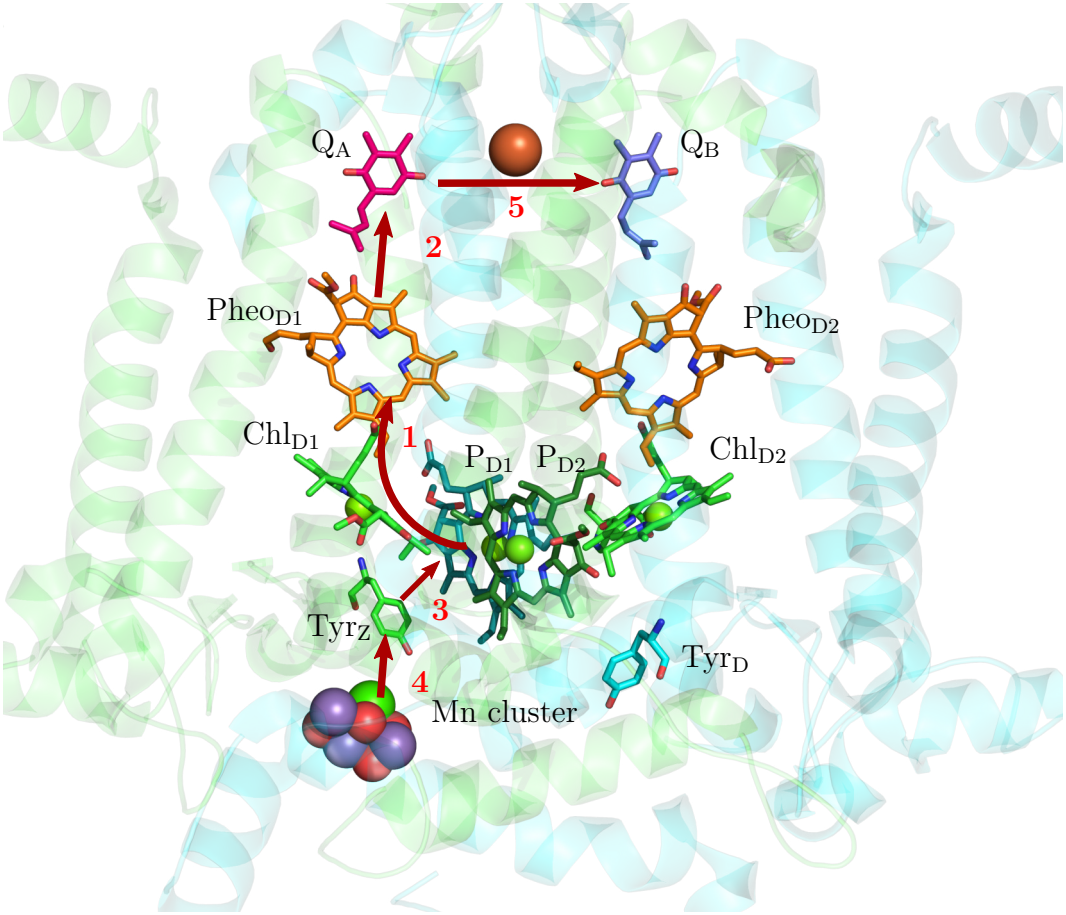

Figure 1.3: Sequence of charge separation events in PSII. 1) Primary charge separation event. The curved arrow indicates that the location of the initially formed charge-separated pair is variable. 2) Electron transfer from $Pheo_{D1}$ to Q_A. 3) Electron transfer from Tyr_Z to P^+_{D1}. 4) Oxidation of the Mn_4O_5Ca cluster by Tyr_Z. 5) Electron transfer from Q_A to Q_B. For clarity only the D1 and D2 subunits and the central cofactors without their aliphatic tails are shown. (Image was created using the Umena et al. (2011) structure; PDB ID: 3WU2).

is necessary for any work on PSII.

Overall charge separation in PSII is similar to that in bacterial reaction centres (reviewed in Diner and Rappaport (2002)). There are however a range of important differences.

The pigments P_{D1} and P_{D2} in PSII are not as symmetrically aligned, as their counterparts in purple bacteria. This leads to a smaller excitonic coupling of P_{D1}/P_{D2} (85-150 cm^{-1}) than in its counterpart in purple bacteria (500-1000 cm^{-1}). Therefore, there is no long-wavelength trap in PSII that fixes the localisation of the exciton to a specific pigment. Indeed the coupling of the P_{D1}/P_{D2} to their respective Chl_{D1}/Chl_{D2} neighbours and the coupling of those to the pheophytins is, although smaller, of comparable order of magnitude ($\approx$50 cm^{-1}). The ambient thermal energy is enough to ensure that the excitation could be on any of the four central chlorophylls and also the two pheophytins. What then occurs in the first few picoseconds after excitation is a slew of different charge separation reactions, potentially involving, P^+_{D1}/P^-_{D2}, P^+_{D1}/Chl^-_{D1},$Chl^+_{D1}/Pheo^-_{D1}$ and so on (Dekker and Van Grondelle, 2000).

It seems plausible that different primary charge pairs may be formed depending on minor changes in structure and environment that may be significant in terms of function. If, for example, the cation were located on Chl_{D2} instead of P_{D1} under conditions of high photon flux, it would result in efficient electron transfer from the β-carotene/Cyt $b559$/Chlz_{D2} side-pathway (Romero et al., 2010; Faller et al., 2005).

A few tens of picoseconds after initial charge separation, electron transfers lead to a situation similar to purple bacteria reaction centres with the charge pair $P^+_{D1}/Pheo^-_{D1}$ formed. Consequently the next stabilisation of the charge transfer, the electron transfer to Q_A, happens in about 300 ps (Grabolle and Dau, 2005).

When Q_A is still reduced, the quantum yield of charge separation is low and the excitation energy is rapidly lost as fluorescence or heat (Schatz et al., 1988; van Mieghem et al., 1995). At time-scales larger than 100 µs fluorescence is a reliable marker of the redox state of Q_A and is used in fluorescence based imagining and measurement techniques.

1.2.2 The electron-donor side and the S-state model

The lumenal side of PSII, also called the electron-donor side, is the side where the Mn_4O_5Ca-cluster catalyses the water oxidation. Research on both the donor and acceptor side benefits from the ability to synchronise the S-states of the Mn_4O_5Ca-cluster in a given PSII sample. Therefore, the S-state model of the Mn_4O_5Ca-cluster is briefly introduced here.

After formation of P^+, a proton-coupled electron transfer from Tyr_Z re-reduces P^+. Upon oxidation the $Tyr_Z^{\bullet+}$ looses its proton to an adjacent histidine (D1-His190). Subsequently the $Tyr_Z^{\bullet}$ radical oxidises the Mn_4O_5Ca-cluster (Rappaport and Diner, 2008). As mentioned before, based upon work done by Joliot et al. (1969), Kok et al. (1970) proposed a mechanism in which the cluster cycles through five different states, S_0 - S_4. S_0 - S_3 reflect four different valence states of the manganese in the cluster. From each state to the next, one electron is removed from the cluster via Tyr_Z and thus one oxidizing equivalent is stored. The S_4 state is considered to be $S_3Tyr_Z^{\bullet}$ with no detectable further oxidation of the manganese until S_0 is formed.

Interestingly the deprotonation pattern of the cluster is 1,0,1,2 instead of 1,1,1,1 meaning, that no proton is released on the $S_1 \rightarrow S_2$ transition. Whilst on the first two transitions, electron transfer precedes proton transfer, it is thought that on the subsequent two turn-overs the order is reversed. In total four electrons are removed from two water molecules in one step, upon formation of the S_4-state, resulting in the formation of one oxygen molecule (Dau et al., 2012; Zaharieva et al., 2016).

The S-state stable in the dark is the S_1-state. Whilst S_2 and S_3 recombine with electrons from the acceptor side within seconds, the S_0 state is oxidized to S_1 in the dark by Tyr_D. This may be a mechanism for preventing over-reduction of the Mn_4O_5Ca cluster and subsequent loss of the manganese ions (Styring and Rutherford, 1987).

Doubt remains about the exact mechanism of the water oxidation. Two different types of mechanisms are at present suggested for the O–O bond-formation step in Photosystem II. The first one is a coupling between an oxyl radical and a bridging oxo (Siegbahn, 2008). The second one is a nucleophilic water attack on a terminal oxo (or

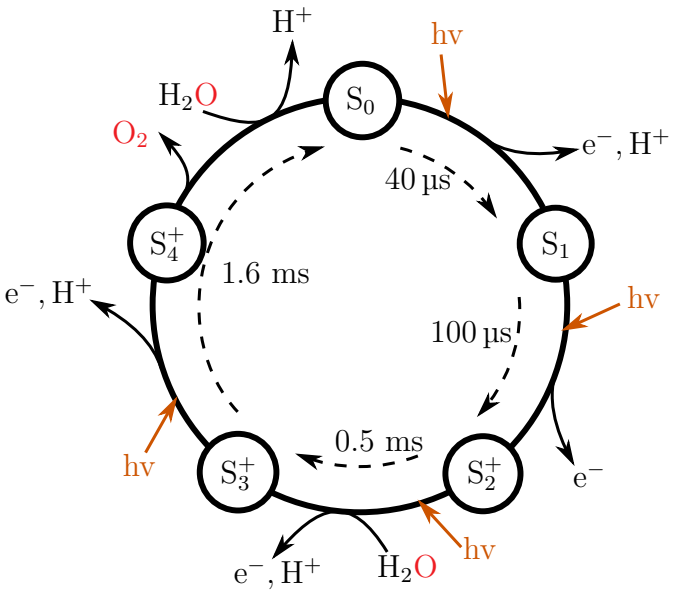

Figure 1.4: The S-state cycle. Also shown are halftimes for the various steps of the cycle.

oxyl) group (Sproviero et al., 2008). Whilst spectroscopic experiments are in better agreement with the former model (Cox et al., 2011, 2014), definite experimental validation of either mechanism is still elusive.

1.2.3 The electron-acceptor side

Vinyard et al. (2013) calculated from the half times of the S states that the theoretical maximum rate of water oxidation by the Mn_4O_5Ca cluster is 500 - 1000 s^{-1}. In contrast, experimental oxygen-evolution rates from PSII vary between 25 and 88 s^{-1}. This large discrepancy is explained by the acceptor side chemistry.

The quinone-iron-acceptor complex of PSII accepts the electrons generated by photochemical charge separation. Quinone reduction is a two electron/two proton process, conversely it requires two charge separation events to be completed. Under normal conditions, the rate-limiting step in PSII is the transfer of electrons from Q_A to Q_B and Q_BH_2 exchange with the plastoquinone pool in the thylakoid membrane.

Not only is the acceptor side limiting the overall rate of PSII, the slow rates also lead to the prolonged presence of unstable, high energy intermediates. This in turn can lead to damaging reactions, necessitating complex and costly repair mechanisms (Aro et al., 1993; Vass and Aro, 2008; Pospíšil, 2016). Here a general introduction into the structure, mechanism and energetics of the acceptor side is provided. More detailed introductions into the energetics and kinetics of the acceptor side will be provided in the corresponding Chapters 3 and 4.

The structure of the acceptor side

The structure of the PSII acceptor side bears many similarities to the one found in bacterial reaction centres, there are, however, profound differences between the systems. In bacterial reaction centres, the acceptor side has been extensively studied and is better understood (Wraight, 2004). Firstly, the bacterial reaction centre is shielded from the cytoplasm by the large H-subunit. In PSII the quinone site is exposed, allowing for electron transfer to soluble acceptors. Furthermore, a number of conserved residues, important for function in bacterial reaction centres, are not present in PSII. Glutamate-L212, for example, which appears to be a prerequisite for the second protonation step in bacterial reaction centres, is replaced with an Alanine in PSII. Whilst in bacterial reaction centres only the headgroup and one isoprenyl group of Q_B are bound to the protein, in PSII, due to the subunits surrounding the D_1/D_2 core, the quinone is entirely surrounded by PSII subunits. All this has implications for the mechanism and protonation pathways of Q_B so that whilst the bacterial reaction centre quinone site may be used as a template for the study of the PSII acceptor side, mechanistic differences should be expected.

Q_A, the primary electron acceptor, is a plastoquinone located between the $Pheo_{D1}$ and the non-heme iron, functioning as a one electron transmitter to Q_B. It is bound to the protein mostly by van-der-Waals interactions of the isoprenyl tail with the protein and lipids. The main interactions that fix the headgroup to the specific site in the protein are the hydrogen bonds formed by the carbonyl residues of the quinone with the protein (Deligiannakis et al., 1999).

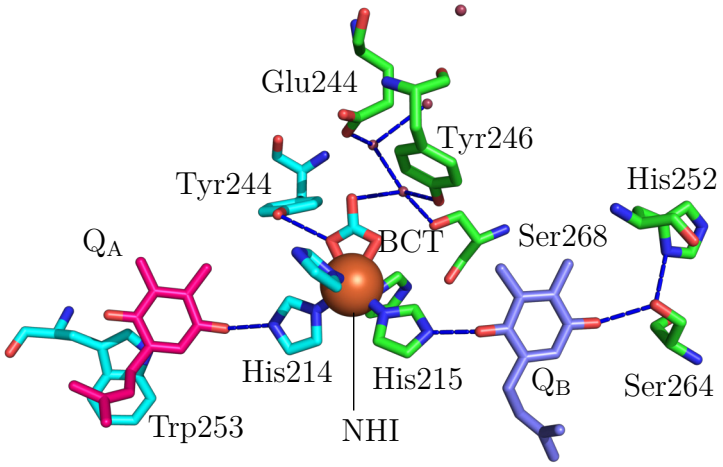

Figure 1.5: Acceptor side of PSII. Shown are the Cofactors Q_A and Q_B, the non-heme iron, its bicarbonate ligand and amino-acids that provide hydrogen bonds or ligands to the cofactors (generated using the Umena et al. (2011) structure; PDB ID: 3WU2).

The non-heme iron is a hexa-coordinate high-spin Fe^{II} with a distorted octahedral geometry. It is ligated in distorted octahedral configuration by the nitrogens of four histidyl residues coming from the D1 and D2 proteins and a bidentate bicarbonate (in purple bacteria reaction centres a glutamate ligates the iron instead of a bicarbonate (Deisenhofer and Michel, 1989)). One of the histidines on each sides is also involved in a hydrogen bond to the respective quinone.

The role of the non-heme iron and of its bicarbonate ligand is still not completely clear. Although it is placed between the two quinones, its redox potential is generally seen as too positive, for an active role in electron transfer. Suggestions for the role of the non-heme iron so far include: purely structural, regulation of electron transfer and involvement in degradation and/or production of radical oxygen species (see Müh and Zouni (2013) for a review on these hypotheses). Bicarbonate can be replaced with many small molecules such as formate, acetate, glycolate, glyoxalate, cyanide, NO, fluoride and others. This is usually accompanied with significant reduction in electron transfer rates (Petrouleas and Diner, 1990; Van Rensen, 2002). The

replacement of the bicarbonate with cyanide or hydroxide also leads to a change of spin-state from high to low-spin of the iron complex (Deligiannakis et al., 1997; Koulougliotis et al., 1993; Sanakis et al., 1994).

Recently Brinkert et al. (2016) rationalized the loss of bicarbonate, and the thereby induced shift of the Q_A redox potential under certain conditions as a sink (CO_2) to source (PSII) feedback mechanism. Because the reductive pentose-phosphate cycle uses the electrons generated by the light reactions to reduce CO_2, low CO_2 concentrations could block the electron flow in the light reactions and result in an over reduction of the quinone pool which would then lead to damage of PSII. Therefore, the down regulation of PSII, induced by the debinding of bicarbonate as a result of low CO_2 concentrations, would constitute a regulatory mechanism to prevent this damage. *In vivo* validation of this effect has, however, not yet been produced.

The secondary quinone, Q_B, is the final electron acceptor of PSII and not tightly bound to the protein. Instead, it can exchange with quinones in the thylakoid membranes and when reduced, transfers electrons to the Cyt b_6f complex. The headgroup carbonyls form two hydrogen bonds similar to Q_A, the proximal carbonyl forms a hydrogen bond to a histidyl ligand of the non-heme iron (D1-His215) and the distal carbonyl forms a hydrogen bond to a serine residue (D1-Ser264), which itself accepts an H-bond from D1-His252. This histidine is located on the protein surface in contact with the aqueous medium (Crofts et al., 1987). The exact number and position of water molecules near Q_B can not be determined definitively as it differs in the current crystallographic data. There are two water molecules in close vicinity of His252 in the structure by Umena et al. (2011). The structure from Suga et al. (2014) resolved three waters in that area. Another water molecule, not present in either of those crystal structures, has been proposed by Saito et al. (2013a) as a bridging water in an H-bond network from the D1-Tyr246 to the D1-His215. This water could be important for the protonation of $QBH^{\bullet -}$. The authors speculate that it is not visible in the crystal structure because of the X-ray beam generating $OH^{\bullet}$. This hypothesis is problematic, because the Suga et al. (2014) structure is

supposedly radiation damage free.

An additional third quinone site has been postulated based on crystallographic data by Guskov et al. (2009), but this was not confirmed by subsequent crystal structures. Nevertheless, there is good evidence that more than one mobile quinone is available in most preparations of PSII (Fufezan et al., 2005; Krivanek et al., 2007). Whether this quinone is bound to a well defined binding site, where specific residues fix its position, but is lost during PSII preparations or alternatively there is no third site, is not currently known. The aforementioned lipid patch within PSII, as well as the two quinone diffusion channels towards the Q_B site are obvious choices for the location of additional mobile quinones bound to PSII (Müh et al., 2012; Van Eerden et al., 2017).

Mechanism of quinone electron transfer

Mechanistic details for the electron transfer in PSII are not yet known. However, based on the crystal structure, the analogy to bacterial reaction centres, and *in silico* methods, reasonable suggestions can be made. The most concerted effort in this direction comes from work by Saito et al. (2013a). In this thesis, the kinetics of the quinone electron transfer were studied, therefore the proposed model for the electron and proton transfer steps will be briefly introduced.

Saito et al. (2013a) describe the Q_B reduction in five steps. Firstly, one electron is transferred from $Q_A^{\bullet -}$ to Q_B, which results in the uptake of a proton from the outside by D1-His252, which is H-bonded to the D1-Ser264. Secondly, the presence of $Q_A^{\bullet -}$, formed on the second turnover, leads to the protonation of the distal carbonyl group of $Q_B^{\bullet -}$ by the D1-Ser264. This protonation occurs with the concerted arrival of a proton on the D1-Ser264 from the previously protonated D1-His252, yielding again, the neutral histidine. Thirdly, the neutral semiquinone $Q_B^{\bullet}$ may be transiently formed before arrival of the electron from $Q_A^{\bullet -}$. Fourthly, the proximal carbonyl oxygen of the now negatively charged $Q_BH^{\bullet -}$ has a single-well H-bond to the D1-His215. This means there is no activation energy required to transfer the proton, resulting in the formation of Q_BH_2. Finally, the neutral quinol stays bound until the

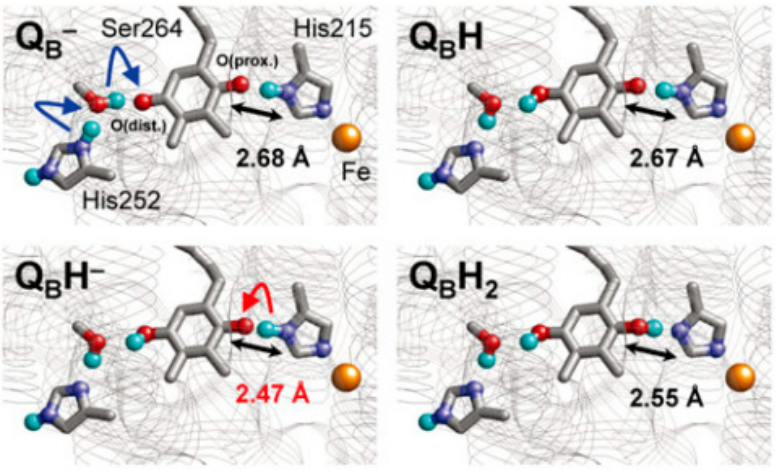

Figure 1.6: Changes in H-bond network geometry of Q_B in response to reduction Saito et al. (2013a).

D1-His215 anion is reprotonated. The protonation pathway for this second proton is unknown, however, the authors suggest a route involving the bicarbonate ligand and the previously mentioned water molecule in the Q_B site, that is not present in the crystal structure.

One interesting feature of this mechanism is that the orientations of the two tyrosines D1-Tyr246 and D2-Tyr244 (and the bicarbonate ligand) differ in the QM/MM calculations depending on the location of the anion on either Q_A or Q_B. This might offer a long-sought-after, mechanistic explanation of the so-called gating effect.

1.3 Energetics, Damage and Regulation

In this work the midpoint potential of the $Q_B/Q_B^{\bullet-}/Q_BH_2$ couples have been determined. These values are of direct importance for the energetic picture of PSII and therefore a brief introduction into the energetics of PSII together with the current views of damage routes and tuning within PSII will be presented here.

The charge separation reactions within PSII are reversible. In the best case, the reversal of charge separation poses an efficiency loss of solar conversion, in

the worst case it leads to the damage of the enzyme, necessitating complex repair and replacement processes (Rappaport et al., 2002; Nixon et al., 2010). Therefore, sufficient free-energy drops from one intermediate state to the next are necessary to favour the forward reactions over the back reactions, and subsequently, quickly remove the reaction products. Large drops in free-energy however also limit the solar conversion efficiency, as a smaller proportion of the energy in each photon is stored in the chemical bonds, that are made in the process, and more energy is lost to heat.

Therefore, since the divergence from the common ancestor of bacterial and oxygenic reaction centres, the free-energy levels of the intermediate states have been evolutionary tuned, in a compromise between three main factors: the energetic efficiency, the kinetic efficiency and the prevention of damage under the emerging presence of oxygen. Consequently, determining the free-energy level of these transiently formed, charge separated states during the turnover of PSII is essential for our understanding of the enzyme, as it constrains the mechanistic models and yields insights into the trade off's unique to PSII, and efficiency constrains of PSII.

Despite the importance, to date, only the midpoint potentials of Q_A and PheoD1 have been directly measured. This is due to the fact that the donor side cofactors are too oxidizing and no good mediators exist. Nevertheless, using kinetic measurements of all the involved forward and back-reactions, and the energy of the absorbed photon, the so far determined values of E_m can be used to fix the other cofactors using kinetically derived estimates of the free-energy changes ΔG between the intermediate states. Although some problems with this approach will be discussed later, a rather consistent model now exists. Figure 1.7 shows the estimated free-energy changes occurring upon forward electron transfer in PSII.

The biggest free-energy drop occurs from the $P^+Pheo^-_{D1}$ to the $P^+Q^-_A$ state. This has been rationalized as a way to prevent damaging back reactions.[3] Mainly three different pathways of charge recombination are discussed in PSII (blue arrows in Figure 1.7). These are the direct route, by recombination of the $P^+Q^-_A$ state, the

[3]More detailed discussions of the exact values and rationales of the intermediate states are provided in the reviews by Rappaport and Diner (2008), Cardona et al. (2012) and Rutherford et al. (2012).

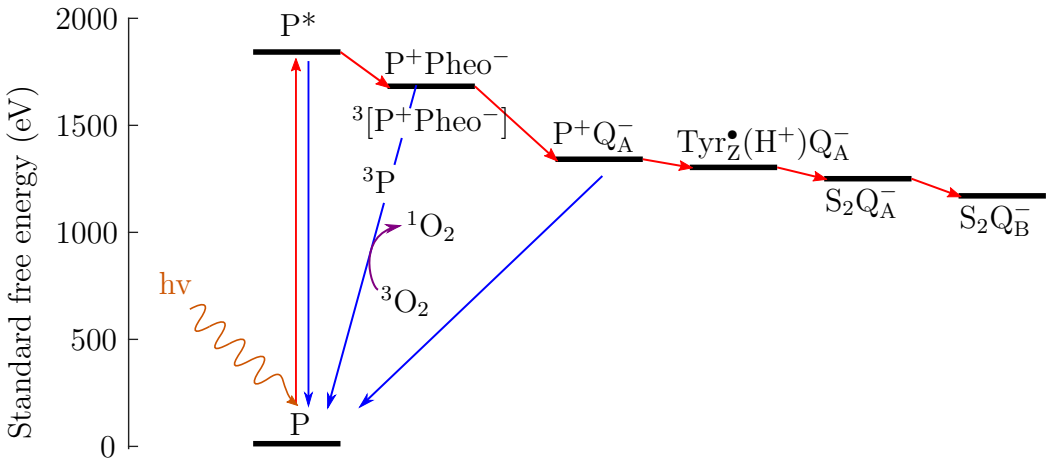

Figure 1.7: Estimated free energy changes within PSII. The red arrows represent forward charge separation, whilst the blue arrows show the main back reactions.

indirect route, via reforming of the $P^+Pheo^-_{D1}$ state, and the excitonic route, via the reforming of P* with the subsequent re-emission of a photon to reach the ground state. In PSII the dominant route is the indirect one involving the $P^+Pheo^-_{D1}$ state. When this state is reformed from the $P^+Q^-_A$ state, due to spin dephasing, in most centres the lower energy triplet state $^3P^+Pheo^-_{D1}$ is formed. When this state recombines the chlorophyll triplet ^3P is rapidly formed, which reacts with oxygen to form highly reactive singlet oxygen $^1O_2$ and the ground state ^1P. Whilst this is likely to be the main damaging reaction occurring in PSII (Fufezan et al., 2002; Rehman et al., 2013), a range of other damaging routes, such as a direct interaction of the non-heme iron with oxygen, or donor side related damage have also been suggested (Vass and Aro, 2008; Keren and Krieger-Liszkay, 2011; Pospíšil, 2012). In any case, a larger gap in free-energy from the $P^+Pheo^-_{D1}$ to the $P^+Q^-_A$-state is expected to reduce the rate of damage of PSII by favouring the direct recombination route over the triplet forming indirect route.

In reality, the situation is more complicated, because, as will be described in

the following section, the redox potential of Q_A is tuned in response to different environmental conditions and, depending on the exact conditions, four different values are currently accepted for the redox potential of Q_A.

It should be pointed out that the previously mentioned assumption, that the free-energy change associated with a given reaction within PSII is equal to the difference in redox potential between the electron donors and acceptors measured under equilibrium conditions, is problematic. In fact, for the only case where it is possible to evaluate this strategy so far, the electron transfer between $Pheo_{D1}$ and Q_A, Rappaport and Diner (2008) have shown that the ΔG value must be considerably smaller than the ΔE value determined from equilibrium redox titrations if there is to be any driving force for the advancement of the manganese cluster.

Multiple explanations can be found for such discrepancies. Firstly, the two methods do not probe the redox cofactors in comparable states. Whilst redox titrations necessitate thermodynamic equilibrium to be maintained between the cofactor that is titrated and the solution that is poised and a given potential, kinetic measurements are per definition non-equilibrium measurements. The free-energy of intermediate states may differ significantly in these situations, and energetic relaxation in the protein environment (such as proton transfer, conformational changes) need to be taken into account. This is especially relevant for the electron transfer on the acceptor side of PSII, where proton transfer and some form of gating mechanism must occur.

Secondly, the different cofactors in PSII are located closely together and this may result in significant electrostatic interactions between the different cofactors. In this case the free-energy level of a given cofactor is influenced by the redox state of nearby electron carriers. This introduces the problem that throughout a redox titration where the potential is poised externally, all of the cofactors that are accessed by the redox mediators, sequentially dependent upon their potential, undergo a redox change in the same direction (i.e. all are either reduced or oxidized). In kinetic experiments however, two nearby cofactors involved in an electron transfer reaction will oxidise and reduce each other (one will be oxidized at the expense of the other). Consequently, if the electrostatic interaction between the two is significant, the

difference between their equilibrium E_ms will differ from the free-energy change associated with the electron transfer between them (Rappaport and Diner, 2008). For example, in all measurements of the midpoint potential of Q_A so far, Q_B was in its fully reduced state, Q_BH_2, whilst under functional conditions either Q_B or $Q_B^{\bullet-}$ is present.

1.3.1 Redox tuning of the quinone acceptor side

As the energetics of the acceptor side quinones and their regulation are at the centre of this thesis, the current knowledge will be reviewed here in more detail. This allows for the presentation of the aims of this thesis in the next section.

Krieger et al. (1995) reported that previously over 35 different values for the $Q_A/Q_A^{\bullet-}$ - redox couple had been published. They measured two different potentials for $Q_A/Q_A^{\bullet-}$ depending on the presence of the Mn_4O_5Ca-cluster. A low potential form (E_m = -81 mV ± 16 mV) for intact PSII centres and a high potential form (E_m = 64 mV ± 25 mV) in the absence of the cluster or even in absence of only the Ca^{2+} - ion (Krieger et al., 1995). Shibamoto et al. (2009) reported values for the high and low potential form that were 80 mV more negative than the values reported by Krieger (-140 mV intact PSII; 20 mV Mn-depleted PSII). Brinkert et al. (2016) were able to show that the discrepancy between the two sets of values can be explained by a change in the K_D of the bicarbonate ligand to the non-heme iron when Q_A is reduced, leading to the de-binding of the bicarbonate and an up shift in the $Q_A/Q_A^{\bullet-}$ redox potential under the conditions used by Krieger et al. (1995).

Both, the effect of the presence of the Mn_4O_5Ca-cluster and the redox tuning effect of bicarbonate on the potential of Q_A are rationalized as protection against photodamage.

During photoactivation, which is the process of assembling the active enzyme complex, the Mn_4O_5Ca cluster, the rate at which the donor side can donate electrons, is limited. In this case the lifetime of photo-generated charge separated states is longer than under functional conditions. This leads to increased rates of recombination based photodamage (Johnson et al., 1995). The higher potential Q_A reduces this

photodamage by increasing the gap between $P^+Q_A^-$ and P^+Pheo^- and favouring the direct route of recombination over the indirect route which leads to triplet formation.

Similarly, if there is a block in electron flow downstream of PSII, the quinone pool and Q_B will eventually become fully reduced, again, increasing the lifetime of the $Q_A^{\bullet-}$ state and increase the chance of recombination based photodamage. The bicarbonate effect has been rationalized as a "sink to source" regulation to prevent damage of PSII in this kind of situation (Brinkert et al., 2016). In conclusion, the redox potential of Q_A is tightly regulated in response to environmental conditions to protect against damaging charge recombination reactions resulting from prolonged lifetimes of the reactive intermediates of charge separation.

The secondary electron acceptor Q_B is the only exchangeable, mobile electron acceptor within PSII. This, in combination with its two-electron chemistry, poses a unique set of constrains. It is the only redox component within PSII where kinetic control by removing the product of the electron transfer is not possible. Instead, the first electron arriving on Q_B forms the semiquinone $Q_B^{\bullet-}$. This highly reactive molecule needs to be stabilized until a second electron can be generated and transferred to the quinone site (Rutherford et al., 2012). The simplest way to prevent energy loss would be to slow down the backward reaction rate. This could be done either, by making the back-reaction strongly uphill in energy or, by introducing a kinetic barrier in form of a high activation energy between the reactant and product configurations. Which strategy is used by PSII and how it is achieved on a molecular level is not yet clear.

To begin with, the redox potentials for the two redox couples $Q_B/Q_B^{\bullet-}$ and $Q_B^{\bullet-}/Q_BH_2$ are not well studied. It is reasonable to assume that the redox potential of the Q_B couples lies between the values of Q_A and the value for a free plastoquinone in the membrane ($\approx$ 120 mV (Golbeck and Kok, 1979)). Early estimates were based on kinetic measurements of the forward and back reactions rates (Diner, 1977). This approach predicts a difference in ΔE_m of 70 mV (Robinson and Crofts, 1983) between the $Q_A/Q_A^{\bullet-}$ and $Q_B/Q_B^{\bullet-}$ couples. A similar approach, but based on thermoluminescence measurements, yields a difference in ΔE_m of $\approx$ 80 mV

(Minagawa et al., 1999; Rappaport and Lavergne, 2009). If the value currently thought to represent the midpoint potential of Q_A under functional conditions is used as a reference (E_m = -145 mV, Brinkert et al. (2016)), the Q_B couples should be around -60 mV.

This does not agree with the only attempt of an EPR detected redox titration of Q_B reported in the literature so far which yielded a redox potential of $E_m \approx 0$ mV (Corrie et al., 1991) for both Q_B couples in PSII from *Phormidium laminosum*. Furthermore, a recent determination, using FT-IR measurements by Kato et al. (2016), yielded even more positive redox potentials of $E_m(Q_B/Q_B^{\bullet-}) = 93$ mV and $E_m(Q_B^{\bullet-}/Q_BH_2) = 213$ mV for intact PSII core complexes from *T. elongatus*.[4]

Because of this uncertainty in terms of the redox potential, to date the influence of the different configurations of the PSII on the redox potential of Q_B (Q_A, non-heme iron, bicarbonate, donor side influence etc.) is unknown.

Another aspect, unique to the quinone in the Q_B-site, is that it is in constant exchange with the quinone pool and therefore a relay of the pool redox state into PSII. Therefore, it is plausible that regulation of PSII occurs in the opposite direction as previously discussed, i.e. that Q_B and Q_BH_2 affect the acceptor side and PSII function differentially. This hypothesis is supported by the fact that different herbicides which bind at the Q_B site, through the connection via the non-heme iron, have different effects on the E_m of Q_A (Krieger-Liszkay and Rutherford, 1998).

In conclusion, previous data on the redox potential of the two Q_B couples spans almost the entire range of possible values and reliable information on any sort of adaptation or regulation of Q_B in response to environmental changes is non existent.

1.4 Objectives of the Research Projects

PSII research in general, and research on PSII from *T. elongatus* in particular, is biased towards the understanding of the donor side reactions. Whilst the partitioning

[4]Slightly different values were obtained for Mn-less PSII: $E_m(Q_B/Q_B^{\bullet-}) = 87$ mV and $E_m(Q_B^{\bullet-}/Q_BH_2) = 157$ mV

of PSII in two, more or less, independent halves benefits the conceptual understanding of PSII, in reality the processes on both sides are not independent, and research based on that idea is inevitably flawed. The acceptor side is of importance to understand the energetic and kinetic constrains of PSII and their mechanistic causes. Damage to PSII occurring due to the acceptor side chemistry is not fully understood, neither are the regulatory mechanisms within PSII to protect against this damage.

The work presented in this thesis therefore is focused on the acceptor side of PSII. As more detailed introductions into the background, methods and experimental design will be provided in the respective chapters, here it is sufficient to briefly state the objectives of the chapters.

1.4.1 Redox potential of Q_B

An accurate and reliable determination of the redox potential of the two Q_B redox couples has, so far, been elusive. Yet this is an important value, capable of shedding light onto the energetics and regulation of PSII. One aim of this thesis, presented in Chapter 3, is therefore to measure the redox potential of Q_B. This is to be done, mainly, using EPR detected redox titrations, although other methods should be explored as well.

1.4.2 Kinetic study of quinone electron transfer

The second topic of this thesis is a kinetic study of electron transfer on the acceptor side of PSII. This is relevant for two reason: Firstly, reliable kinetic measurements are an important first step towards understanding the processes occurring on the acceptor side. Secondly, as will be covered in more detail in Chapter 4, an accurate determination of the rates of electron transfer, in samples relevant to current research, is necessary for gaining useful information, no matter which aspect of PSII is studied. A range of different spectroscopic probes should be used to determine the rates of the electron transfer processes occurring on the acceptor side of PSII.

2 Materials and Methods

2.1 Culturing of T. elongatus

2.1.1 Culture conditions

All cyanobacteria were grown in DTN medium (Mühlenhoff and Chauvat, 1996) supplemented with 10 mM $NaHCO_3$ at 45 °C. Liquid cultures of 5 - 30 ml and 50 - 150 ml were grown in sterile 60 ml and 225 ml vented flasks (Corning) respectively, shaking at 150 rpm under $20\,\mu mol\,m^{-2}\,s^{-1}$ light in an incubated shaker (Agitorb 200C, Aralab). Liquid cultures of 200 ml, 1000 ml and 2000 ml were grown in 500 ml, 3000 ml and 5000 ml wide-necked Erlenmeyer flasks with cotton plugs in an incubated shaker (Innova 44, New Brunswick Scientific). CO_2-supplemented cultures were sparged with filter-sterilised 5 % ($\frac{v}{v}$) CO_2 in air at $150\,ml\,min^{-1}$. Cultures were also maintained on 40 ml solid DTN with 1.4% ($\frac{w}{v}$) Bacto Agar (BD), 20 mM $NaHCO_3$ in 90 mm Petri dishes. Where required, mutant cultures were supplemented with $40\,\mu g\,ml^{-1}$ kanamycin and $5\,\mu g\,ml^{-1}$ chloramphenicol.

2.1.2 Optical density and absorption spectra measurements

Absorbance spectra and wavelength-specific optical densities were measured using 1 cm path length disposable cuvettes in a UV/visible spectrophotometer (Shimadzu UV-1601). The cell densities of liquid cultures were used to track growth phases, measured by optical density at 750 nm. The minimal absorption at this wavelength means that the majority of the optical density will be due to light scattering, roughly proportional to cell density and independent of cell pigment concentration.

2.2 Purification of PSII

2.2.1 Preparation of thylakoid membranes

T. elongatus cells, either the CP43HIS D_2-Y160F strain (Sugiura et al., 2004) or the CP47HIS strain (Sedoud et al., 2011b), were grown until 18 L of culture reached an Optical density (OD) of 0.6 at 750 nm. After harvesting by filtration with a Sartocon Hydrosart Microfiltration Cassette (0.2 µm; Sartorius Stedim UK Limited, Epsom, UK), the cells were centrifuged (11280 g, 10 min), washed once with buffer 1 (40 mM MES, 2.5 mM $MgCl_2$, 2.5 mM $CaCl_2$, 10% glycerol, 1 M betaine, 10 mM $NaHCO_3$, pH 6.5 adjusted with NaOH), resuspended in the same buffer, containing 0.2% (w/v) BSA, 1 mM BA, $5\,\mu g\,ml^{-1}$ DNase I and protease inhibitor cocktail (05 056 489 001; Roche, Basel, Switzerland) added, to a Chl concentration of $\approx 1.5\,mg_{Chl}\,ml^{-1}$. The cells were ruptured by being processed twice through a high pressure (20 kpsi) disruption system (Constant Systems Ltd., Northants, UK). All following steps were carried out in dim green light at 4 °C. Unbroken cells were removed by centrifugation (1,500 g, 5 min, 4 °C). Thylakoids were resuspended at $1\,mg_{Chl}\,ml^{-1}$ in buffer 1 and stored in aliquots in liquid nitrogen, or used immediately.

2.2.2 Purification of PSII by Ni-affinity chromatography

PSII purification from *T. elongatus* was done using Ni-affinity chromatography based on the method of Sugiura and Inoue (1999) with modifications described below. This method relies on the presence of a HIS-tag. Here either mutants with HIS-tagged CP43 (Sugiura et al., 2004) or CP47 (Sedoud et al., 2011b, supporting information) were used. Thylakoids ($1\,mg_{Chl}\,ml^{-1}$, in buffer 1) were treated with 0.8% (w/v) n-dodecyl-β-D-maltoside (β-DDM, Biomol, Germany). After brief, gentle mixing the suspension was centrifuged (60 min, 185,000 × g) to remove the non-solubilized material. The supernatant was then applied to an FPLC column containing an equal volume of Probond Ni-affinity-resin (Invitrogen, Netherlands) that had been pre-equilibrated with buffer 2 (buffer 1 + 15 mM imidazole, 0.03% (w/v) β-DDM,

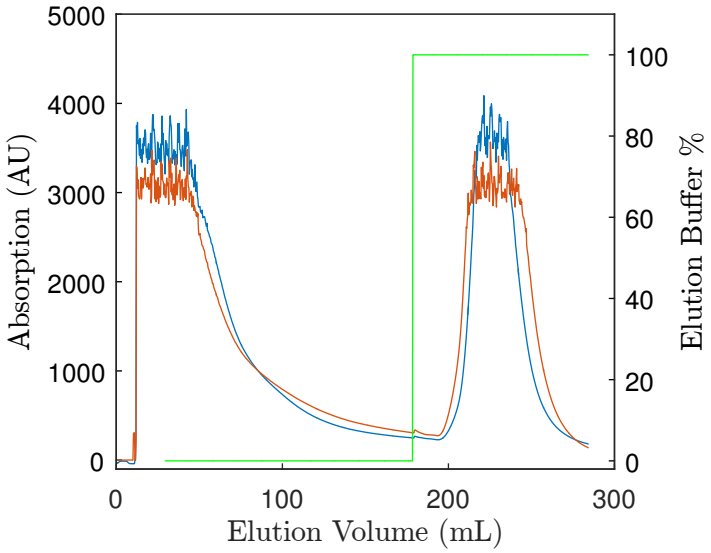

Figure 2.1: Typical elution profile of purified PSII with Ni-affinity chromatography. Shown in blue/orange is the absorbance measured at 280/440 nm. Shown in green is the percentage of the elution buffer B3.

pH 6.5 adjusted with NaOH). The resin was washed with buffer 2 until the OD_{670} value of the eluate decreased below 0.05 using the AKTA Purifier 10 (GE Healthcare Life Sciences, USA). PSII core complexes were then eluted with buffer 3 (buffer1 + 300 mM imidazole, 0.06% (w/v) β-DDM, pH 6.5 adjusted with concentrated HCl) and collected in fractions of 50 mL. Figure 2.1 shows a typical chromatogram. If no anion exchange step was required, fractions with an $OD_{670} > 0.1$ were concentrated and washed using centrifugal filters (100 kDa Amicon Ultra-15, Millipore-Merck, Germany). PSII core complexes were resuspended in buffer 1 at a Chl concentration of 1 to 1.5 $mg_{Chl}\,ml^{-1}$ and stored in liquid N_2 until usage. The estimate of Chl concentration was done by solubilizing the biological material in methanol and using an extinction coefficient of 79.95 $mg\,ml^{-1}\,cm^{-1}$ at 665 nm (Porra et al., 1989).

When samples were to be used for immediate anion exchange chromatography, instead of buffer 2 and 3, the buffers TP2 and TP3, listed in Table 2.1 were used to allow for subsequent binding of the protein to the anion-exchange-column.

Table 2.1: Buffers used for anion exchange chromatography of PSII.

Buffer TP2	15 mM Imidazole, 20 mM MES, 2.5 mM $MgCl_2$, 2.5 mM $CaCl_2$, 0.5 M D-mannitol, 0.03% β-DDM, pH 6.5.
Buffer TP3	TP2, but with 300 mM Imidazole.
Buffer UnoQ1	5 mM $MgSO_4$, 20 mM MES, 2.5 mM $MgCl_2$, 2.5 mM $CaCl_2$, 0.5 M mannitol, 0.03% β-DDM.
Buffer UnoQ2	UnoQ1, but with 200 mM $MgSO_4$.

2.2.3 Purification of PSII by anion exchange chromatography

The PSII solution after the Ni-affinity-chromatography step was loaded directly onto a Bio-Rad UNO Q-12 column, preequilibrated with 2 Column volume (CV) of buffer UnoQ1 using the AKTA Purifier 10 system. The column was washed with 2 CV of UnoQ1 or until $OD_{280} < 0.025$. PSII complexes were eluted with a linear gradient from 0-60% buffer UnoQ2 over 180 ml at a flow rate of 4.5 ml/ min in 2 ml fractions. The five resulting peaks were pooled separately and concentrated using Amicon Ultracel-100,000 MWCO centrifugal filters before storing at -80 °C. Figure 2.2 shows a typical elution profile from the anion-exchange-column. Peaks two and three represent the active monomer and dimer fractions (Douglass, 2015). These pools exhibit the highest oxygen evolution activity. Pool one does not evolve oxygen but was reported to bind psb27, a protein implicated in biogenesis and repair of PSII. Pool 4 evolves less oxygen than the active pools two and three, therefore it was suggested that this represents a dimer wherein only one monomer is active (Nowaczyk et al., 2006). The nature of the inactive pool five is not yet clear.

2.2.4 Oxygen evolution measurements

Oxygen evolution activity of PSII samples was measured in buffer 1 supplemented with 0.5 mM 2,6-Dichloro-p-Benzoquinone (DCBQ) and 1 mM Ferricyanide (FeCN) at 2.5 to 10 $\mu g_{Chl}\,ml^{-1}$ of PSII using a Clark-type electrode (Oxygraph, Hansatech

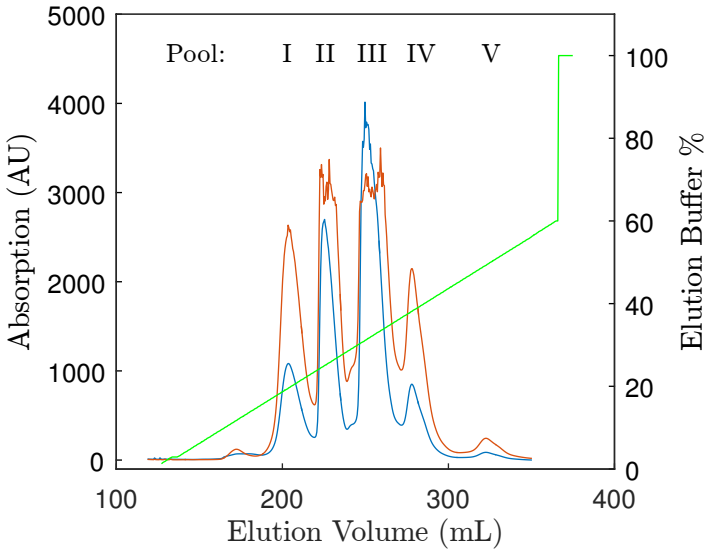

Figure 2.2: Typical elution profile of purified PSII in anion exchange chromatography. Shown in blue/orange is the absorbance measured at 280/440 nm. Shown in green is the percentage of the elution buffer TP3. Pools I and II are monomeric whereas Pools III and IV are dimeric isoforms of PSII. The nature of Pool V is unknown (Douglass, 2015; Nowaczyk et al., 2006).

Instruments Limited, UK) at 25 °C under saturating red light (>10 000 µmol m^2 s^{-1}). Each measurement was at least triplicated and the average value used. The oxygen evolution activity was typically 2500 - 3500 $\mu mol_{O_2}\, mg^{-1}_{Chl}$. Figure 2.3 shows a typical oxygen evolution trace.

2.2.5 Manganese depletion of PSII cores

To remove the Manganese cluster from PSII core complexes, HA buffer (10 mM hydroxylamine, 2 mM EDTA, 80 mM MOPS, 20 mM $NaHCO_3$, 0.06% (w/v) β-DDM, pH 7) was added to an equal volume of PSII core complexes (1 $mg_{Chl}\, ml^{-1}$) and incubated in the dark at 4°C for 1 h. The sample was then washed three times with wash buffer (1 mM EDTA, 40 mM MOPS, 10 mM $NaHCO_3$, 0.03% (w/v) β-DDM,

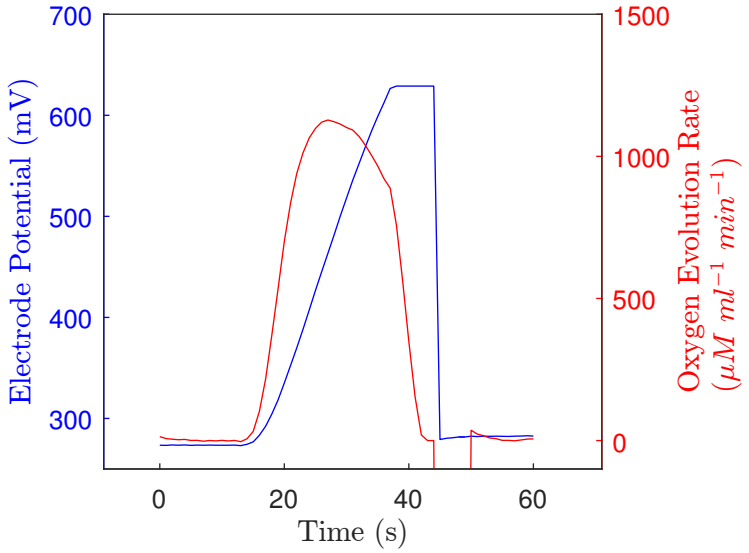

Figure 2.3: Typical measurement of oxygen evolution activity. PSII concentration $10\,\mu g_{Chl}\,ml^{-1}$ Rate average over 5 s.

pH 7) using centrifugal filters. After this procedure no more oxygen evolution could be measured.

2.3 Kinetic Measurements

A set of infra-red LED's (IR dragon 940 nm, OSRAM, Germany) was used in combination with night-vision-goggles (NVMT Spartan 2x24, Yukon, Lithuania) to facilitate handling of the samples in darkness. The JTS-10 setup was assembled by Sven De Causmaecker with help of Jeffrey Douglass. The dual-laser setup was designed and built in Paris (Beal et al., 1999).

2.3.1 C550 shift measurements

The Pheophytin adjacent to Q_A has an absorbance peak at 548 nm. Upon the presence of an electron on Q_A this absorbance peak shifts to 540 nm. Figure 2.4

shows the difference in absorbance between a dark adapted sample and a sample 100 µs after an saturating single turn-over flash.

This absorbance shift can be used to measure the redox state of Q_A and hence the $Q_A^{\bullet-}$ reoxidation kinetics. To eliminate absorbance changes not arising form the redox state of Q_A, the absorbance change is measured at 540 nm and 548 nm. The difference of the two datasets should only contain changes related to the redox state of Q_A.

An LED- pump-probe spectrometer JTS-10 (biologic) was used to measure changes in absorption after excitation. Samples were illuminated by a saturating laser flash (Continuum Minilite II, frequency doubled to 532 nm, 5 ns FWHM) in combination with a Minidye dye pumping system (GSI group France), equipped with a dye, dissolved in methanol, emitting at 690 nm (LD698, Exiton). The intensity of the laser pulse, measured at the sample side of the JTS-10 with a power meter (Newport Power Meter, Model 1918-c), was $2\,\mathrm{mJ\,cm^{-2}}$. The wavelength of the detection LED was set using a custom-made rotating filter system. Interference filters (543 nm, LL02-543-50, Semrock; 554 nm, FWHM 6 nm, Biologic) were placed in a rotating holder inside of the JTS-10. The wavelength of the resulting detection light was measured with a spectrometer (Model BTC-110S, science-surplus, grating 900 l/mm) and adjusted to the desired value by rotating the filter.

PSII samples were thawed in the dark on ice for 30 min. Subsequently, the concentration was adjusted to 0.6 µM PSII ($20\,\mu g_{Chl}\,ml^{-1}$) in buffer 1 and where required Decylplastoquinone (10-PQ) (final concentration 6 µM) and FeCN (final concentration 0.6 - 6 µM) were added to the sample in absolute darkness. Subsequently, a 700 µl sample was loaded in darkness into the JTS-10 and incubated for 5 minutes at the required temperature before measuring the flash-induced absorption change.

In single-flash experiments the absorption was measured 50 µs, 100 µs, 200 µs, 350 µs, 800 µs, 1.5 ms, 3 ms, 6 ms, 12 ms, 25 ms, 50 ms, 100 ms, 200 ms, 400 ms, 1 s, 2 s, 4 s, 8 s, 15 s and 30 s after the actinic flash. In experiments with multiple flashes, the flash rate was 1 Hz and the absorption was measured at the following time points after each flash: 50 µs, 100 µs, 200 µs, 350 µs, 800 µs,1.5 ms, 3 ms, 6 ms,

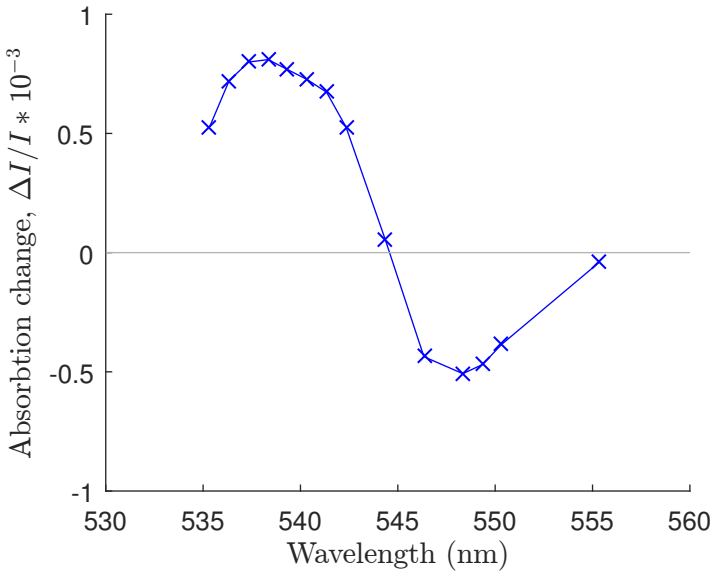

Figure 2.4: Difference spectrum of absorbance before and 100 µs after a saturating laser flash. Data collected on a dual-laser system described in Section 2.3.2.

13 ms, 25 ms, 50 ms, 100 ms, 200 ms and 600 ms.

Measurements at both wavelength were triplicated. The average 548 nm measurements were then subtracted from the averaged 540 nm measurements to yield the decay curve.

To fit the data automated scripts were written using Matlab (Mathworks) with a decay function consisting of two exponentials and one hyperbolic components for experiments with one flash (Equation 2.1) or a two exponential decay function for experiments with multiple flashes (Equation 2.2).

$$A(t) = A_1 e^{-t \times k_1} + A_2 e^{-t \times k_2} + \frac{A_3}{1 + t \times k_3} + Y_0 \tag{2.1}$$

$$A(t) = A_1 e^{-t \times k_1} + A_2 e^{-t \times k_2} + Y_0 \tag{2.2}$$

Here A(t) is the variable absorbance yield, A_1 - A_3 are the amplitudes, k_1 - k_3 are the time constants and Y_0 represents the fraction of centres that have not decayed within the time frame of the experiment.

To calculate half times $t_{1/2}$ from the time constants, Equation 2.3 is used for exponential decay components and Equation 2.4 is used for hyperbolic components:

$$t_{1/2} = \ln 2 \times \frac{1}{k} \tag{2.3}$$

$$t_{1/2} = \frac{1}{k} \tag{2.4}$$

2.3.2 Semiquinone absorption measurements

Measurements at 320 nm were carried out on a dual laser system (Beal et al., 1999). Here the absorption changes are sampled at discrete times by short flashes. These flashes were provided by a Neodymium:Yttrium-Aluminum-Garnet (Nd:YAG) (355 nm) pumped Optical Parametric Oscillator (OPO), which produces monochromatic flashes (1 nm full-width at half-maximum) with a duration of 5 ns. Excitation was provided by a second Nd:YAG-pumped (532 nm) OPO, which produces mono-

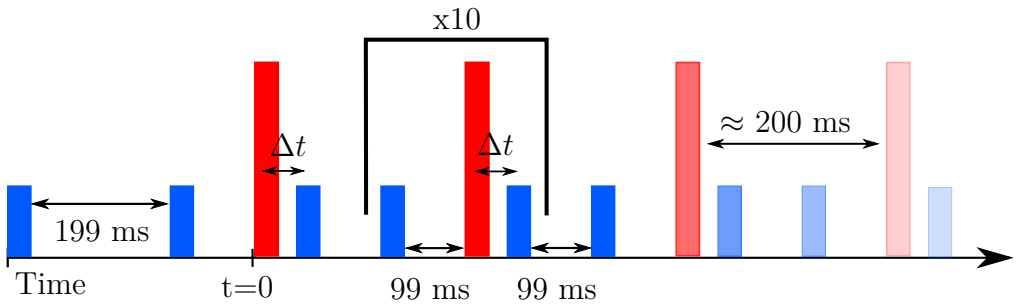

Figure 2.5: Flash timings of the actinic and detection lasers used in the 320 nm measurements of $Q_A^{\bullet-} \rightarrow Q_B^{\bullet-}$ electron transfer. Red: actinic laser flashes at 690 nm; Blue: detection laser flashes at 320 nm. ΔT was varied between 15 µs and 20 ms. The black bracket represents the repeat unit for 10 flashes.

chromatic saturating flashes at 695 nm (1 nm full-width at half-maximum) with a duration of 5 ns. The path-length of the cuvette was 2.5 mm.

The flash rate of the detection laser is maximally 10 Hz and so on a given sample only one time point was measured after each saturating flash in a series of ten saturating flashes at 5 Hz. Figure 2.5 depicts the here described flash regime.

PSII core complexes were used at a concentration of 20 $\mu g_{Chl}\,ml^{-1}$. If required, the electron acceptors FeCN (10 μM) and 10-PQ (10 μM) were added to the sample mixture in the dark.

Data points were collected at 15 µs, 30 µs, 50 µs, 100 µs, 200 µs, 400 µs, 800 µs, 1.5 ms, 3 ms, 5 ms, 10 ms and 20 ms after each actinic flash. Each time point in the kinetic was measured at least three times, with a fresh sample each time. Figure 2.6 shows the resulting traces. These were then rearranged into a single data set for each flash (see Figure 4.4). The data analysis was similar to Section 2.3.1, however data was fitted with only one exponential component and a constant.

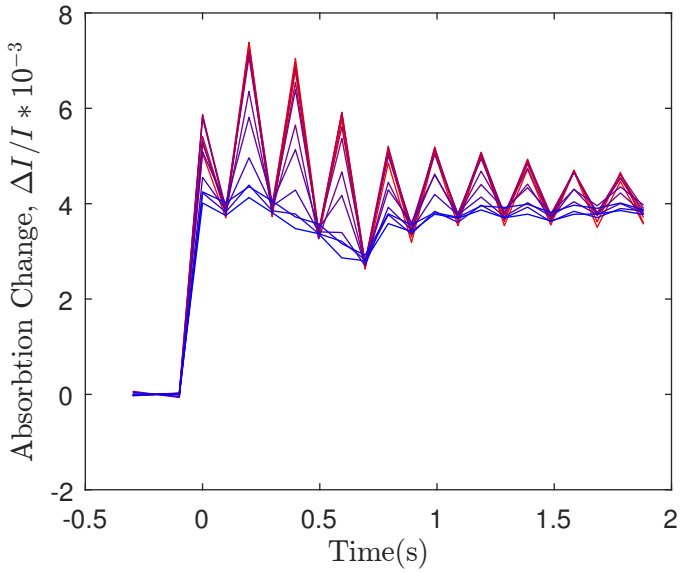

Figure 2.6: Semiquinone Absorption Measurements showing the decay of Q_A on ten subsequent flashes. The different traces represent data points at different time intervals after each flash. The colour of the traces is graded according to the Δt between red (15 µs) and blue (20 ms).

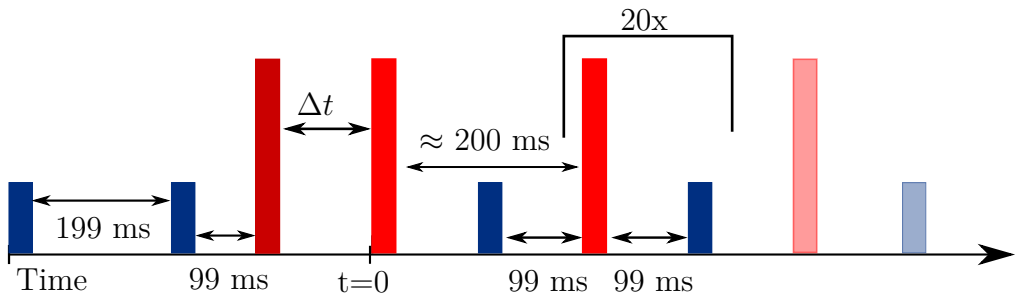

Figure 2.7: Flash timings of the actinic and detection lasers for the 292 nm measurements of S-state turnover. Red: actinic laser flashes at 690 nm; Blue: detection laser flashes at 292 nm. Δt was varied between 0.1 µs and 10 ms. The black bracket represents the repeat unit for a total of 20 flashes.

2.3.3 S-State turnover measurements

Absorption changes associated with the stepwise oxidation of the manganese cluster can be measured at 292 nm. These were measured using the same dual-laser setup as described in Section 2.3.2.

To measure the S-state turnover efficiency in dependence of the $Q_A^{\bullet -}$ reoxidation kinetics, one additional flash was given at a variable time (Δt = 0.1 µs - 10 ms) before the start of a flash series. The ability of the subsequent flash to advance the S-states, is correlated with the oxidation state of Q_A which depends on the Δt between the saturating flashes.

No detection flash is given between this additional actinic flash and the start of the flash series. The $S_4 \rightarrow S_0$ transition is the slowest S-state turnover with a half time of ≈1 ms. The time delay of 99 ms between the actinic and detection flashes, therefore, ensures that the donor side chemistry, i.e. the oxidation of the manganese cluster, is complete in all centres, regardless of the current S-state, before the detection flash is triggered. Figure 2.7 shows the flash timings used in this experiment.

Figure 2.8 shows a representative absorption pattern. Clear period of four oscillations can be observed for all values of Δt. If Δt is small in comparison with the half time of $Q_A^{\bullet -}$ reoxidation, the the first flash of the series does not lead to stable

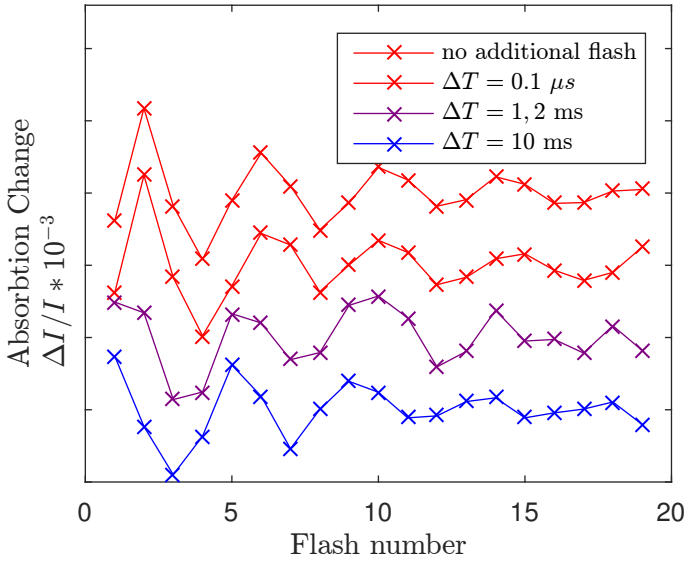

Figure 2.8: Absorption change at 292 nm, measured 99 ms after each of a series of single turnover flashes. The ΔT of an additional flash before the first flash was varied in each trace as indicated. The raw data was corrected for a linear increase of absorption resulting from the accumulation of reduced quinone (Lavergne, 1987).

charge separation, the manganese cluster is not oxidized further and the absorption pattern is not altered (red traces in Fig. 2.8). If Δt is much larger than the half time of $Q_A^{\bullet -}$ reoxidation, the additional flash yields the same pattern, but shifted by one flash (blue trace). For intermediate values of Δt a mixture of the two cases is observed (purple trace). To determine the kinetic of the $Q_A^{\bullet -}$ reoxidation, the difference in absorption of the first two flashes was plotted as a function of Δt as described in Equation 2.5.

$$F_2 - F_1/2(F_2 + F_1) \tag{2.5}$$

The data was analysed as described in Section 2.3.1. Either one or two exponential components were used in the fit of the data. The determination of the kinetic of the $Q_A^{\bullet -}$ reoxidation in dependence of the $S_2 \rightarrow S_3$ was carried out in the same way,

with the exception that the additional flash was inserted before the second flash of the flash series (See Appendix Fig. 6.2 for the exact flash spacing).

2.3.4 Rate pattern analysis using a Markov-model

To analyse the rate patterns generated by the C550 shift measurements on subsequent flashes, Equation 2.6 was used.

$$t_{1/2}(n) = \begin{pmatrix} x \\ (1-x)(1-m) \\ (1-x)m \end{pmatrix}^T \times \begin{pmatrix} 1-\alpha & \alpha & 0 \\ 0 & 1-\alpha & \alpha \\ 0 & \alpha & 1-\alpha \end{pmatrix}^n \times \begin{pmatrix} t_{1/2}(Fe^{3+}) \\ t_{1/2}(Q_B) \\ t_{1/2}(Q_B^{\bullet-}) \end{pmatrix} \quad (2.6)$$

The model parameters were obtained using the *lsqcurvefit* function in Matlab. This function uses a trust-region-reflective algorithm to find the best parameter set for the observed dataset (Coleman and Li, 1996). Table 2.2 lists the upper and lower boundaries for the parameters used in the fitting. Depending on how many flashes were used for the analysis, one or two parameters were constrained to a fixed value.

Table 2.2: Table of boundaries used in the Markov model fit depending on the number of flashes used for the fit. Values listed in brackets are the lower and upper boundaries. If only one number is listed, that parameter was constrained to that value.

	x	m	$t_{1/2}(Q_B^{\bullet-})$ (ms)	$t_{1/2}(Q_B)$ (µs)	$t_{1/2}(Fe^{3+})$ (µs)	α
4 flashes	(0, 1)	(0, 1)	(1, 5)	(200, 800)	50	0.87
5 flashes	”	”	”	”	(0, 70)	0.87
>5 flashes	”	”	”	”	”	(0.7, 1)

2.4 EPR-detected Redox Titrations

EPR was used to detect the redox state of Q_B in dependence of the applied potential. The titrations were carried out in a gas tight apparatus similar to the one described by Dutton (1971), at 15 °C, under bicarbonate-enriched argon atmosphere and in absolute darkness. The potential was measured using a platinum measuring electrode and a silver-chloride reference electrode calibrated with quinhydrone. This setup was provided by Wolfgang Nitschke, CNRS, Marseille.

A set of infra-red LED's (IR dragon 940 nm, OSRAM, Germany) was used in combination with night-vision-goggles (NVMT Spartan 2x24, Yukon, Lithuania) to facilitate working in darkness.

In the titrations at pH 6.5, PSII was resuspended in buffer 1. In the titrations at pH 7, PSII was resuspended in a titration buffer (BT: 40 mM MOPS, 2.5 mM $MgCl_2$, 2.5 mM $CaCl_2$, 10% glycerol, 1 M betaine, 10 mM $NaHCO_3$, pH 7). For each titration multiple PSII preparations were pooled to yield 7-10 ml of purified PSII core complexes at $0.7\,\mu g_{Chl}\,ml^{-1}$. Mediators were added to each titration, at a concentration of 50 µM, according to Table 2.3. Afterwards, the titration mixture was left to equilibrate in total darkness, under oxygen-free argon, for at least 2 h before starting the titration. Reductive titrations were carried out using freshly prepared sodium dithionite solutions while oxidative titrations were carried out using Ferricyanide solutions, both of varying concentration.

For each measurement a sample of ≈150 µl was removed from the titration vessel under oxygen-free argon. The samples were flash frozen, using an ethanol bath at 200 K, and then immersed in liquid nitrogen. Samples were loaded into the EPR machine in darkness.

EPR spectra were recorded on a Bruker ElexSys X-band spectrometer fitted with an Oxford Instruments liquid helium cryostat and temperature control system. Illumination at 77 K was carried out in an unsilvered dewar with a halogen lamp. Each sample was illuminated for 20 minutes. To make sure that illumination was uniform, samples were rotated by 90° every 5 minutes. Saturation was checked by an additional 20 minutes illumination, which in general did not result in a change

of the signal.

The S_2 multiline signal was generated by illumination with a halogen lamp for 10 seconds, using an ethanol bath at 200 K.

Table 2.3: Conditions and mediators used in the individual redox titrations.

PSII		CP47-HIS		D_2-Y160F		D_2-Y160F		D_2-Y160F	
pH		6.5		6.5		7		7	
Buffer		B1		B1		BT		BT	
Manganese cluster		Yes	Yes	Yes	No	Yes	Yes	Yes	No
Mediators	$E_{M_{pH\ 7}}$								
TMPD	300			x	x	x	x	x	x
DAD	240	x	x						
DCPIP	217	x	x	x	x	x	x	x	x
1,2-Naptha-quinone	145	x	x	x	x				
PMS	80				x	x	x	x	x
Thionine	64					x	x	x	x
PES	55	x	x	x	x	x	x	x	x
Metylene blue	11	x	x	x	x	x	x		
Pyocyanine	-34			x	x	x	x		
ITS	-46							x	x
Resorufin	-50					x	x		
Indigo carmine	-125							x	x
2-Hydroxy-1,4-naphtaquinone	-145			x	x				
Anthraquinone-2,6-disulfonate	-184			x	x			x	

2.5 Thermoluminescence and Luminescence Measurements

To measure thermoluminescence and luminescence from PSII core complexes, I designed and built a dedicated measurement device. The specifics of this device are described in Appendix Section 7.

PSII core complexes were suspended in buffer 1 (20 % glycerol instead of 10 % to prevent an artefact caused by thawing of the sample at 0 °C) at a concentration of $20\,\mu g_{Chl}\,ml^{-1}$. Samples were dark-adapted for 1 h at 4 °C, loaded onto the sample plate in absolute darkness and, if required, 10 µM 3-(3,4-Dichlorophenyl)-1,1-Dimenthylurea (DCMU) was added, on the sample plate, to a sample containing 4 µg of Chl. Excitation flashes were provided at 4 °C by the second harmonic of a Nd-YAG laser (Minilite II, Continuum, CA, USA), using ≈ 5-ns pulses at 532 nm and then chilled within 20 s to 253 K with liquid N_2. The frozen samples were then heated at either 20 or $30\,°C\,min^{-1}$ and luminescence was detected with a photomultiplier (H7422-50, Hamamatsu, Japan). The signal was amplified using a transimpedance amplifier (C7319, Hamamatsu, Japan) and digitized using a microcontroller board based on the Atmel SAM3X8E ARM Cortex-M3 CPU (Arduino Due).

Luminescence experiments were carried out in the same device at a set temperature. The variation in temperature was typically not above ±0.1 °C. Before giving a flash and measuring the luminescence decay, samples were incubated at the set temperature for 30 s.

2.5.1 Thermoluminescence measurements in function of pH

To measure thermoluminescence at defined pH values, concentrated PSII samples ($2\,mg_{Chl}\,ml^{-1}$) were diluted into appropriate buffers to a concentration of $20\,\mu g_{Chl}\,ml^{-1}$. The buffers were chosen to have a small and similar temperature dependence. Table 2.4 lists the used buffers and their temperature dependence. Measurements were carried out as described in Section 2.5.

Table 2.4: Buffer compositions for pH dependent thermoluminescence experiments.

pH range	buffer		
5.65-6.65	40 mM MES (-0,011ΔpKa/10°C)	+	2.5 mM $MgCl_2$, 2.5 mM $CaCl_2$, 20% glycerol, 1 M betaine.
6.65-7.65	40 mM MOPS (-0,013ΔpKa/10°C)		
7.65-8.65	40 mM HEPES (-0,014ΔpKa/10°C)		

3 Energetics of the Secondary Electron Acceptor Q_B

As outlined in Chapter 1, the energetic properties of the terminal electron acceptor Q_B are important for understanding the function of PSII and its adaptation to different conditions. Currently, severe disagreement exists on the values for the redox potentials of the couples $Q_B/Q_B^{\bullet-}$ and $Q_B^{\bullet-}/Q_BH_2$. Estimates based on kinetic rates (Diner, 1977) and thermoluminescence measurements (Rappaport and Diner, 2008) are opposed by a recent spectroelectrochemical determination (Kato et al., 2016).

To understand the extent and significance of these diverging results and also the experimental design of the present work, the theoretical background for the two-electron chemistry will be introduced in Section 3.1.

Section 3.2 will present EPR detected redox titrations that were used to directly measure the concentration of the semiquinone $Q_B^{\bullet-}$ as a function of the applied potential. This data was used to determine the redox potential of the two couples $Q_B/Q_B^{\bullet-}$ and $Q_B^{\bullet-}/Q_BH_2$. Furthermore, the relative binding affinities of the Q_B site to the quinone and quinol were calculated from this data. To back up these results, an empirical method was devised to use pH-dependent thermoluminescence measurements to estimate the difference in redox potentials between the $Q_A/Q_A^{\bullet-}$ and $Q_B/Q_B^{\bullet-}$ couples. This will be presented in Section 3.3. Finally, EPR titrations on bacterial reaction centres and PSII already present in the literature were re-analysed using the correct formulae. These are useful for comparisons with the data obtained in this work and the discussion of the underlying models. In Section 3.5,

the obtained results are discussed in the context of the literature. The work of Kato et al. (2016) will be reviewed and reinterpreted in the context of the here obtained results. Furthermore, differences concerning the kinetic estimates of Diner (1977) will be analysed and the emerging energetic model discussed.

3.1 Introduction to Quinone Two-electron Chemistry

Quinones are lipid-soluble molecules that can react with two electrons and two protons, forming a quinol. In biological energy conversion, quinones are used for chemiosmosis. Here, reversible oxidation and reduction of the quinone happen on different sides of the membrane whereby energy in form of a chemical gradient across the membrane is produced (Mitchell, 2011). Quinone redox chemistry is found in all branches of life, suggesting that it could have been present in the last universal common ancestor (Ducluzeau et al., 2014). To understand the energetics of these processes, a thermodynamic approach is necessary. The free energy change (ΔG) of a given reaction is related to the free energy change under standard conditions (ΔG°) as follows:

$$\Delta G = \Delta G^\circ + RT \left(\frac{[Products]}{[Substrates]} \right) \tag{3.1}$$

Here R is the gas constant and T is the temperature. When this reaction occurs in an electrochemical cell the electrochemical potential (E) of that reaction is defined as the decrease in Gibbs free energy per Coulomb of charge transferred, where n is the number of transferred electrons and F the Faraday constant:

$$E = -\frac{\Delta G}{nF} \tag{3.2}$$

This leads to the Nernst Equation:

$$E = E_0 - \frac{RT}{nF} ln \left(\frac{[Products]}{[Substrates]} \right) \tag{3.3}$$

When molecules such as quinones, can undergo multiple subsequent redox re-

actions, the situation is more complicated. Depending on the redox potential of the involved steps and the nature of the environment (solvent, protein etc.), the redox transitions range from two widely separated one-electron reduction/oxidations with a stable intermediate, to strongly cooperative transitions, where both electrons are transferred at the same time and no thermodynamically stable intermediate is observed. Michaelis (1932) worked out the theoretical relationships between the oxidized species **O** (quinone), the intermediate **I** (semiquinone), and the reduced species **R** (quinol). The dependence of the relative concentration of these species on the potential is shown in Figure 3.1 A for a number of different values of ΔE. The following equations apply:

$$\Delta E = E_1 - E_2 \tag{3.4}$$

$$E_m = (E_1 + E_2)/2 \tag{3.5}$$

$$\begin{aligned} E =& E_1 + \left(\frac{RT}{F}\right) ln \left(\frac{[O]}{[I]}\right) \\ =& E_2 + \left(\frac{RT}{F}\right) ln \left(\frac{[I]}{[R]}\right) \\ =& E_m + \left(\frac{RT}{F}\right) ln \left(\frac{[O]}{[R]}\right) \end{aligned} \tag{3.6}$$

The concentration of intermediate semiquinone is dependent on the applied potential as follows[1]:

$$[I] = \frac{1}{\left(1 + 10^{E - E_m - \frac{\Delta E}{2}(RT)^{-1}F} + 10^{E_m - \frac{\Delta E}{2} - E(RT)^{-1}F}\right)} \tag{3.7}$$

When ΔE is positive and large, that is, when the redox potential of the first reduction step $Q_B/Q_B^{\bullet -}$ is substantially more positive than that of the second step $Q_B^{\bullet -}/Q_BH_2$, a thermodynamically stable intermediate semiquinone can be observed. In this case, the titration curves of the reduced and oxidized forms approach that of one-electron Nernst curves and the reaction can be described by the equation in

[1] See Appendix 6.1 for a detailed derivation

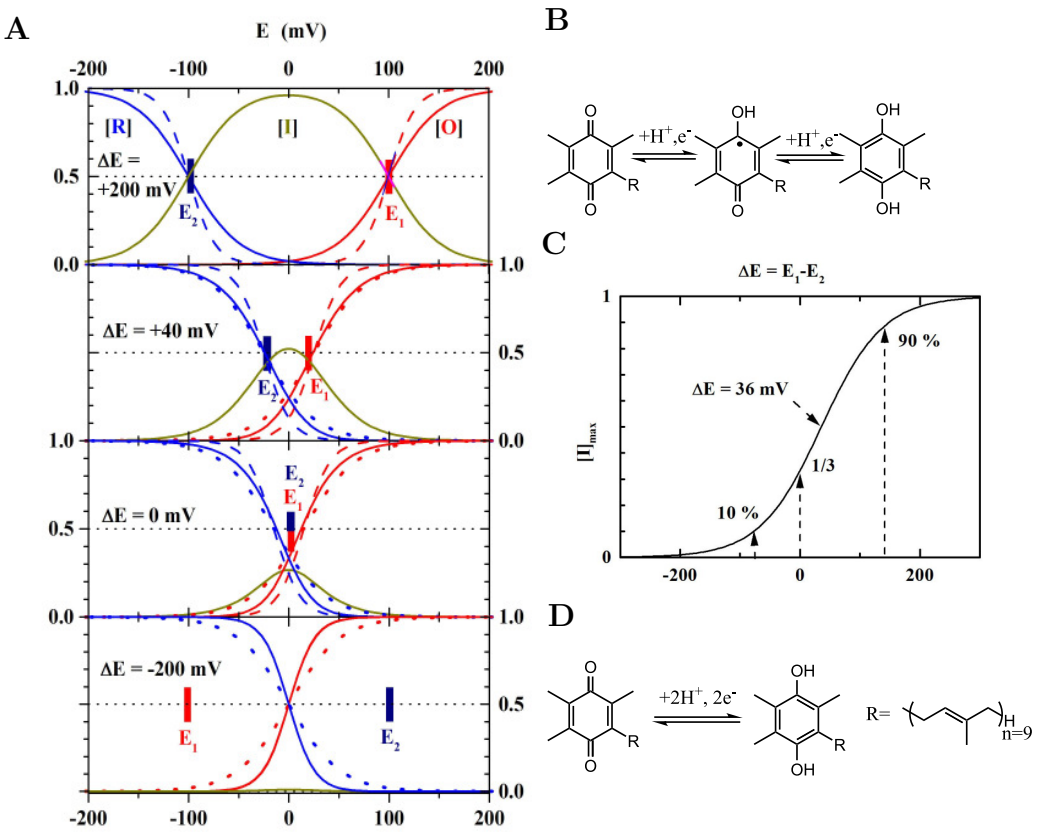

Figure 3.1: Quinone two-electron redox chemistry. The plots in A show the concentrations of the reduced, intermediate and oxidised form in dependence of the potential E for different values of ΔE. The plot in C shows the maximal thermodynamically stable amount of the intermediate state in dependence of ΔE (Nitschke, 2016). B and D show the reduction of a plastoquinone either in two one electron steps (B) or in a concerted two-electron reduction (D).

Figure 3.1 B. When the ΔE is very negative, no stable semiquinone can be observed (Equation in Figure 3.1 D). In this case, the titration curves of the reduced and oxidized forms approach that of two-electron Nernst curves.

Between those two extremes a number of notable phenomena occur. Firstly, the amount of stable intermediate as a fraction of the total, at the midpoint E_m is in directly related to the ΔE of the two couples. This relationship is shown in the graph in Figure 3.1 C. Secondly, even if the percentage of stable intermediate is not known, the ΔE can be inferred from the width of the bell-shaped titration curve of the intermediate semiquinone for values of $\Delta E >\approx$-50 mV. For lower values of ΔE the width of the curve eventually becomes constant and the curve thus scale-invariant (Robertson et al., 1984). Finally, if the concentration of the oxidised or reduced form are measured instead of the intermediate, then only in the approximate range of $-50\ mV < \Delta E < 50\ mV$ do the titration curves deviate enough from the pure one- or two-electron Nernst curves so that information on the ΔE value can be extracted.

When an unknown system is investigated, it is therefore beneficial to monitor the concentration of the intermediate form as it offers the highest chance to fully characterize the system. For the plastoquinone Q_B in PSII, the intermediate semiquinone is a paramagnetic radical $Q_B^{\bullet -}$ which allows for a quantification by EPR measurements.

3.2 EPR-detected Redox Titrations of PSII Core Complexes

EPR detects unpaired electrons in atoms or molecules by their magnetic susceptibility. Organic molecules almost always have filled electron shells and, due to the Pauli exclusion principle, these electrons are almost always paired. This means that most biological samples are EPR silent. Proteins that bind transition metals, such as manganese, iron or copper may break this rule. Here, partially filled d-shells of the metal can lead to paramagnetism. The other notable exceptions are metastable intermediates as found in photo-active proteins. Often, the characteristics that make

molecules suitable for EPR measurements are also important for their function. This makes EPR especially useful in comparison to other techniques, where it can be more difficult to separate between the signals and the background. Consequently, EPR detected redox titrations have been widely used to determine the redox potentials of redox-active biomolecules.

EPR studies of PSII are complicated by the comparatively large number of EPR-active components. Multiple signals for the non-heme iron, the quinones, the reaction centre pigments (chlorophylls and pheophytins), the light collecting chlorophylls, the Mn_4O_5Ca cluster, the cytochromes and the carotenoids have been investigated. These studies are further complicated by the fact that the EPR-active spin-systems can interact with each other leading to even more complicated spectra. Despite multiple scientific careers being spent on interpreting these signals, discoveries of new signals or re-attributions of known signals still occur.

In analogy to the bacterial reaction centres, the first measured EPR signal from PSII that was attributed to the acceptor side quinones, arises from the semiquinone form of Q_A which interacts magnetically with the high-spin ferrous iron Fe^{2+}, producing two EPR signals at g~1.82 and g~1.9 (Rutherford and Zimmermann, 1984). Similar signals were observed for $Fe^{2+}Q_B^-$ (Zimmermann and Rutherford, 1986). All these signals, however, are small and broad and not suitable for a quantitative titration. Instead, we have used a more recently discovered $Q_B^{\bullet-}Fe^{2+}$ signal which was assigned to the low-field edge of the ground state doublet of $Q_B^{\bullet-}$ (Sedoud et al., 2011a). This signal was overlooked before because under most conditions it is covered by the large free organic radical signal from $TyrD^{\bullet+}$. The $Q_B^{\bullet-}Fe^{2+}$ signal is not a conventional first-derivative Gaussian signal typical of an organic free radical; rather, it is a positive spike with a peak maximum at g=2.004 when measured at high microwave power (160 mW). A very similar signal centred at g=2.003 is measured when $Q_A^{\bullet-}Fe^{2+}$ is present. When both semiquinones are present, these signals disappear and instead a positive spike at g~1.66 is observed (Hallahan et al., 1991; Fufezan et al., 2005).

The g~1.66 signal can also be used for the quantification of $Q_B^{\bullet-}$ after low tem-

perature illumination is used to generate $Q_A^{\bullet-}$ in nearly all of the centres (Corrie et al., 1991). Because no electron transfer occurs from $Q_A^{\bullet-}$ to Q_B or to $Q_B^{\bullet-}$ at temperatures below 100 K (Fufezan et al., 2005), the g~1.66 signal can be used to assess the concentration of semiquinone $Q_B^{\bullet-}$ in the sample independently from the g~2 signal.

In the following sections, both of these signals are used in redox titrations of PSII core complexes from *T. elongatus*. Initial titrations were carried out at pH 6.5. The results of these titrations led to the modification of the experimental conditions and a mutant strain lacking Tyr_D was used at pH 7 with different set of redox mediators. The data were used to determine the midpoint potentials of the two half reactions by fitting the data with the theoretical model described in Section 3.1. Furthermore, the relative binding affinities of the Q_B site to the quinone and quinol forms of Q_B were calculated.

3.2.1 PSII core complexes at pH 6.5

EPR spectra of PSII core complexes at pH 6.5 were measured at a series of electrode potentials as described in Section 2.4. At each potential, dark spectra and spectra after saturating illumination at 77 K were recorded. Figure 3.2 Panel A shows the high-power scans of the dark samples poised at different electrode potentials. A conventional first-derivative Gaussian signal typical of an organic free radical is gradually replaced by a positive spike centred at g~2. This is likely to be due to Tyr_D not being fully reduced at the start of the titration. The redox potential of the $Tyr_D^{\bullet+}/Tyr_D$ couple is estimated to be at $\approx$ 730 mV (Vass and Styring, 1991). Prior to the titration the sample was incubated at $\approx$ 250 mV for more than 2 h. The tyrosine should therefore be reduced and not produce the observed first-derivative Gaussian signal. The redox mediators, however, are specifically selected to minimize the equilibration with the donor side of PSII to prevent the reduction of the Mn_4O_5Ca-cluster. The observed signal is therefore likely to be due to a kinetically stable $Tyr_D^{\bullet+}$ that is out of thermodynamic equilibrium (Saito et al., 2013b). This signal masks the positive spike signal which can therefore not be used as a measurement of $Q_B^{\bullet-}$

concentration in this titration.

Figure 3.2 Panel B shows the same samples after illumination at 77 K. The g~1.66 signal can be observed in some of the samples and is largest at 109 mV. In a fraction of the samples, the 77 K illumination led to the formation of a competing signal with marked turning points at g = 1.835, 1.8, 1.68. This signal closely resembles the "formate-signal" under comparable conditions as described by Sedoud et al. (2011b) (g = 1.84, 1.81, 1.68). In their work, this signal, arising from $Q_B^- Fe^{2+}$, was generated by the addition of formate to remove the bicarbonate ligand. No formate was present in this experiment but the addition of sodium bicarbonate suppressed this signal temporarily (see samples poised at 24 mV and 109 mV). This observation was indicative for the mechanism of bicarbonate-mediated redox tuning of Q_A to protect PSII against photo damage under conditions where the downstream electron flow is blocked. This is described in detail in Brinkert et al. (2016).

From the appearance of the characteristic six-line spectrum hexa-aqua Mn^{2+}, it is apparent that over the course of the experiment the Mn_4O_5Ca-cluster is being reduced and loses its structural integrity. This is most apparent from 24 mV onwards but in smaller amounts already visible earlier.

3.2.2 Titration of D_2Y160F-PSII core complexes at pH 7

To avoid the problem of the free radical signal from $Tyr_D^\bullet$ interfering with the measurement, as described in Section 2.4, a mutant was used in which the Tyr_D is replaced with a phenylalanine (D_2-Y160F) (Sugiura et al., 2004). To avoid the loss of the bicarbonate during the titration the pH was increased to pH 7 and 10 mM sodium bicarbonate was added to the titration buffer. A different set of mediators was chosen to minimize the loss of the manganese cluster whilst retaining rapid equilibration of the acceptor side (see Section 2.4 for details).

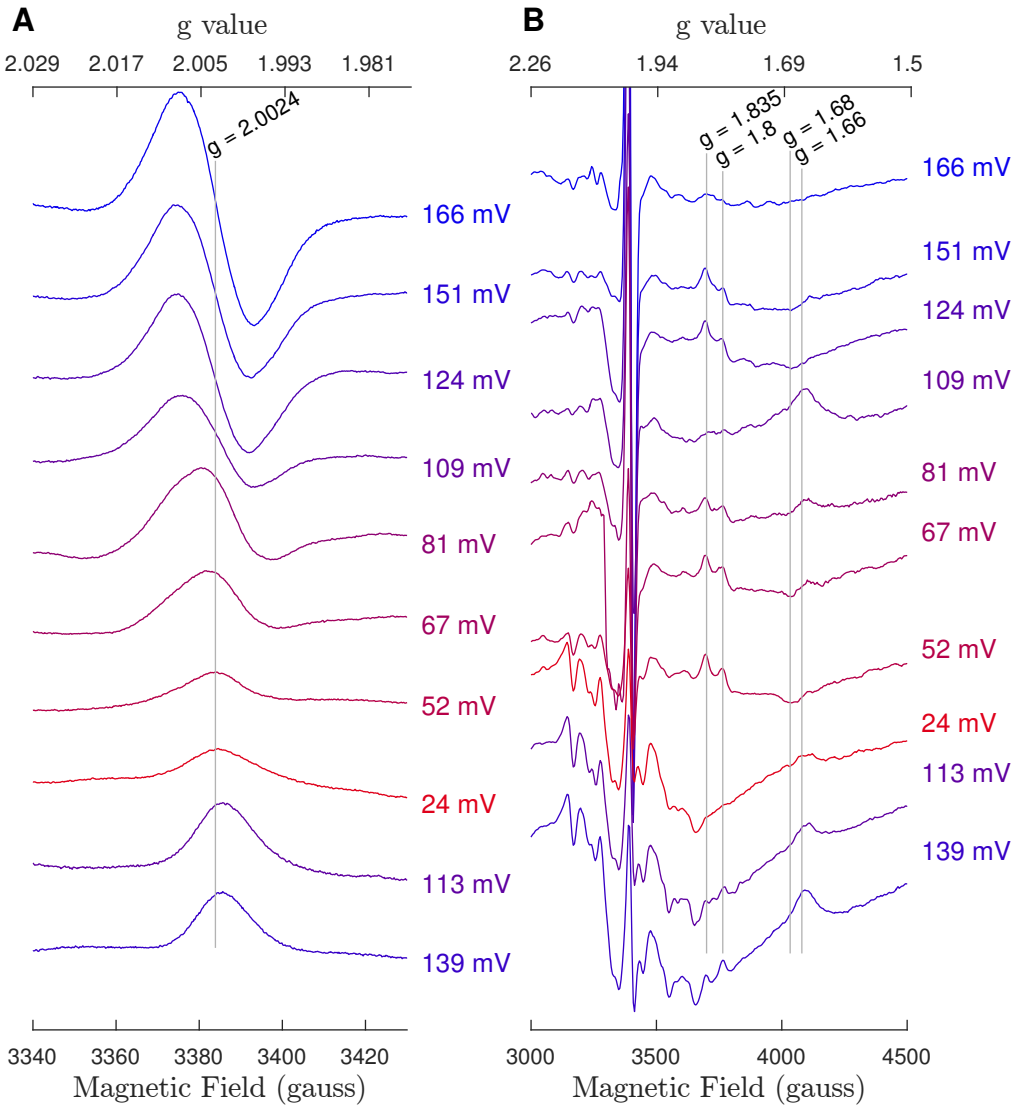

Figure 3.2: EPR spectra of PSII cores poised at different electrode potentials. Panel A shows scans of the radical region around g = 2 at high microwave power (Power: 205.1 mW; modulation amplitude 10.53 G). Panel B shows broad scans of the samples in Panel A after 77 K Illumination (Power: 20 mW, modulation amplitude: 25.35 G). The colours represent the measured potential of the sample, where red means more oxidizing and blue more reducing.

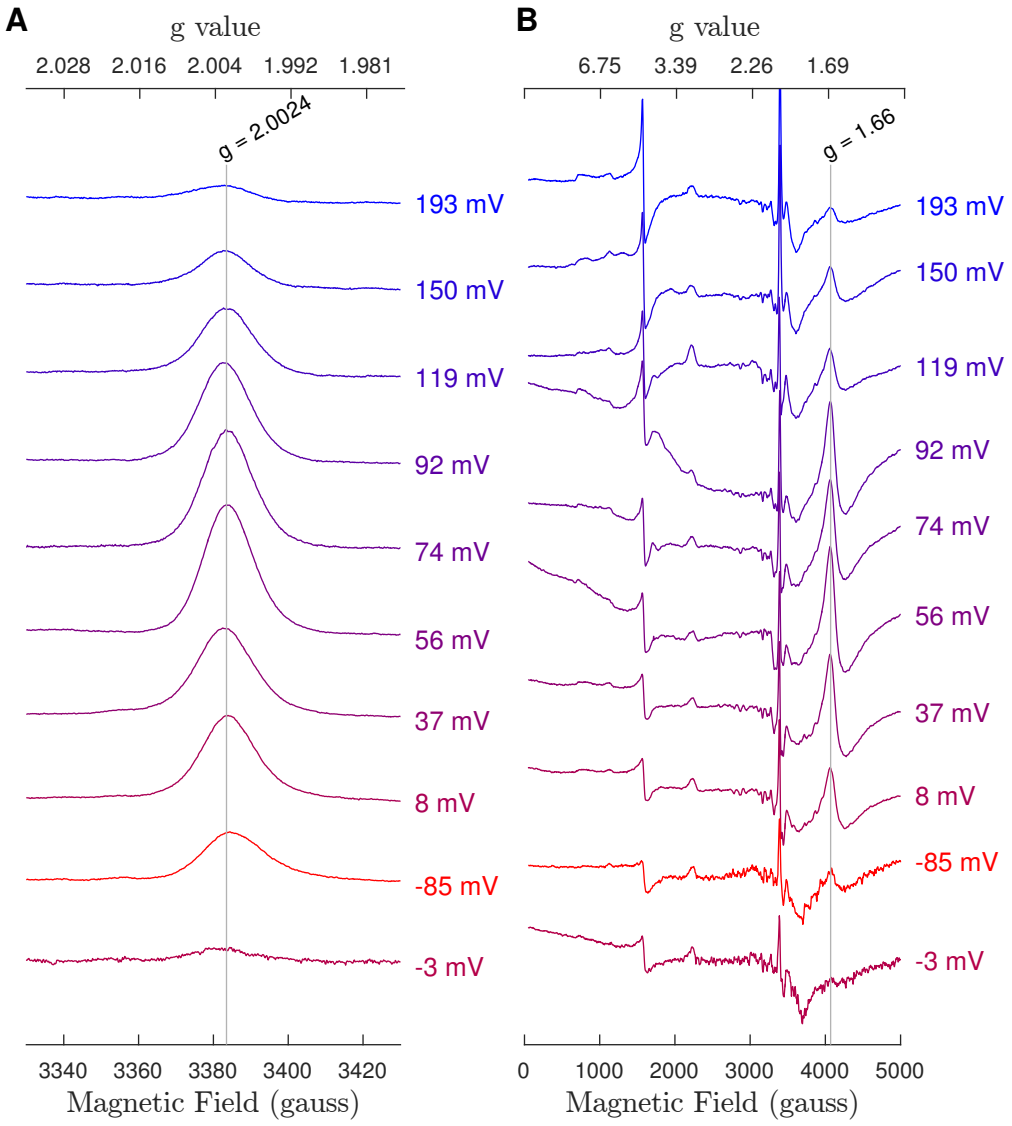

Figure 3.3: EPR spectra of PSII poised at different potentials. Panel A shows the radical region (Power: 205.1 mW; modulation amplitude 10.53 G). Panel B shows a wide scan (Power: 20 mW, modulation amplitude: 25.35 G) after low temperature illumination. The colours represent the measured potential of the sample, where red means more oxidizing and blue more reducing.

Redox titration of intact D_2Y160F-PSII core complexes

EPR spectra of intact D_2-Y160F PSII core complexes were measured at a series of electrode potentials as described in Section 2.4. At each potential, dark spectra and spectra after illumination at 77 K were recorded. Fig. 3.3 Panel A shows scans of the radical region around g~ 2. The appearance and disappearance of a positive spike signal can clearly be observed. As described above, this signal has previously been assigned to the low-field edge of the ground state doublet of the semiquinone $Q_B^{\bullet-}Fe^{2+}$ (Sedoud et al., 2011a). Fig. 3.3 Panel B shows a full spectrum scan of the same samples as in Panel A after illumination at 77 K. At $\approx$ 4000 gauss the g~1.66 signal increases and decreases in a similar way to the semiquinone signal in Panel A. To assess the fraction of the PSII centres in the semiquinone state, a comparable sample without mediators was dark-adapted for 1 h and the size of the g~2 signal was measured. Afterwards, the sample was illuminated at 77 K and then thawed and refrozen in total darkness. The g~2 signal was measured again. The sum of the amplitudes of $Q_B^{\bullet-}$ spectra before and after this treatment correspond to that of a sample with 100 % $Q_B^{\bullet-}$ present. This value was used to normalize the amplitudes of the observed semiquinone signals.

Figure 3.4 shows a plot of the normalized semiquinone signals versus the measured potential. Data from three individual titrations were combined. Titrations were carried out both in oxidizing and reducing directions. At the peak at 67 mV, about 55 % of the centres form a stable $Q_B^{\bullet-}$ semiquinone. Data were fit with a Nernst curve using the model first established by Michaelis (1932). The resulting potentials for the two couples are $E_m(Q_B/Q_B^{\bullet-}) = 92 \pm 18$ mV and $E_m(Q_B^{\bullet-}/Q_BH_2) = 43 \pm 18$ mV.

The retention of the Mn_4O_5Ca-cluster was assessed in two ways, firstly, by the presence of free Mn^{2+} signals in the EPR spectra and secondly by the ability of the sample to form the S_2 multiline signal on illumination at 200 K. Before adding redox mediators, no free manganese was observed. After the addition of redox mediators and equilibration in the dark a small amount of free manganese was detected. This could stem from centres that have lost the extrinsic polypeptides at the luminal side of PSII during the purification and are thus susceptible to reductive attack. The

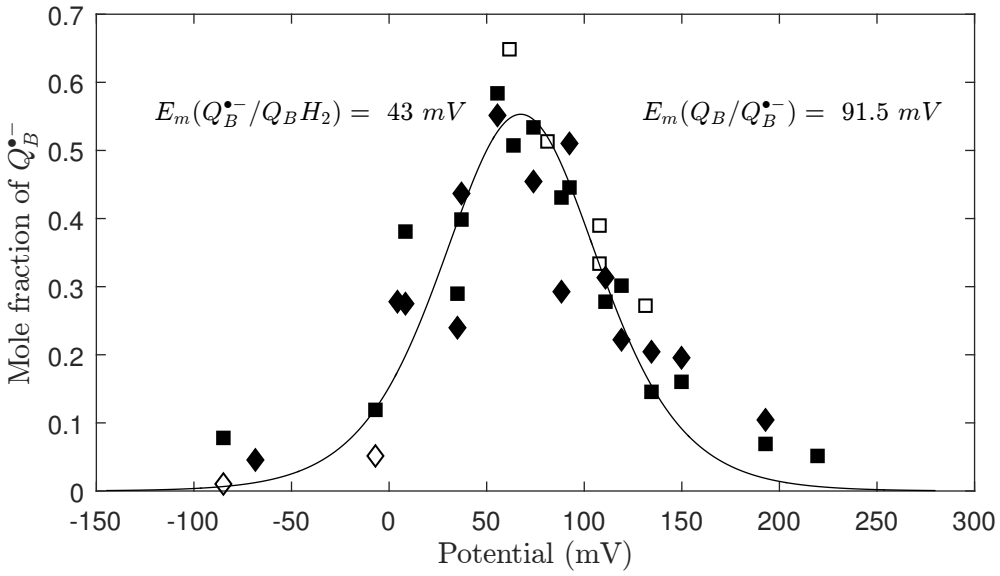

Figure 3.4: Titration of $Q_B^{\bullet-}$ using two independent EPR signals. Open and closed squares: oxidizing and reducing titration of the g ~ 2 signal from $Q_B^{\bullet-}$Fe. Open and closed diamonds: oxidizing and reducing titrations of the $Q_A^{\bullet-}$FeQ$_B^{\bullet-}$ at g~1.66 signal. Data from three separate titrations are cumulated.

size of the free manganese signals did not increase during the titration.

Further evidence that the manganese cluster is retained in most centres is the ability to generate the S_2 multiline signal by illumination at 200 K. Illumination at this temperature has been shown to oxidise the Mn_4O_5Ca-cluster from S_1 to S_2 but not to higher S-states, as this is the only S-state transition that does not involve a deprotonation event (Brudvig et al., 1983; Styring and Rutherford, 1988). This is taken as an indication that the majority of the centres did not lose the Mn_4O_5Ca-cluster during the course of the titration. Although the intensity of the multiline signal decreased at the lowest potentials, it recovered again at higher potentials. This is probably due to a reduction of Q_A to $Q_A^{\bullet-}$ at low potentials in the dark. Under these conditions, the multiline signal is either not formed or modified by the presence of a $Pheo_{D1}^{\bullet-}$ radical (see Fig 3.5 Panel A).

When comparing data points on the low potential side of the maximum (< 67 mV) to those on the high potential side, it is apparent that there is a difference in quantity and quality of data points, with data on the low potential side being sparser and noisier. This stems from the fact that it was technically more difficult to acquire data points in this range. There are a number of reasons that could explain this phenomenon. Firstly, good mediators in the range between phenazine ethosulfate (55 mV) and indigotetrasulfonate (−46 mV) that did not lead to loss of the Mn_4O_5Ca cluster could not be found. Whilst the present mediators should in principal be enough to ensure good mediation of the electrode potential to the sample, it was found that more mediators were necessary to ensure rapid equilibration of the sample than is usual and in the region around 0 mV the equilibration of the sample remained slow. Therefore, some of the noise could be explained by poor mediation.

Secondly, a problem arises from the possible contribution of $Q_A^{\bullet-}$ in the dark at low potentials. The redox potential for the $Q_A/Q_A^{\bullet-}$ couple, although previously subject to much debate in the literature, has been measured to be $E_m(Q_A/Q_A^{\bullet-}) = -145$ mV (Brinkert et al., 2016; Ido et al., 2011; Shibamoto et al., 2009). Therefore, only very little $Q_A^{\bullet-}$ should be expected in the range of this titration. Upon loss of the Mn_4O_5Ca-cluster, however, the redox potential shifts to −22 mV to protect the complex against harmful back reactions (Johnson et al., 1995; Brinkert et al., 2016; Krieger et al., 1993). This more positive potential is within the range of the titration of Q_B and, as discussed above, there is a small fraction of the sample that has lost the Mn_4O_5Ca cluster that could therefore form $Q_A^{\bullet-}$. This potentially influences both EPR signals used in the titration. The influence of $Q_A^{\bullet-}$ on the g~2 signals depends on the redox state of Q_B. $Q_A^{\bullet-}$ in the presence of Q_BH_2 would increase the measured signal, as the low-field edge signals of the ground state doublets of both semiquinones are very close together ($Q_A^{\bullet-}Fe^{2+}$ g = 2.003; $Q_B^{\bullet-}Fe^{2+}$ g = 2.004 (Sedoud et al., 2011a) and are difficult to distinguish if they are both present. If, however, $Q_A^{\bullet-}Fe^{2+}$ is formed in the presence of $Q_B^{\bullet-}$, the g~1.66 biradical signal would be formed in the dark and the semiquinone signal at g~2 would appear smaller. Indeed, a g~1.66 signal can be observed in the dark in samples at 8 mV and −26 mV that corresponds to ≈ 5% of

the centres. Fig. 3.5 Panel B shows these spectra in comparison to the illuminated sample at 56 mV.

The biradical signal at g~1.66 is also affected by the presence of $Q_A^{\bullet-}$ in the dark. It has been shown that the illumination conditions used in this experiment can produce a stable pheophytin D1 radical in centres where $Q_A^{\bullet-}$ is already present before the illumination (Klimov et al., 1980b, 1979, 1980a). In the current case, this could lead to the formation of a three radical state $Pheo^{\bullet-}Q_A^{\bullet-}Q_B^{\bullet-}$, which has not previously been reported, or the $Pheo^{\bullet-}Q_A^{\bullet-}Q_BH_2$ state. Under conditions used in this experiment (i.e. low temperature and high microwave power) a large split signal resulting from the $Pheo^{\bullet-}$ interacting with the $Q_A^{\bullet-}Fe^{2+}$ system centred around g~ 2 with a width 50 g was first reported by Klimov et al. (1980b,a) and later titrated by Rutherford and Mathis (1983). In the titration reported here, a perturbation of the g~2 signal starts to appear in illuminated samples at high microwave power around 0 mV and a $Pheo^{\bullet-}$ signal is the dominant signal observed at potentials below -68 mV. Although the effect of $Pheo^{\bullet-}$ on the biradical signal at g~1.66 is unknown, this will only happen in centres that already show this signal in the dark and the error should therefore also be small (<5%).

Redox titration of manganese-depleted D_2-Y160F PSII core complexes

Manganese depleted PSII cores were prepared as described in Section 2.2.5 from material that was previously used in titrations of intact PSII. The conditions described in Section 2.4 were used for the titration of this sample. So far, it was only possible to do one oxidative titration under these conditions. Figure 3.6 Panel A shows the EPR spectra of radical region of samples before 77 K illumination, while Panel B shows the full spectra after illumination. Fig. 3.7 shows the plot of the values versus the potentials. No independent estimate of the maximal $Q_B^{\bullet-}$ signal was obtained for this experiment; instead, the value obtained for the Mn containing titration was used for normalisation. Although the chlorophyll concentration used in this experiment was adjusted to be the same as in the Mn-containing titration, this approach is problematic. It relies on the assumption that the g~2 and the g~1.66 signals are the

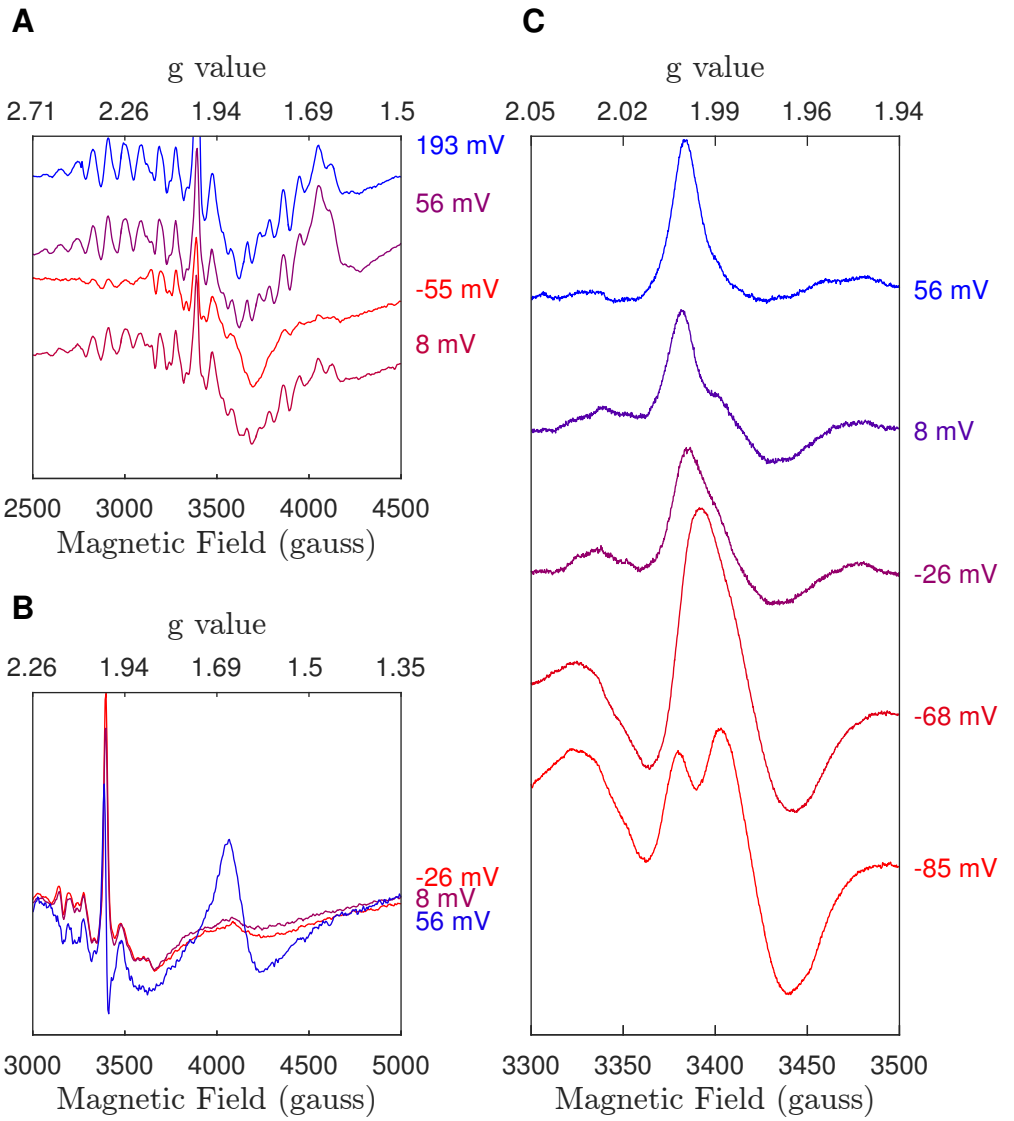

Figure 3.5: EPR spectra showing the S_2 multiline signals that are indicative of a functional manganese cluster (Panel A); the g~1.66 signal in the dark in comparison to an illuminated sample at 56 mV (Panel B); and the $Pheo^{\bullet-}$ radical generated by low temperature illumination (Panel C). EPR conditions Panels A and B: Power: 20 mW; modulation amplitude: 25.35 G. EPR conditions Panel C: (Power: 205.1 mW; modulation amplitude 10.53 G).

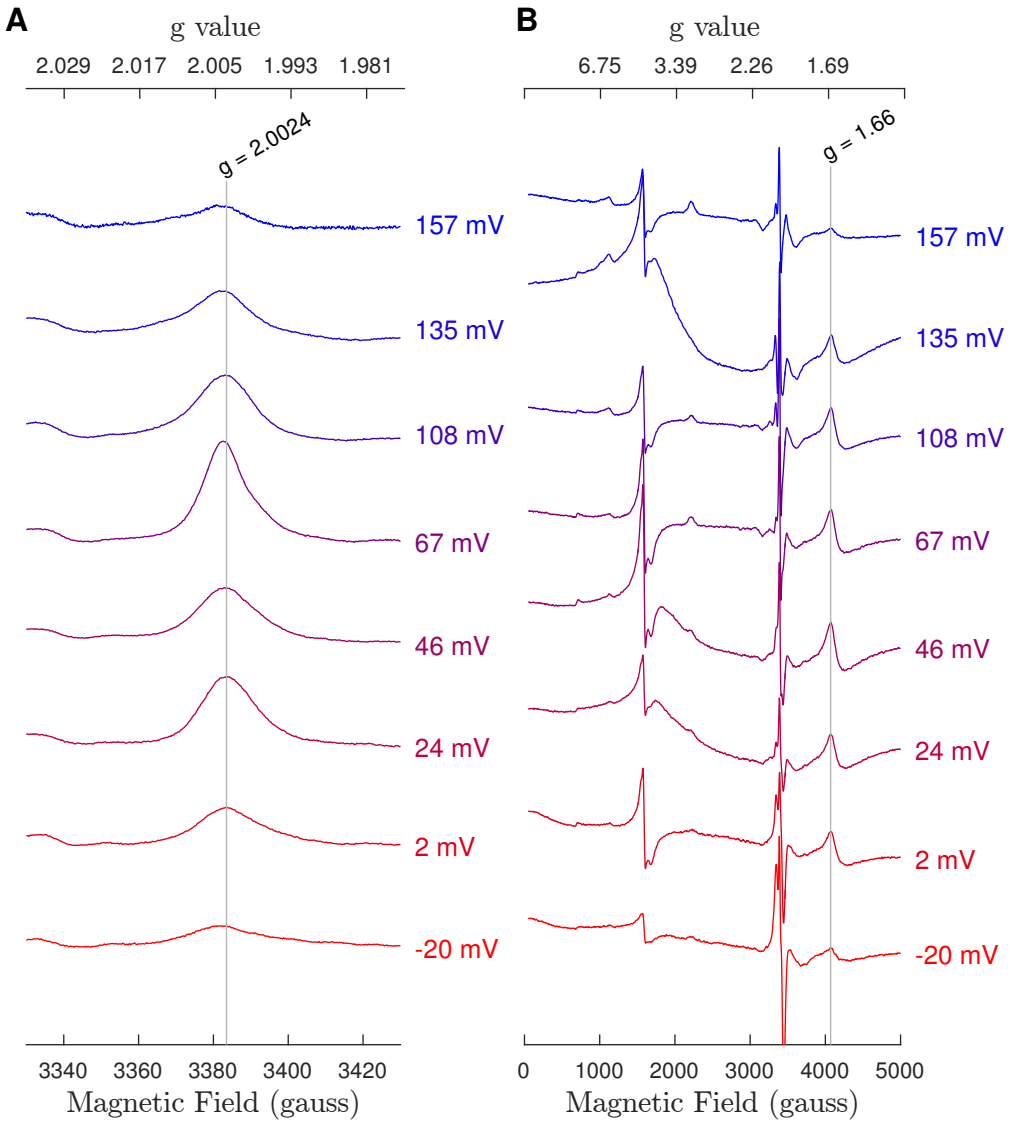

Figure 3.6: EPR spectra of Mn-less PSII poised at different potentials. Panel A shows the radical region (Power: 205.1 mW; modulation amplitude: 10.53 G). Panel B shows a wide scan (Power: 20 mW, modulation amplitude: 25.35 G) after low temperature illumination. The colours represent the measured potential of the sample, where red means more oxidizing and blue more reducing.

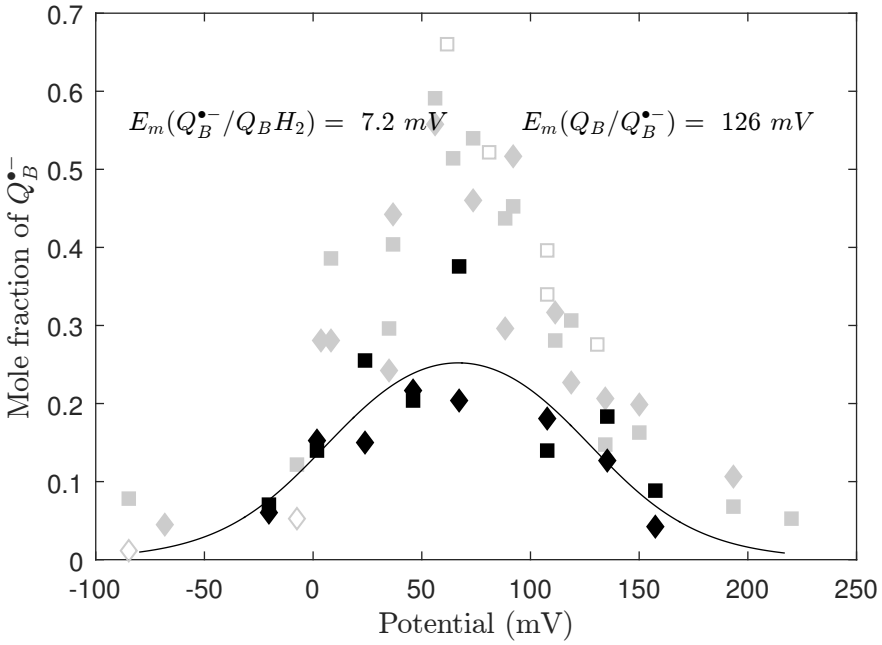

Figure 3.7: Redox titration of Mn-less PSII in comparison to intact PSII. Black squares: g~2 signal; black diamonds: g~1.66 signal, Grey: Intact PSII titrations.

same size for the same amount of $Q_B^{\bullet-}$ with and without the Mn_4O_5Ca cluster. The nature of the perturbation of the acceptor side by removal of the Mn_4O_5Ca cluster is not yet completely understood and this assumption is therefore tentative.

The curve measured using Mn-depleted PSII is similar to that of intact PSII. The maximum, although with a smaller amplitude, is centred around the same potential as the titration of the intact PSII (67 mV). In principal, as described in Section 3.1, when the half-width of the obtained curve is >70 mV, it is not necessary to know the size of a hypothetical 100 % $Q_B^{\bullet-}$ signal to arrive at an unambiguous solution for the values of the two redox couples. This fact is used to fit the data and the resulting potentials for the two couples are $E_m(Q_B/Q_B^{\bullet-}) = 126 \pm 25$ mV and $E_m(Q_B^{\bullet-}/Q_BH_2) = 7 \pm 25$ mV. Due to the sparsity and noise of the data, however, uncertainty remains about the relevance of this fit result.

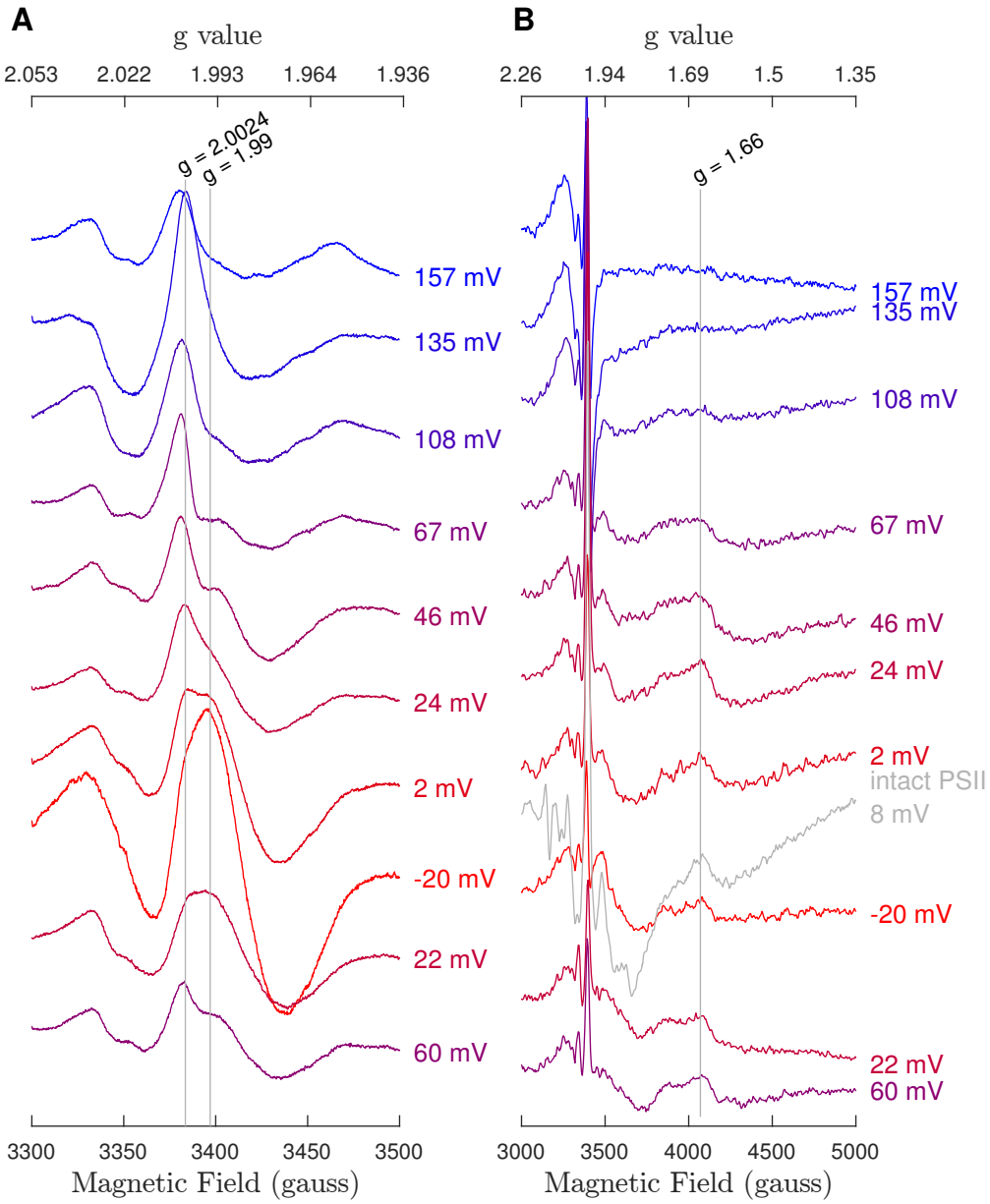

Figure 3.8: EPR spectra of Mn-less PSII samples poised at different electrode potential. Panel A shows the EPR scans of the radical region after 77 K illumination. Panel B shows the full scans before illumination. The grey spectrum from a PSII sample with intact Mn_4O_5Ca cluster is shown on the same scale to offer a comparison of the size and shape of the g~1.66 signal under those conditions.

As previously discussed, upon loss of the Mn_4O_5Ca cluster, the redox potential of the of $Q_A/Q_A^{\bullet-}$ couple shifts to -22 mV. The potential interference of $Q_A^{\bullet-}$ on the here used signals has been described in the previous section. Due to the complete removal of the Mn_4O_5Ca cluster this effect should be larger than in the titration of the untreated PSII sample. Figure 3.8 Panel A shows the EPR scans of the radical region after 77 K illumination. The split pheophytin signal that is generated by the 77 K illumination when Q_A is already reduced, is indeed observed at more positive potentials and to a larger degree than in the titration of untreated PSII samples. Panel B shows the full scans before illumination. A small g~1.66 signal can be observed from 67 mV onward. The broadened shape of the signal impedes the quantification of this signal (The grey spectrum in figure 3.8 panel B shows the signal from an intact PSII sample under comparable conditions).

3.2.3 Relative affinity of the quinone and quinol for the Q_B site

All quinone redox states have different affinities for the Q_B binding site. A stabilisation of a reactant or product state by the protein results in a tighter binding of that species and a free energy change in favour of that species. The redox potentials of the quinone within PSII and free quinone are known. The ratio of binding constants of quinone/quinol for PSII can be calculated as follows:

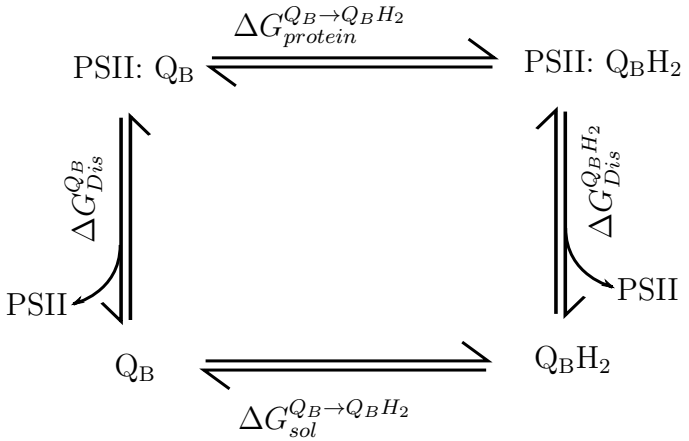

Figure 3.9: Relationship between the equilibrium dissociation energy and the redox energies of the reactions in solution and in the protein.

From Figure 3.9 we get:

$$\Delta G^{Q_B \to Q_B H_2}_{Protein} = \Delta G^{Q_B}_{Dis} + \Delta G^{Q_B \to Q_B H_2}_{Pool} - \Delta G^{Q_B H_2}_{Dis} \tag{3.8}$$

which is equivalent to:

$$\Delta G^{Q_B \to Q_B H_2}_{Protein} - \Delta G^{Q_B \to Q_B H_2}_{Pool} = \Delta G^{Q_B}_{Dis} - \Delta G^{Q_B H_2}_{Dis} \tag{3.9}$$

With eq. 3.1 one can then derive the ratio of the binding constants:

$$K^{Q_B}_D / K^{Q_B H_2}_D = e^{\frac{\Delta G^{Q_B \to Q_B H_2}_{Protein} - \Delta G^{Q_B \to Q_B H_2}_{Pool}}{RT}} \tag{3.10}$$

The ΔG of a reaction is related to the midpoint potential E_m via eq. 3.2 and therefore:

$$K_D^{Q_B}/K_D^{Q_BH_2} = e^{\frac{-nF(E_m(Protein)-E_m(Pool))}{RT}} \tag{3.11}$$

The E_m(Protein) is equal to the average of the two half reactions and therefore the peak of the titration in Section 3.2.2 at 67 mV. The E_m(Pool) for the reduction of a quinone to the quinol has not been determined in *T. elongatus* but it should be very similar to the value measured by Golbeck and Kok (1979) in *Scenedesmus* of $\approx$ 112 mV at pH 7. Inserting this into the equation above, the binding affinity of the quinone to the Q_B site in relation to the quinol is obtained.

$$K_D^{Q_B}/K_D^{Q_BH_2} \approx 40$$

This means that the quinone is 40 times more strongly bound to the Q_B site than the quinol and that debinding of PQH_2 is thermodynamically favourable with the release of 45 meV as heat.

3.3 Gap Estimates Based on Thermoluminescence Measurements

Thermoluminescence has been measured in semiconductors, minerals, inorganic and organic crystals, and complex biological systems such as the photosynthetic apparatus (Ducruet and Vass, 2009). It is a photon emission that follows the detrapping of a previously trapped charge-separated state induced by heating of the sample. Thermoluminescence from PSII was first observed by Arnold and Sherwood (1959) in dried chloroplast samples and thermoluminescence measurements have since been useful towards understanding the energetics of the cofactors within PSII (Rutherford et al., 1982, 1984b). In the following section, the processes occurring in PSII that are responsible for the TL bands will be described briefly.

Metastable radical pairs occur within PSII due to the multi-electron chemistry on both sides of PSII (see Figure 3.10). Given enough time, these states will return

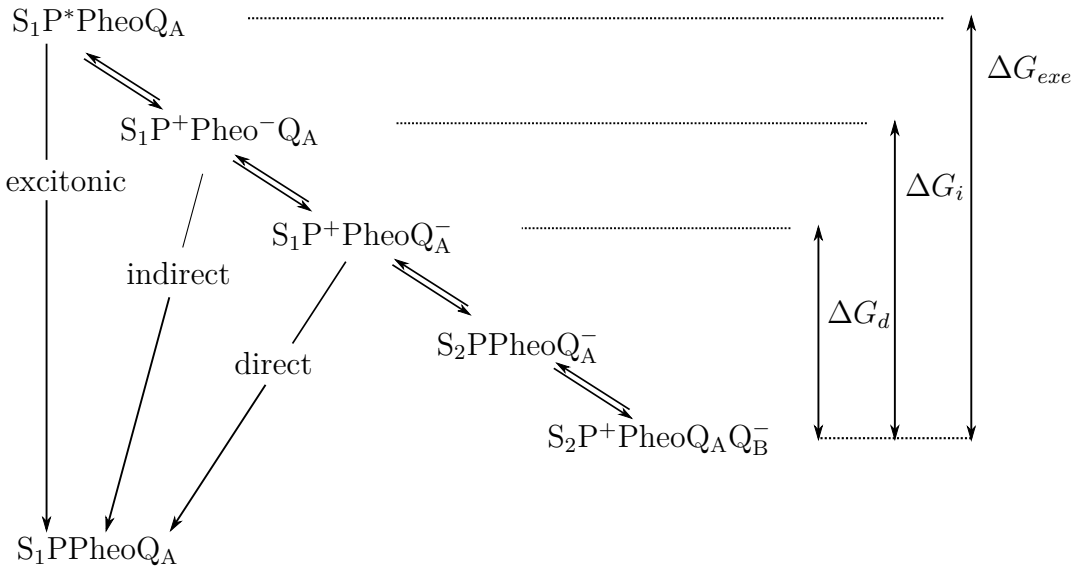

Figure 3.10: Diagram of the transient charge separated states and the back reaction routes.

to the ground state. The route by which this deactivation happens depends on the nature of the charge separated state and the external conditions. Although other pathways exist, the following three are considered most important within the context of thermoluminescence (Rappaport and Diner, 2008). (1) The direct route is the direct charge recombination from $Q_A^{\bullet -}$ to P^+ via electron tunnelling. (2) The indirect route occurs when $Pheo^-$ is reformed before recombination occurs. Both these routes occur radiationless and only the third route, the reformation of the exited state P* (3), leads to the emission of a photon. The relative contribution of this route under normal conditions is small (De Grooth and van Gorkom (1981) estimate 3-4%). Nevertheless, the emitted light can be measured and the temperature at which this occurs is indicative of the energetic landscape of the measured sample.

There are, however, a number of complications that prevent the extraction of relevant thermodynamic parameters and make TL curves difficult to interpret. Firstly, the standard free energy levels of a charge separated pair is influenced by both the energetics of the donor and the acceptor molecule. Secondly, all of the involved

charge separated states, depicted in Figure 3.10, influence the relative contributions of the three recombination routes and therefore the peak intensities and positions in TL curves. Often no simple relationship between peak temperature and the standard free energy level of any charge separated pair exists, and even when specific mutants are compared, it can be difficult to understand the reason behind observed changes in the TL curve.

TL measurements are non-equilibrium measurements of competing kinetic processes that each are temperature dependent. As the temperature continuously changes during the measurement, so do the rates of the involved processes. The effect of the temperature and the change thereof (the scan rate) on the TL curves is therefore also not trivial. (In principle, faster scan rates lead to peaks that are shifted to higher temperature and more intense.)

Rappaport et al. (2005) developed numerical calculations based on a theoretical model of the underlying processes of TL as a tool to interpret the results of TL measurements. These calculations were adapted by Rose et al. (2008) to interpret the TL curves from *Chlamydomonas reinhardtii* samples with mutations around the Q_B site. An almost linear dependence of the peak temperature of TL on ΔG_d of $\approx 0.4°$ meV^{-1} Rappaport and Lavergne (2009) is obtained in this model. Here, ΔG_d is the energy difference between state with the lowest free energy and the $P^+Q_A^-$ state (see Figure 3.10).

The model predicts an energy gap between Q_A and Q_B of only 30 meV. Because the TL band resulting from $S_2Q_A^-$ recombination [2] is commonly measured in the presence of DCMU, the authors add another 50 meV based on the work of Krieger-Liszkay and Rutherford (1998), who found a 50 meV shift for the binding of DCMU to the Q_B site.

To test the predictions of the numerical model and to overcome some of the difficulties in interpreting TL experiments, the pH dependence of the TL emission band caused by recombination from the $S_2Q_B^{\bullet -}$ state was measured.

[2] In the literature the thermoluminescence emissions from the $S_2Q_A^{\bullet -}$ and $S_2Q_B^{\bullet -}$ states are called the Q- and B-bands. For clarity, in this work, this nomenclature is not used and instead thermoluminescence bands are referred to by the state that is presumed to be causing them.

As stated above, the peak temperature of a TL emission band depends on the standard free energy of the involved radical pair. As shown before, this can be related to the Nernst equation 3.3. The two half reactions involved in are

$$S_2 + e^- \leftrightarrow S_1 \tag{3.12}$$

$$Q_B + e^- + H^+ \leftrightarrow Q_B^{\bullet -}(H^+) \tag{3.13}$$

Only the second half-reaction involves a proton. By inserting the constants into the Nernst equation it becomes obvious that the redox potential of Q_B shifts with -59 mV per pH Unit.

$$E = E^\circ - \frac{RT}{nF} ln \left(\frac{[S_2][Q_B^{\bullet -}]}{[S_1][Q_B][H^+]} \right) \tag{3.14}$$

$$pH = -log[H^+] \tag{3.15}$$

$$E = E^\circ - \frac{2.303\ RT\ pH}{nF} log \left(\frac{[S_2][Q_B^{\bullet -}]}{[S_1][Q_B]} \right) \tag{3.16}$$

$$E = E^\circ - 59mV\ pH\ log \left(\frac{[S_2][Q_B^{\bullet -}]}{[S_1][Q_B]} \right) \qquad \text{(at 25°C)} \tag{3.17}$$

This means that by varying the pH only the midpoint potential of Q_B is affected and therefore only the free-energy level of the final state in Figure 3.10 is modified. This allows empirical measurement of the dependence of the peak position of the TL emission band on ΔG_d. Knowing the redox potential of the $Q_A/Q_A^{\bullet -}$ couple and the peak position in TL of the $S_2Q_A^{\bullet -}$ recombination band, the redox potential of the $Q_B/Q_B^{\bullet -}$ couple can be estimated.

3.3.1 Thermoluminescence measurements in dependence of pH

Figure 3.11 shows the thermoluminescence curves of long-dark-adapted PSII samples after one saturating flash at different pH values. In these samples the signal arising from the $S_2Q_B^{\bullet -}$ recombination is the main component. Similar to the observations

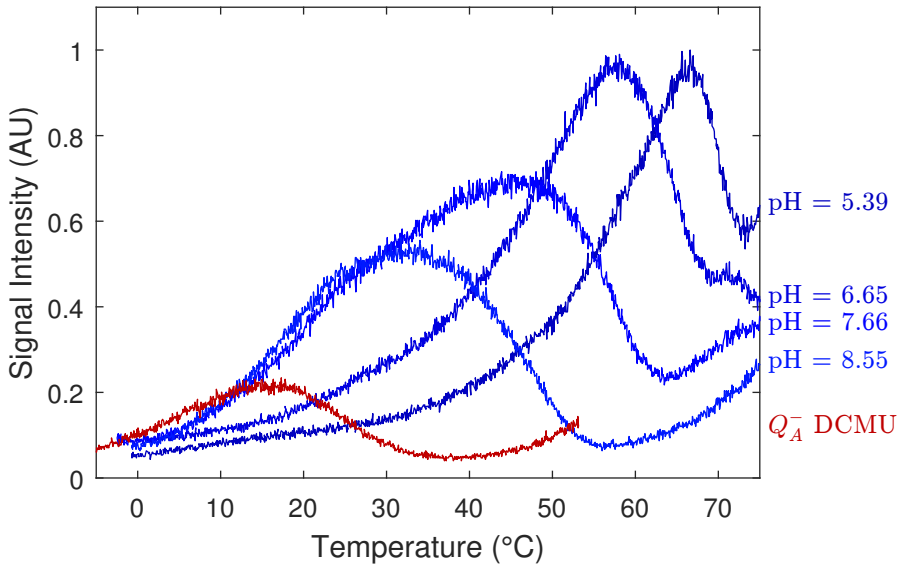

Figure 3.11: Graph of $S_2Q_A^{\bullet-}$DCMU (red) and $S_2Q_B^{\bullet-}$ TL curves at different values of pH (blue) after one saturating laser flash at 4°C. DCMU blocks electron transfer from $Q_A^{\bullet-}$ thereby enabling the observation of the $S_2Q_A^{\bullet-}$ recombination instead of the $S_2Q_B^{\bullet-}$ recombination.

by Rutherford et al. (1984b), a clear shift of the peak positions to lower temperatures with increasing pH can be seen. This shift is accompanied with a change in intensity and shape of the peaks. Additionally, the DCMU-generated $S_2Q_A^{\bullet-}$ recombination with a peak at 15° C at pH 7 is shown (red). Figure 3.12 shows a plot of the peak temperatures versus the pH from two experiments with different heating rates. A linear dependence of -9.1 K per pH unit can be observed in both cases. Using the relationship given by the Nernst equation, this translates to a $\Delta E = 6.45$ mV K^{-1}. With a difference in peak positions of 37 K between the $S_2Q_A^{\bullet-}$ and $S_2Q_B^{\bullet-}$ peaks, a gap of 236 mV is obtained. Given a potential for $Q_A/Q_A^{\bullet-}$ of -144 mV, this would result in a potential of 93 mV for the $Q_B/Q_B^{\bullet-}$ couple. This is in very good agreement with the 92 mV value measured by EPR titration.

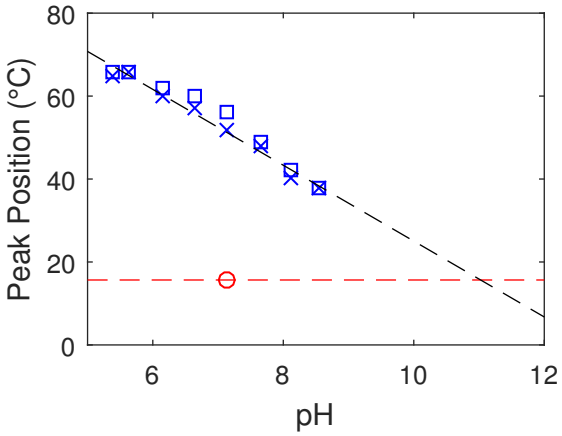

Figure 3.12: Plot of thermoluminescence peak temperatures vs. pH. Blue crosses: Peak temperatures of the $S_2Q_B^{\bullet-}$ band at a scanning rate of $0.33°Cs^{-1}$. Blue squares: Peak temperatures of the $S_2Q_B^{\bullet-}$ band at a scanning rate of $0.5°Cs^{-1}$. Red circle: Peak temperature of the $S_2Q_A^{\bullet-}$ band at pH 7.14.

3.4 Re-evaluation of Bacterial Reaction Centres

EPR detected redox titrations have been used to establish the midpoint potentials of the quinones in bacterial reaction centres (Rutherford, 1979; Rutherford and Evans, 1980; Heathcote and Rutherford, 1986). Furthermore, Corrie et al. (1991) have reported the only titration of the g~1.66 signal from PSII membranes prepared from *Phormidium laminosum*, a thermophile cyanobacterium. None of these experiments have been analysed using the correct formulae. Instead, one-electron Nernst-curves were fit to all observed transitions. Whilst there is a case were this approach leads to a correct result, under most conditions it is wrong and will lead to false conclusions. To better compare the data from the present work to the data present in the literature these were reanalysed using the correct formulae (See equation 3.7).

Figure 3.13 shows the reanalysed data and the obtained fits. The three titrations from bacterial reaction centres, used the g~1.8 signal, which originates from $Q_A^{\bullet-}$Fe and $Q_B^{\bullet-}$Fe. If it is assumed that the amplitude of this signal is equal for equal

Table 3.1: Fit values for reevaluated titrations

Organism	fit type	% of total Q_B [%]	peak pos. [mV]	Delta [mV]	peak pos. @ pH 7 [mV]
Rh. sphaeroides[a]	const.	76	4± 12	72± 74	63
(pH 8)	free	52	5± 9	36± 83	64
Rh. viridis[b]	const.	64	16± 25	55± 175	75
(pH 8)	free	29	16± 11	-5± 178	75
C. vinosum[c]	const.	30	97± 23	-6± 30	97
(pH 7)	free	58	94± 31	45± 230	94
Ph. laminosum[d] (pH 8)	free	27	28± 8	-21± 164	86

[a] Rutherford and Evans (1980) [b] Rutherford (1979)
[c] Heathcote and Rutherford (1986) [d] Corrie et al. (1991)

concentrations of $Q_A^{\bullet-}$ and $Q_B^{\bullet-}$, the amplitude of the signal at very low potential, where both quinones are fully reduced, can be used as an estimate for the maximal signal. The amount of stable semiquinone $Q_B^{\bullet-}$ can then be determined as a fraction of this signal. If, however, this assumption does not hold, an unambiguous solution can only be obtained when the half width of titration curve of the intermediate $Q_B^{\bullet-}$ is larger than 70 mV (Robertson et al., 1984). This is the case for all four titrations. For the bacterial reaction centres, one fit with the maximum constrained and one unconstrained fit was done. In principal, these fits should yield the same result and if they do not, either the assumption that the g~1.8 signal at low potential is a valid measure of the maximal amplitude is wrong, or the data quality is insufficient. In the *Phormidium laminosum* titration, as the g~1.66 signal is used, there is no information on the maximal signal size available and therefore only an unconstrained fit model was applied.

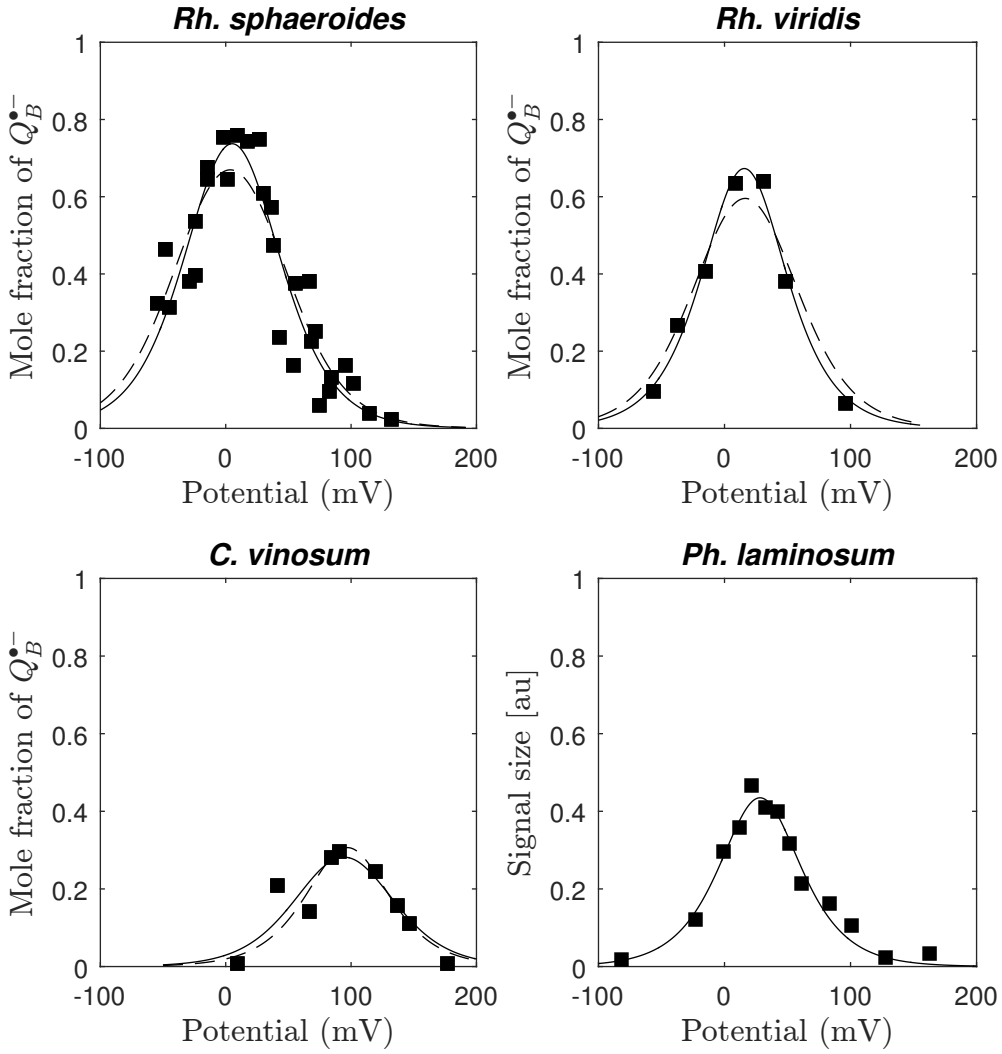

Figure 3.13: Reevaluated titrations from bacterial reaction centres and PSII from literature data (Rutherford, 1979; Rutherford and Evans, 1980; Heathcote and Rutherford, 1986; Corrie et al., 1991). Solid lines are the fit curves for the unconstrained fits., dashed lines are the fit curves for fits where the maximum was constrained by the Q_A g~1.8 signal at low potential (Data not shown).

3.5 Discussion

In the following section the energetic picture arising from the work presented here will be discussed and compared to previous work on bacterial reaction centres and PSII. An outlook on emerging questions and future work concludes the chapter.

3.5.1 Energetics of the terminal electron acceptor Q_B

The midpoint potential of the terminal electron acceptor of PSII, Q_B, was measured directly using two separate EPR signals. Due to the issues with the debinding of the bicarbonate and the retention of the Mn_4O_5Ca cluster, no values for the midpoint potentials of the two reduction steps could be obtained from the titration at pH 6.5. Nevertheless, the approximate maximum at ≈100 mV is in accordance with the maximum obtained at pH 7 at 67 mV. Furthermore, the observed phenomenology lead to the discovery of the mechanism of the bicarbonate effect (Brinkert et al., 2016). The titration at pH 7 did not suffer from the debinding of the bicarbonate ligand to the non-heme iron. Also, the Mn_4O_5Ca cluster retained its structural integrity throughout the experiment. Some equilibration problems and a possible interference of a signal arising from $Q_A^{\bullet-}$ were encountered on the low potential side of the titration. However, these did not significantly impede the determination of the midpoint potentials of the two couples. The estimate of the fraction of semiquinone in relation to the total amount of semiquinone at the midpoint of the titration is in good agreement with the value derived from the width of the curve. The potentials derived from the data for the two redox couples are $E_1(Q_B/Q_B^{\bullet-})$≈90 mV and $E_2(Q_B^{\bullet-}Q_BH_2)$≈40 mV. Figure 3.14 shows a plot of the redox potentials of the two quinone reduction steps in relation to the potentials of the other cofactors in PSII.

To understand the significance of these measurements, two main parameters should be discussed. These are firstly, the average of the two redox couples (E_m=(E_1+E_2)/2) in relation to the value for a free quinone, and secondly, the difference in midpoint potentials ($\Delta E = E_1 - E_2$) between the two redox couples E_1 and E_2. The E_m was

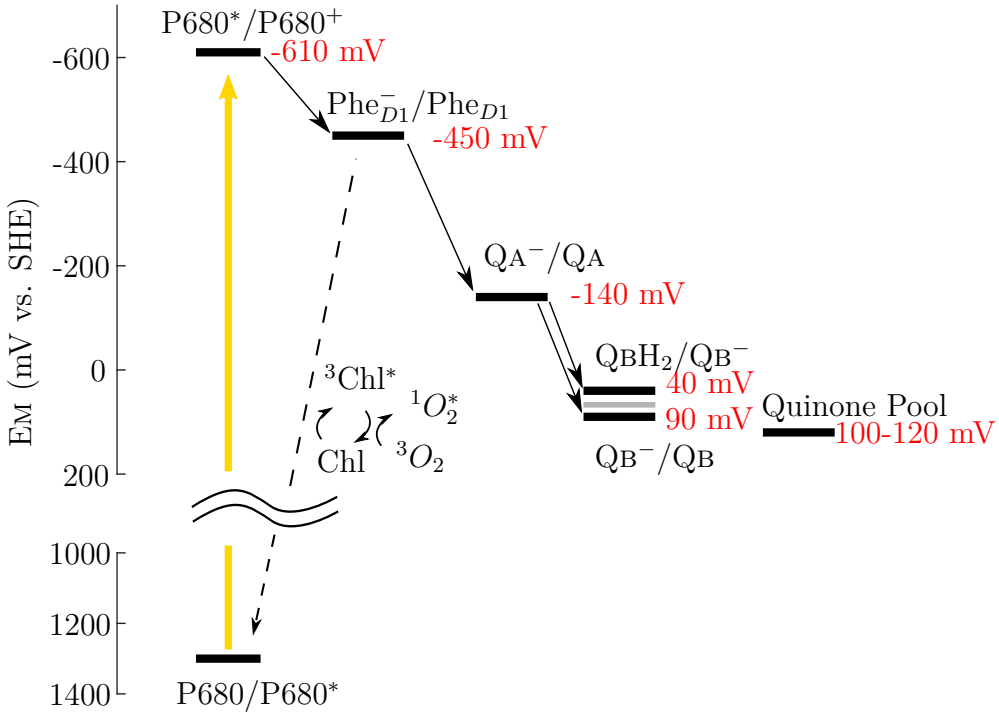

Figure 3.14: Schematic view of the redox potentials of the different cofactors in PSII. The grey line indicates the average between the two Q_B couples at 65 mV.

used to calculate the ratio of the dissociation constants of the quinone and quinol forms ($k_{D\ ox}/k_{D\ red}$) of the Q_B binding site. Here, an E_m more negative than that of an unbound quinone results in a preferential binding of the oxidized quinone and a larger driving force for the dissociation of the reduced quinol. The ΔE is indicative of the degree of stabilisation of the semiquinone radical $Q_B^{\bullet -}$ in the site, with more positive values of ΔE equating to more stabilisation.

Preferential binding of the quinone in the Q_B site

The ratio of the binding constants of the quinone and quinol forms were calculated from the measured E_m of the quinone reduction in PSII. An approximately 40-fold preferential binding of the quinone is found. Considering that PSII is a water plastoquinone oxidoreductase, it appears logical that this would be the case. Interestingly, a tighter binding of quinone versus quinol has also been recently observed in a coarse grain MD simulation of PSII in the membrane.(Van Eerden et al., 2017) This downshift of the E_m seems to be absent in the bacterial systems. There, the E_m coincides with the approximate redox potentials of free ubiquinones. This means that there is less driving force to eject the quinol from the site and no preferential binding of the quinone. Two main rationales could explain this difference. Firstly, because the bacterial reaction centre is much smaller than PSII, the quinone tail remains largely in the membrane with only the head group and a part of the isoprene tail entering the protein. Therefore, it is likely that less driving force is needed to eject the quinol from the site. In PSII, on the other hand, the quinone needs to enter and leave by one of two channels (Müh et al., 2012) (or three according to Van Eerden et al. (2017)) into a hydrophobic patch within PSII and from there bind into the Q_B site. Secondly, the size of the quinone pool is considered to be larger in the bacterial systems (Crofts and Wraight, 1983), which would constitute a different mechanism for ensuring that mainly the quinone is bound to the Q_B site.

Stabilisation of the semiquinone state in comparison to bacterial reaction centres

The stabilisation of $Q_B^{\bullet-}$ of $\Delta E \approx 60$ mV in PSII is indicative of a strong stabilisation of the semiquinone state. The case in bacterial reaction centres is not as clear. It depends on the assumptions that are made for fitting the titration data. Although there is tentative evidence in the case of the *Rh. sphaeroides* titration (Rutherford and Evans, 1980), there is no definitive proof for the assumption that the g~1.8 signals generated at low potential can be used as a normalisation for the size of the semiquinone signal. On the other hand, the determination of the ΔE from the width of the curve is very sensitive to noise and so the associated uncertainty is large. Nevertheless, it seems to be the case that the stabilisation of the semiquinone in the related bacterial reaction centres is smaller than in PSII from *T. elongatus*, ranging between 0-30 mV.

It should be pointed out that a ΔE of zero does not mean that there is no stabilisation of the semiquinone; instead, it is stabilized to the point where both reduction steps have the same driving force, and is still a large thermodynamic stabilisation of the semiquinone state compared to a quinone that is free in the membrane (see Figure 3.14).

These differences to PSII are informative, when viewed in a structural and functional context. In the bacterial reaction centre, the energy difference between the P^+Pheo^- charge-separated state and the subsequent $P^+Q_A^-$ is much larger than in PSII. Therefore, and due to the absence of oxygen, back reactions are much less of a problem than in PSII.

In the case of PSII, back reactions from $P^+Q_A^-$ lead to rapid damage of the complex (Rutherford et al., 2012). It could be beneficial to stabilize the semiquinone $Q_B^{\bullet-}$ to prevent back reactions to Q_A. This would, however, come at cost because a more positive $E_1(Q_B/Q_B^{\bullet-})$ must yield a more negative $E_2(Q_B^{\bullet-}/Q_BH_2)$ if the E_m is to remain the same. Therefore, back reactions from the fully reduced quinol Q_BH_2 would become more likely and the benefit would depend on the oxidation state of the quinone pool.

A study on the redox state of the plastoquinone pool from *Synechocystis* PCC 6803 found that under most conditions the pool is largely oxidized and even in very dense cultures in the stationary phase the fraction of reduced quinol did not exceed 50% (Schuurmans et al., 2014). Under these conditions, a strong stabilisation of $Q_B^{\bullet -}$ would indeed be beneficial in terms of protection against back reactions.

3.5.2 Previous work on the redox potential of Q_B

EPR detected redox titration from PSII membrane fragments from Ph. laminosum

The titration of the g~1.66 signal from membrane fragments prepared from *Ph. laminosum* by Corrie et al. (1991) yielded a curve centred at a lower potential and with a smaller width than in the titration from PSII core complexes presented in this chapter. Setting aside the uncertainty of this result (no normalisation of the g~1.66 signal was done, no reversibility was obtained, it was done at pH 8 and the intactness of the Mn_4O_5Ca cluster was not monitored) this raises the question of species dependence of the stabilisation of the semiquinone. PSII is constrained in its ability to modify the energetics of the cofactors due to its role as a water plastoquinone oxidoreductase. The oxidative potential needed for water oxidation and the usage of red photons sets the energy available in P^*. On the other side, the use of plastoquinone in oxidative photosynthesis sets a limit on the quinone potentials. Therefore, any optimisation for different ecological niches with different temperatures, light conditions etc. would have to target the energetics of the pheophytin and the quinones including the semiquinone state.[3] Further studies on a range of different organisms would be required to assess the nature of the discrepancies between the two titrations.

[3] A notable exception are the far red light harvesting species that use chlorophyll D or F for light harvesting. (Chen et al., 2005, 2010)

Kinetic estimates based on backreaction rates.

Before it was possible to titrate the quinones, estimates on their potentials were made based on the kinetics of different acceptor side reactions. Most notably this was done by Diner (1977) and Lavergne (1982) but also Bouges-bocquet (1973, 1975); Van Best and Duysens (1975); Robinson and Crofts (1983) have provided insights into the kinetics of the acceptor side reactions. See Petrouleas and Crofts (2005) for a relatively recent review of those works.

The underlying assumption of these studies is that the equilibrium constant K_E

$$K_E = \frac{Q_A Q_B^{\bullet -}}{Q_A^{\bullet -} Q_B}$$

can be estimated by a proxy measurement of some kind. In general, an apparent equilibrium constant is determined from kinetic rate constants of a selection of forward and back reactions using steady state approximations. Then the $\Delta\Delta$G and $\Delta\Delta$E between the Q_A and Q_B can be calculated via Eq. 3.1 and 3.2. Diner (1977) measured the disappearance of the S_2 state over time at different redox states of the quinone pool by measuring the yield of oxygen produced by a series of flashes after a variable time after a first saturating xenon flash. Lavergne (1982), on the other hand, used fluorescence measurements to measure the kinetics and concentration dependence of the binding of DCMU to Photosystem II. Both of these studies derive an equilibrium constant $K_E \approx$ 15-20 ($\rightarrow \Delta E$ 75 mV) although the underlying assumptions and formulas used are diverging and mutually exclusive (Lavergne, 1982). This equilibrium constant is too small for the ΔG of 234 meV, determined in this work ($K_E \approx 7000$).

Flaws can be found in all of these publications, which stem mainly from the limited understanding and availability of methods at the time. To name a few: the back reaction from Q_A is assumed to be a first order process, which it is not (Rappaport et al., 2005; de Wijn and van Gorkom, 2002). No gating mechanism is considered, which would significantly alter the models and results of both studies. It is likely that a gating mechanism similar to the one described in bacterial reaction centres

(Kleinfeld et al., 1984; Graige et al., 1998) exists in Photosystem II (Garbers et al., 1998; Reifarth and Renger, 1998; Fufezan et al., 2005). Also, both of the discussed works (Diner, 1977; Lavergne, 1982) assume equal binding of the quinone and quinol to the Q_B site, which according to the results in the present work is not the case. The effect of different molecules in the Q_B binding site such as DCMU on the redox potential of Q_A and the back reaction rates, is not considered. It should be noted that a similar approach to estimate the equilibrium constant from the kinetics of the different back reactions in bacterial reaction centres was also not in agreement with values derived by other approaches (Crofts and Wraight, 1983). It can therefore be concluded that without better understanding of the gating mechanism, the exact binding constants and pK's of the different species etc., this approach is unlikely to yield correct results.

Thermoluminescence measurements

The energy gap determined by numerical simulations (Rappaport and Lavergne, 2009) is much smaller (80 meV)[4] than what was determined in this work (234 meV). The predicted ΔG_d dependence of 0.4 °C meV^{-1} could not be verified experimentally in Section 3.3. Instead, a slope of 0.15 °C meV^{-1} (1/6.45 °C^{-1} meV) was observed. This means that the theoretical model used is not a good enough representation of the true processes occurring in TL. As pointed out by Rappaport and Lavergne (2009) themselves, the model does not capture the kinetic heterogeneity of the electron transfer processes or any potential gating effect. To assess whether this is sufficient to explain the observed discrepancies would require an extensive overhaul of the model used, which was beyond the scope of this work.

One other problematic aspect of the numerical simulation is that, at first, a free energy gap of only 30 meV is obtained between Q_A and Q_B, which leads the authors to take a DCMU induced shift (+50 meV) into account to arrive at the 80 meV free energy change. This value was determined by Krieger-Liszkay and Rutherford

[4] A strangely small value for the temperature gap between the $S_2Q_A^-$ and $S_2Q_B^-$ bands of 12 °C is used. This is probably a mistake, as all values in the literature are around 20 °C (Rutherford et al., 1982, 1984a). With this correction their energy gap would be 100 meV.

(1998) via fluorescence based redox titrations of Q_A and therefore the 50 meV shift refers to a situation in which Q_BH_2 is bound at the Q_B site. How this relates to a system in which Q_B is present is unknown.

The here obtained relationship of 0.15 °C mV^{-1} yields an energy gap of 232 meV, which is in good agreement with the data from the EPR-detected redox titrations. This does not include a potential DCMU shift of 50 meV.

According to the calibration obtained in this work, a 50 meV shift would translate into a shift of TL peak position by 7.5 °C. Rutherford et al. (1982) compare a DCMU induced $S_2Q_A^-$ band to a $S_2Q_A^-$ band generated by reduction with small quantities of sodium dithionite and observes only a very small up-shift of the DCMU generated peak (≈2 °C, difficult to determine exactly due to a freezing artefact at 0 °C). Wydrzynski and Inoue (1987) compare a DCMU induced $S_2Q_A^-$ band to a $S_2Q_A^-$ band generated by heptane/isobutanol extraction of Q_B and do not observe a difference in peak position. Krieger-Liszkay and Rutherford (1998) compare a DCMU induced $S_2Q_A^-$ band to a $S_2Q_A^-$ band generated by prolonged detergent treatment to remove Q_B and report an up-shift of 10 °C for the DCMU-generated peak. It should be noted, that in thermoluminescence experiments in this work (see Appendix Figure 6.1) and in Sedoud (2012) on isolated core complexes of PSII from *T. elongatus* the DCMU-generated $S_2Q_A^-$ band is at a slightly lower, instead of at higher temperature, in comparison to a $S_2Q_A^-Q_BH_2$ band generated by giving multiple flashes.

Whether these reported shifts are truly due to DCMU binding or stem from perturbations of the system by the different experimental methods is difficult to say. Overall, the effect of molecules on the Q_B side on the redox potential of Q_A needs further, more careful investigation. Until this is resolved, methods based on thermoluminescence will involve a certain degree of uncertainty.

FT-IR-detected titration of Q_B

The midpoint potentials obtained in the present work differ significantly from a recently published study in which the ability to form $Q_B^{\bullet -}$ by a single saturating flash as a function of the applied potential was monitored by FT-IR measurements (Kato

et al., 2016). This was used as a measurement of the concentration of the oxidized quinone which decreases when the potential is lowered. At pH 6.5, what Kato et al. (2016) found was a curve almost indistinguishable from an n=2 Nernst curve centred around 155 mV. A fitting of the data yielded redox potentials of $E_1(Q_B/Q_B^{\bullet-})$ = 90 mV, $E_2(Q_B^{\bullet-}/Q_BH_2)$ = 210 mV (ΔE = -120 mV, E_m = 155 mV).

As illustrated in Figure 3.1, only in the range of -50 mV< ΔE < 50 mV does the shape of the concentration curve of the oxidized and reduced species deviate enough from the respective one or two electron Nernst curves to allow for a reliable determination of the redox couples. In the case of Kato et al. (2016), the curve is too close to a standard n = 2 Nernst curve to allow for a determination of the two redox couples, especially considering that only seven data points were measured. The reported ΔE = -120 mV from this fit would indicate that the semiquinone is not stabilized within the site. This would mean that almost no thermodynamically stable $Q_B^{\bullet-}$ could be observed at any point in a titration. The significant amount of thermodynamically stable semiquinone that was observed in this work, is clear evidence for a stabilised $Q_B^{\bullet-}$.

Given the reproducibility of our experiment, the fact that a preliminary result exists in the literature in PSII (Corrie et al., 1991) and very similar results have been reported in the homologous purple bacterial reaction centres (Rutherford and Evans, 1980), there is little reason to doubt the present result. Furthermore, it makes much more mechanistic sense (see discussion below). In the following, a rationalisation on how Kato et al. (2016) obtained the conflicting result is attempted.

The data of Kato et al. (2016) deviates little from an n = 2 curve with an E_m(pH 6.5) = 155mV (at pH 7 this would be 125mV) that is very close, albeit slightly more positive (preferential binding of the reduced quinol to the Q_B site), to the value expected for the PQ/PQH_2 couple: i.e. E_m(pH 7) = 117mV (Golbeck and Kok, 1979). Whilst a preparation of PSII cores does not have a plastoquinone pool as such, there is still the possibility for free plastoquinone that is not bound to the Q_B site, either in the hydrophobic patch or around PSII or dissolved in the detergent micelles. It has been reported that similar preparations of PSII core complexes to

the one used in this work contain at least one more quinone (Fufezan et al., 2005; Krivanek et al., 2007).

If it is assumed that the redox potential of a quinone is more positive when it is bound in the Q_B site than when it is free, then, in a reductive titration, the free quinone will be reduced before a quinone in the Q_B site. If enough time for equilibration is given, this reduced free quinone will exchange with the quinone in the site. If the mediation with the site then is poor, i.e. the mediators are at the wrong redox potential or don't have rapid enough access to the Q_B site, this quinone will remain reduced without regard to the true potential because the electrons cannot be taken away. In such a case, the potential of the free quinone would be measured with an n = 2 Nernst dependency.

Given that only three mediators were used in their titration, out of which only one was in the appropriate range (1-methoxy-5-methylphanazinium methosulfate, Em = +63 mV) it is likely that, due to insufficient mediation, the potential of free plastoquinone was measured.

3.5.3 Conclusion and future work

Based on the data from the EPR titrations and the TL measurements, a model of the energetic regulation within PSII can be constructed. In contrast to earlier models, it is now apparent that there is more driving force to reduce Q_B as its potential is more oxidizing than previously assumed. The E_m of the two reactions is however still low enough to allow for preferential binding of the quinone over the quinol (see Fig. 3.14). The stabilisation of the semiquinone $Q_B^{\bullet -}$ allows for a two-step reduction with each step transferring one electron and one proton. It is not yet possible to reconcile the discrepancy between estimates of the energy gaps based on kinetic measurements and the energy gaps estimated here on the equilibrium redox titrations and the TL monitored back reactions. However, it seems likely that a gating mechanism, like that studied in purple bacterial reaction centres (Kleinfeld et al., 1984; Wraight, 2004), may be responsible for the discrepancy.

In contrast to Q_A, which upon loss of the Mn_4O_5Ca cluster shifts 145 mV more

positive, the E_m of the two Q_B couples does not shift under these conditions. It might, however, be that the stabilisation of $Q_B^{\bullet-}$ is slightly higher when the Mn_4O_5Ca cluster is absent. To determine if this is the case, more titrations with the Mn-less system would need to be done to be able to fit the data with high enough certainty. Furthermore, because in this system a higher fraction of Q_A will be reduced, the influence of this on the Q_B EPR signals needs to be quantified more carefully.

In this context it would also be interesting to test if it is possible to create a system where the Q_A potential is more positive than either one or both of the Q_B couples. In this case, a titration of Q_B would not be influenced by a varying concentration of Q_A. Secondly, it would be valuable to determine the Q_A potential in the presence of the quinone Q_B or the semiquinone $Q_B^{\bullet-}$. Until now, all determinations of the Q_A redox potential have been done in the presence of the quinol Q_BH_2, however, the redox state of Q_B might influence the exact potential of Q_A. As, under functional conditions, the reduction of Q_A happens light-induced and therefore mostly in the presence of the oxidized Q_B this value is of physiological relevance. It is often used to calculate the E_m values of the other cofactors in PSII which can not be measured directly. It is already known that different molecules in the Q_B site influence the redox potential of Q_A. Therefore, a more detailed investigation could be valuable for a better understanding of the system.

Furthermore, it is interesting that a biradical state was produced in the dark in a fraction of the centres. This raises the question whether this also happens under certain naturally occurring conditions, such as during photoactivation of Mn_4O_5Ca cluster, and if this state has relevance for sensing or signalling of stress conditions. Due to the distinctive biradical EPR signal at g~1.66 this state should be relatively easy to monitor and therefore study its relevance.

Finally, due to the slightly diverging results obtained by Corrie et al. (1991), the question of species dependence and isoform dependence of the Q_B redox potentials is raised. The TL method to determine the redox potentials could be very helpful as it should be applicable to a range of different samples and needs much less time and sample volume than EPR titrations. If this method reliably measures the E_m gap

between Q_A and Q_B, it could be used to screen a large number of organisms under different conditions to answer some of the questions mentioned above.

A manuscript for publication of the results presented in this chapter is currently in preparation.

4 Investigation of the Kinetics of Quinone Electron Transfer

The aim of the work presented in this chapter is to gain a better understanding of the timescale and nature of the processes that occur after the reduction of Q_A in samples relevant to current research.

Section 4.1 will introduce the rational for the presented experiments based on previous work on the kinetics of the electron transfer reactions. Section 4.2 explores the use of C550 shift measurements to determine the kinetics of electron transfer on consecutive saturating single turnover flashes. The decay of $Q_A^{\bullet-}$ in a long dark-adapted sample is significantly faster on the first flash than on subsequent ones. Small period-of-two oscillations in the rates are observed on subsequent flashes. The kinetics of $Q_A^{\bullet-}$ reoxidation specifically by $Q_B^{\bullet-}$ were measured using a semiquinone absorption band at 320 nm in Section 4.3. Absorbance changes at 292 nm caused by the oxidation of the manganese cluster are presented in Section 4.4. By using these absorbance changes as a probe of successful charge separation and by varying the time between two actinic flashes these measurements were used to determine the $Q_A^{\bullet-}$ reoxidation kinetics at faster timescales than previous measurements on highly purified PSII samples in solution and on PSII crystals.

In Section 4.5 the information from the previous sections is used to develop a theoretical model of the acceptor side. The model allows for a better interpretation of the data and provides new insights into the composition of the sample in the dark. Section 4.6 discusses the ramifications of these measurements for the mechanism of electron transfer between the quinones and PSII research in general.

4.1 Introduction

Kinetic measurements are an invaluable tool for deducing the reaction mechanisms of chemical reactions. In PSII, the rates of the excitation and redox events are of fundamental importance for the understanding of the complex and the limits of photosynthesis. They have therefore been the subject of decades of research. The rate of electron transfer between the quinones is of special importance as it determines the rate at which photons can be absorbed productively by PSII.[1]. This is because when Q_A is reduced, the quantum yield of charge separation is low; due to the electrostatic effect of the charged $Q_A^{\bullet-}$ on the neighbouring pheophytin anion radical, the redox potential of the pheophytin is made more negative, bringing it close to the level of P* and therefore eliminating the driving force for charge separation (Rappaport et al., 2002).

Based on an edge-to-edge distance of the quinones of 14.3 Å, Moser et al. (2005) calculated the electron tunnelling rate constant to be $\approx 0.4\,\mu s$. This is about three orders of magnitude faster than what is experimentally observed, showing that for this reaction, in contrast to most others in PSII, the electron tunnelling process is not the rate-limiting step. Instead, the reoxidation kinetics of $Q_A^{\bullet-}$ show a multiphasic decay with components ranging from ≈ 0.2 ms to longer than a second.

Using fluorescence yield measurements on spinach thylakoids, de Wijn and van Gorkom (2001) assigned four phases to the decay of $Q_A^{\bullet-}$. These were attributed to (1) the oxidation of $Q_A^{\bullet-}$ by a quinone in the Q_B site ($t_{1/2}$ = 200-400 µs), (2) by a semiquinone in the Q_B site ($t_{1/2}$ = 600-800 µs), (3) by an empty Q_B site ($t_{1/2}$ = 2-3 ms) where a quinone needs to bind, and (4) by a site in which hydroquinol is still bound and needs to exchange with a quinone ($t_{1/2} \approx 0.1$ s).

Due to the overlap of these components and intrinsic heterogeneities, for most samples it is not possible to de-convolute the decay kinetics in this way. Instead, most work in the literature uses three components to fit the decay kinetics. These

[1] The electron transfer between the quinones is not the slowest process in the light reactions. The reoxidation of the hydroquinol at the b_6f complex is even slower (5-10 ms), which under some conditions could be limiting oxygenic photosynthesis (Tikhonov, 2013; Hasan and Cramer, 2012)

represent the oxidation of $Q_A^{\bullet-}$ by Q_B and $Q_B^{\bullet-}$ (fast phase), by quinone entering an empty Q_B site or exchanging with Q_BH_2 (intermediate phase) and by recombination with the manganese cluster when forward electron transfer cannot occur (slow phase).

A range of values for the half-time of these phases, all derived from fluorescence yield measurements, can be found in the literature for different samples: 0.39-1.1 ms, 6.4-22 ms and 1.5-10 s for PSII membranes isolated from plants (Boisvert et al., 2007; Chernev et al., 2011; Sigfridsson et al., 2004; Vass et al., 1992, 2002); 550-660 µs, 6.2-7 ms and 9.7-13.3 s for Synechocystis cells (Cser and Vass, 2007; Deák et al., 2014; Sicora et al., 2008); ≈1 ms, ≈30 ms and ≈50 s for *T. elongatus* cells (Deák et al., 2014; Deák and Vass, 2008; Kós et al., 2008); 0.78-1.5 ms, 9-90 ms and 5-10 s for PSII dimers purified from *T. elongatus* and 3.7-3.6 ms, 35-46 ms and 5-13 s for PSII monomers purified from *T. elongatus* (Kargul et al., 2007; Mamedov et al., 2007; Zimmermann et al., 2006).

Whilst the three-component analysis of fluorescence decay data has been very useful in many cases, it is problematic for studying the electron transfer mechanism of the quinones itself.

Firstly, fluorescence measurements of PSII have an intrinsic lower limit of time resolution. Below ≈ 100 µs the induced fluorescence can not be used as an indicator of the redox state of Q_A because of the possible presence of strong fluorescence quenchers such as long lived P_{680}^+ (de Wijn and van Gorkom, 2001). Furthermore, experimental difficulties make fluorescence measurements unreliable at fast timescales. Artefacts resulting from excitation of delayed fluorescence in the glass or cathode material of the detector by the strong prompt fluorescence of the PSII particles as well as by scattered light of the excitation flash are often a problem (Buchta et al., 2007).

Secondly, the inability to separate the different electron transfer processes is problematic. The reoxidation kinetics of $Q_A^{\bullet-}$ by Q_B or $Q_B^{\bullet-}$ are too close together to be easily discriminated in fluorescence measurements. To better understand the electron transfer mechanism and the gating effect, it would be useful if these processes could be monitored independently.

The knowledge of the exact kinetics of those processes are also a necessary re-

quirement for studies of PSII from *T. elongatus* that require the generation of homogeneous S-states of the manganese cluster. Efficient oxidation of the manganese cluster, using saturating single turnover flashes, is only possible when Q_A is oxidized at the time of the flash. Therefore detailed knowledge of the decay kinetics of Q_A and the exact nature of the resting state of relevant samples, i.e. isolated PSII cores from *T. elongatus*, are of importance for generating pure, advanced S-states in those samples. This is necessary for many methods studying the donor side of PSII and the mechanism of water splitting.

The absence of these data has compromised recent high profile work using X-ray free electron laser (XFEL) crystallography to study the S_3 state of PSII microcrystals from *T. elongatus* (Kupitz et al., 2014a). Here a flash spacing of 210 µs was used between two saturating flashes to generate the S_3 state. Considering the reported halftime of >800 µs for the fast phase in *T. elongatus*, it is unlikely that this treatment generated a large fraction of the desired S-state. In his Ph.D. thesis, Jeffrey Douglass, using fluorescence induction decay measurements on isolated PSII dimers, measured a halftime of 610 µs for the decay of the fast phase (Douglass, 2015). Although this is faster than previously reported, it is still three times longer than the flash spacing used by Kupitz et al. (2014a). Furthermore, he showed that samples that were dark-adapted for a long time (overnight) and samples that were incubated with ferricyanide decayed even faster, with halftimes of 400 µs and 120 µs respectively. It was argued that both long dark adaptation and incubation with ferricyanide resulted in faster decays because of a) a reduction of the amount of $Q_B^{\bullet-}$ present at the start and b) a presumed oxidation of the non-heme-iron to Fe^{3+}. Reports on the kinetics of the electron transfer from $Q_A^{\bullet-}$ to Fe^{3+} in the literature are somewhat divergent but in general the process is presumed to be fast. Boussac et al. (2011) reported a halftime of 55 µs for *T. elongatus* samples. These experiments highlight the fact that the exact history of the sample, i.e. how much light exposure was received at what time, can be very important when dealing with isolated PSII samples.

The applicability of J. Douglass' data is limited due to the used material and methods. Firstly, the kinetics are at the very limit of what can be measured with

fluorescence techniques, casting doubt on the obtained halftimes and relative contributions. Secondly, a non-saturating 20 µs LED flash was used to excite the sample. Multiple turnovers of the manganese cluster could not be studied due to the lack of sample saturation. Also the comparatively long excitation flash is likely to lead to double hits in centres that have the oxidized iron present, which could lead to an underestimation of the fraction of oxidized iron in those samples.

Thirdly, it is possible that the kinetics of the samples used by Douglass (2015) differ from the ones used by Kupitz et al. (2014a). It is possible that the decay kinetics in crystals are significantly altered compared to solubilized PSII cores. Furthermore, the preparation methods of the samples are different. To obtain micro-crystals of PSII, many purification steps including multiple recrystallisations, carried out in absolute darkness, are necessary. WT-PSII is purified from cell extract (grown in a different type of bioreactor) using a set of anion-exchange columns (Kupitz et al., 2014b). In the work of J. Douglass, a CP47-HIS-tagged mutant strain was used to purify PSII (see also section 2.2). All these differences could lead to differences in lipid composition, Q_B site occupancy, presence of extrinsic polypeptides, etc., which might influence the electron transfer kinetics at the quinone site.

The aim of this work is therefore twofold. Firstly, due to the limitations of the fluorescence based approaches, different methods to measure the electron transfer between the quinones should be explored. Secondly, samples that are relevant to current topics in the field, such as XFEL crystallography and studies on the mechanism of water oxidation, should be used.

4.2 $Q_A^{\bullet-}$ Reoxidation Kinetics by C550 Shift Measurements

Knaff and Arnon (1969) report the first spectroscopic measurement of the relaxation of C550 and Erixon and Butler (1971) demonstrated the linear dependence of the absorption change on the concentration of $Q_A^{\bullet-}$. Van Gorkom (1974) determined the C550 to be an electrochromic shift in the spectrum of the D_1-pheophytin caused by the charged $Q_A^{\bullet-}$. The measurement of the C550 shift should overcome some of the limitations of the fluorescence methods used previously. Firstly, there is no PSII-intrinsic time limitation on absorption measurements at short times after a saturating flash like in fluorescence. Secondly, the extinction coefficient of PSII for light at 550 nm is comparably low, which should reduce actinic effects caused by the measurement light.

4.2.1 C550 shift measurement of one saturating flash

Here the C550 shift was used to measure the decay kinetics of $Q_A^{\bullet-}$ using a modified JTS-10 (BioLogic) as described in section 2.3.1.

Figure 4.1 Panel A shows the decay of $Q_A^{\bullet-}$ from isolated PSII cores that were dark-adapted overnight, after a single saturating laser flash. A fit function with two exponential and one hyperbolic component was applied to the data. Panel B shows the effect of 6 µM ferricyanide (E_m ≈466 mV at pH 6.5, 1:10 PSII:FeCN) on the $Q_A^{\bullet-}$ decay of an otherwise similar sample. Ferricyanide should be able to oxidise any $Q_B^{\bullet-}$ present (E_m ≈120 mV at pH 6.5, see chapter 3). It has also been shown that ferricyanide can oxidise the non-heme iron, albeit at a slow rate (spinach chloroplasts [Chl] = 0.5 µM; FeCN 30 µM, $t_{1/2}$ = 10 min (Ikegami et al., 1973)). The addition of ferricyanide should therefore lead to faster rate of electron transfer. The kinetic parameters from both experiments are listed in Table 4.1.

The fast phase, after long dark adaptation, has a halftime of 380 µs and the addition of ferricyanide leads to a faster decay with a halftime of 170 µs. The intermediate

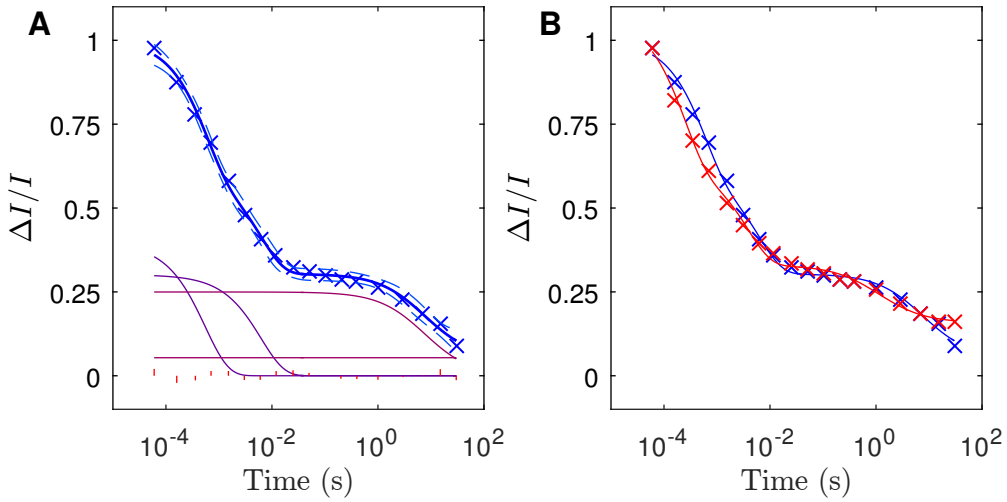

Figure 4.1: Kinetics of $Q_A^{\bullet-}$ decay measured by C550 shift. Panel A shows the decay of long dark adapted PSII cores after a saturating single turnover flash (blue crosses). Furthermore, the fit (blue), the confidence interval (light blue, dashed), the individual components of the fit (exponentials: purple; hyperbolic, constant: burgundy) and the residuals (red) are plotted. Panel B shows a comparison of the same data (blue) with a sample to which after dark adaptation overnight 6 µM FeCN was added (red). Both measurements are an average of five biological replicates.

Table 4.1: Fit parameters for the multiphasic decay in PSII cores. Data are the average ± standard deviation of five biological replicates.

	PSII cores			
	>12 h dark		+6 µM FeCN	
A_1 (%)	41.78	± 9.46	49.06	± 7.64
A_2 (%)	31.83	± 9.79	32.20	± 7.06
A_3 (%)	26.39	± 7.61	18.74	± 3.06
$t_{1/2}$ 1 (ms)	0.38	± 0.17	0.16	± 0.06
$t_{1/2}$ 2 (ms)	4.35	± 2.14	2.66	± 1.11
$t_{1/2}$ 3 (s)	7.64	± 6.82	1.13	± 0.90
Y0	5.68	± 7.99	17.30	± 2.78
Rsq	0.995		0.996	

phase is fit with a halftime of 4 and 2 ms respectively. The slow phase has a halftime of about 7 s and 1 s. These data are very similar to what was obtained by J. Douglass in a comparable fluorescence measurement (fast phase: 400 µs after long dark adaptation, 120 µs with ferricyanide; intermediate phase: 3 ms in both cases).

The fact that no slow component was observed in his measurement can be rationalized by the fact that a more purified sample, made of only PSII dimers, was used in his experiment. This is because the fraction of centres without a functioning manganese cluster should be reduced in this sample.

As mentioned earlier, these phases each fit multiple processes with presumably different kinetics. This makes it impossible to conclude the effect ferricyanide has on the PSII sample from this data alone. If the over-night dark-adaptation leads to a complete oxidation of the quinone pool, the faster rate of the fast phase after addition of ferricyanide, could be due to an oxidation of the non-heme-iron. The oxidation state of the quinone pool is unclear. The fact that in both experiments the addition of ferricyanide also leads to an increased amplitude of the first phase (more centres with oxidised quinone available) and a decreased amplitude of the

intermediate phase (centres in which no oxidised quinone is available) suggests that ferricyanide leads to a faster first phase by oxidising plastoquinol.

4.2.2 C550 measurement of consecutive single turnover flashes

The study of consecutive, saturating, single-turnover flashes instead of just one (not saturating) flash is of interest for a number of reasons. To study the mechanism of electron transfer to Q_B and $Q_B^{\bullet-}$ as well as the quinone exchange processes, consecutive flashes allow for a better understanding of the system because these processes will contribute to varying, degrees to the overall decay in a flash-dependent manner. In the simplest scenario, one would assume to observe the reoxidation of $Q_A^{\bullet-}$ by Q_B on the first flash and $Q_B^{\bullet-}$ on the second flash. On subsequent flashes, depending on the amount of quinone present in the sample, one would assume that quinone exchange processes become dominant in the decay of the $Q_A^{\bullet-}$ signal.

Saturating, single turnover flashes, i.e. flashes that maximise the number of PSII centres absorbing one photon, whilst minimizing the amount of centres absorbing multiple photons, are desired because this minimizes mixing of the different states over the flash series. As will be shown later, the emerging rate patterns, in combination with the present knowledge of the system, allow for a deconvolution of the processes happening after each flash, and the determination of the starting state of the system.

As mentioned before, most experiments in which it is necessary to generate pure advanced S-states also rely on consecutive, single turnover flashes. Here, the $Q_A^{\bullet-}$ decay kinetics need to be taken into account to choose adequate flash spacings.

Whilst it should in principle be possible to measure fluorescence decay with saturating single turnover flashes, in practice this is difficult to do. This is mainly because light emissions not directly related to the stimulated fluorescence occur at a similar wavelength and are therefore difficult to avoid. The C550 measurement has the advantage of separating the signal at ≈550 nm, from the artefacts resulting from the strong actinic flash at longer wavelength.

Figure 4.2 panel A shows the C550 change of dark-adapted PSII cores, for ten

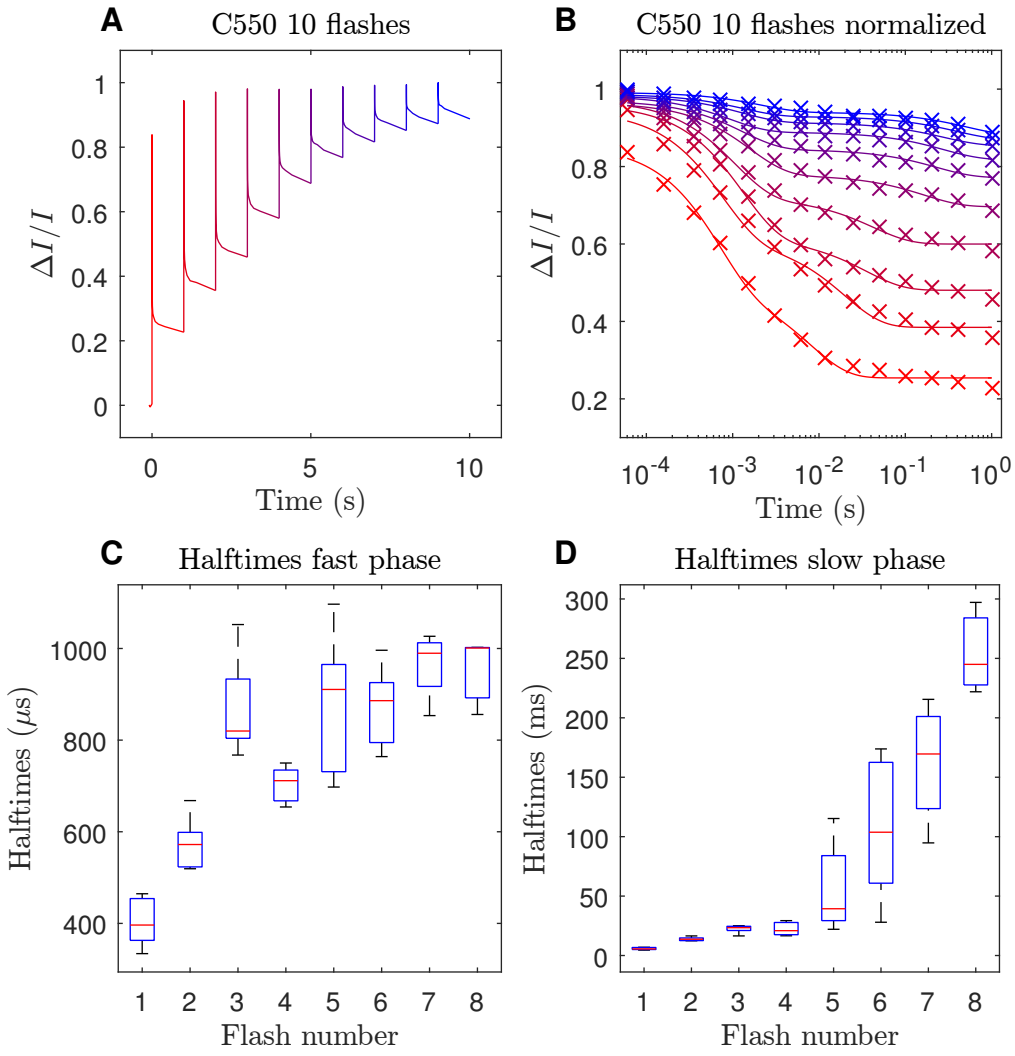

Figure 4.2: C550 shift of ten consecutive single turnover flashes. Panel A: PSII cores after long dark adaptation. Panel B: Two exponential fit for each flash; logarithmic plot. Panel C and D: Statistical analysis of the half-times of the fast **C** and slow phase **D** of five biological replicates of long dark-adapted PSII cores. On each box, the central mark is the median, the edges of the box are the 25th and 75th percentiles, the whiskers extend to the most extreme data points.

consecutive laser flashes, spaced one second apart. The first measuring point 60 µs after the first flash reaches 84% of the maximal amount of $Q_A^{\bullet-}$ which is reached after three flashes. This is in agreement with the quantum yield of charge separation being 0.85-0.9 (Cuni et al., 2004). With the chosen flash spacing, the decay after each flash does not reach the previous baseline. Instead, the proportion of centres that are capable of charge separation decreases with each flash, due to the reduction of the available quinone electron acceptors.[2] Panel B shows a two exponential fit of each flash of the same experiment, on a logarithmic timescale. It is apparent that both decay components get slower over the series of flashes. Panel C and D show a box plot of the statistical analysis of the obtained rates for the two phases of five replicates (see Appendix Table 6.1 for a summary of the fit parameters for each flash).

Either back reactions with the manganese cluster or slow oxidation by oxygen via Q_A should, over time, lead to a starting state in which Q_B is fully oxidized. If Q_B is fully oxidised at the start, when giving a series of saturating flashes, one would expect a dampened period of two oscillation pattern for the fast phase, resulting from the alternating electron transfer to Q_B and $Q_B^{\bullet-}$. Although the samples were dark-adapted overnight and light contaminations were reduced to a minimum, this is not what is observed in the experiment. Instead, the halftime for the first flash is faster than all subsequent flashes. There is some oscillation on flashes two to five, however it dampens out quickly and there is an underlying upwards trend of the halftimes.

The slow phase on the first flash is more than twice as fast (6 ms halftime) than the on the second flash (14 ms). The halftimes of the third and fourth flash are identical and slower again (22 ms). Most notable however is the drastic shift in halftimes from the fifth flash onwards, where subsequent flashes get successively slower. Furthermore, the deviation between individual samples increases from the fifth flash onwards. Although it is currently still difficult to attribute these rates

[2]When additional electron acceptors, such as DCBQ and ferricyanide are added, the variable absorption upon flash illumination is retained to a larger degree (data not shown).

to discrete physiological processes, the marked shift from the fifth flash onwards suggests that there are only two quinones directly available for electron transfer in most PSII centres: Q_B and one other "pool" quinone.

Other evidence for a second quinone available in PSII preparations from *T. elongatus* exists in the literature (Fufezan et al., 2005; Krivanek et al., 2007) although the exact location or nature of the binding site is controversial (Cardona et al., 2012). An additional quinone has been observed in the crystal structure by Guskov et al. (2009) but not in later crystallographic work.

It should be noted that the two-exponential fit components are not entirely independent. The underlying up-shift in the rate pattern of the fast phase is therefore likely caused by the up-shift of the slow phase. This is especially noticeable from the fifth flash onwards. Furthermore, the two-exponential fit does not perfectly describe the decays and considerable residuals remain in all time domains. This can be seen as an indication that the real decay of the sample is made up of more than two uniform components. The alternative possibility that at least a fraction of the residuals is due to artefacts picked up in the measurement method, can not be strictly excluded.

4.3 Semiquinone UV Absorption Measurements

UV absorption measurements have been important in identifying quinone molecules as electron carriers in photosynthesis (Bishop, 1959) and identifying Q_A as the primary acceptor in PSII (Stiehl and Witt, 1968; van Gorkom, 1974).

Figure 4.3 shows a light-minus-dark difference spectrum of sub-chloroplast particles from spinach and of isolated plastoquinone. Apart from the bound plastoquinone spectrum being slightly shifted to longer wavelength, the spectra look very similar. This was taken as an indication that the quinone is the primary electron acceptor in PSII.

The absorption maximum of the semiquinone radical at 320 nm can be used for kinetic measurements of $Q_A^{\bullet-}$ reoxidation. As observed by Lavergne (1991), when $Q_A^{\bullet-}$ is oxidized by Q_B, no change in the light-minus-dark spectrum occurs because both

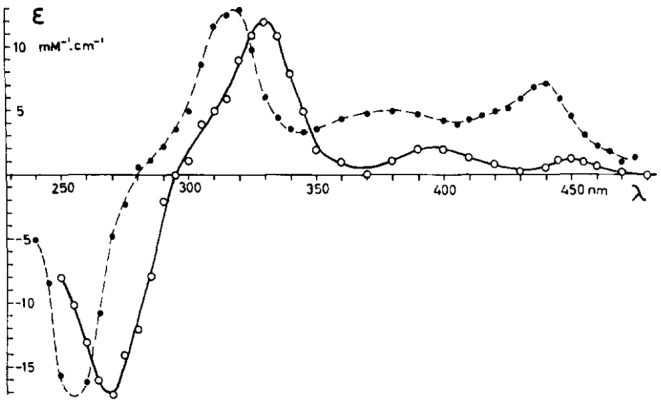

Figure 4.3: Light minus dark spectrum of spinach sub-chloroplasts particles (open circles) and free plastoquinone (filled circles). Reprinted from van Gorkom (1974) with permission from Elsevier.

semiquinones $Q_A^{\bullet-}$ and $Q_B^{\bullet-}$ have the same absorption spectrum and no overall change in semiquinone concentration occurs. The $Q_A^{\bullet-}$ to $Q_B^{\bullet-}$ electron transfer, however, leads to formation of Q_BH_2 and thus a change in overall semiquinone concentration. Measurements at this wavelength can therefore be used to measure the $Q_A^{\bullet-} \rightarrow Q_B^{\bullet-}$ electron transfer only, without interference from the $Q_A^{\bullet-} \rightarrow Q_B$ electron transfer.

The unambiguous determination of the kinetics of one of the components in electron transfer between the quinones is useful because it facilitates the deconvolution of the joint decay curves. Furthermore, the study of the electron transfer mechanism is easier if the different decay components can be studied separately. Here the effect of additional electron acceptors and the temperature dependence on the rate of electron transfer from $Q_A^{\bullet-}$ to $Q_B^{\bullet-}$ was studied.

4.3.1 Electron transfer rate to $Q_B^{\bullet-}$

Figure 4.4 Panel A shows the absorption change at 320 nm after a series of saturating flashes. The decays are fit well with one exponential component. This indicates that indeed the 320 nm measurement can separate the $Q_B/Q_B^{\bullet-}$ decays. The decay on the first flash is smaller than on all subsequent flashes. For a completely dark-adapted

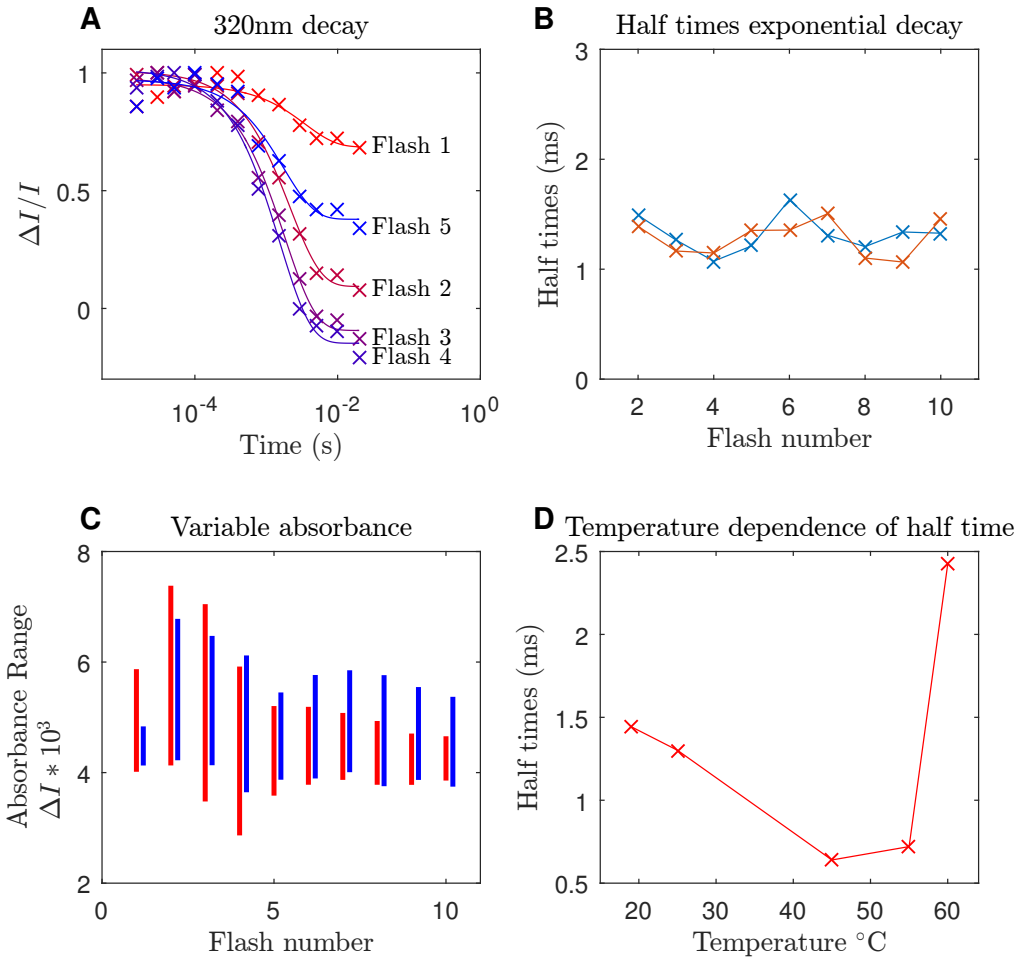

Figure 4.4: Semiquinone decay measurements at 320 nm. Panel A: PSII core complexes, no additions, flashes one to five (red to blue). Panel B: Comparison of halftimes of exponential decay of PSII core complexes without(red) and with ferricyanide and 10-PQ (blue), 25 °C. Panel C: Comparison of absolute decay sizes of PSII core complexes without(red) and with ferricyanide and 10-PQ (blue). Panel D:Dependence of halftime on temperature, PSII core complexes with ferricyanide and 10-PQ.

sample, however, i.e. no $Q_B^{\bullet-}$ present, no semiquinone decay at all should be observed. The decay on the first flash, therefore, indicates that $\approx 20\%$ of centres still have $Q_B^{\bullet-}$ present. The alternative possibility, the oxidation of $Q_A^{\bullet-}$ by oxidised non-heme iron is excluded due to the halftime of the decay being too slow for this process.

Panel B shows a plot of the halftimes of the decays of ten subsequent 6 Hz flashes. PSII core complexes without additions are compared to samples where 10-PQ and ferricyanide were added as additional electron acceptors. Tables 6.2 and 6.3 summarize the fit parameters. The effect of the added electron acceptors on the halftimes is negligibly small. The average halftimes are 1.32 ± 0.15 ms (PSII core complexes) and 1.35 ± 0.2 ms (PSII core complexes + 10PQ + ferricyanide). There is a small oscillation of the halftimes visible in both samples. A tentative period of four oscillation which is more predominant in the sample with added electron acceptors is visible. It would suggests an effect of the donor side on the rates of electron transfer, which has been postulated before (Cardona et al., 2012) but the effect is small and ten flashes are not enough to validate this with certainty.

While there is little effect of the additions on the rates of electron transfer, changes can be seen when the amplitudes of the decays are considered. The normalisation of the data in Panel A facilitates the comparison in terms of rates but obfuscates absolute changes in absorption. Figure 4.4 Panel C therefore shows the absolute variation in absorption at 320 nm for each flash.

The amplitude of the first flash is reduced by the addition of 10-PQ and ferricyanide. This is most likely explained by an oxidation of residually, present $Q_B^{\bullet-}$ by ferricyanide. The amount of ferricyanide added (6 µM ferricyanide :0.6 µM PSII)is not able to completely abolish this decay on the first flash.

The amplitude of the peak after the fifth flash (see also Panel A) is considerably smaller than that of flashes two to four. This can not be explained with simple acceptor side oscillations. Here, the decrease in variable absorption on the fifth flash in the sample without addition can be readily observed (red bars). The amplitude of flashes five to ten is $\approx 36\%$ of flashes two to four. This effect is mitigated to a large extent by the addition of the Q_B analogue 10-PQ and the oxidant ferricyanide (blue

bars) where the amplitude remains at ≈ 72% after flash four. The data supports previous conclusions of two quinones being available for electron transfer in most of the centres. The fraction of centres that are able to carry out electron transfer beyond that either represent a sub fraction of the sample with more quinones available, or are centres where $Q_B^{\bullet-}$ is regenerated by reoxidation of the quinol. This is however unlikely as the only process conceivable on this timescale would be a recombination with Tyrosine Z in centres that have no manganese cluster present ($t_{1/2} \approx 10$ ms, Zimmermann et al. (2006)). A value of 36 % would be incompatible with other kinetic data.

Temperature dependence of electron transfer from $Q_A^{\bullet-}$ to $Q_B^{\bullet-}$

To measure the temperature dependence of the electron transfer from $Q_A^{\bullet-}$ to $Q_B^{\bullet-}$, the previously described experiment was repeated at different temperatures. Figure 4.4 Panel D shows the obtained halftimes in dependence of the temperature. A decrease in halftime with temperature is observed until 45 °C, the growth temperature of the organism. This decrease levels of towards 55 °C and at 60 °C there is a sharp increase in halftime. Shlyk-Kerner et al. (2006), using fluorescence decay measurements on intact cells from *T. elongatus* ,observed a similar dependence albeit without the decrease at high temperatures. It is argued that not denaturation but changes in local protein flexibility are causing the plateau in the halftimes.

Using the linear form of the Eyring-Equation 4.1

$$ln(\frac{k}{T}) = \frac{-\Delta H^{\ddagger}}{R} * \frac{1}{T} + ln(\frac{k_B}{h}) + \frac{\Delta S^{\ddagger}}{R} \tag{4.1}$$

the activation enthalpy can be estimated by plotting $ln(k/T)$ against $1/T$ (data not shown) (Eyring, 1935). The gradient then equals $-\Delta H^{\ddagger}/R$. The activation enthalpy for electron transfer is 22.5 kJ/Mol (average of flashes two to four). It should be noted that only three data points were used to obtain the gradient. More data points were recorded but had to be discarded due to an artefactual signal that influenced the fit results. Shlyk-Kerner et al. (2006) obtain an activation enthalpy of 19.7 kJ/Mol

(data calculated from figure 2). It is likely that this value is down shifted due to the use of fluorescence decay measurements to obtain the rate constants, as the obtained rate in this case is a combination of the reoxidation of $Q_A^{\bullet -}$ by Q_B and $Q_B^{\bullet -}$.

4.4 S-State Turnover as a Measure of $Q_A^{\bullet -}$ Reoxidation Kinetics

The flash spacing used by Kupitz et al. (2014a) to generate a sample with a high fraction of centres in S_3 has been criticized before as too short to efficiently generate the desired state (Douglass, 2015; Sauter et al., 2016). A number of rationales have been put forward as to how two flashes spaced 200 µs apart might lead to S_3 formation. Firstly, PSII in crystals could exhibit faster electron transfer either due to the purity of the sample, or due to the effect of the crystal lattice. Secondly, the addition of non-native quinones such as DCBQ might speed up the electron transfer. Thirdly, the manganese cluster might be oxidised even if Q_A is still reduced. Support for these hypothesises in the literature is slim. Due to the nature of the micro-crystalline sample, however, the kinetics of which have not yet been studied, rejection would be premature.

Here, the turnover of the S-states of the manganese cluster in function of the flash spacing was measured directly using UV-absorption measurements. This was done on redissolved PSII micro-crystals and suspensions of PSII micro-crystals. To consistently obtain micro-crystals of PSII, more purification steps than used in this work are required. The samples were prepared and provided by the group of P. Fromme according to Kupitz et al. (2014b). The data is, therefore, of direct relevance for experiments using laser flashes to advance the S-states on crystalline PSII samples. Figure 4.3 in Section 4.3 showed the light-minus-dark absorption spectrum of PSII in the UV. This spectrum is dominated by the semiquinone. Therefore, the wavelength of the isobestic point of the semiquinone, 292 nm), is commonly used to measure the absorption changes of the manganese cluster (van Leeuwen et al., 1992, 1993a,b; Lavergne, 1987, 1991).

4.4.1 Absorbance change at 292 nm of PSII dimers and micro crystals

As described in section 2.3.3, a series of actinic flashes at a rate of 5 Hz was given to a PSII sample and the absorbance change at 292 nm was monitored 100 ms after each flash. The absorption oscillates with a pattern of four, corresponding to the turnover of the S-states. An additional flash was inserted at a variable time after the first flash. The ability to alter the pattern of four oscillation of this flash was studied as a function of the time between the first flash and the additional flash.

Figure 4.5 Panel A shows the result of this experiment for redissolved PSII crystals. This sample should therefore mainly contain intact PSII dimers (Kupitz et al., 2014b). The data is normalized to resemble the $Q_A^{\bullet-}$ decay kinetics from previous sections (see section 2.3.3 for details). Little decay is observed on the first four data points (0.1 - 10 µs), showing that the time resolution of the measurements is sufficiently high to capture the entire process. The decay is best fit with two exponential components. The first component, with a halftime of 44 µs, amounts to ≈35% of the decay. The second component, with a halftime of 344 µs, amounts to 65% of the decay. It was previously shown that the non-heme iron, under certain conditions, can be oxidized (Zimmermann and Rutherford, 1986; Petrouleas and Diner, 1987; Boussac et al., 2011) and the electron transfer from $Q_A^{\bullet-}$ to an oxidized non-heme iron in *T. elongatus* has a halftime of ≈50 µs (Boussac et al., 2011). The observed fast phase could, therefore, be caused by an oxidized non-heme iron in about 35% of the centres. The halftime of the second component is consistent with halftimes reported for the $Q_A^{\bullet-}$ to Q_B electron transfer. No significant fraction of a slower component, like that associated with the $Q_A^{\bullet-}$ to $Q_B^{\bullet-}$ electron transfer, was observed in the measurement. This is most likely explained by the preparation and storage methods of the sample. In the Fromme group, PSII preparations are done in absolute darkness, and the samples are never frozen but instead stored at 4°C until usage. This probably leads to very little $Q_B^{\bullet-}$ being formed during the preparation and several days time are available to allow it to become oxidized in the dark.

Panel B shows the influence of DCBQ on the kinetics of the S-state turnover. The

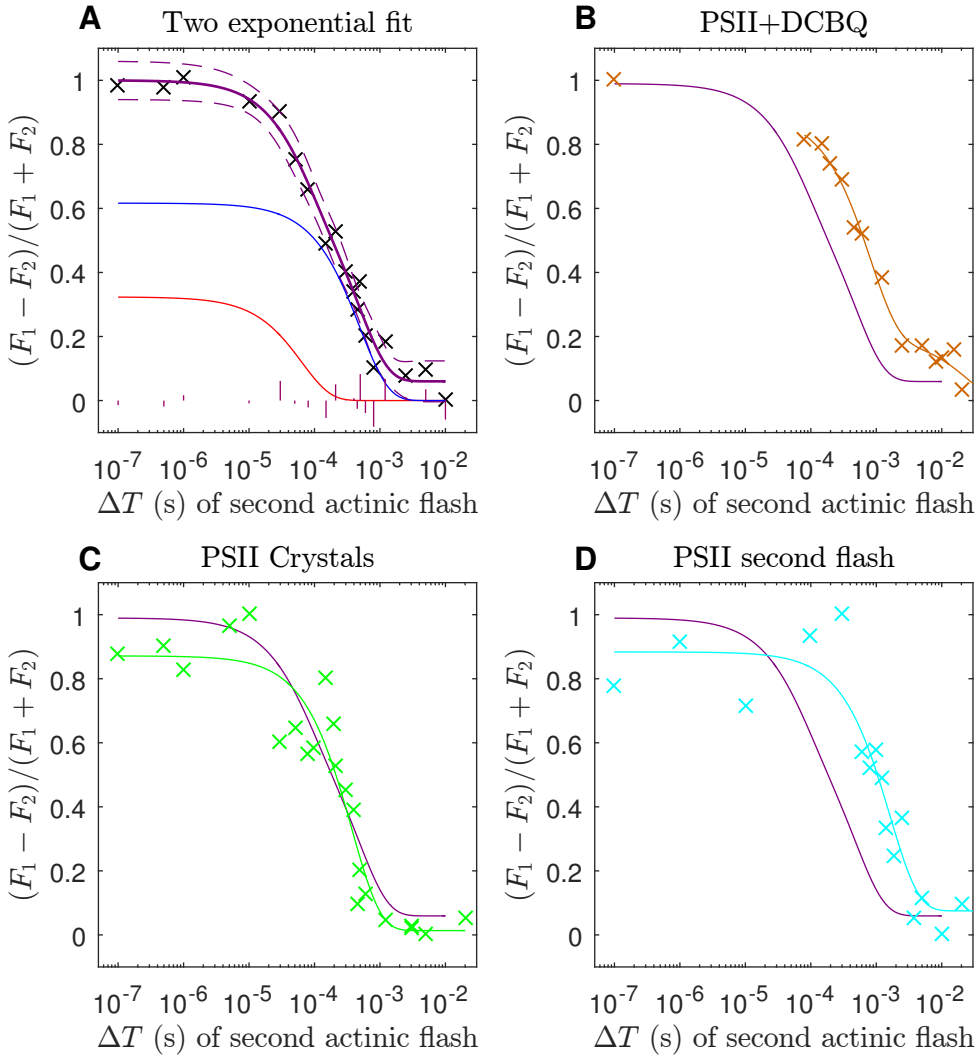

Figure 4.5: S-state turnover measurements. Panel A: two-exponential fit of redissolved crystals of PSII dimers. Panel B: redissolved crystals of PSII dimers with DCBQ (orange). Panel C: Measurement of suspended PSII micro-crystals. Panel D: The additional flash was inserted at a variable time after the second flash to monitor the S_2 to S_3 transition. For better comparison the fit of Panel A is plotted in all graphs.

main decay is significantly slowed down with a halftime of 550 µs. Additionally, an even slower phase with an amplitude of 22% and a halftime of 17 ms can be observed. Due to sample volume limitations, about 20% of the decay happening between 0.1 µs and 80 µs could not be resolved. DCBQ (E_M = 315 mV @ pH 7) is more oxidizing than the natural plastoquinone (see Chapter 3), therefore, the driving force of the reaction should be larger when DCBQ is oxidizing $Q_A^{\bullet-}$. That the reaction is still slower is probably explained by the lack of the isoprenyl tail in DCBQ, as it has been calculated that the interactions of the tail are important for quinone binding and headgroup positioning (Hasegawa and Noguchi, 2012; Warncke et al., 1994), which in turn is likely to be important for the efficient electron transfer. This hypothesis is supported by the fact that 10-PQ (having a decyl-chain instead of the isoprenyl chain) also slows down the electron transfer in C550 shift measurements (data not shown, halftime of first flash 470 µs) but not in the 320 nm measurements (see Figure 4.4). This could be explained by interactions to stabilize the negative charge of the semiquinone pulling the molecule into place.

Panel C shows the S-state turnover measurement on a suspension of PSII micro-crystals as used in free-electron-laser crystallography experiments. This measurement is noisier than when redissolved PSII core complexes were used. This is likely due to unnoticed aggregation of the micro crystals over the time course of the experiment (samples at shorter ΔT). This prevents a detailed analysis of the decay, however, the overall decay appears to be similar to the one from Panel A. Fitting the data with one exponential yields an approximate halftime for the efficiency of an additional flash of ≈260 µs in PSII micro-crystals. This shows that no significant speed-up occurs in PSII micro-crystals. Furthermore, this shows that two flashes spaced 210 µs apart will only yield up to ≈ 40% of S_3.

All experiments in Figure 4.5 were done on long dark-adapted samples in which the majority of the centres should be in the S_1 state. The additional flash therefore tests the $S_1 \rightarrow S_2$ transition. If the additional flash is inserted after the second actinic flash, the $S_2 \rightarrow S_3$ transition can be tested. Panel D shows this experiment on redissolved PSII crystals. Again, the noise of the data is too large to allow for

multicomponent fitting. The noise here results from the fact that the absorbance change associated with the $S_2 \rightarrow S_3$ transition is smaller than the $S_1 \rightarrow S_2$ transition (see Figure 2.6 or van Leeuwen et al. (1993b) for a more detailed investigation). The approximate half-time for this transition is 800 µs. This slow-down of the halftime indicates a higher fraction of centres with electron transfer from $Q_A^{\bullet -}$ to $Q_B^{\bullet -}$. Appendix Table 6.4 summarizes the fit parameters for all fits in Figure 4.5.

All observed decay rates can be attributed to reactions on the acceptor side of PSII. These experiments, therefore, show that the turn over of the S-states is indeed limited by the reactions of the acceptor side. It was observed that about 35% of centres in this samples show a fast decay with a halftime of 44 µs. Micro-crystals do not show a faster decay of $Q_A^{\bullet -}$ than dissolved PSII dimers, and the non native electron acceptor DCBQ shows a slower decay rate than samples without additions.

4.5 Rate Pattern Analysis

The key advantage of a series of saturating flashes over single or unsaturating flashes is that information about the nature of the system can be gained from analysing any emerging patterns. Most prominently, the observation of a period of four oscillation of the oxygen yield on a series of saturating flashes by Joliot et al. (1969) led to the development of the S-state model of the manganese cluster by Kok et al. (1970). By recognizing that the Kok model is a Markov process (i.e. a stochastic, memory-less sequence), many different experimental data have been fit by iterative (recursive) mathematical algorithms (Delrieu, 1974; Lavorel, 1976).

Similar models have been used to analyse period of two oscillations in the fluorescence amplitude during a series of flashes in spinach chloroplasts (Shinkarev and Wraight, 1993; Shinkarev, 2004). In the here presented work with isolated PSII, it was not possible to consistently reproduce the period of two oscillations observed by other researchers (Bowes and Crofts, 1980; Robinson and Crofts, 1983; Eaton-Rye and Govindjee, 1988; de Wijn and van Gorkom, 2001). Instead, two fast decays were observed at the start of a series of saturating flashes, followed by a marked deceleration and a very limited period of two oscillation. This pattern can not be accounted for by the previously developed model (Shinkarev, 2004).

There are, however, a series of indications that this model is not applicable to isolated PSII. Firstly, in isolated PSII there is no quinone pool that gets constantly reoxidized and is able to uphold prolonged oscillations. Therefore, the amount of observable oscillations should be limited and the redox state of Q_B at the start might be different from that in intact membranes. Secondly, electron transfer to the non-heme iron is not included in the previous model. This is likely to be a severe limitation, as in Section 4.4 it was already shown that a considerable amount of the fast decay may be attributed to electron transfer to an oxidized non-heme iron.

Here, a simple Markov-model has been developed to describe the acceptor side processes, depicted in Figure 4.6. The following three states are considered: (1) $Fe^{3+}Q_B$, the acceptor side with an oxidised non-heme iron; (2) $Fe^{2+}Q_B$, the acceptor side with a reduced non-heme iron; (3) $Fe^{2+}Q_B^{\bullet-}$ the acceptor side with Q_B being in

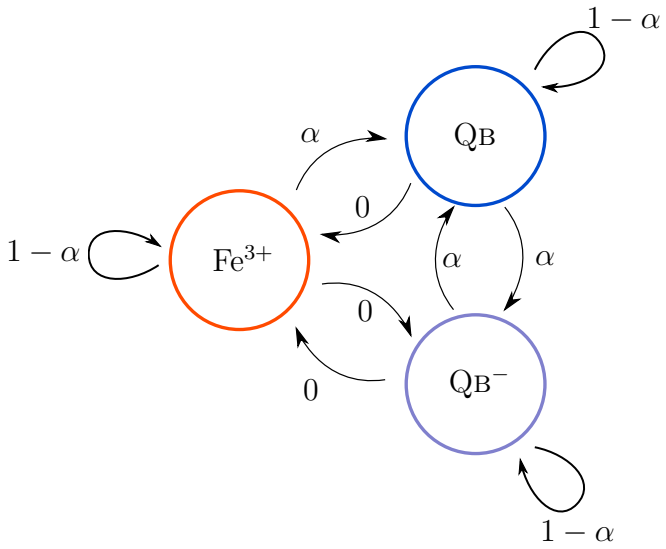

Figure 4.6: State diagram for the PSII acceptor side. The circles represent the three relevant states for the fast phase decay component. Arrows indicated possible transitions and their probabilities. α is the quantum yield of charge separation.

the semiquinone form.

The $Fe^{3+}Q_B$ state can only transition into the $Fe^{2+}Q_B$ state and there is no process regenerating this state, i.e the non-heme iron reduction is irreversible. The $Fe^{2+}Q_B$ state therefore can only transition into the $Fe^{2+}Q_B^{\bullet-}$ state and this can transition back to the $Fe^{2+}Q_B$ state. This, in essence, is a description of the two step reduction of Q_B, and then replacement of Q_BH_2 with a new oxidized quinone.

Other states, such as the hydroquinol binding in the Q_B-site or the site being empty, were not included in the model. This is because centres in these state should not contribute to the oscillations of the fast phase, which is the process that is modelled here. Furthermore, they should play a minor role as long as oxidized quinone is available.

This state diagram is represented by the transition matrix A (Equation 4.2).

$$A = \begin{pmatrix} 1-\alpha & \alpha & 0 \\ 0 & 1-\alpha & \alpha \\ 0 & \alpha & 1-\alpha \end{pmatrix} \tag{4.2}$$

Here, the simplification that α, the quantum yield of charge separation, is independent of the donor side (i.e. S-state independent) has been made. While this is not the case, the error introduced by using an average value should be small and an inclusion of the donor side in the model would introduce more variables than can be resolved with the current data. For the same reasons, a similar simplification was made concerning the rates of electron transfer in the rate vector R (Eq. 4.3), i.e. that the rates are independent of the oxidation state of the manganese cluster.

$$R = \begin{pmatrix} k_{Fe^{3+}} \\ k_{Q_B} \\ k_{Q_B^{\bullet -}} \end{pmatrix} \tag{4.3}$$

The initial distribution of the states I (Eq. 4.4) is represented by two variables: x, the proportion of centres with an oxidized non-heme iron; and m, the proportion of centres with a semiquinone $Q_B^{\bullet -}$.

$$\begin{aligned} I = & \begin{pmatrix} [Fe^{3+}] & [Q_B] & [Q_B^{\bullet -}] \end{pmatrix} \\ = & \begin{pmatrix} x & (1-x)(1-m) & (1-x)m \end{pmatrix} \end{aligned} \tag{4.4}$$

From these equations, the observed rate in dependence of the flash number (n) is given by Equation 2.6.

$$k(n) = I \times A^n \times R \tag{2.6}$$

In practice, to conform with the previous sections, halftimes of decays were used instead of rates. For exponential decays, halftimes and rates are simply connected

by Equation (2.3).

$$t_{1/2} = \ln 2 \times k \tag{2.3}$$

The model presented here, uses six independent variables (x, m, α, t_{1-3}). Using iterative, recursive algorithms, the best fit for these variables can be determined from the observed rate pattern if the above-mentioned assumptions are valid for at least the first six flashes. In practice, using reasonable assumptions justified by knowledge of the system, the variables can be constrained to obtain a fit from fewer data points.

4.5.1 Rate pattern analysis of the C550 shift data

This model was used to analyse the rate pattern obtained in the C550 shift measurements of long dark-adapted PSII core complexes (Section 4.2) as described in Section 2.3.4. Figure 4.7 shows the fit of the acceptor side Markov-model to the C550 shift measurements shown in Figure 4.2. The insert shows the initial distribution of states obtained by the fit. Table 4.2 lists the obtained initial state distribution and the halftimes of electron transfer.

The model can reproduce the observed aggregate halftimes of the first five flashes. The rise in halftimes of the subsequent flashes can not be reproduced. It is likely that this rise in halftimes is an artefact of the three exponential fit. Because of the marked increase of the second-phase halftime on the fifth flash of below 10 ms to over 100 ms, a larger proportion of the decay is fit by the first exponential component; hence, the increase of the halftime of the fast phase. This limits the analysis to the first five flashes and five variables in the model. Therefore, the quantum yield of the flashes α was constrained according to previous measurements (α=0.87).

All other variables in the fit in Figure 4.7 were only loosely constrained ($0 < t_1 < 70$; $200 < t_2 < 800$; $1000 < t_3 < 5000$; $0 < x < 1$; $0 < m < 1$). The halftime of the electron transfer to the non-heme iron (58 µs) fits very well with what was observed in Section 4.4 (44 µs) and also the value obtained by Boussac et al. (2011) (55 µs). This is remarkable, because the first data point of the C550 shift measurements is

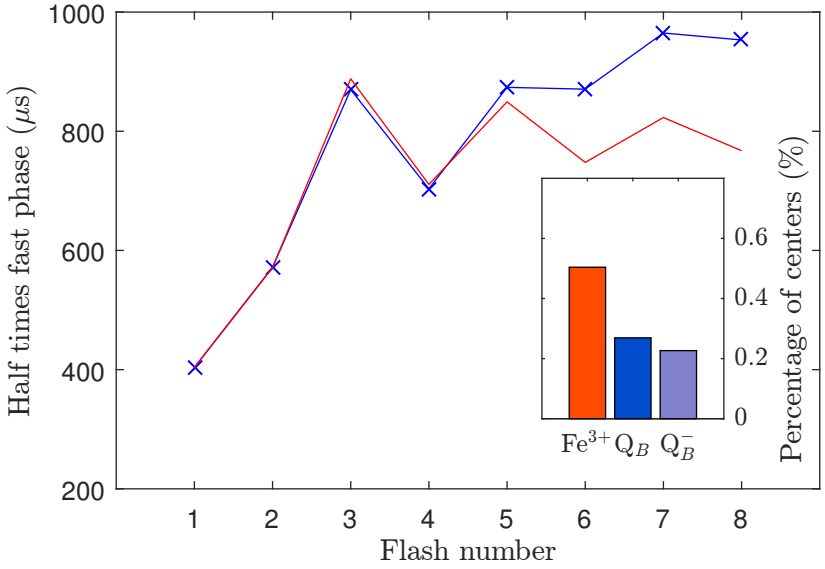

Figure 4.7: Markov-model fit of C550 shift measurements described in Section 4.2. The blue crosses shows the measured, averaged halftimes for each flash. The red line shows the fit obtained using Equation 2.6. The insert shows the obtained distribution of initial states.

Table 4.2: Parameters derived from the Markov-model fit. The halftimes in parenthesis are the values measured in Sections 4.3 and 4.4

	Initial percentage of centres (%)	Half-time of electron transfer (µs)	Half-time measured in previous sections ((µs))
$Q_A^- \rightarrow Fe^{3+}$	50	58	(44)
$Q_A^- \rightarrow Q_B$	27	369	(344)
$Q_A^- \rightarrow Q_B^{\bullet -}$	23	1213	(1320)

at 50 µs (i.e. the halftime of the ET) and only three data points are in the time domain of this process.

The halftime of the electron transfer to Q_B (368 µs) also is in good agreement with the value obtained in Section 4.4 (344 µs). To date, there are no reported measurement for this process for *T. elongatus* in the literature; however, de Wijn and van Gorkom (2001) report a halftime of 200-300 µs for this electron transfer in thylakoids from spinach. The difference may be due to the thermophyllic nature of *T. elongatus*. The growth temperature of the organism is 45 °C whilst the experiments were done at 20 °C.

The halftime of the electron transfer to $Q_B^{\bullet-}$ (1.2 ms) lies well within the range of values obtained in the 320 nm measurements for this process (1-1.5 ms; See Figure 4.4 **B**). Again, this is somewhat slower than the value obtained by de Wijn and van Gorkom (2001) (800 µs) and in this case the temperature dependence has been measured, and at the growth temperature of *T. elongatus* the halftime was 640 µs.

The overall good agreement with the values derived by other spectroscopic measurements, indicates that the model is a good description of the PSII acceptor side. Importantly, this also means that the initial distribution of the states can be regarded as a good approximation of the real situation[3].

The effect of overnight dark adaptation under different conditions

As the initial distribution of the redox states of the PSII sample after overnight dark adaptation was unexpected, further experiments with overnight dark adaptation under different conditions were made to better understand the phenomenology. The experiment in Figure 4.8 tests the oxidation of the non-heme iron as well as the stability of $Q_B^{\bullet-}$ during long dark adaptation. A sample was briefly illuminated with room light ($\approx$ 20 s) and then incubated in complete darkness for 12 h under different conditions. A series of flashes was then given and the kinetics of the decay of the

[3] If instead of the loosely constrained model a fully constrained model, where the halftimes are fixed to the values derived in the previous sections is used, the obtained distribution of initial states is almost identical (Fe^{3+}: 50%; Q_B: 29%; $Q_B^{\bullet-}$: 21%; See Appendix Figure 6.3) and the obtained rate pattern is still a good approximation for the observed values.

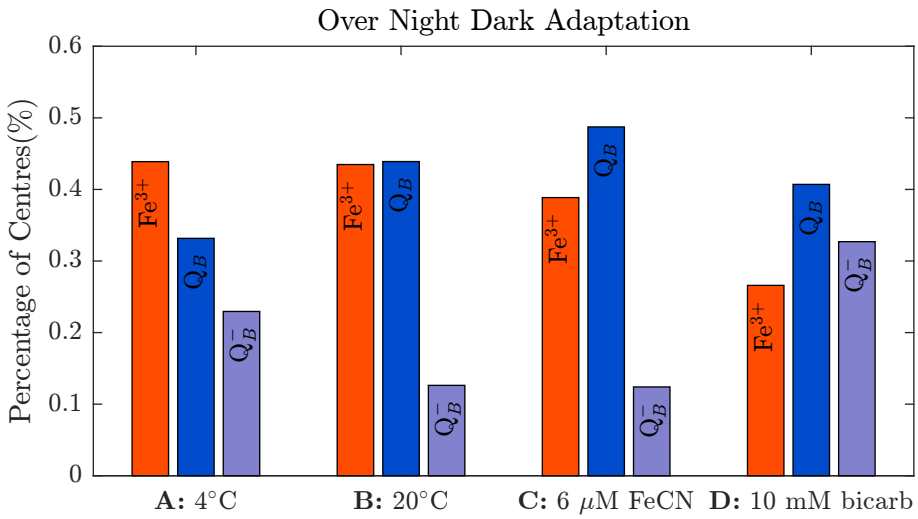

Figure 4.8: Overnight dark adaptation under varying conditions. **A:** Overnight dark adaptation at 4°C. **B:** Overnight dark adaptation at room temperature (20°C). **C:** Overnight dark adaptation at 4°C with ferricyanide. **D:** Overnight dark adaptation at 4°C with 10 mM bicarbonate (detailed rate pattern analyses are shown in Figure 6.4).

C550 shift measured. From the rate pattern analysis, the initial state after dark adaptation was obtained. Figure 4.8 Panel **A** and **B** show the effect of temperature on the overnight dark adaptation. In this work, overnight dark adaptation was, unless otherwise stated, always done at 4 °C. This is also the temperature at which crystal samples were stored. As observed previously, there is a significant proportion of centres that have $Q_B^{\bullet-}$ present. Overnight dark adaptation at 20 °C leads to comparatively more oxidised Q_B and less $Q_B^{\bullet-}$ whilst the proportion of centres with oxidized non-heme iron remains the same. This implies a marked temperature dependence of the oxidation of $Q_B^{\bullet-}$ possibly by oxygen.

The addition of 6 µM ferricyanide overnight at 4 °C leads to a similar composition as in Figure 4.8 Panel **B**, however, with slightly less oxidized iron in favour of oxidized Q_B. The fact that that much $Q_B^{\bullet-}$ is observed is to some extent surprising. It suggests that either the amount of reduced quinone per centre was underestimated, or that other redox active components are present in the sample. Furthermore, the slightly lower amount of oxidized non-heme iron in the presence of ferricyanide suggests that the latter speeds up the electron transfer rate on the first flash mainly by oxidizing $Q_B^{\bullet-}$ rather than the non-heme iron.

Addition of bicarbonate in **D** leads to a marked increase in $Q_B^{\bullet-}$, compensated mainly by a decrease in oxidized non-heme iron, suggesting that indeed bicarbonate plays a role in tuning the redox potential of the non-heme-iron and the absence of bicarbonate favours the oxidation of the non-heme-iron by $Q_B^{\bullet-}$.

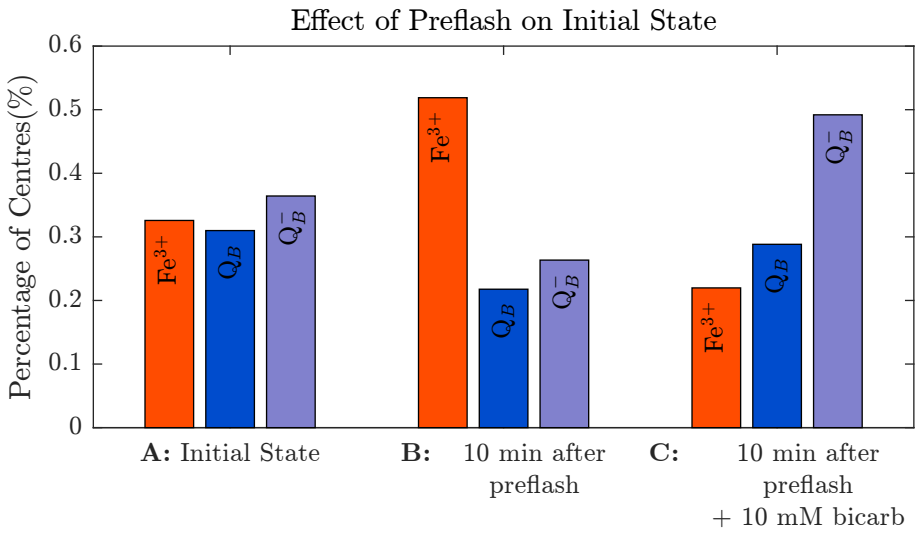

Figure 4.9: Effect of preflash on initial state. **A:** PSII sample dark-adapted for 2 h. **B:** Identical PSII sample ten minutes after a single preflash. **C:** Identical PSII sample ten minutes after addition of 10 mM bicarbonate and a single preflash (Detailed rate pattern analyses are shown in Figure 6.5).

The effect of short dark adaptation after a single preflash

To gain information on the timescale of these acceptor side processes, the effect of a short dark adaptation after a single preflash was investigated. First, the composition of the sample was determined by a series of flashes. Then in two identical PSII samples, a preflash was given, either with or without added bicarbonate. After 10 minutes of incubation in the dark, a series of flashes was given and the rate pattern analysis was used to determine the composition of the sample.

Figure 4.9 Panel **A** shows the composition of the sample, dark-adapted for ≈ 1 h after thawing. After the preflash, the sample without bicarbonate (Figure 4.9 Panel **B**) shows a large fraction of oxidized non-heme iron after 10 minutes of incubation. The addition of bicarbonate (Figure 4.9 Panel**C**) leads to a much smaller fraction of oxidized non-heme iron and more $Q_B^{\bullet -}$, indicating that the oxidation of the non-heme iron is slowed down in this sample.

If it is assumed that the flash reduces ≈ 87% of the centres that had an oxidized

iron at the start of the experiment, the presence of 20% of oxidized non-heme iron after 10 min in the sample with added bicarbonate shows that the oxidation is not completely prevented. This could be either due to a fraction of samples still not being able to bind bicarbonate, or the oxidation, although being slowed down, still occurring in all of the centres.

Discussion of rate pattern analysis

Two main insights arise from the rate pattern analyses. Firstly, $Q_B^{\bullet-}$ can be present in the sample even after long dark adaptation. The recombination of $Q_B^{\bullet-}$ with S_2 was shown to occur with a halftime of 22 s in pea chloroplasts (Robinson and Crofts, 1983). The slowest component, attributed to the $Q_B^{\bullet-}S_2$ recombination has a halftime of ≈15 s in luminescence experiments on isolated PSII cores from *T. elongatus* (see Appendix Figure 6.7). Furthermore, it was shown that if back-reactions with the manganese cluster are not possible, $Q_A^{\bullet-}$ can be oxidised by molecular oxygen with a halftime of 60 s (A. Fantuzzi personal communication, unpublished). Therefore, the presence of $Q_B^{\bullet-}$ after long dark adaptation is surprising as it was suspected to either recombine with the manganese cluster or react with oxygen via Q_A.

The marked effect of temperature on the effect of dark adaptation points to a kinetic inhibition of the oxidation of the semiquinone $Q_B^{\bullet-}$. Furthermore, it could be that additional quinones to those bound in the Q_B site are present in the sample that are reduced. Due to the preferential binding of the quinone this would not be immediately observable, but could lead to a fraction of $Q_B^{\bullet-}$ being formed from back reactions of Q_BH_2 with advanced states of the manganese cluster. This could also explain why a ten-times excess of ferricyanide over PSII did not lead to a full oxidation of the quinones.

Secondly, there is large proportion of centres that have an oxidized non-heme iron after dark incubation. This also was not previously reported and is most likely the cause of the fast decay of $Q_A^{\bullet-}$ after the first flash. The proportion of centres with oxidized non-heme iron was diminished by the addition of bicarbonate. The redox potential of the non-heme iron (430 mV at pH 6.5 in spinach chloroplasts (Bowes

et al., 1979)) is too high for a participation in native electron transfer between the quinones. Due to the positive redox potential in comparison with the quinones, it is then also not expected to be oxidised under functional conditions.

There are, however, reports in the literature that show that the non-heme iron can be oxidised under some circumstances. To understand the current phenomenon, it is useful to analyse these circumstances in more detail. As mentioned previously, it was first shown by Zimmermann and Rutherford (1986) that the non-heme iron can be oxidized by the unstable semiquinone form of certain high-potential quinones (phenyl-p-benzoquinone, dimethylbenzoquinone and benzoquinone). By detecting EPR-signals originating from the oxidized Fe^{3+} they were able to show alternating oxidation of the iron by the photoreduced semiquinone on odd-numbered flashes which was followed by photoreduction of the iron on even-numbered flashes in a flash series.

Boussac et al. (2011) demonstrated that addition of DCMU in the presence of $Q_B^{\bullet-}$ leads to the oxidation of the non-heme iron in a fraction of PsbA3-PSII core complexes, but not in PsbA1-PSII core complexes. It was concluded that DCMU lowers the redox potential of the non-heme iron, allowing for oxidation by $Q_B^{\bullet-}$ in PsbA3-PSII core complexes. Furthermore, the redox potential of the non-heme iron in PsbA1-PSII core complexes should be higher than in the PsbA3 variant, as no oxidation was observed here.

Further indications for the possibility of an oxidation of the non-heme iron by the semiquinone $Q_B^{\bullet-}$ come from *in silico* calculations. Ishikita and Knapp (2005) calculated that the redox potential of the non-heme iron is lowered to 268 mV when $Q_B^{\bullet-}$ is present. This is still ≈150 mV more positive than the $Q_B^{\bullet-}/Q_BH_2$ couple. However, if it is assumed that after reduction Q_BH_2 irreversibly leaves the site with a driving force of ≈ 30 meV, and is replaced by oxidised Q_B, a slow oxidation of the non-heme iron seems feasible.

In a QM/MM study focused on the PT/ET mechanism of the PSII acceptor side Saito et al. (2013a) reject the possibility of a carbonate (CO_3^{2-}) instead of a bicarbonate (HCO_3^-) ligand being bound to the non-heme iron because this would

lower its redox potential below that of Q_B resulting in Fe^{3+} being stable even in the presence of $Q_B^{\bullet -}$. This highlights the importance of the bicarbonate ligand for the redox potential of the non-heme iron. Based on the work in Section 3.2.1, Brinkert et al. (2016) showed that the bicarbonate ligand is easily lost at pH 6.5, the pH of the kinetic experiments shown here.

It is therefore hypothesized that the oxidation of the non-heme iron is caused by $Q_B^{\bullet -}$, in centres that lack the bicarbonate ligand.

4.6 Discussion of the Kinetic Electron Transfer Studies

The aims formulated in Section 4.1 have been achieved to a large extent. Three different spectroscopic techniques were used to analyse the kinetics of electron transfer on the acceptor side of PSII. Although some of these methods were used on PSII preparations from *T. elongatus* before, this work presents the to date most concerted effort to develop these methods, and extend the fluorescence-based approaches. Whilst most of the work was done using solubilized PSII core complexes from *T. elongatus*, evidence that micro-crystals show comparable behaviour was produced. The rates of electron transfer from $Q_A^{\bullet -}$ to the non-heme iron, to Q_B, and to $Q_B^{\bullet -}$ were determined using a combination of the three methods. The rate pattern analysis, developed in this work, leads to new insights about the state of the acceptor side in PSII core preparations. The implications of these findings with regard to the literature will be discussed in this section. An outlook on emerging questions and future work concludes the chapter.

4.6.1 Rates of electron transfer in T. elongatus

Previously, fluorescence based measurements of the electron transfer on the acceptor side of PSII were analysed using three components. These components, however, do not represent discrete electron transfer processes; instead, they constitute average

values from a mixture of processes that happen in the respective time domains.

The use of discrete exponential components has been criticized as arbitrary and approximate and a more complex description in terms of a rate distribution has been proposed and used in the literature (Bergantino et al., 2003; Boussac et al., 2013). Whilst this approach in some cases yielded similar or better fits of the experimental data (data not shown, furthermore often fits using this model were a lot worse than the conventional approach), it was not clear how this more complex approach would lead to a better understanding of the electron transfer reactions.

Instead, the approach pursued here was to reduce the complexity of the data by choosing more selective methods and better control of the sample. In this work, mainly the processes that constitute the fast phase were studied in PSII core complexes from *T. elongatus*. Three electron transfer processes, the electron transfer from $Q_A^{\bullet-}$ to the non-heme iron, to Q_B, and to $Q_B^{\bullet-}$ have been characterized. It was shown that a model of the acceptor side based on these three processes can accurately describe the rate pattern of the fast phase on consecutive single turnover flashes, demonstrating that these three processes are indeed determining the fast phase of electron transfer.

Rate of electron transfer between quinones

The electron transfer rate from $Q_A^{\bullet-}$ to $Q_B^{\bullet-}$ was measured using the absorption at 320 nm. This method allowed for an unambiguous determination of the rate because it is exclusively sensitive to the $Q_A^{\bullet-}$ to $Q_B^{\bullet-}$ electron transfer. A measurement of the temperature dependence showed that at physiological temperatures the rate is similar to previous estimates (de Wijn and van Gorkom, 2001).

Unfortunately no analogous method for measuring exclusively the electron transfer to Q_B, without contributions from other processes exists. It was also not possible to generate a sample in which this electron transfer is the only process occurring in a majority of the centres.

However, the rate of electron transfer from $Q_A^{\bullet-}$ to Q_B can be estimated when the rate to $Q_B^{\bullet-}$ is known. Because the average halftime of the two processes is ≈ 800 µs

(Zimmermann et al., 2006; Douglass, 2015, this work), if the electron transfer to $Q_B^{\bullet-}$ has a halftime of ≈ 1.2-1.3 ms, the electron transfer halftime to Q_B must be around 300-400 µs.

This estimate was confirmed using two methods. Using the rate pattern of five consecutive flashes, the contributions of the individual components and their halftimes were deconvoluted. The halftime of the electron transfer to Q_B was 369 µs. Secondly, using the S-state turnover measurements on a PSII sample provided by P. Fromme and her group, a decay with a halftime of 344 µs was found and attributed to the $Q_A^{\bullet-}$ to Q_B electron transfer.

Considering the inaccuracies of the methods, and the not explicitly considered, but possible S-state dependencies, a halftime of ≈350 µs is a reasonable conclusion from the present data.

Electron transfer from Q_A to the non-heme iron

To explain the fast rates of electron transfer after long dark adaptation on the first two single turn-over flashes, it was necessary to include an additional fast electron transfer component. Based on the halftime of ≈50 µs, this components was attributed to the electron transfer to an oxidized non-heme iron.

The existence of this electron transfer has previously been largely ignored in the literature. However, neither the existence of an additional fast phase, nor the attribution to the non-heme iron are without precedence. In fact, a close examination of the previous literature reveals that this is observed frequently, but mostly ignored (Dekker et al., 1984; Lavergne, 1991; de Wijn and van Gorkom, 2001) de Wijn and van Gorkom (2001) for example limit their analysis, without a good explanation, to flashes 2-5. Interestingly, their first flash is not in agreement with their model, precisely because of an additional faster component.

Bowes and Crofts (1980) measured binary oscillations in the decay of fluorescence yield 250 µs after each flash in a series of saturating laser flashes as a function of an applied potential. At potentials higher than Eh > 350 mV, they also find a faster component in the decay following the first flash. The binary oscillation was

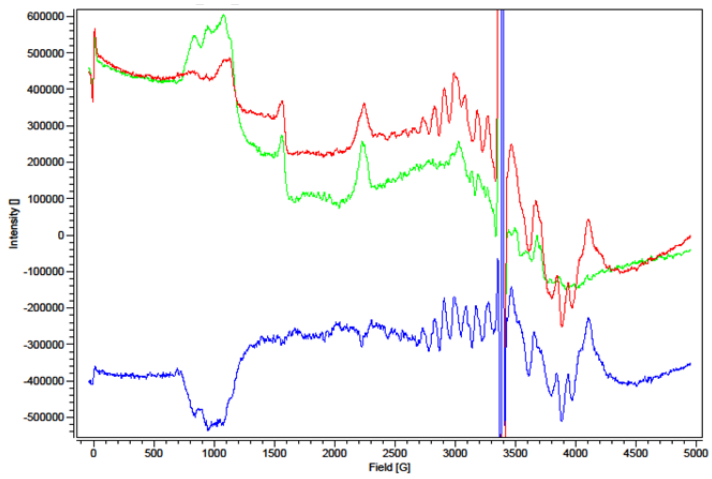

Figure 4.10: EPR spectra of PSII crystals at 4.2 K, 20 mW. Green: Dark spectrum; Red: After illumination at 200 K; Blue: Difference of the red and green spectra. Data printed with permission of A. Boussac and J. Shen.

still apparent but delayed by one flash. In fact, the observed pattern looks very reminiscent of what is observed in this work, and the potential of > 350 mV is indicative for the oxidized non-heme iron.

Evidence that this also occurs in micro-crystals of PSII is provided by A. Boussac (personal communication, unpublished). EPR measurements on micro-crystals, provided by the group of J. Shen, were done before and after illumination at 200 K. Figure 4.10 shows the resulting spectra and the difference spectrum. The broad feature near 1000 gauss is indicative of an oxidized non-heme iron in a fraction of the centres. This feature disappears after illumination at 200 K, showing the reduction of the non-heme iron. The formation of the g~1.66 signal, connected to the formation of the $Q_A^{\bullet-}Fe^{3+}Q_B^{\bullet-}$ state, further proves that a fraction of centres had a stable $Q_B^{\bullet-}$ in the dark. Due to the limited number of EPR spectra of PSII-micro-crystals and the complexity of the signals, the absolute fractions of the non-heme iron and semiquinone cannot be accurately determined. Comparison with EPR-spectra of other PSII samples, however, allows for an approximate estimate (data not shown) and it is estimated that the sample shown in Figure 4.10 contains 30-50% oxidized

non-heme iron and about 20-40% semiquinone.

Although this needs to be investigated more rigorously, the fact that both oxidized non-heme iron and the semiquinone were found in a dark-adapted sample of PSII micro-crystals lends support to the validity of the rate pattern analysis and its relevance for micro-crystals of PSII.

Nature of the second phase

The second exponential component has been used to fit processes with halftimes between 2 and 100 ms and was associated mainly with quinone exchange processes. An empty site, where a new quinone still needs to bind, is responsible for a rather fast reoxidation of $Q_A^{\bullet-}$ with a halftime of 2-3 ms. When instead the quinol Q_BH_2 is bound, the reoxidation occurs with a halftime of 0.1 s Crofts and Wraight (1983). This scheme is supported by evidence from the work by de Wijn and van Gorkom (2001).Here, assuming the $Q_A^{\bullet-} \rightarrow Q_B^{\bullet-}$ decay to be monophasic and the initial distribution of S-state to be known, the authors de-convolute the observed decays on a series of flashes and show that the 2-3 ms phase only occurs on flashes where mainly Q_B is present. As no detailed description of the de-convolution method used by de Wijn and van Gorkom (2001) is provided, it was not possible to reproduce their result.

In this work, the second phase showed a very marked pattern (see Figure 4.2), where the first two flashes showed fast decay of the middle phase with halftimes of 6 and 14 ms, the halftime of flashes three and four was identical, with a halftime of 22 ms and subsequent flashes showed a rapid increase in halftimes up to over 200 ms. It is also noteworthy that the standard deviation for flashes one to four is much smaller than for subsequent flashes, indicating that the processes on these flashes are more homogeneous than on subsequent flashes.

This, however, indicates that the middle phase is comprised of at least three different processes occurring with halftimes in the range of 5, 20, >100 ms. Furthermore, no reasonable model could be found that would correlate any of these phases solely to centres where Q_B is present instead of $Q_B^{\bullet-}$ as was done by de Wijn and van

Gorkom (2001).

The amplitude of this second phase is consistently larger than 30%, both in this work on isolated cores, and in others on more intact PSII preparations (Douglass, 2015; Kós et al., 2008; Deák et al., 2014). If this phase truly represents centres without quinone, however, this would mean that a quinone is not bound in more than 30% of the centres, which is not in agreement with estimates for the K_D of the quinone (Petrouleas and Crofts, 2005).

These discrepancies are addressed to some extent in the literature. Joliot et al. (1990, 1992) propose a "fast pool" of about 6 plastoquinones associated with a halftime of $Q_A^{\bullet-}$-reoxidation of 30 ms and a "slow pool" with a halftime of 0.8 s in spinach thylakoids. While the usefulness of these works for data on isolated PSII core complexes is rather limited, it does show that the acceptor side processes on this timescale and the gating mechanism are not yet fully understood in terms of the underlying kinetics.

4.6.2 Implications for current work in the field

PSII core complexes have come to replace more intact preparations as the *de facto* standard for experiments on the mechanism of PSII due to their favourable properties for structural and spectroscopic studies. The accurate characterisation of the reactions occurring in this kind of sample is of immediate importance for current work on the mechanism of PSII.

The implications for flash-timings of free electron laser experiments have already been mentioned in Section 4.4. The data presented show that not more than 40% of the desired S_3-state could have been generated in the work by Kupitz et al. (2014a). This, however, is more than was expected based on previous knowledge.

The existence of a large fraction of oxidized non-heme iron in the dark has further implications on the interpretation of similar experiments. Suga et al. (2017) also used serial femtosecond time-resolved x-ray crystallography and saturating single-turnover flashes to study the S_3-state in PSII micro-crystals. Here, a more favourable flash spacing of 10 ms was chosen. Among the largest differences observed between

the dark sample and the twice-flashed-state were differences at the non-heme iron. Figure 4.11 shows the isomorphous difference Fourier map between the twice-flashed state and the dark state. The reduction of electron density at the non-heme iron is ascribed to an increase in the distance between the bicarbonate and the non-heme iron. Although a reduction of the non-heme iron is not ruled out, the authors propose that this change is result from rearrangement of the H-bond network around bicarbonate and/or reorientation of BCT upon two-flash illumination, which might be caused by the involvement of bicarbonate in the proton transfer for Q_B protonation (Suga et al., 2017).

In light of the data from this work, this interpretation seems less likely. Instead, the movement of the bicarbonate is probably caused by a reduction of the fraction of centres that have an oxidized non-heme iron present in the dark.

XFEL measurements are still measurements of ensembles, and therefore averages over all the present states. It is obvious from the work presented here, that more effort needs be put into understanding the dark-stable state of the used sample. Methods to generate more homogeneous samples need to be developed if this method is to generate mechanistically useful data.

4.6.3 Future work on the kinetics of quinone electron transfer

The work presented in this chapter extends the previous kinetic studies of PSII core complexes from *T. elongatus* and provides new insights into the acceptor side of Photosystem II.

It is recognised that parts of this work considering micro-crystals and the methods involving the dual laser setup would benefit from simple repetition of the experiments, as simple improvements of the methods could yield significantly improved datasets that would allow for stronger conclusions.

Due to the sudden, tragic passing of Fabrice Rappaport, the dual laser machine that was used extensively in this work became unavailable. One attempt to reactivate the setup since then has been unsuccessful; however, this should be successful in time. Additionally, the availability of PSII micro-crystals was very limited due to the

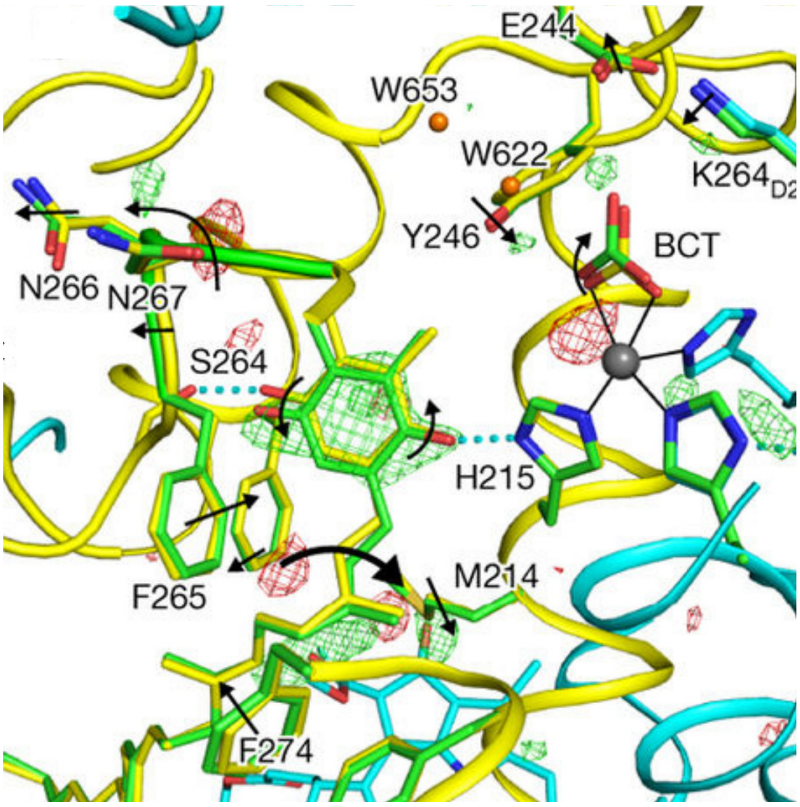

Figure 4.11: Isomorphous difference Fourier map between the 2F-state and the dark-state of the pre-flashed samples in green (positive) and red (negative) contoured at ± 5.0 σ. D_1 and D_2 subunits are coloured in yellow and cyan, respectively, in the S_1 state and green in the S_3 state. Shown are the structural changes around the Q_B/non-heme iron-binding site. Black arrows indicate the movements of atoms from the S_1 to the S_3 state. Reprinted by permission from Macmillan Publishers Ltd: Suga et al. (2017).

difficulties associated with the making, maintenance and transport of these samples.

Due to doubts about the quinone content in the preparations that include only PSII dimers (or monomers), this material was not used extensively in this chapter (a more detailed description of this problem can be found in the work of Douglass (2015)). Preparations from the Fromme lab, using an optimized anion-exchange-column do not seem to suffer from this problem. Therefore, the optimization of the protocol for retention of the quinone during the preparation of PSII dimers would be useful. Some evidence that PSII dimers have a lower amount of oxidized non-heme iron, and have the potential to show a longer continuity of the rate pattern, has been found during the course of this work (See Appendix Figure 6.6).

A more homogeneous sample that could sustain the rate oscillations for longer would be very helpful for the interpretation of the observed effects. Furthermore, the mechanistic implications of the dimerisation could be studied more effectively.

Tentative evidence for the oxidation of the non-heme iron by $Q_B^{\bullet -}$, possibly in centres that lack the bicarbonate ligand, was found using the rate pattern analysis, and backed up by initial EPR-measurements. The fact that the "fast first flash effect" has also been observed in more intact PSII membrane preparations points to a possible physiological relevance of this processes.

Therefore, a more in-depth study of the oxidation of the non-heme iron and the role of the bicarbonate binding site in regulation of PSII appears highly warranted. Kinetic approaches, such as the ones developed in this work could offer more valuable insights into the process.

Due to the fact that the maths underlying the rate pattern analysis was only developed during the write-up stage of this thesis, interpretations and possible experiments that are obvious now, were not realized in time. Therefore more work in this domain could prove useful.

Nevertheless, other methods should be considered as well. A better understanding of the EPR signals arising from the oxidized non-heme iron in different samples would be beneficial. Furthermore, pulsed EPR studies on the acceptor side could potentially be of great value for deducing the protonation pathways for the protonation of Q_B.

For such studies to be possible, it would be necessary to produce a sample in which the semiquinone radical is not perturbed by the non-heme iron. Whilst this could be achieved in a few different ways, so far all attempts remained unsuccessful (data not shown). A better understanding of the system might allow for new ways of producing such a sample.

It is obvious that ways to generate pure PSII states, both on the donor and on the acceptor side, in the dark and after a series of flashes would be beneficial for the use of time resolved femto-second XFEL measurements. Here, the rate pattern analysis might prove to be a fast and easy tool to analyse possible treatment regimes.

Pending on the ability to repeat or validate the experiments using the dual-laser setup and PSII micro crystals, the results presented in this chapter are being prepared for publication.

5 Conclusions and Outlook

Despite the notion that research on Photosystem II is complete (P. Siegbahn, Bioenergetics Christmas meeting, 2016, London), considerable inconsistencies and unknowns in our understanding of PSII persist. Apart from the quest for the holy grail of PSII, the mechanism of water oxidation, currently the understanding of the energetics of PSII, photoactivation, the electron transfer kinetics, the so-called gating mechanism, the associated protonation pathways and the role of the non-heme iron with its bicarbonate ligand is also still incomplete. In this work, some open questions were answered, whilst new ones were raised.

The measurement of the terminal electron acceptor of PSII, Q_B, allows for a better understanding of the stabilisation of charge separation within PSII. The redox potentials of the two Q_B couples show that PSII pays a significantly larger energetic price than previously assumed, to stabilize the electron on $Q_B^{\bullet-}$.

The fact that the midpoint potential of the quinone in the site does not coincide with that of the plastoquinone pool suggests that, in contrast to bacterial reaction centres, energy is expended to ensure preferential binding of the quinone and the ejection of the quinol from PSII. The molecular details and energetics allowing for a rapid exchange of the quinone with the pool warrant for further study (pathways of quinone exchange, intra-PSII quinone pool etc.). This has not been considered as an energetic cost in previous works on the energetics of photosynthesis.

Spectroscopic methods were used to determine the electron transfer kinetics on the acceptor side of PSII from *T. elongatus*. This is, to my knowledge, the first complete assignment and measurement of all electron transfer processes happening in the sub-millisecond to millisecond time scale in PSII. Uncertainties remain on the nature of

slower processes happening on the tens and hundreds of milliseconds timescale. These may be associated with quinone exchange processes; other explanations, such as slow electron transfers between the quinones, resulting from some form of conformational or other form of inhibition, should be considered as possible explanations as well.

Photosystem II research in recent years has seen a focus on the donor side reactions and the mechanism of water oxidation by the manganese cluster. Due to the availability of crystallographic data, and other favourable traits, a large fraction of this work has relied on isolated PSII core complexes from *T. elongatus*. In terms of the acceptor side, those experiments relied upon the knowledge from PSII membrane preparations from other organisms and in some aspects from bacterial reactions centres.

It is shown here, that this reliance on knowledge from other, albeit related systems, can lead to rather problematic flaws in experimental design and interpretation of the results. In a broader view it should be realized that the separation of PSII in more or less unrelated donor and acceptor side reactions, that can be studied at separate pace and intensity is inherently problematic.

Both principal topics of this thesis have highlighted the need for a better understanding of the regulatory role of the non-heme iron and its bicarbonate ligand. Initial evidence that, debinding and/or replacement of the bicarbonate ligand, as well as the oxidation of the non-heme iron might be important factors for the *in vivo* regulation of PSII and the protection from damaging side reactions was found and have already been extended upon.

The knowledge and methodologies generated in this thesis should rapidly lead to better biochemistry when using isolated PSII core complexes from *T. elongatus*. This should be highly beneficial for potentially high-impact methods such as XFEL measurements of particular states of PSII, opening-up the possibility of structural analysis of the mechanisms on the donor and acceptor side of PSII.

Measurements such as the ones presented in this thesis will also be important when studying photoactivation. The process of assembling PSII and "switching it on" is still largely not understood. It is, however, very likely, that some aspects of

the current mysteries within PSII will be addressed by research on this topic.

In conclusion, there still is a steady stream of new, interesting and meaningful questions pertaining PSII. The fact, that these are answered with better methods at ever increasing detail allows for an optimistic outlook on the future work in this field.

Bibliography

Allen, J. F. and Pfannschmidt, T. (2000). Balancing the two photosystems: photosynthetic electron transfer governs transcription of reaction centre genes in chloroplasts. *Philos. Trans. R. Soc. London B Biol. Sci.*, 355(1402):1351–1359.

Arnold, W. and Sherwood, H. (1959). Energy Storage in Chloroplasts. *J. Phys. Chem.*, 63:2.

Aro, E. M., Virgin, I., and Andersson, B. (1993). Photoinhibition of Photosystem II. Inactivation, protein damage and turnover. *Biochim. Biophys. Acta*, 1143(2):113–34.

Bald, D., Kruip, J., and Rögner, M. (1996). Supramolecular architecture of cyanobacterial thylakoid membranes: How is the phycobilisome connected with the photosystems? *Photosynth. Res.*, 49(2):103–118.

Beal, D., Rappaport, F., and Joliot, P. (1999). A new high-sensitivity 10 ns time-resolution spectrophotometric technique adapted to in vivo analysis of the photosynthetic apparatus. *Rev. Sci. Instrum.*, 70(1):202.

Bergantino, E., Brunetta, A., Touloupakis, E., Segalla, A., Szabò, I., and Giacometti, G. M. (2003). Role of the PSII-H Subunit in Photoprotection: Novel aspects of D_1 turnover in *Synechocystis* 6803. *J. Biol. Chem.*, 278(43):41820–41829.

Bertini, I., Bryant, D. A., Ciurli, S., Dikiy, A., Fernández, C. O., Luchinat, C., Safarov, N., Vila, A. J., and Zhao, J. (2001). Backbone dynamics of plastocyanin in both oxidation states: Solution structure of the reduced form and comparison with the oxidized state. *J. Biol. Chem.*, 276(50):47217–47226.

Bishop, N. I. (1959). The Reactivity of a Naturally Occurring Quinone (Q-255) in Photochemical Reactions of Isolated Chloroplasts. *Proc Natl Acad Sci U S A*, 45(12):1696–1702.

Boisvert, S., Joly, D., Leclerc, S., Govindachary, S., Harnois, J., and Carpentier, R. (2007). Inhibition of the oxygen-evolving complex of photosystem II and depletion of extrinsic polypeptides by nickel. *BioMetals*, 20(6):879–889.

Bouges-bocquet, B. (1973). Electron transfer between the two photosystems in spinach chloroplasts. *Biochim. Biophys. Acta - Bioenerg.*, 314(2):250–256.

Bouges-bocquet, B. (1975). No Title. In Avron, M., editor, *Proc. 3rd Int. Congr. Photosynth.*, pages 579–588,. Elsevier.

Boussac, A., Rappaport, F., Brettel, K., and Sugiura, M. (2013). Charge recombination in $SnTyr_Z^{\bullet}Q_A^{\bullet-}$ radical pairs in D_1 protein variants of Photosystem II: long range electron transfer in the Marcus inverted region. *J Phys Chem B*, 117(12):3308–3314.

Boussac, A., Sugiura, M., and Rappaport, F. (2011). Probing the quinone binding site of Photosystem II from Thermosynechococcus elongatus containing either Psb_{A1} or Psb_{A3} as the D1 protein through the binding characteristics of herbicides. *Biochim. Biophys. Acta - Bioenerg.*, 1807(1):119–129.

Bowes, J. M. and Crofts, A. R. (1980). Binary oscillations in the rate of reoxidation of the primary acceptor of Photosystem II. *Biochim. Biophys. Acta*, 590(3):373–384.

Bowes, J. M., Crofts, A. R., and Itoh, S. (1979). A high potential acceptor for Photosystem II. *BBA - Bioenerg.*, 547(2):320–335.

Brinkert, K., De Causmaecker, S., Krieger-Liszkay, A., Fantuzzi, A., and Rutherford, A. W. (2016). Bicarbonate-induced redox tuning in Photosystem II for regulation and protection. *Proc. Natl. Acad. Sci. U. S. A.*, 113(43):12144–12149.

Brudvig, G. W., Casey, J. L., and Sauer, K. (1983). The effect of temperature on the formation and decay of the multiline EPR signal species associated with photosynthetic oxygen evolution. *Biochim. Biophys. Acta - Bioenerg.*, 723(3):366–371.

Buchta, J., Grabolle, M., and Dau, H. (2007). Photosynthetic dioxygen formation studied by time-resolved delayed fluorescence measurements - Method, rationale, and results on the activation energy of dioxygen formation. *Biochim. Biophys. Acta*, 1767(6):565–574.

Cardona, T., Sedoud, A., Cox, N., and Rutherford, A. W. (2012). Charge separation in photosystem II: a comparative and evolutionary overview. *Biochim. Biophys. Acta*, 1817(1):26–43.

Chen, M., Schliep, M., Willows, R., Cai, Z.-L., Neilan, B., and Scheer, H. (2010). A red-shifted chlorophyll. *Science (80-.).*, 329:5597.

Chen, M., Telfer, A., Lin, S., Pascal, A., Larkum, A. W. D., Barber, J., and Blankenship, R. E. (2005). The nature of the photosystem II reaction centre in the chlorophyll d-containing prokaryote, Acaryochloris marina. *Photochem. Photobiol. Sci.*, 4(12):1060.

Chernev, P., Zaharieva, I., Dau, H., and Haumann, M. (2011). Carboxylate shifts steer interquinone electron transfer in photosynthesis. *J. Biol. Chem.*, 286:5368–5374.

Coleman, T. F. and Li, Y. (1996). An Interior Trust Region Approach for Nonlinear Minimization Subject to Bounds. *SIAM J. Optim.*, 6(2):418–445.

Corrie, A. R., Nugent, J. H. A., and Evans, M. C. W. (1991). Identification of EPR signals from the states $Q_A^{\bullet-}Q_B^{\bullet-}$ and $Q_B^{\bullet-}$ in photosystem II from *Phormidium laminosum*. *Biochim Biophys Acta*, 1057(3):384–390.

Cox, N., Rapatskiy, L., Su, J.-H., Pantazis, D. A., Sugiura, M., Kulik, L. V., Dorlet, P., Rutherford, A. W., Neese, F., Boussac, A., Lubitz, W., and Messinger, J. (2011).

Effect of Ca^{2+}/Sr^{2+} substitution on the electronic structure of the oxygen-evolving complex of photosystem II: A combined multifrequency EPR, ^{55}Mn-ENDOR, and DFT study of the S_2 state. *J. Am. Chem. Soc.*, 133(10):3635–3648.

Cox, N., Retegan, M., Neese, F., Pantazis, D. A., Boussac, A., and Lubitz, W. (2014). Electronic structure of the oxygen-evolving complex in photosystem II prior to O-O bond formation. *Science (80-.).*, 345(6198):804–808.

Crofts, A. R., Robinson, H., Andrews, K., VanDoren, S., and Berry, E. (1987). *Catalytic Sites for Reduction and Oxidation of Quinones*. Springer US, Boston, MA.

Crofts, A. R. and Wraight, C. A. (1983). The electrochemical domain of photosynthesis.

Cser, K. and Vass, I. (2007). Radiative and non-radiative charge recombination pathways in Photosystem II studied by thermoluminescence and chlorophyll fluorescence in the cyanobacterium *Synechocystis* 6803. *Biochim. Biophys. Acta*, 1767(3):233–243.

Cuni, A., Xiong, L., Sayre, R. T., Rappaport, F., and Lavergne, J. (2004). Modification of the pheophytin midpoint potential in photosystem II: Modulation of the quantum yield of charge separation and of charge recombination pathways. *Phys. Chem. Chem. Phys.*, 6(20):4825.

Dau, H., Zaharieva, I., and Haumann, M. (2012). Recent developments in research on water oxidation by photosystem II.

De Grooth, B. and van Gorkom, H. J. (1981). External electric field effects on prompt and delayed fluorescence in chloroplasts. *Biochim. Biophys. Acta - Bioenerg.*, 635(3):445–456.

de Wijn, R. and van Gorkom, H. J. (2001). Kinetics of Electron Transfer from Q_A to Q_B in Photosystem II. *Biochemistry*, 40(39):11912–11922.

de Wijn, R. and van Gorkom, H. J. (2002). S-state dependence of the miss probability in Photosystem II. *Photosynth. Res.*, 72(2):217–22.

Deák, Z., Sass, L., Kiss, E., and Vass, I. (2014). Characterization of wave phenomena in the relaxation of flash-induced chlorophyll fluorescence yield in cyanobacteria. *Biochim. Biophys. Acta*, 1837(9):1522–32.

Deák, Z. and Vass, I. (2008). Oscillating yield of flash-induced chlorophyll fluorescence decay in intact cells of *Thermosynechococcus elongatus*. In *Photosynth. Energy from Sun*, pages 573–576. Springer Netherlands, Dordrecht.

Deisenhofer, J., Epp, O., Miki, K., Huber, R., and Michel, H. (1985). Structure of the protein subunits in the photosynthetic reaction centre of *Rhodopseudomonas viridis* at 3Åresolution. *Nature*, 318:618–624.

Deisenhofer, J. and Michel, H. (1989). The Photosynthetic Reaction Center from the Purple Bacterium *Rhodopseudomonas viridis*. *Science (80-.).*, 245(4925):1463 –1473.

Dekker, J. P. and Boekema, E. J. (2005). Supramolecular organization of thylakoid membrane proteins in green plants. *Biochim. Biophys. Acta*, 1706(1706):12–39.

Dekker, J. P., van Gorkom, H. J., Wensink, J., and Ouwehand, L. (1984). Absorbance Difference Spectra of the successive Redox States of the Oxygen-Evolving Apparatus of Photosynthesis *. *Biochim. Biophys. Acta*, 767:1–9.

Dekker, J. P. and Van Grondelle, R. (2000). Primary charge separation in Photosystem II. *Photosynth. Res.*, 63:195–208.

Deligiannakis, Y., Hanley, J., and Rutherford, A. W. (1999). 1D- and 2D-ESEEM study of the semiquinone radical Q_A^- of Photosystem II. *J. Am. Chem. Soc.*, 121(33):7653–7664.

Deligiannakis, Y., Jegerschöld, C., and Rutherford, A. W. (1997). EPR and ESEEM study of the plastoquinone anion radical $Q_A^{\bullet -}$ in Photosystem II treated at thigh pH. *Chem. Phys. Lett.*, 270(5-6):564–572.

Delrieu, M. (1974). Simple Explanation of the Misses in the Cooperation of Charges in Photosynthetic O_2 Evolution. *Photochem. Photobiol.*, 20(5):441–454.

Diner, B. A. (1977). Dependence of the deactivation reactions of Photosystem II on the redox state of plastoquinone pool a varied under anaerobic conditions. Equilibria on the acceptor side of Photosystem II. *BBA - Bioenerg.*, 460(2):247–258.

Diner, B. A. and Rappaport, F. (2002). Structure, dynamics, and energetics of the primary photochemistry of photosystem II of oxygenic photosynthesis. *Annu. Rev. Plant Biol.*, 53(1):551–580.

Douglass, J. S. (2015). *Structural and functional studies on Photosystem II from Thermosynechococcus elongatus*. PhD thesis, Imperial College London.

Ducluzeau, A. L., Schoepp-Cothenet, B., Baymann, F., Russell, M. J., and Nitschke, W. (2014). Free energy conversion in the LUCA: Quo vadis? *Biochim. Biophys. Acta-Bioenergetics*, 1837(7):982–988.

Ducruet, J.-M. and Vass, I. (2009). Thermoluminescence: experimental. *Photosynth. Res.*, 101(2-3):195–204.

Dutton, P. L. (1971). Oxidation-reduction potential dependence of the interaction of cytochromes, bacteriochlorophyll and carotenoids at 77 K in chromatophores of *Chromatium D* and *Rhodopseudomonas gelatinosa*. *Biochim. Biophys. Acta (BBA)-Bioenergetics*, 226(1):63–80.

Eaton-Rye, J. J. and Govindjee (1988). Electron transfer through the quinone acceptor complex of Photosystem II in bicarbonate-depleted spinach thylakoid membranes as a function of actinic flash number and frequency. *BBA - Bioenerg.*, 935(3):237–247.

Erixon, K. and Butler, W. L. (1971). The relationship between Q, C 550 and cytochrome b559 in photoreactions at -196 degrees in chloroplasts. *Biochim. Biophys. Acta*, 234(3):381–389.

Eyring, H. (1935). The Activated Complex in Chemical Reactions. *J. Chem. Phys.*, 3(2):107–115.

Faller, P., Fufezan, C., and Rutherford, A. W. (2005). Side-path electron donors: cytochrome b559, chlorophyll z and beta-carotene. In *Photosyst. II Light. Water-Plastoquinone Oxidoreductase*, pages 347–365. Springer, Dordrecht.

Ferreira, K. N., Iverson, T. M., Maghlaoui, K., Barber, J., and Iwata, S. (2004). Architecture of the photosynthetic oxygen-evolving center. *Science*, 303(5665):1831–1838.

Fufezan, C., Rutherford, A. W., and Krieger-Liszkay, A. (2002). Singlet oxygen production in herbicide-treated photosystem II. *FEBS Lett.*, 532(3):407–410.

Fufezan, C., Zhang, C., Krieger-Liszkay, A., and Rutherford, A. W. (2005). Secondary quinone in photosystem II of *Thermosynechococcus elongatus*: semiquinone-iron EPR signals and temperature dependence of electron transfer. *Biochemistry*, 44(38):12780–12789.

Garbers, A., Reifarth, F., Kurreck, J., Renger, G., and Parak, F. (1998). Correlation between protein flexibility and electron transfer from $Q_A^{\bullet -}$ to Q_B in PSII membrane fragments from spinach. *Biochemistry*, 559(33):11399–11404.

Golbeck, J. H. and Kok, B. (1979). Redox titration of electron acceptor Q and the plastoquinone pool in Photosystem II. *BBA - Bioenerg.*, 547(2):347–360.

Grabolle, M. and Dau, H. (2005). Energetics of primary and secondary electron transfer in Photosystem II membrane particles of spinach revisited on basis of recombination-fluorescence measurements. *Biochim. Biophys. Acta*, 1708(2):209–18.

Graige, M. S., Feher, G., and Okamura, M. Y. (1998). Conformational gating of the electron transfer reaction $Q_A^{\bullet -}Q_B \rightarrow Q_A Q_B^{\bullet -}$ in bacterial reaction centers of *Rhodobacter sphaeroides* determined by a driving force assay. *Proc. Natl. Acad. Sci. U. S. A.*, 95(20):11679–84.

Guskov, A., Kern, J., Gabdulkhakov, A., Broser, M., Zouni, A., and Saenger, W. (2009). Cyanobacterial photosystem II at 2.9 Å∼resolution and the role of quinones, lipids, channels and chloride. *Nat. Struct. Mol. Biol.*, 16:334–342.

Hallahan, B. J., Ruffle, S. V., Bowden, S. J., and Nugent, J. H. A. (1991). Identification and characterisation of EPR signals involving Q_B semiquinone in plant Photosystem II. *BBA - Bioenerg.*, 1059(2):181–188.

Hasan, S. S. and Cramer, W. A. (2012). On rate limitations of electron transfer in the photosynthetic cytochrome b_6f complex. *Phys. Chem. Chem. Phys.*, 14(40):13853–60.

Hasan, S. S., Yamashita, E., Baniulis, D., and Cramer, W. A. (2013). Quinone-dependent proton transfer pathways in the photosynthetic cytochrome b_6f complex. *Proc. Natl. Acad. Sci.*, 110(11):4297–4302.

Hasegawa, K. and Noguchi, T. (2012). Molecular interactions of the quinone electron acceptors Q_A, Q_B, and Q_C in photosystem II as studied by the fragment molecular orbital method. *Photosynth. Res.*, 120(1-2):113–123.

Heathcote, P. and Rutherford, A. W. (1986). An E.P.R. Signal Arising form Q_B^-Fe in *Chromatium vinosum*. In *Prog. Photosynth. Res. Vol.1*, pages 201–204. Dordrecht.

Ido, K., Gross, C. M., Guerrero, F., Sedoud, A., Lai, T.-L. L., Ifuku, K., Rutherford, A. W., and Krieger-Liszkay, A. (2011). High and low potential forms of the Q_A quinone electron acceptor in Photosystem II of *Thermosynechococcus elongatus* and spinach. *J. Photochem. Photobiol. B.*, 104(1-2):154–7.

Ikegami, I., Katoh, S., and Kato, S. (1973). Studies on chlorophyll fluorescence in chloroplasts II. Effect of ferricyanide on the induction of fluorescence in the

presence of 3-(3,4-dichlorophenyl)-1,1-dimethylurea. *Plant Cell Physiol.*, 14(5):829–836.

Ishikita, H. and Knapp, E.-W. (2005). Oxidation of the non-heme iron complex in photosystem II. *Biochemistry*, 44(45):14772–83.

Johnson, G. N., Rutherford, A. W., and Krieger, A. (1995). A change in the midpoint potential of the quinone Q_A in Photosystem II associated with photoactivation of oxygen evolution. *Biochim. Biophys. Acta - Bioenerg.*, 1229:202–207.

Joliot, P., Barbieri, G., and Chabaud, R. (1969). Un Nouveau Modele des Centre Photochimiques du Systeme II*. *Photochem. Photobiol.*, 10(5):309–329.

Joliot, P., Lavergne, J., and Béal, D. (1990). Organization of the Plastoquinone Pool in Chloroplasts: Evidence for Clusters of Different Sizes. In *Curr. Res. Photosynth.*, pages 1839–1842. Springer Netherlands, Dordrecht.

Joliot, P., Lavergne, J., and Béal, D. (1992). Plastoquinone compartmentation in chloroplasts. I. Evidence for domains with different rates of photo-reduction. *Biochim. Biophys. Acta (BBA)/Protein Struct. Mol.*, 1101(1):1–12.

Jordan, P., Fromme, P., Witt, H. T., Klukas, O., Saenger, W., and Krau??, N. (2001). Three-dimensional structure of cyanobaoterial photosystem I at 2.5 Å∼resolution. *Nature*, 411(6840):909–917.

Kargul, J., Maghlaoui, K., Murray, J. W., Deak, Z., Boussac, A., Rutherford, A. W., Vass, I., and Barber, J. (2007). Purification, crystallization and X-ray diffraction analyses of the *T. elongatus* PSII core dimer with strontium replacing calcium in the oxygen-evolving complex. *Biochim. Biophys. Acta - Bioenerg.*, 1767(6):404–413.

Kato, Y., Nagao, R., and Noguchi, T. (2016). Redox potential of the terminal quinone electron acceptor Q_B in photosystem II reveals the mechanism of electron transfer regulation. *Proc. Natl. Acad. Sci.*, 113(3):620–625.

Keren, N. and Krieger-Liszkay, A. (2011). Photoinhibition: molecular mechanisms and physiological significance. *Physiol Plant*, 142(1):1–5.

Kirilovsky, D. (2007). Photoprotection in cyanobacteria: the orange carotenoid protein (OCP)-related non-photochemical-quenching mechanism. *Photosynth. Res.*, 93(1):7–16.

Kleinfeld, D., Okamura, M. Y., and Feher, G. (1984). Electron-Transfer Kinetics in Photosynthetic Reaction Centers Cooled to Cryogenic Temperatures in the Charge-Separated State: Evidence for Light-Induced Structural Changes. *Biochemistry*, 23(24):5780–5786.

Klimov, V. V., Allakhverdiev, S. I., Demeter, S., and Krasnovskii, A. A. (1979). Photoreduction of pheophytin in the photosystem 2 of chloroplasts depending on the oxidation-reduction potential of the medium. *Dokl. Akad. Nauk SSSR*, 1(249):227–230.

Klimov, V. V., Dolan, E., and Ke, B. (1980a). EPR properties of an intermediary electron acceptor (pheophytin) in photosystem-II reaction centers at cryogenic temperatures. *FEBS Lett.*, 112(1):97–100.

Klimov, V. V., Dolan, E., Shaw, E. R., and Ke, B. (1980b). Interaction between the intermediary electron acceptor (pheophytin) and a possible plastoquinone-iron complex in photosystem II reaction centers. *Proc. Natl. Acad. Sci. U. S. A.*, 77(12):7227–7231.

Knaff, D. B. and Arnon, D. I. (1969). Spectral evidence for a new photoreactive component of the oxygen-evolving system in photosynthesis. *Proc. Natl. Acad. Sci. U. S. A.*, 63(3):963–969.

Kok, B., Forbush, B., and McGloin, M. (1970). Cooperation of charges in photosynthetic O_2 evolution–I. A linear four step mechanism. *Photochem. Photobiol.*, 11(6):457–475.

Kós, P. B., Deák, Z., Cheregi, O., and Vass, I. (2008). Differential regulation of *psbA* and *psbD* gene expression, and the role of the different D1 protein copies in the cyanobacterium *Thermosynechococcus elongatus* BP-1. *Biochim. Biophys. Acta - Bioenerg.*, 1777(1):74–83.

Koulougliotis, D., Kostopoulos, T., Petrouleas, V., and Diner, B. A. (1993). Evidence for CN^- binding at the PS II non-heme Fe^{2+}. Effects on the EPR signal for $Q_A^-Fe^{2+}$ and on Q_AQ_B electron transfer. *Biochim. Biophys. Acta - Bioenerg.*, 1141:275–282.

Krieger, A., Rutherford, A. W., and Johnson, G. N. (1995). On the determination of redox midpoint potential of the primary quinone electron acceptor, Q_A, in Photosystem II. *BBA - Bioenerg.*, 1229(2):193–201.

Krieger, A., Weis, E., and Demeter, S. (1993). Low-pH-induced Ca^{2+} ion release in the water-splitting system is accompanied by a shift in the midpoint redox potential of the primary quinone acceptor Q_A. *BBA - Bioenerg.*, 1144(3):411–418.

Krieger-Liszkay, A. and Rutherford, A. W. (1998). Influence of herbicide binding on the redox potential of the quinone acceptor in photosystem II: relevance to photodamage and phytotoxicity. *Biochemistry*, 37(50):17339–44.

Krivanek, R., Kern, J., Zouni, A., Dau, H., and Haumann, M. (2007). Spare quinones in the Q_B cavity of crystallized photosystem II from *Thermosynechococcus elongatus*. *Biochim. Biophys. Acta - Bioenerg.*, 1767:520–527.

Kühlbrandt, W. and Davies, K. M. (2016). Rotary ATPases: A New Twist to an Ancient Machine.

Kupitz, C., Basu, S., Grotjohann, I., Fromme, R., Zatsepin, N. A., Rendek, K. N., Hunter, M. S., Shoeman, R. L., White, T. A., Wang, D., James, D., Yang, J.-H., Cobb, D. E., Reeder, B., Sierra, R. G., Liu, H., Barty, A., Aquila, A. L., Deponte, D., Kirian, R. A., Bari, S., Bergkamp, J. J., Beyerlein, K. R., Bogan, M. J., Caleman, C., Chao, T.-C., Conrad, C. E., Davis, K. M., Fleckenstein, H., Galli, L., Hau-Riege, S. P., Kassemeyer, S., Laksmono, H., Liang, M., Lomb, L., Marchesini,

S., Martin, A. V., Messerschmidt, M., Milathianaki, D., Nass, K., Ros, A., Roy-Chowdhury, S., Schmidt, K., Seibert, M., Steinbrener, J., Stellato, F., Yan, L., Yoon, C., Moore, T. A., Moore, A. L., Pushkar, Y., Williams, G. J., Boutet, S., Doak, R. B., Weierstall, U., Frank, M., Chapman, H. N., Spence, J. C. H., and Fromme, P. (2014a). Serial time-resolved crystallography of photosystem II using a femtosecond X-ray laser. *Nature*, 513(7517):261–265.

Kupitz, C., Grotjohann, I., Conrad, C. E., Roy-Chowdhury, S., Fromme, R., and Fromme, P. (2014b). Microcrystallization techniques for serial femtosecond crystallography using photosystem II from *Thermosynechococcus elongatus* as a model system. *Philos. Trans. R. Soc. Lond. B. Biol. Sci.*, 369(1647):20130316.

Lavergne, J. (1982). Mode of action of 3-(3,4-dichlorophenyl)-1,1-dimethylurea. Evidence that the inhibitor competes with plastoquinone for binding to a common site on the acceptor side of Photosystem II. *BBA - Bioenerg.*, 682(3):345–353.

Lavergne, J. (1987). Optical-difference spectra of the S-state transitions in the photosynthetic oxygen-evolving complex. *BBA - Bioenerg.*, 894(1):91–107.

Lavergne, J. (1991). Improved UV-visible spectra of the S-transitions in the photosynthetic oxygen-evolving system. *Biochim. Biophys. Acta - Bioenerg.*, 1060(2):175–188.

Lavorel, J. (1976). Matrix analysis of the oxygen evolving system of photosynthesis. *J. Theor. Biol.*, 57(1):171–185.

Liu, L.-n. (2016). Distribution and dynamics of electron transport complexes in cyanobacterial thylakoid membranes. *BBA - Bioenerg.*, 1857(3):256–265.

Mamedov, F., Nowaczyk, M., Thapper, A., Rögner, M., and Styring, S. (2007). Functional characterization of monomeric photosystem II core preparations from *Thermosynechococcus elongatus* with or without the Psb27 protein. *Biochemistry*, 46(18):5542–51.

Meier, T., Faraldo-Gómez, J. D., and Börsch, M. (2011). ATP-Synthase - A Paradigmatic Molecular Machine. In Frank, J., editor, *Mol. Mach. Biol.*, pages 208–238. Cambridge University Press, New York.

Michaelis, L. (1932). Theroy of the reversible two-step oxidation. *J. Biol. Chem.*, 96(3):703–715.

Minagawa, J., Narusaka, Y., Inoue, Y., and Satoh, K. (1999). Electron Transfer between Q_A and Q_B in Photosystem II Is Thermodynamically Perturbed in Phototolerant Mutants of *Synechocystis* sp . PCC 6803. *Biochemistry*, 38(2):770–775.

Mitchell, P. (2011). Chemiosmotic coupling in oxidative and photosynthetic phosphorylation. *Biochim. Biophys. Acta - Bioenerg.*, 1807(12):1507–1538.

Moser, C. C., Page, C. C., and Leslie Dutton, P. (2005). Tunneling in PSII. *Photochem. Photobiol. Sci.*, 4:933–939.

Müh, F., Glöckner, C., Hellmich, J., and Zouni, A. (2012). Light-induced quinone reduction in photosystem II. *Biochim. Biophys. Acta (BBA)-Bioenergetics*, 1817(1):44–65.

Müh, F. and Zouni, A. (2013). The nonheme iron in photosystem II. *Photosynth. Res.*, pages 295–314.

Mühlenhoff, U. and Chauvat, F. (1996). Gene transfer and manipulation in the thermophilic cyanobacterium *Synechococcus elongatus*. *Mol. Gen. Genet. MGG*, 252(1-2):93–100.

Nitschke, W. (2016). 2-electron redox chemistry.

Nitschke, W., Feiler, U., and Rutherford, A. W. (1990). Photosynthetic reaction center of green sulfur bacteria studied by EPR. *Biochemistry*, 29:3834–3842.

Nixon, P. J., Michoux, F., Yu, J., Boehm, M., and Komenda, J. (2010). Recent advances in understanding the assembly and repair of photosystem II.

Nowaczyk, M., Hebeler, R., Schlodder, E., Meyer, H. E., Warscheid, B., and Rögner, M. (2006). Psb27, a cyanobacterial lipoprotein, is involved in the repair cycle of photosystem II. *Plant Cell*, 18:3121–3131.

Overmann, J. (1997). Mahoney Lake: A Case Study of the Ecological Significance of Phototrophic Sulfur Bacteria. *Adv. Microb. Ecol.*, 15:251–288.

Petrouleas, V. and Crofts, A. R. (2005). The iron-quinone acceptor complex. In *Photosyst. II*, pages 177–206. Springer-Verlag, Berlin/Heidelberg.

Petrouleas, V. and Diner, B. A. (1987). Light-induced oxidation of the acceptor-side Fe(II) of Photosystem II by exogenous quinones acting through the Q_B binding site. I. Quinones, kinetics and pH-dependence. *Biochim. Biophys. Acta - Bioenerg.*, 893(2):126–137.

Petrouleas, V. and Diner, B. A. (1990). Formation by NO of nitrosyl adducts of redox components of the Photosystem II reaction center. I. NO binds to the acceptor-side non-heme iron. *Biochim. Biophys. Acta - Bioenerg.*, 1015:131–140.

Porra, R., Thompson, W., and Kriedemann, P. (1989). Determination of accurate extinction coefficients and simultaneous equations for assaying chlorophylls a and b extracted with four different solvents: verification of the concentration of chlorophyll standards by atomic absorption spectroscopy. *Biochim. Biophys. Acta - Bioenerg.*, 975(3):384–394.

Pospíšil, P. (2012). Molecular mechanisms of production and scavenging of reactive oxygen species by photosystem II.

Pospíšil, P. (2016). Production of Reactive Oxygen Species by Photosystem II as a Response to Light and Temperature Stress. *Front. Plant Sci.*, 7.

Rappaport, F., Cuni, A., Xiong, L., Sayre, R. T., and Lavergne, J. (2005). Charge recombination and thermoluminescence in photosystem II. *Biophys. J.*, 88(3):1948–58.

Rappaport, F. and Diner, B. A. (2008). Primary photochemistry and energetics leading to the oxidation of the Mn_4Ca cluster and to the evolution of molecular oxygen in Photosystem II. *Coord. Chem. Rev.*, 252(3-4):259–272.

Rappaport, F., Guergova-kuras, M., Nixon, P. J., Diner, B. A., and Lavergne, J. (2002). Kinetics and pathways of charge recombination in photosystem II. *Biochemistry*, 41(26):8518–8527.

Rappaport, F. and Lavergne, J. (2009). Thermoluminescence: theory. *Photosynth. Res.*, 101(2-3):205–216.

Rehman, A. U., Cser, K., Sass, L., and Vass, I. (2013). Characterization of singlet oxygen production and its involvement in photodamage of Photosystem II in the cyanobacterium *Synechocystis* PCC 6803 by histidine-mediated chemical trapping. *Biochim. Biophys. Acta - Bioenerg.*, 1827(6):689–698.

Reifarth, F. and Renger, G. (1998). Indirect evidence for structural changes coupled with $Q_B^{\bullet-}$ formation in photosystem II. *FEBS Lett.*, 428(3):123–126.

Robertson, D. E., Prince, R. C., Bowyer, J. R., Matsuura, K., Dutton, P. L., and Ohnishi, T. (1984). Thermodynamic properties of the semiquinone and its binding site in the ubiquinol-cytochrome c (c2) oxidoreductase of respiratory and photosynthetic systems. *J. Biol. Chem.*, 259(3):1758–1763.

Robinson, H. H. and Crofts, A. R. (1983). Kinetics of the oxidation—reduction reactions of the photosystem II quinone acceptor complex, and the pathway for deactivation. *FEBS Lett.*, 153(1):221–226.

Romero, E., van Stokkum, I. H. M., Novoderezhkin, V. I., Dekker, J. P., and van Grondelle, R. (2010). Two different charge separation pathways in photosystem II. *Biochemistry*, 49(20):4300–7.

Rose, S., Minagawa, J., Seufferheld, M., Padden, S., Svensson, B., Kolling, D. R. J., Crofts, A. R., and Govindjee (2008). D1-arginine257 mutants (R257E, K, and

Q) of *Chlamydomonas reinhardtii* have a lowered Q_B redox potential: Analysis of thermoluminescence and fluorescence measurements. *Photosynth. Res.*, 98(1-3):449–468.

Ruban, A. V. (2016). Non-photochemical chlorophyll fluorescence quenching: mechanism and effectiveness in protection against photodamage. *Plant Physiol.*, 170:pp.01935.2015.

Rutherford, A. W. (1979). *Electron Paramagnetic Resonance Studies of Photosynthetic Electron Transport in Purple Bacteria*. PhD thesis, University College London.

Rutherford, A. W., Crofts, A. R., and Inoue, Y. (1982). Thermoluminescence as a probe of Photosystem II photochemistry. The origin of the flash-induced glow peaks. *Biochim. Biophys. Acta - Bioenerg.*, 682(3):457–465.

Rutherford, A. W. and Evans, M. C. W. (1980). Direct measurement of the redox potential of the primary and secondary quinone electron acceptors in *Rhodopseudomonas sphaeroides* (wild-type) by EPR Spectrometry. *FEBS Lett.*, 110(2):257–261.

Rutherford, A. W., Govindjee, and Inoue, Y. (1984a). Charge accumulation and photochemistry in leaves studied by thermoluminescence and delayed light emission. *Proc. Natl. Acad. Sci. U. S. A.*, 81(4):1107–1111.

Rutherford, A. W. and Mathis, P. (1983). A relationship between the midpoitn potential of the primary acceptor and low temperature photochemistry in Photosystem II. *FEBS Lett.*, 154(2):328–334.

Rutherford, A. W., Osyczka, A., and Rappaport, F. (2012). Back-reactions, short-circuits, leaks and other energy wasteful reactions in biological electron transfer: Redox tuning to survive life in O_2. *FEBS Lett.*, 586(5):603–616.

Rutherford, A. W., Renger, G., Koike, H., and Inoue, Y. (1984b). Thermoluminescence as a probe of photosystem II. The redox and protonation states of the

secondary acceptor quinone and the O2-evolving enzyme. *Biochim. Biophys. Acta - Bioenerg.*, 767(3):548–556.

Rutherford, A. W. and Zimmermann, J. L. (1984). A new EPR signal attributed to the primary plastosemiquinone acceptor in Photosystem II. *BBA - Bioenerg.*, 767(1):168–175.

Saito, K., Rutherford, A. W., and Ishikita, H. (2013a). Mechanism of proton-coupled quinone reduction in Photosystem II. *Proc. Natl. Acad. Sci.*, 110(3):954–959.

Saito, K., Rutherford, A. W., and Ishikita, H. (2013b). Mechanism of tyrosine D oxidation in Photosystem II. *Proc. Natl. Acad. Sci.*, 110(19):7690–7695.

Sanakis, Y., Petrouleas, V., and Diner, B. A. (1994). Cyanide Binding at the Non-Heme Fe^{2+} of the Iron-Quinone Complex of Photosystem II: At High Concentrations, Cyanide Converts the Fe^{2+} from High (S = 2) to Low (S = 0) Spin. *Biochemistry*, 33(33):9922–9928.

Sauter, N. K., Echols, N., Adams, P. D., Zwart, P. H., Kern, J., Brewster, A. S., Koroidov, S., Alonso-Mori, R., Zouni, A., Messinger, J., Bergmann, U., Yano, J., and Yachandra, V. K. (2016). No observable conformational changes in PSII. *Nature*, 533(7603):E1–E2.

Schatz, G. H., Brock, H., and Holzwarth, A. R. (1988). Kinetic and Energetic Model for the Primary Processes in Photosystem II. *Biophys. J.*, 54(3):397–405.

Schuurmans, R. M., Schuurmans, J. M., Bekker, M., Kromkamp, J. C., Matthijs, H. C. P., and Hellingwerf, K. J. (2014). The Redox Potential of the Plastoquinone Pool of the Cyanobacterium *Synechocystis* sp PCC 6803 Is under Strict Homeostatic Control. *Plant Physiol.*, 165(1):463–475.

Sedoud, A. (2012). *Transfert d ' electrons dans le photosysteme II.* PhD thesis, Universite Paris Sud.

Sedoud, A., Cox, N., Sugiura, M., Lubitz, W., Boussac, A., and Rutherford, A. W. (2011a). Semiquinone-iron complex of Photosystem II: EPR signals assigned to the low-field edge of the ground state doublet of $Q_A^{\bullet-}Fe^{2+}$ and $Q_B^{\bullet-}Fe^{2+}$. *Biochemistry*, 50(27):6012–6021.

Sedoud, A., Kastner, L., Cox, N., El-Alaoui, S., Kirilovsky, D., and Rutherford, A. W. (2011b). Effects of formate binding on the quinone-iron electron acceptor complex of photosystem II. *Biochim. Biophys. Acta - Bioenerg.*, 1807(2):216–226.

Shibamoto, T., Kato, Y., Sugiura, M., and Watanabe, T. (2009). Redox potential of the primary plastoquinone electron acceptor Q_A in photosystem II from *Thermosynechococcus elongatus* determined by spectroelectrochemistry. *Biochemistry*, 48(45):10682–10684.

Shinkarev, V. P. (2004). Photosystem II: oxygen evolution and chlorophyll a fluorescence induced by multiple flashes. In *Chlorophyll a Fluoresc. a Signat. Photosynth.*, pages 198–229. Springer Netherlands, Dordrecht.

Shinkarev, V. P. and Wraight, C. A. (1993). Oxygen evolution in photosynthesis: From unicycle to bicycle. *Biophysics (Oxf).*, 90:1834–1838.

Shlyk-Kerner, O., Samish, I., Kaftan, D., Holland, N., Sai, P. S. M., Kless, H., and Scherz, A. (2006). Protein flexibility acclimatizes photosynthetic energy conversion to the ambient temperature. *Nature*, 442(7104):827–830.

Sicora, C. I., Brown, C. M., Cheregi, O., Vass, I., and Campbell, D. A. (2008). The *psbA* gene family responds differentially to light and UVB stress in *Gloeobacter violaceus* PCC 7421, a deeply divergent cyanobacterium. *Biochim. Biophys. Acta - Bioenerg.*, 1777(2):130–139.

Siegbahn, P. E. M. (2008). A structure-consistent mechanism for dioxygen formation in photosystem II. *Chem. - A Eur. J.*, 14(27):8290–8302.

Sigfridsson, K. G., Bernát, G., Mamedov, F., and Styring, S. (2004). Molecular interference of Cd^{2+} with Photosystem II. *Biochim. Biophys. Acta - Bioenerg.*, 1659(1):19–31.

Sobti, M., Smits, C., Wong, A. S., Ishmukhametov, R., Stock, D., Sandin, S., and Stewart, A. G. (2016). Cryo-EM structures of the autoinhibited E. coli ATP synthase in three rotational states. *Elife*, 5(DECEMBER2016):e21598.

Sproviero, E. M., Gascon, J. A., McEvoy, J. P., Brudvig, G. W., and Batista, V. S. (2008). Quantum mechanics/molecular mechanics study of the catalytic cycle of water splitting in photosystem II. *J. Am. Chem. Soc.*, 130(11):3428–3442.

Stiehl, H. H. and Witt, H. T. (1968). Die kurzzeitigen ultravioletten Differenzspektren bei der Photosynthese. *Zeitschrift fur Naturforsch. - Sect. B J. Chem. Sci.*, 23(2):220–224.

Styring, S. and Rutherford, A. W. (1987). In the oxygen-evolving complex of Photosystem II the so state is oxidized to the S1 State by D+ (Signal II slow). *Biochemistry*, 26(9):2401–2405.

Styring, S. and Rutherford, A. W. (1988). Deactivation kinetics and temperature dependence of the S-state transitions in the oxygen-evolving system of Photosystem II measured by EPR spectroscopy. *Biochim. Biophys. Acta - Bioenerg.*, 933(2):378–387.

Suga, M., Akita, F., Hirata, K., Ueno, G., Murakami, H., Nakajima, Y., Shimizu, T., Yamashita, K., Yamamoto, M., Ago, H., and Shen, J.-R. (2014). Native structure of photosystem II at 1.95 Å resolution viewed by femtosecond X-ray pulses. *Nature*, 517(7532):99–103.

Suga, M., Akita, F., Sugahara, M., Kubo, M., Nakajima, Y., Nakane, T., Yamashita, K., Umena, Y., Nakabayashi, M., Yamane, T., Nakano, T., Suzuki, M., Masuda, T., Inoue, S., Kimura, T., Nomura, T., Yonekura, S., Yu, L.-J., Sakamoto, T., Motomura, T., Chen, J.-H., Kato, Y., Noguchi, T., Tono, K., Joti, Y., Kameshima,

T., Hatsui, T., Nango, E., Tanaka, R., Naitow, H., Matsuura, Y., Yamashita, A., Yamamoto, M., Nureki, O., Yabashi, M., Ishikawa, T., Iwata, S., and Shen, J.-R. (2017). Light-induced structural changes and the site of O=O bond formation in PSII caught by XFEL. *Nature*, 543(7643):131–135.

Sugiura, M. and Boussac, A. (2014). Variants of photosystem II D1 protein in *Thermosynechococcus elongatus*. *Res. Chem. Intermed.*, 40(9):3219–3229.

Sugiura, M. and Inoue, Y. (1999). Highly purified thermo-stable oxygen-evolving photosystem II core complex from the thermophilic cyanobacterium *Synechococcus elongatus* having His-tagged CP43. *Plant Cell Physiol.*, 40(12):1219–31.

Sugiura, M., Rappaport, F., Brettel, K., Noguchi, T., Rutherford, A. W., and Boussac, A. (2004). Site-Directed Mutagenesis of *Thermosynechococcus elongatus* Photosystem II: The O_2-Evolving Enzyme Lacking the Redox-Active Tyrosine D. *Biochemistry*, 43(42):13549–13563.

Tikhonov, A. N. (2013). The cytochrome b_6f complex at the crossroad of photosynthetic electron transport pathways. *Plant Physiol. Biochem.*, 81(December):1–20.

Umena, Y., Kawakami, K., Shen, J.-R., and Kamiya, N. (2011). Crystal structure of oxygen-evolving photosystem II at a resolution of 1.9 Å. *Nature*, 473(7345):55–60.

Van Best, J. and Duysens, L. N. M. (1975). Reactions between primary and secondary acceptors of Photosystem II in *Chlorella pyrenoidosa* under anaerobic conditions as studied by chlorophyll a fluorescence. *Biochim. Biophys. Acta - Bioenerg.*, 408(2):154–163.

Van Den Heuvel, R. H., Svergun, D. I., Petoukhov, M. V., Coda, A., Curti, B., Ravasio, S., Vanoni, M. A., and Mattevi, A. (2003). The active conformation of glutamate synthase and its binding to ferredoxin. *J. Mol. Biol.*, 330(1):113–128.

Van Eerden, F. J., Melo, M. N., Frederix, P. W. J. M., Periole, X., and Marrink, S. J. (2017). Exchange pathways of plastoquinone and plastoquinol in the photosystem II complex. *Nat. Commun.*, 8:15214.

van Gorkom, H. J. (1974). Identification of the reduced primary electron acceptor of Photosystem II as a bound semiquinone anion. *BBA - Bioenerg.*, 347(3):439–442.

van Leeuwen, P. J., Heimann, C., Gast, P., Dekker, J. P., and van Gorkom, H. J. (1993a). Flash-induced redox changes in oxygen-evolving spinach Photosystem II core particles. *Photosynth Res*, 38(2):169–176.

van Leeuwen, P. J., Heimann, C., and van Gorkom, H. J. (1993b). Absorbance difference spectra of the S-state transitions in Photosystem II core particles. *Photosynth. Res.*, 38:323.

van Leeuwen, P. J., van Gorkom, H. J., and Dekker, J. P. (1992). Analysis of UV Absorption Changes with Periodicity 4 in Oxygen-Evolving Photosystem-II Membranes. *J. Photochem. Photobiol. B-Biology*, 15(1-2):33–43.

van Mieghem, F., Brettel, K., Hillmann, B., Kamlowski, A., Rutherford, A. W., and Schlodder, E. (1995). Charge recombination reactions in photosystem II. I. Yields, recombination pathways, and kinetics of the primary pair. *Biochemistry*, 34(14):4798–4813.

Van Rensen, J. J. S. (2002). Role of bicarbonate at the acceptor side of Photosystem II. *Photosynth. Res.*, 73:185–192.

Vass, I. and Aro, E.-M. (2008). Photoinhibition of photosynthetic electron transport. In *Prim. Process. Photosynth. Basic Princ. Appar. 1*, pages 393–425. Royal Society of Chemistry Cambridge, UK.

Vass, I. and Styring, S. (1991). pH-dependent charge equilibria between tyrosine-D and the S states in photosystem II. Estimation of relative midpoint redox potentials. *Biochemistry*, 30:830–839.

Vass, I., Styring, S., Hundal, T., Koivuniemi, A., Aro, E.-M., and Andersson, B. (1992). Reversible and irreversible intermediates during photoinhibition of photosystem II : Stable reduced Q_A species promote chlorophyll triplet formation. *Proc. Natl. Acad. Sci. U. S. A.*, 89(4):1408–1412.

Vass, I., Turcsányi, E., Touloupakis, E., Ghanotakis, D., and Petrouleas, V. (2002). The mechanism of UV-A radiation-induced inhibition of photosystem II electron transport studied by EPR and chlorophyll fluorescence. *Biochemistry*, 41(32):10200–8.

Vinyard, D. J., Ananyev, G. M., and Dismukes, G. C. (2013). Photosystem II: The Reaction Center of Oxygenic Photosynthesis. *Annu. Rev. Biochem.*, 82(1):577–606.

Warncke, K., Gunner, M. R., Braun, B. S., Gu, L., Yu, C.-a. a., Bruce, J. M., and Dutton, P. L. (1994). Influence of hydrocarbon tail structure on quinone binding and electron-transfer performance at the Q_A and Q_B sites of the photosynthetic reaction center protein. *Biochemistry*, 33(25):7830–41.

Watanabe, M., Semchonok, D. A., Webber-Birungi, M. T., Ehira, S., Kondo, K., Narikawa, R., Ohmori, M., Boekema, E. J., and Ikeuchi, M. (2014). Attachment of phycobilisomes in an antenna-photosystem I supercomplex of cyanobacteria. *Proc. Natl. Acad. Sci.*, 111(7):2512–2517.

Wraight, C. A. (2004). Proton and electron transfer in the acceptor quinone complex of photosynthetic reaction centers from Rhodobacter sphaeroides. *Front. Biosci*, 9(1-3):309–337.

Wydrzynski, T. and Inoue, Y. (1987). Modified Photosystem II acceptor side properties upon replacement of the quinone at the Q_B site with 2,5-dimethyl-p-benzoquinone and phenyl-p-benzoquinone. *Biochim. Biophys. Acta - Bioenerg.*, 893(1):33–42.

Yadav, K. N. S., Semchonok, D. A., Nosek, L., Kouril, R., Fucile, G., Boekema, E. J., and Eichacker, L. A. (2017). Supercomplexes of plant photosystem I with cytochrome b_6f, light-harvesting complex II and NDH. *Biochim. Biophys. Acta - Bioenerg.*, 1858(1):12–20.

Zaharieva, I., Dau, H., and Haumann, M. (2016). Sequential and coupled proton and electron transfer events in the S2→S3 transition of photosynthetic water

oxidation revealed by time-resolved X-ray absorption spectroscopy. *Biochemistry*, 55(50):acs.biochem.6b01078.

Zimmermann, J. L. and Rutherford, A. W. (1986). Photoreductant-induced oxidation of Fe^{2+} in the electron-acceptor complex of Photosystem II. *BBA - Bioenerg.*, 851(3):416–423.

Zimmermann, K., Heck, M., Frank, J., Kern, J., Vass, I., and Zouni, A. (2006). Herbicide binding and thermal stability of photosystem II isolated from *Thermosynechococcus elongatus*. *Biochim. Biophys. Acta - Bioenerg.*, 1757(2):106–114.

Zouni, A., Witt, H. T., Kern, J., Fromme, P., Krauss, N., Saenger, W., and Orth, P. (2001). Crystal structure of photosystem II from *Synechococcus elongatus* at 3.8Åresolution. *Nature*, 409:739–743.

6 Appendix

6.1 Formulas for Redox Titrations

From Michaelis (1932) we get the following relations:

$$[O] = Suv/(uv + u + 1) \tag{6.1}$$

$$[I] = Su/(uv + u + 1) \tag{6.2}$$

$$[R] = S/(uv + u + 1) \tag{6.3}$$

where

$$S = [O] + [I] + [R] \tag{6.4}$$

$$u = [I]/[R] \tag{6.5}$$

$$v = [O]/[I] \tag{6.6}$$

Equation 6.2 can also be written as

$$[I] = \frac{S}{v + 1 + u^{-1}} \tag{6.7}$$

From Equation 3.6 the following relationships can be formed:

$$v = 10^{\frac{(E-E_1)F}{RT}} \tag{6.8}$$

$$u = 10^{\frac{(E-E_2)F}{RT}} \tag{6.9}$$

Combining Equations 6.8 and 6.9 with Equation 6.2 the following equation is obtained:

$$[I] = \frac{S}{1 + 10^{\frac{(E-E_1)F}{RT}} + 10^{\frac{(E_2-E)F}{RT}}} \tag{6.10}$$

Which together with Equations

$$\Delta E = E_1 - E_2 \tag{3.4}$$

and

$$E_m = (E_1 + E_2)/2 \tag{3.5}$$

gives the concentration of the intermediate [I] in dependence of E_h, E_m and ΔE

$$[I] = \frac{S}{\left(1 + 10^{E-E_m-\frac{\Delta E}{2}(RT)^{-1}F} + 10^{E_m-\frac{\Delta E}{2}-E(RT)^{-1}F}\right)} \tag{3.7}$$

6.2 Additional Figures for Energetics of Q_B

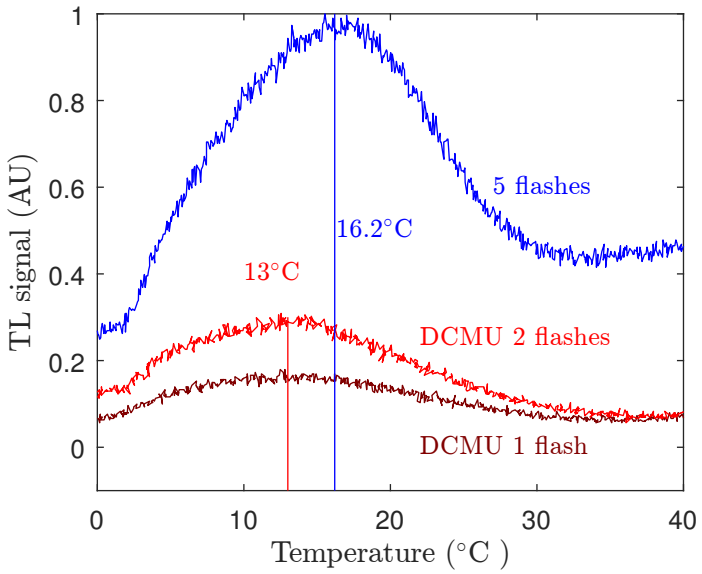

Figure 6.1: Thermoluminescence arising from $S_2Q_A^-$ recombination in PSII core complexes from *T. elongatus* generated either with DCMU (Dark red: DCMU and one flash; red: DCMU and two flashes) or by giving five saturating flashes and fully reducing Q_B (referenced on Page 94).

6.3 Tables and Additional Figures for Kinetic Studies

Table 6.1: Parameters of a two exponential fit of the Q_A^- decay in PSII cores on a series of flashes. Data are average ± standard deviation of five biological replicates. Table referenced on Page 109.

	Flash 1		Flash 2		Flash 3		Flash 4	
A_1 (%)	59.7	± 3.1	61.2	± 3.6	69.0	± 1.9	66.7	± 3.2
A_2 (%)	40.3	± 3.1	38.8	± 3.6	31.0	± 1.9	33.3	± 3.2
$t_{1/2}$ 1 (μs)	404	± 49	572	± 53	870	± 100	703	± 36
$t_{1/2}$ 2 (ms)	5.8	± 0.9	13.9	± 1.5	22.4	± 3.1	22.4	± 5.1
y0 (%)	43	± 0	22	± 4	19	± 5	30	± 5
Rsq	0.99		0.99		0.99		0.99	

	Flash 5		Flash 6		Flash 7		Flash 8	
A_1 (%)	67.2	± 3.7	64.4	± 1.2	61.9	± 2.1	55.5	± 2.3
A_2 (%)	32.8	± 3.7	35.6	± 1.2	38.1	± 2.1	44.5	± 2.3
$t_{1/2}$ 1 (μs)	874	± 143	871	± 81	965	± 66	953	± 69
$t_{1/2}$ 2 (ms)	56.4	± 34.2	107.2	± 54.1	162.4	± 45.0	254.7	± 31.5
y0 (%)	44	± 2	42	± 3	32	± 4	21	± 1
Rsq	0.98		0.98		0.97		0.97	

Table 6.2: Parameters of one exponential fit of 320 nm measurement in PSII cores on a series of flashes. Data are average ± standard deviation of three biological replicates. Table referenced on Page 113.

	$t_{1/2}$ 1 (ms) ± sd		y0 (%) ± sd		Rsq
Flash 1	2.43	± 2.73	258.37	± 37.82	0.78
Flash 2	1.49	± 0.28	10.20	± 5.43	0.99
Flash 3	1.27	± 0.20	-8.71	± 4.37	0.99
Flash 4	1.07	± 0.22	-12.70	± 5.45	0.99
Flash 5	1.21	± 0.63	63.83	± 14.23	0.95
Flash 6	1.63	± 0.53	23.20	± 9.72	0.98
Flash 7	1.31	± 0.29	16.28	± 6.31	0.99
Flash 8	1.21	± 0.64	12.41	± 14.50	0.95
Flash 9	1.34	± 0.65	17.28	± 13.67	0.95
Flash 10	1.33	± 1.02	20.53	± 21.54	0.89

Table 6.3: Parameters of one exponential fit of 320 nm measurement in PSII cores with 10-PQ and ferricyanide on a series of flashes. Data are average ± standard deviation of three biological replicates. Table referenced on Page 113.

	$t_{1/2}$ 1 (ms) ± sd		y0 (%) ± sd		Rsq
Flash 1	5.22	± 13.83	764.29	± 115.95	0.42
Flash 2	1.58	± 0.55	9.87	± 10.57	0.97
Flash 3	1.21	± 0.54	15.39	± 12.52	0.96
Flash 4	1.12	± 0.31	-6.52	± 7.50	0.98
Flash 5	1.68	± 0.76	42.31	± 13.84	0.96
Flash 6	1.50	± 0.57	19.61	± 11.24	0.97
Flash 7	1.46	± 0.76	15.60	± 15.23	0.94
Flash 8	1.27	± 0.49	-0.94	± 10.80	0.97
Flash 9	1.07	± 0.53	24.87	± 13.50	0.95
Flash 10	1.32	± 0.57	20.16	± 12.34	0.96

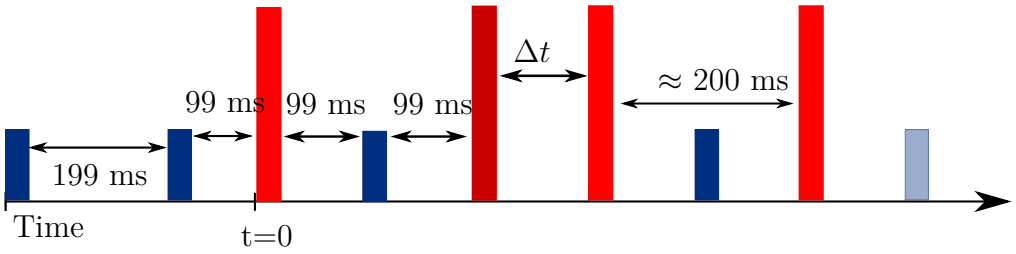

Figure 6.2: Flash timings for 292 nm measurements, $S_2 \rightarrow S_3$ Figure referenced on Page 52

Table 6.4: Parameters of the one or two exponential fit of the S-state turn over measurements at 294 nm. Table referenced on Page 120.

	PSII		DCBQ		Crystalls		Flash2	
A_1(%)	34	±33	78	±13	100	±16	100	±23
A_2(%)	66	±32	22	±15				
$t_{1/2}1(\mu s)$	44	±59	555	±229	259	±103	787	±439
$t_{1/2}2$(ms)	0.344	±0.23	17	±29				
y0(%)	6	±7	-1	±11	2	±13	21	±16
Rsq	0.98		0.98		0.90		0.84	

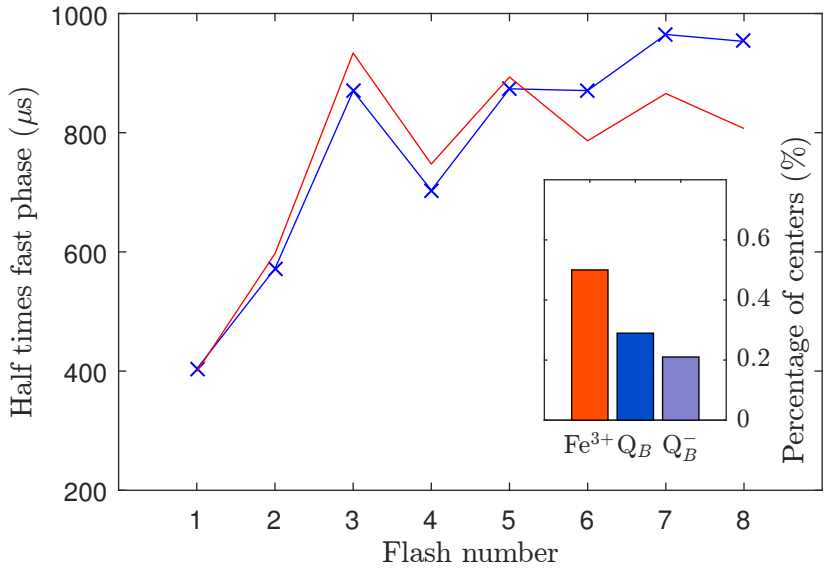

Figure 6.3: Rate pattern analysis with tightly constrained markov model. Figure referenced on Page 126.

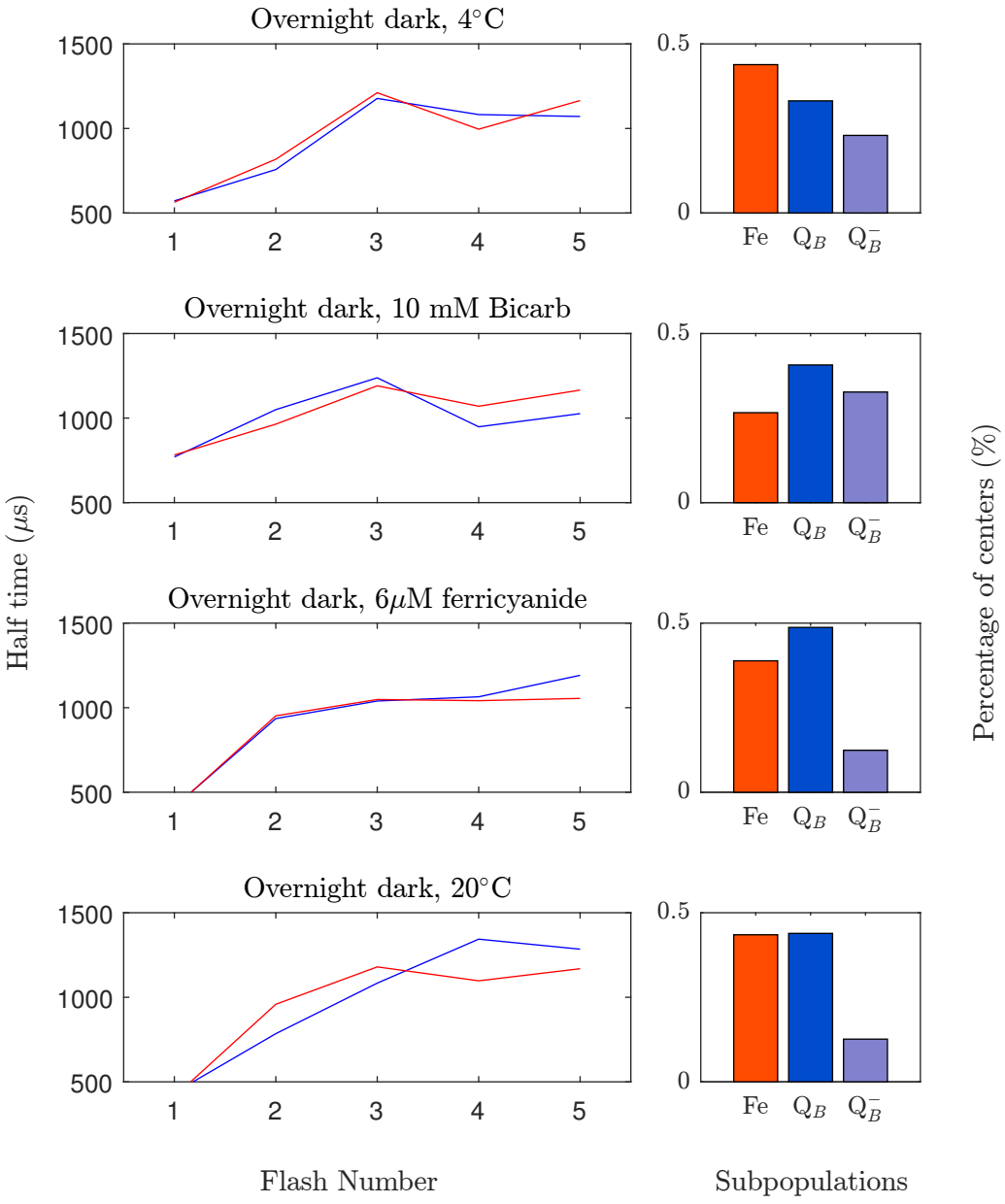

Figure 6.4: Markov model fits for PSII samples dark-adapted overnight. Figure referenced on Page 127.

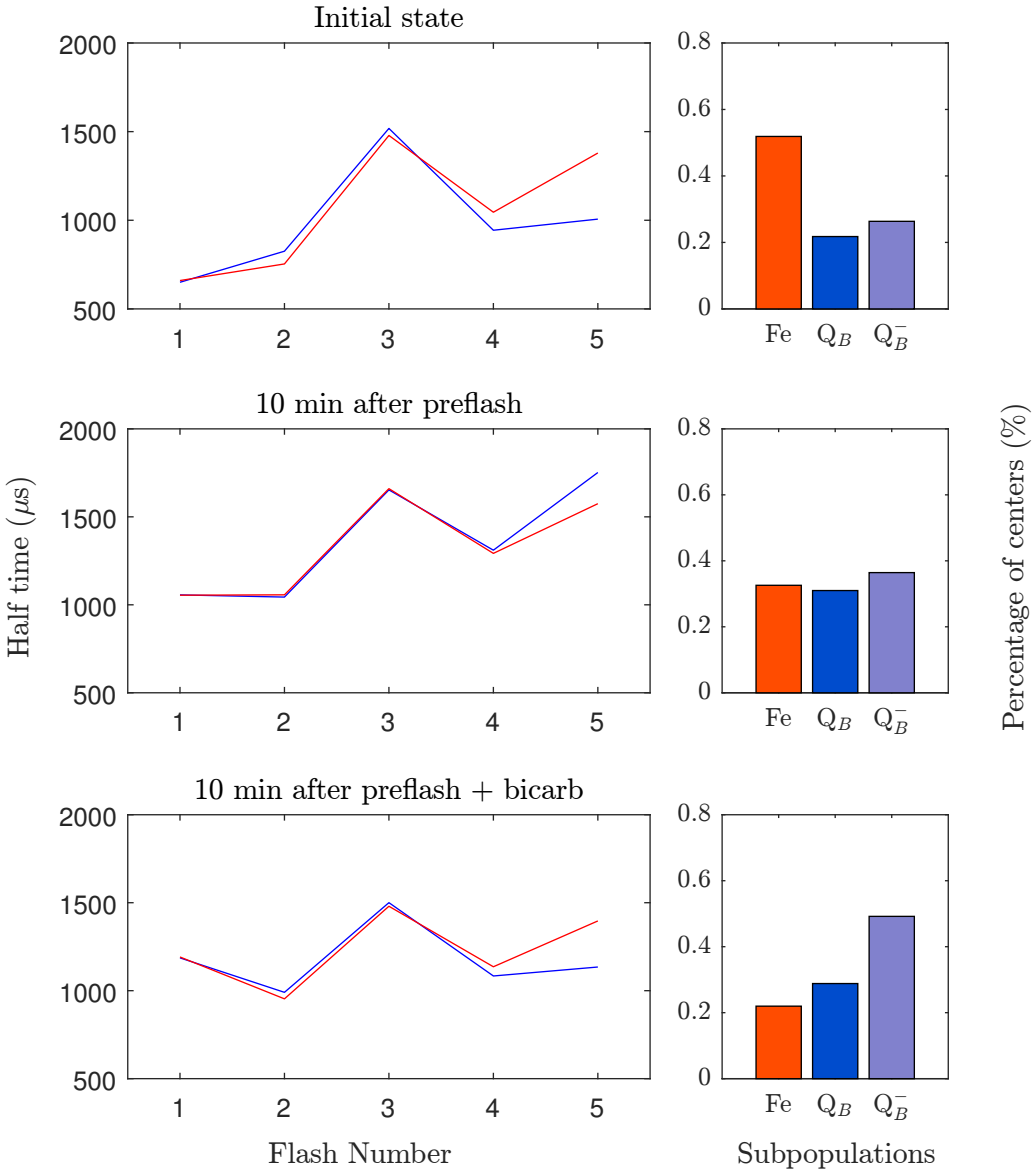

Figure 6.5: Markov model fits for PSII samples after thawing, dark-adapted for 10 minutes after a preflash and dark-adapted for 10 minutes after a preflash with additional 10 mM bicarbonate. Figure referenced on Page 129.

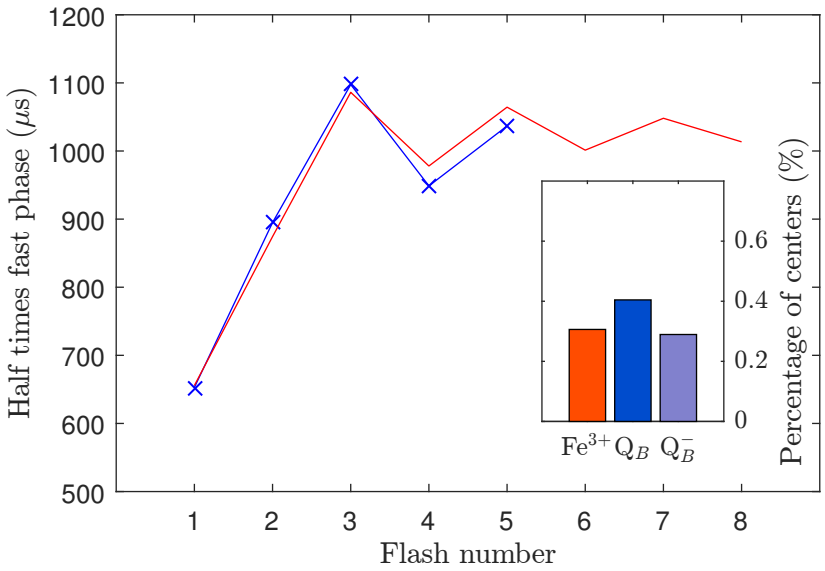

Figure 6.6: Rate pattern analysis PSII dimers. Figure referenced on Page 140.

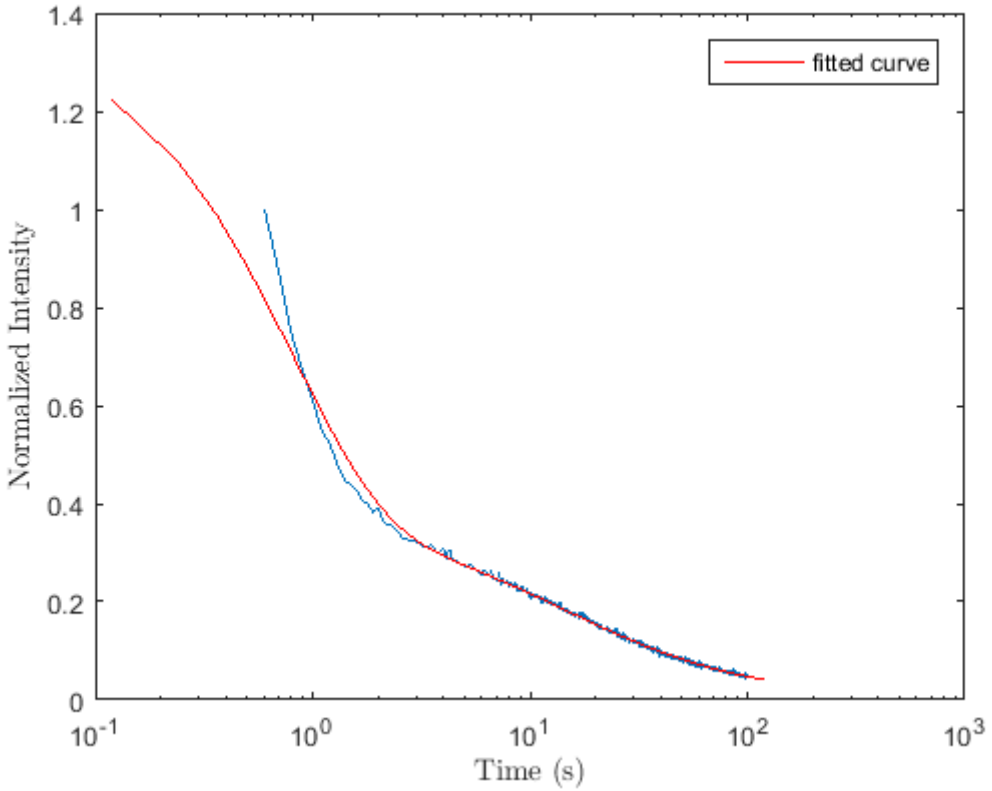

Figure 6.7: Luminescence Decay of PSII core complexes at 15C after a saturating flash. Figure referenced on Page 130.

7 Appendix: Thermoluminescence Measurement Device

The measurement of thermoluminescence emitted by photosynthetic materials is a useful technique to study photosynthesis and characterize samples. At the start of this Ph.D. no working thermoluminescence machine was available in the Rutherford laboratory. Whilst there is one device currently commercially available, this device does not satisfy the required specifications, such as the ability to give saturating single turnover flashes, the ability to do 77K illuminations, the ability to do low temperature TL measurements (200 K onwards) and the tolerance to some amount of residual light in the room. Therefore I designed and built new device from scratch. Apart from soldering capabilities and Ohm's law, which were already present, the knowledge required to build the device was acquired using the internet. The device build over proximately 2.5 years, mostly on evenings and weekends. Susan Parker gave useful suggestions towards optimising the electronics in the later stages of the project. As a documentation of each step, aspect and iteration would be more appropriate for a Ph.D. in engineering than in biophysics, here only a broad overview is given, that might help future users to some extent.

As it was unknown which design would meet the required specifications, let alone how to build such a device, an iterative process of increasing capabilities was chosen. First, key competences for building a TL device, such as the ability to measure and modify the temperature of a metal plate in a computer controlled manner with sufficient accuracy, were developed. Then, a first prototype using an old photomultiplier from a non-functional machine was built and tested. This machine

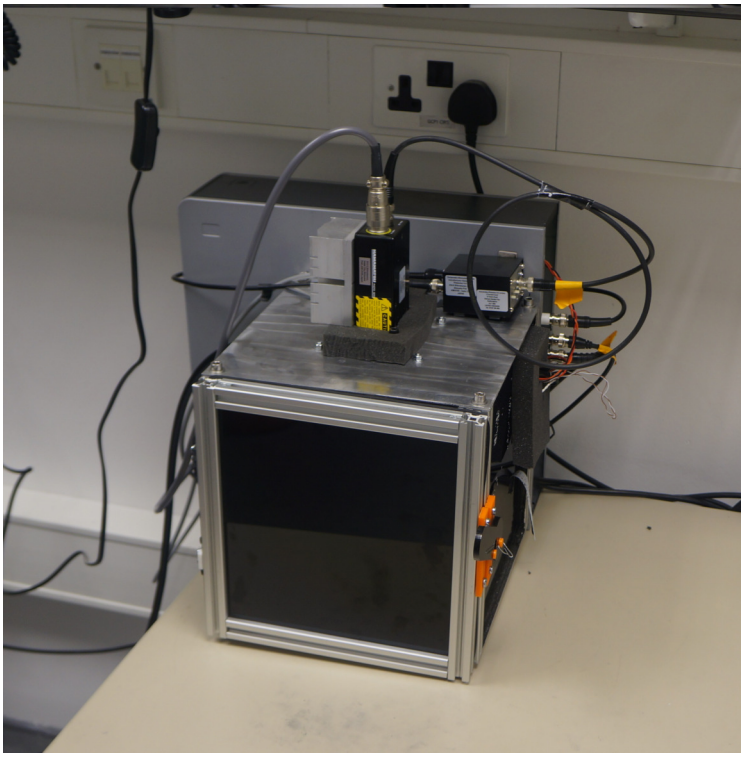

Figure 7.1: Current state of TL machine.

provided the framework to develop all the necessary electronics and programming skills. Based on this experience, the designs of all components were adjusted or entirely redesigned. The completed device is shown in Figure 7.1. The following sections will introduce the design specifics, the optics and illumination methods, the electronics and the programming in more detail. Finally a stepwise usage manual is provided.

7.1 Construction of a Thermoluminescence Device

All physical components were designed in CAD software (Inventor2015, Autodesk) prior to fabrication. Due to bureaucratic reasons, it was not possible to make use of metal working facilities present at Imperial College London. Therefore metal work

was done using a small, hobby-grade rotary tool and a lot of creativity. Some parts were 3D-printed, however, due to requirements concerning accuracy and temperature stability, this method was not applicable to most parts. As milling facilities, although plentiful at Imperial College, could also not be used, laser cutting of wood and plastic was extensively used for many of the components. Laser cutting is limited to two dimensions and material thickness below ≈1 cm, therefore, bigger and more complex parts were realized by layering differently cut acrylic sheets on top of each other. Whilst the overall accuracy and resolution of this method was limited, it allowed for rapid alterations and modifications by adding, removing or changing single layers of the part without having to make a completely new part.

7.1.1 Overall design

TL devices have to fulfil a number of requirements. TL has a very low intensity, the photomultipliers must be very sensitive and shielded from light. Therefore, either the apparatus needs to be shielded from light, or the experimenter must work in absolute darkness. In reality, LED's are hard to avoid in laboratory settings and when the latter route is chosen, TL measurements involve a lot of handling black cloth in the dark. This becomes especially cumbersome, when manual handling to provide sample illumination is required. Therefore a completely enclosed design, requiring minimal manual handling, was pursued. The main chamber of the device was built using 20 x 20 mm Rexroth aluminium profiles and 5 mm aluminium plates. The sides were covered using 5 mm black acrylic sheets. Black silicone was used to completely seal the inside of the device. To allow access to the machine, a door was built using a 3D-printed locking mechanism and 3D-printed hinges.

7.1.2 Sample holder

To be able to illuminate and measure below 100 K, liquid nitrogen immersion was chosen as cooling method. Initially the device was built with a moving sample stage. This stage could be moved along the z-axis (up and down) using a shuttle riding

on a metal profile (Makerslide), screw-driven by a computer-controlled NEMA-17 stepper motor. In essence, this mechanism was copied from an open source CNC-mill design (Shapeoko2), where a similar setup drives the z-axis. This allowed for the sample plate assembly to be first lowered into liquid nitrogen and subsequently moved upwards for illumination and TL measurements.

This approach had two significant disadvantages. Firstly, because only a relative small part of the relatively large sample holder could be lowered into the liquid nitrogen, it was difficult to attain and hold temperatures below 100 K. Secondly, accurate placement of the sample in reference to the photo-multiplier could not be guaranteed.

The current device uses the mechanism initially developed to move the sample stage, to instead move the liquid nitrogen bath up and down. A sample holder, and sample holding mechanism was developed, that 1) allows for complete submersion of the sample holder in liquid nitrogen, 2) thermally isolated the sample holder from the other components of the device, 3) ensures reproducible sample positioning with regard to the photomultiplier, 4) allows for rapid exchange and positioning of the sample holder and 5) keeps the sample holder relatively small and easy to clean.

This mechanism is shown in Figure 7.2. A three-dimensional exploded view of the assembly is shown in Figure 7.3

The sample holder comprises a heat exchanger, a Peltier element and a sample plate. It is connected to the lens assembly via a spring loaded bolt system that can be operated from the outside. An O-ring separates the sample holder from the lens assembly to minimize heat transfer. The lower bolts, that hold the sample holder, are also thermally insulated to minimize condensation and allow for the upper bolts to be comfortably touched even when the lower bolts are very cold. Through pushing down the bolts on the outside the sample holder can be inserted and removed by slightly turning the sample holder to engage or disengage with the bolts. This method is fast and simple and can be done in absolute darkness, with the sample holder being at 77 K. Wearing of nitrile gloves is advised under these conditions to avoid freezing of the experimenters skin against the sample holder.

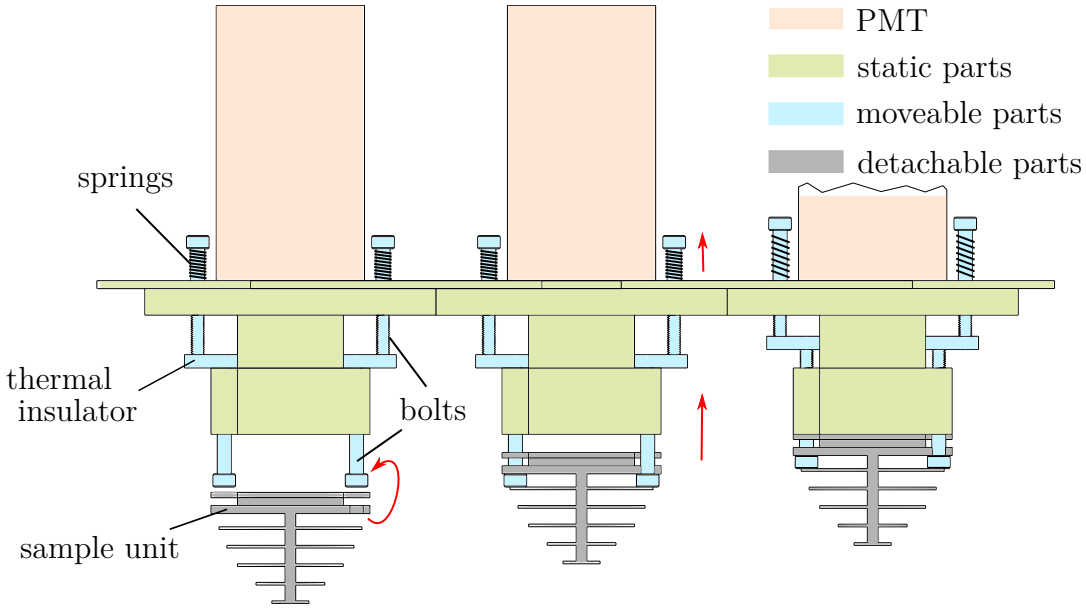

Figure 7.2: Schematic overview of the sample holder mechanism.

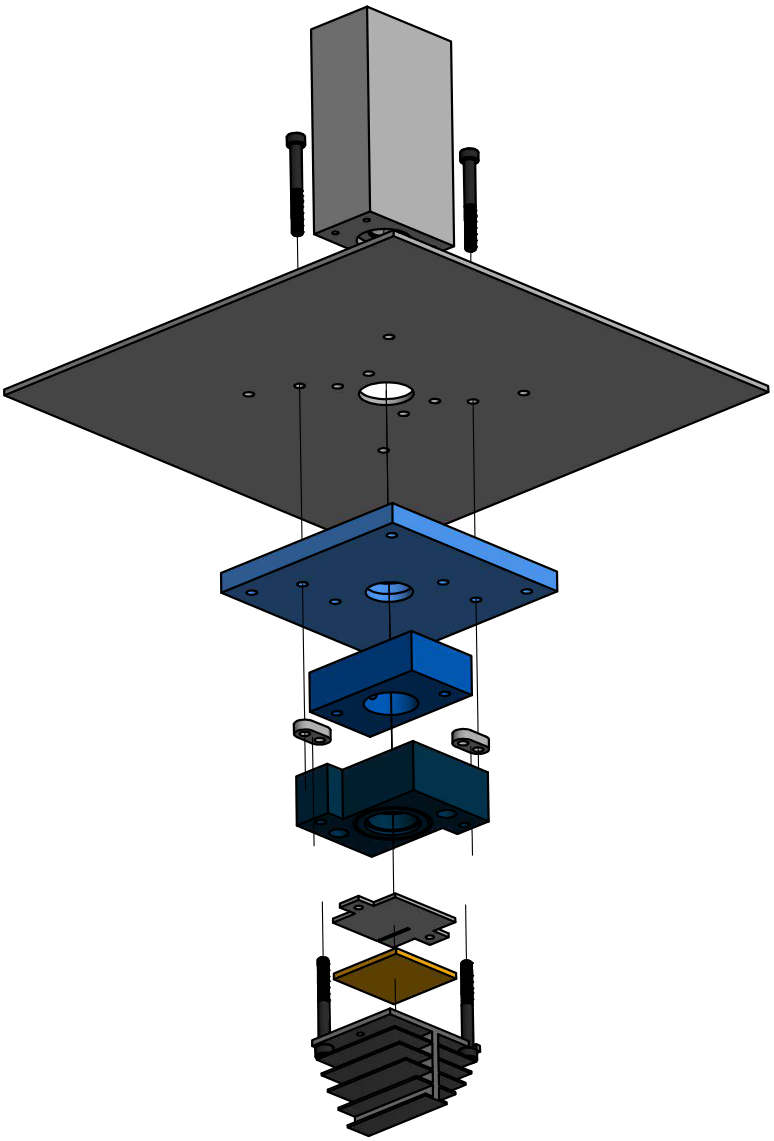

Figure 7.3: Exploded view of the TL machine core assembly.

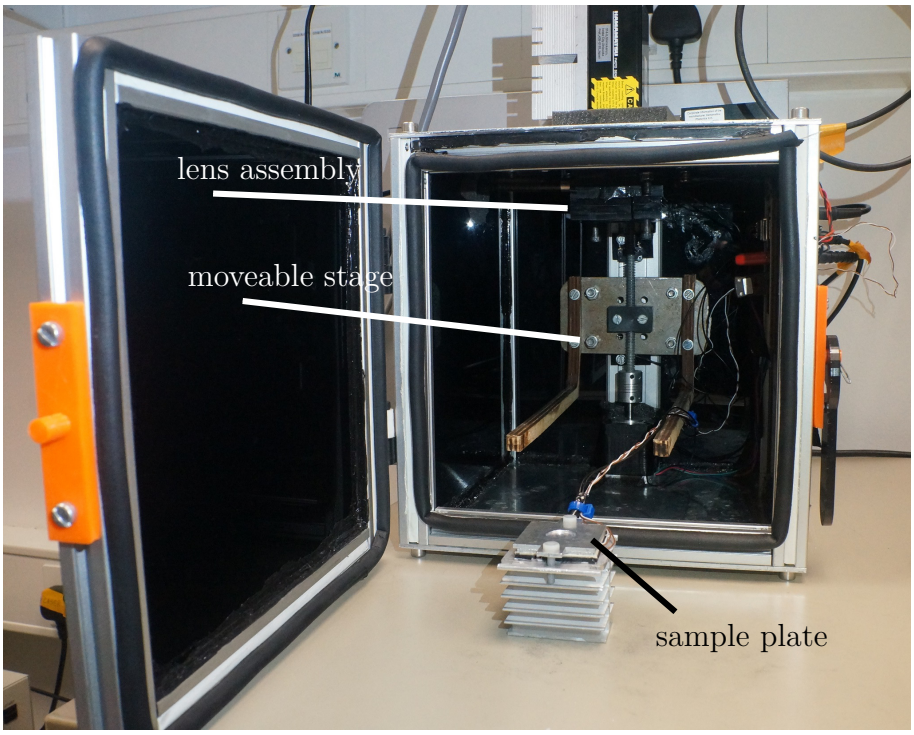

Figure 7.4: Inside of the TL device.

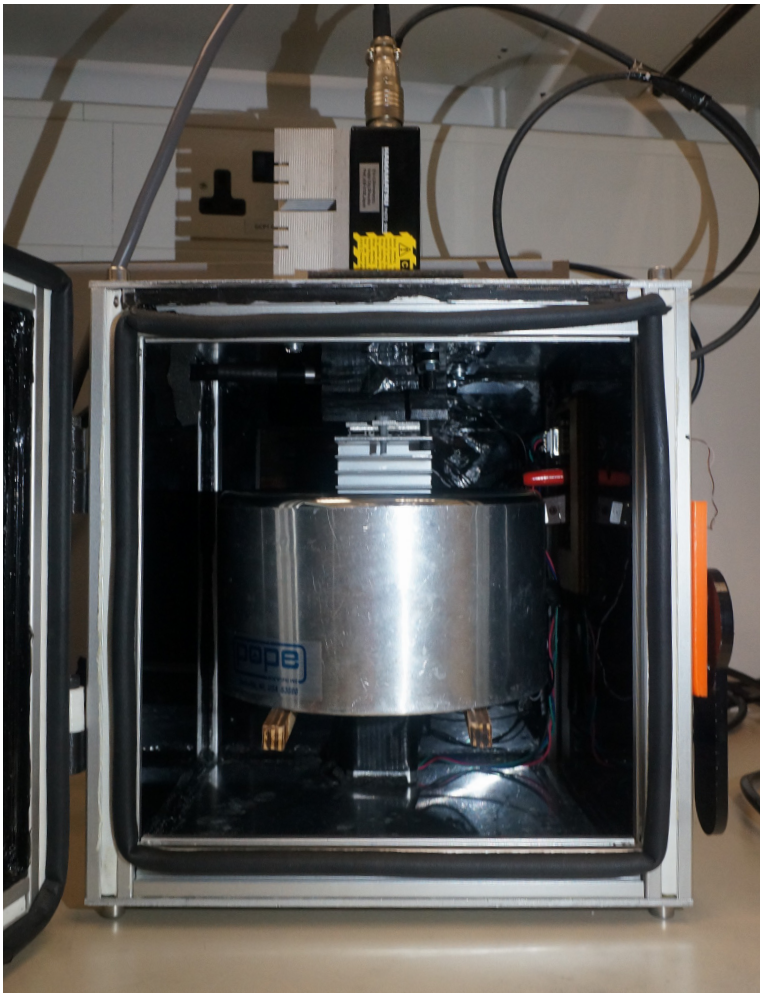

Figure 7.5: Inside of the TL device with liquid nitrogen dewar.

7.2 Optics and Illumination

To give saturating flashes, TL devices commonly use xenon flashes. These have the disadvantage, that they have a long emission tail, leading to multiple turnovers in a fraction of the sample. Furthermore xenon flashes need high voltage electronics that pose a safety hazard. Also xenon flashes are large, so that either some fast, manual switching between illumination and TL measuring channels, or a bifurcated light-guide is required. To circumvent these issues, initially, a set of high power LED's with an appropriately designed fast switching driver circuit, were used. Unfortunately these LED's were not bright enough to ensure saturation, when flashes were used that were short enough to avoid double turnovers (20 µs).

Therefore an optic system that allowed for illumination with an ND:YAG laser, without requiring manual handling or exposure to the laser light was developed. A schematic of this system is shown in Figure 7.6.

Laser flashes are transferred from the laser to the lens assembly via a light-guide, A dichroic mirror (DMLP550R, Cut-off Wavelength: 550 nm, Thorlabs) reflects the laser flash (532 nm, green) onto the lower lens (ACLU2520U, EFL 20,1 mm, Thorlabs) , which focuses the light onto the sample. Thermoluminescence emitted from the sample is condensed by this lens. Due to the longer wavelength of the emitted light (>680 nm) it is transmitted through the dichroic mirror and focused onto the PMT detector plane by a second lens (LA1950, FL 25,3 mm, Thorlabs). A long-pass filter (FELH0650, Cut-On Wavelength: 650 nm, Thorlabs) blocks light not arising from luminescent processes from reaching the detector. This is necessary due to the high intensity of the laser flashes inducing an artefact at the start of a measurement, even though the PMT is powered down. Secondly it prevents background noise in the PMT signal stemming from the xenon flash lamp, that pumps the laser.

To determine the sizes, shapes and distances of the optical components, the system was modelled and optimized using a optical design program (OSLO, Lambda research cooperation). In this way different designs, using one or two lenses, were tested. Figure 7.7 shows the optical analysis of the currently used system. It was found that it is quite hard to focus a large fraction of the emitted light onto the PMT detector.

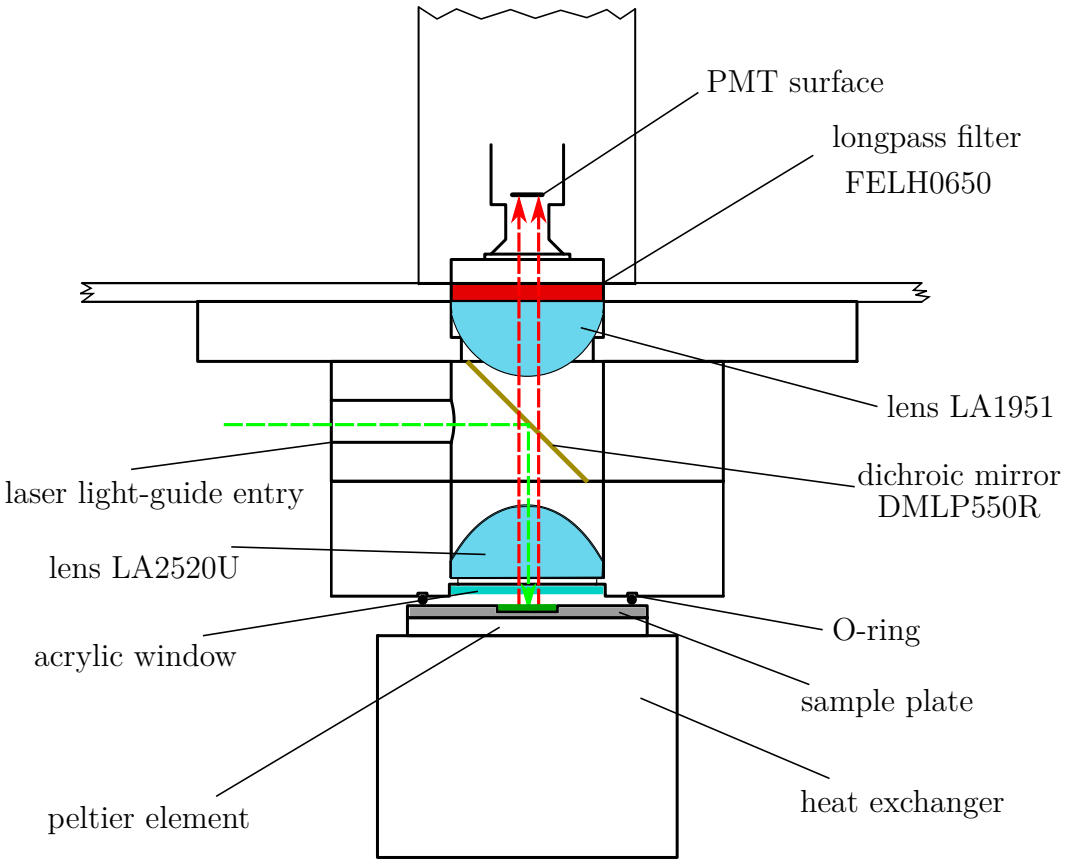

Figure 7.6: Schematic overview of the TL lens assembly.

Potentially a more advanced lens set-up, designed by a professional, could optimize the light collection.

7.2.1 Low temperature illumination

Whilst it is in principal possible to do 77 K illumination inside the instrument it has been found, that it is more practical to freeze the sample within the instrument, but illuminate at 77 K outside of the instrument. This is because illumination times at this temperature can be quite long and considerable build-up of condensation occurs when this is done within the instrument. Furthermore outside of the instrument the complete sample holder can be submerged in liquid nitrogen and more diverse illumination setups can be used.

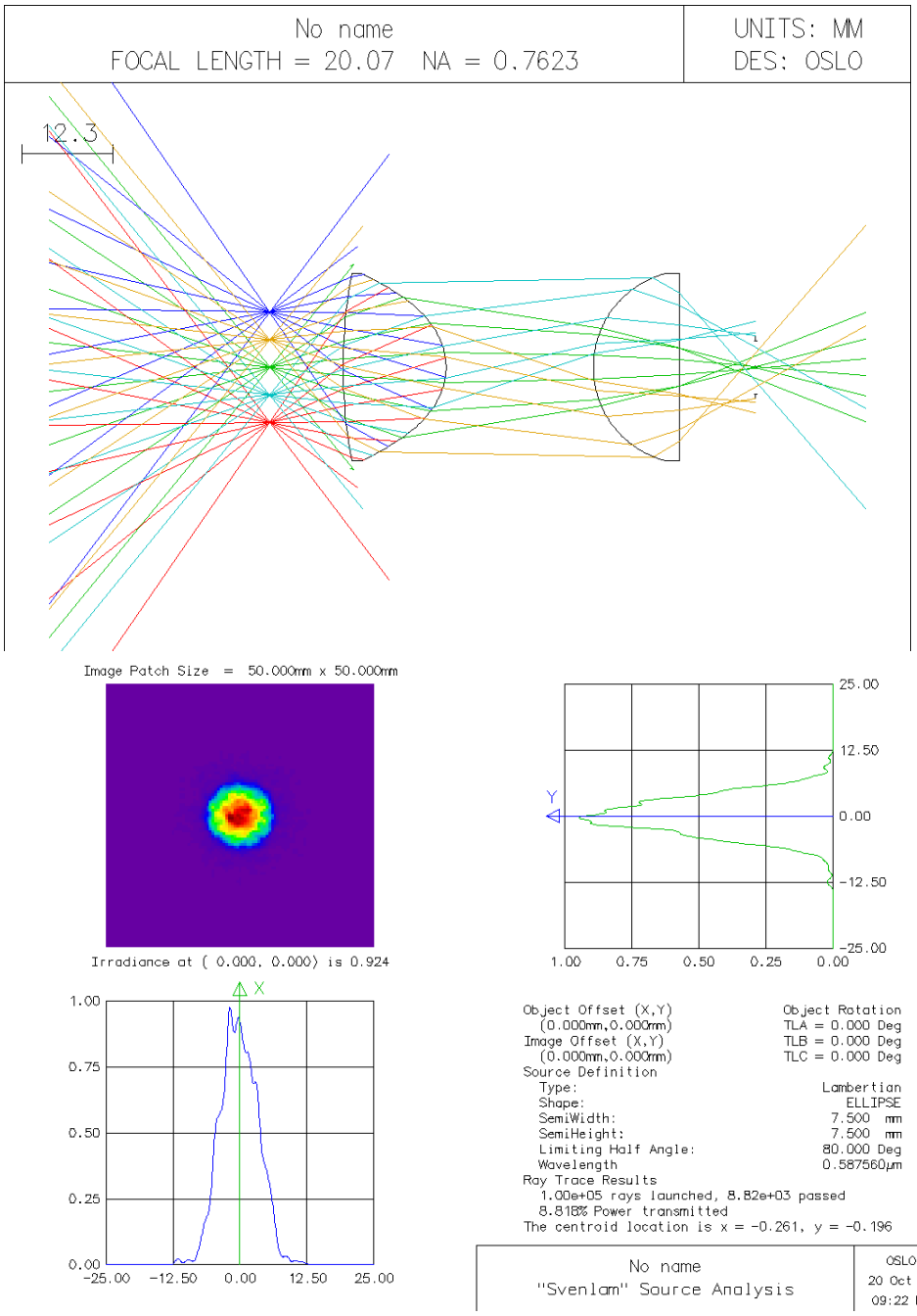

Figure 7.7: Simulation of light collection yield with current lens setup using a lambertian emission pattern.

7.3 Electronics

The electronics of the device were designed around the Arduino open-source electronic prototyping platform. Although more professional solutions, geared towards scientific instrumentation are available, these all suffer from major draw-backs. Firstly often they are proprietary and expensive. Secondly no accessible enthusiast community exists that provides tutorials on basic applications and non-profit driven help when problems arise. Initial prototypes of the TL device used the Arduino Uno and Mega boards. These are widely available, completely open-source, cost around £20, and tutorials on how to realize many of the basic functions required in a TL device can be found online (read temperatures, analog-to-digital conversion, electronic switching, LED drivers etc.).

The current device uses an Arduino Due, which is based on an Atmel SAM3X8E ARM Cortex-M3 CPU. This Processor was chosen mainly due to the larger number of digital I/O and PWM pins than the Uno and the better ADC (12 bit) compared to the Mega. The switch to this processor however also necessitated a complete redesign of the circuits as it operates on a 3.3 V logic level instead of 5 V. Whilst initial circuit tests were done using a breadboard, the complexity of the device rapidly exceeded the level where this approach was practical. Therefore two-layer circuit boards were designed using the EAGLE software (Cadsoft). Figure 7.8 shows the latest connection schematic and Figure 7.9 shows the latest circuit board design. In total three different iterations were produced before the current design. Manufacturing of the boards was done by third party companies in low volumes at low cost (10 cm x 10 cm, 5 boards, 1 oz copper, 20-30 $, Seeed Studio, Shenzhen2U).

Power to the instrument is provided by two separate power supplies. (Astec 40W, 5 V, ±15 V, RS components; TDK-Lambda 150 W, 12 to 18 V, 10 A) This is done to isolate the large and fluctuating current demands from the Peltier element from the signal acquisition circuits.

To measure temperatures ranging from 77 K to 400 K reliably, T-type thermocouples were used. The signals were digitized using a board based on the MAX31856 chip (19 bit precision thermocouple to digital converter with linearisation, Maxim

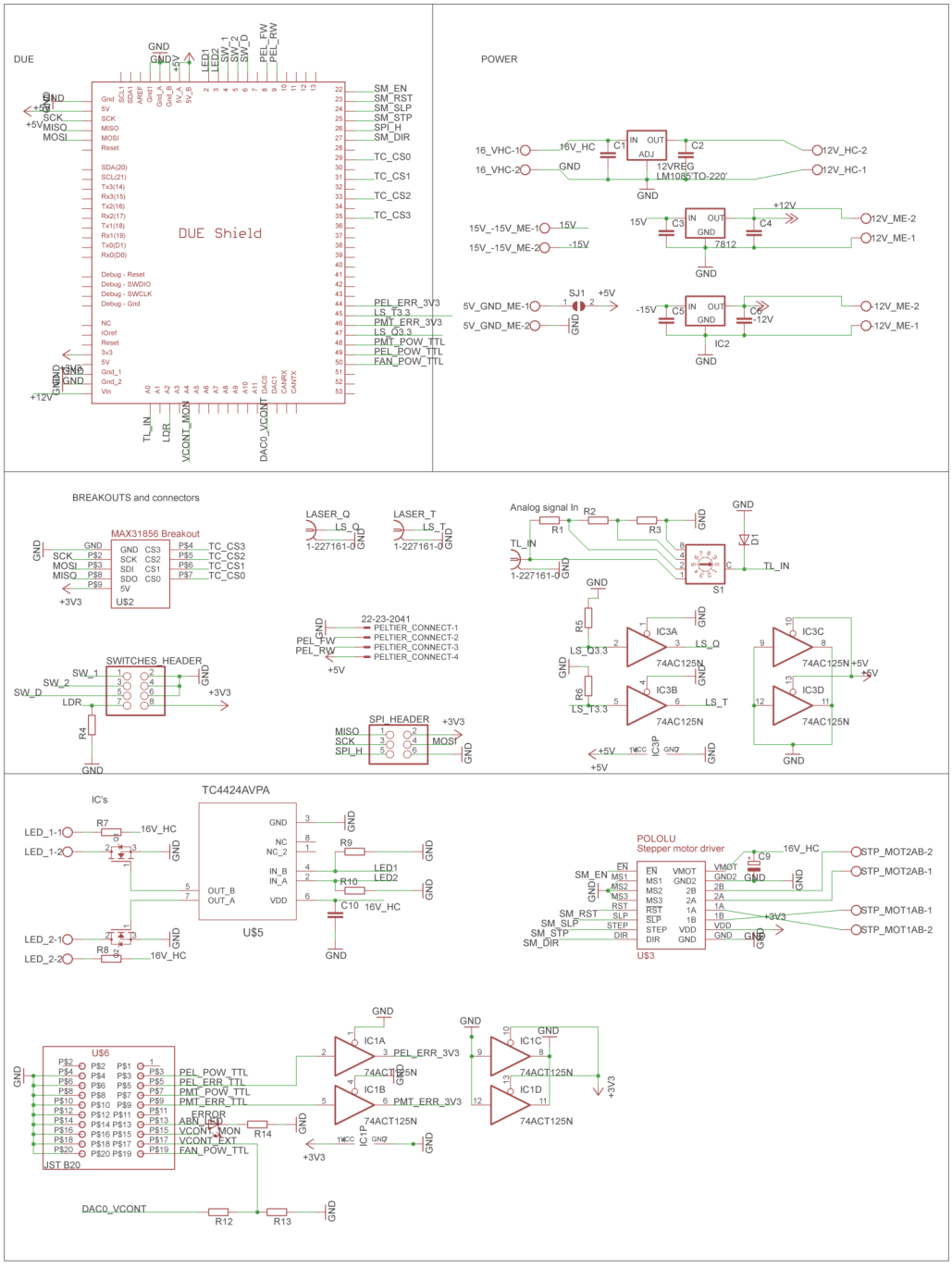

Figure 7.8: Electronics scheme of TL board.

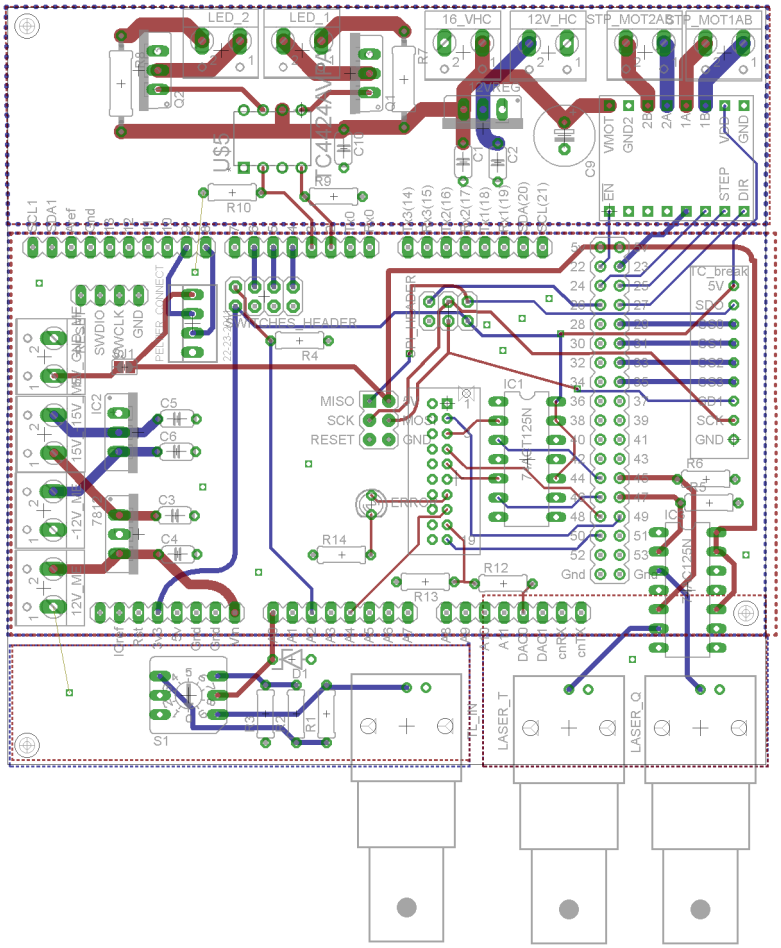

Figure 7.9: Board layout of TL board. Blue traces represent top layer traces, red traces represent bottom layer traces.

Integrated) A custom C++ library was written to use this chip in conjunction with the Arduino.

To power the Peltier element, a high current H-bridge motor driver (BTS7960 24V, 43A H-bridge Motor Driver, Ebay) normally used to control high current servo motors in robotics applications was used. To calculate the appropriate heating or cooling rates a PID library developed and released under the MIT license by Brett Beauregard was used.

To control the Nema-17 stepper motor, the A4988 stepper motor driver (Ebay) was used.

The H7422-50 PMT tube (Hamamatsu) was controlled using the M9012 power supply unit (Hamamatsu).

The electronics were mounted in a used PC case which was fixed to the back of the device (Figure 7.10).

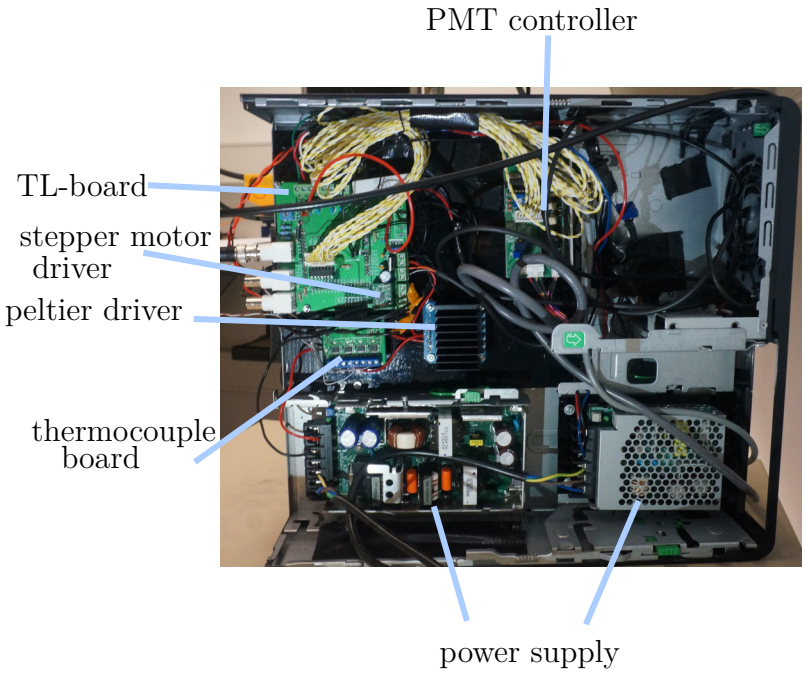

Figure 7.10: TL device electronics.

7.4 Programming

The programming of the device can be split into two main parts. Firstly, the code loaded onto the Arduino that controls the machine and secondly, a graphical user interface (GUI) that is run on a computer connected via USB. The Arduino code was written in C++ using the Arduino IDE and the GUI was written in Matlab. Two standalone versions of the Matlab code were compiled, one for Thermoluminescence measurements and one for Luminescence measurements.

7.4.1 Arduino coding

To allow for sensible usage and control of the machine, a control system was developed. This is based on a finite-state machine approach, common to many automated machines such as vending machines, elevators etc. and was coded using the Arduino environment in C++ (1059 lines of code).

The TL device can be in one of three states. In each state, only a subset of all available commands can be executed (See Table 7.1). This is done to prevent the experimenter from inadvertently flashing the laser whilst the PMT is on, etc. The "Idle" state is the state that is entered when the machine is initially powered on. Only a few commands are available in this state. The "Light" state allows for temperature control and sample illumination. In contrast, the "Dark" state allows temperature control, PMT control and signal acquisition. When changing from one state to another, error checks are performed and if necessary, the state change is aborted.

Table 7.2 lists all the available commands. These commands can be sent using any serial terminal via the USB port (8 Databits , 1 Stopbit, Baudrate 115200, no Parity bit).

Table 7.1: List of available commands depending on the TL machine states

Function	Idle state	Light state	Dark state
switchtoidle	x	x	x
switchtolight	x	x	x
switchtodark	x	x	x
reportsensorvalues	x	x	x
movestepper	x	x	
verbosetoggle	x		
PMTcooltoggle	x	x	x
setPIDTune	x		
sendshortreport		x	
programflashes		x	
setlumines		x	
setholdat		x	x
setholdbelow		x	x
setholdabove		x	x
setnotempcontrol		x	x
setgradientt			x
setPMT			x
settransmitmode			x

Table 7.2: Commands that can be sent to TL machine via serial communication.

Function	Command
switchtoidle	'I'
	Switches machine state to 'Idle'. Turns off any cooling or heating of Peltier; disengages stepper-motor, Erases any planned flashes, transmits or temperature controls. Returns "I"; in verbose mode "Switched to idle"
switchtolight	'L'
	Switches machine state to 'Light'. Erases any planned flashes, transmits or temperature controls, Turns on PMT cooling, Turns off PMT power, Sets PMT gain to 0. Returns "L"; in verbose mode "Switched to light"
switchtodark	'D'
	Switches machine state to 'Dark'. Checks if PMT error is present and returns "F31" or in verbose mode "PELerr or PMTerr are set..." and switches to light mode instead. Otherwise returns "D" or in verbose mode "switched to dark"
reportsensorvalues	'R'
	Request report on values of most sensors and global persistent variables. Returns "machinestate (0:Idle, 1:Light, 2:Dark), currenttime (in ms since poweron), pmtV (PMT voltage read or averaged PMT voltage reads since last report),numdata(Number of Voltage reads that were averaged since last report), Thermocouple 1 temperature (T in K), Thermocouple 2 temperature (T in K), Plate Setpoint (T in K),

Table continues on next page

Table 7.2: (continued)

Function	Command
	PID Output (Value from -256 to 256, heating or cooling sampleplate),E (End of report). In verbose mode report is similar but endstops state and PMT voltage settings are also reported.
movestepper	'Mval1,val2'
	Moves stepper motor that controls hight of moveable stage (Liquid N_2) val1: Direction of movement; 1 for up or 2 for down. val2: Number of steps; constrained between 1 and 10000.
verbosetoggle	'T'
	Toggles between verbose and normal reports of the machine. Use Verbose to control manually and trace bugs.
PMTcooltoggle	'C'
	Enables cooling of PMT with Peltier integrated into the PMT casing. This should be turned on five minutes before first measurement. In practice this has little effect.
setPIDTune	'Aval1,val2,val3'
	Change tuning parameters of the Peltier PID loop that controls how much current flows through the Peltier to reach the desired temperature setpoint. Changing this can result into very different behaviour of the temperature control loop. val1: Kp; val2: Ki; val3: Kd. Values are not constrained within Arduino, you can set any sensible or non sensible value.

Table continues on next page

Table 7.2: (continued)

Function	Command
	Machine returns: “Tuning params set to: Kp: val1 Ki: val2 Kd: val3”. Default values are 20,2,35 for TL mode and 20,2,0.1 for Luminescence mode.
sendshortreport	’Y’
	Request a short report. Is mostly used by Matlab to update display. Reports: “Instrument time, Thermocouple1, Thermocouple2, PlateSetpoint, PIDOutput, E”.
programflashes	’Fval1,val2’
	Fires the laser. val1: number of flashes to be sent (constrained 0-100); val2: flash spacing (time between flashes in ms, constrained 100-10000); Instrument returns ’z’ when all flashes were sent.
setlumines	’Uval1,val2,val3,val4,val5,val6,E’
	This starts the luminescence switch. This is used to switch from light mode to dark mode and turn on PMT as fast as possible when measuring luminescence. This command should only be used when experimenter is experienced with the instrument, because no error checks are performed and the PMT can be seriously overloaded. val1: number of flashes (constrained 0-100); val2: flash spacing (time between flashes in ms, constrained 100 - 10000); val3: optional pause after turning on pmt before transmitting values (in ms constrained 1 - 10000); val4: luminescence measurement time (time in s, constrained 1 - 1000);

Table continues on next page

Table 7.2: (continued)

Function	Command
	val5: averaging timespan, the timespan for averaging box defines the resolution at fast timescales (time in ms, constrained 50 - 1000); val6: Voltage on PMT tube, defines sensitivity of PMT (number, constrained 0 - 185). Machine switches and turns on PMT in about 300 ms.
setholdat	'Hval1'
	Set temperature control to hold at temperature val1 (temperature in K, constrained 1-400); Instrument will heat and cool, use with caution as instrument can rapidly overheat when trying to cool without connection to cold reservoir.
setholdbelow	'Bval1'
	Set temperature control to hold at temperature val1 (temperature in K, constrained 1-400); Instrument will only cool, use with caution as instrument can rapidly overheat when trying to cool without connection to cold reservoir.
setholdabove	'Aval1'
	Set temperature control to hold at temperature val1 (temperature in K, constrained 1-400); Instrument will only heat, this is the safest option to use. Cooling in this mode can be achieved by using liquid nitrogen or other coolant.
setgradientt	'Gval1,val2,val3'

Table continues on next page

Table 7.2: (continued)

Function	Command
	Set a temperature ramp. val1: starting temperature (temperature in K, constrained 1-400); val2: end temperature (temperature in K, constrained 1-400); val3: time of gradient (time in s, constrained 1 - 1000).
setnotempcontrol	'S'
	Removes any temperature control previously set.
setPMT	'Pval1,val2,val3'
	Sets power to the PMT. val1: 0 turns of PMT power, 1 turns on PMT slowly, 2 turns on PMT immediately; val2: sets voltage level (gain) of PMT (number constrained 0 - 185); val3: time the PMT voltage is turned on (time in s, constrained 0 - 1000).
settransmitmode	'Vval1,val2'
	Switches into transmitting mode. As soon as this command is sent, machine will send sensor data in specified intervals until specified endtime. val1: total transmitting time (time in s, constrained 1-1000); val2:averaging timespan, the timespan for averaging box. Longer averaging means less noise but lower resolution. Typically 200 ms is used (time in ms, constrained 50 - 1000).

7.4.2 Matlab coding

Although in principle no GUI is necessary, as the device could be used either manually, or with a simple batch file, it is considerably more user friendly to have a graphical user interface. This was programmed in Matlab and will be briefly described here.

Figure 7.11 shows the main window of the TL software. In the connection box (A)

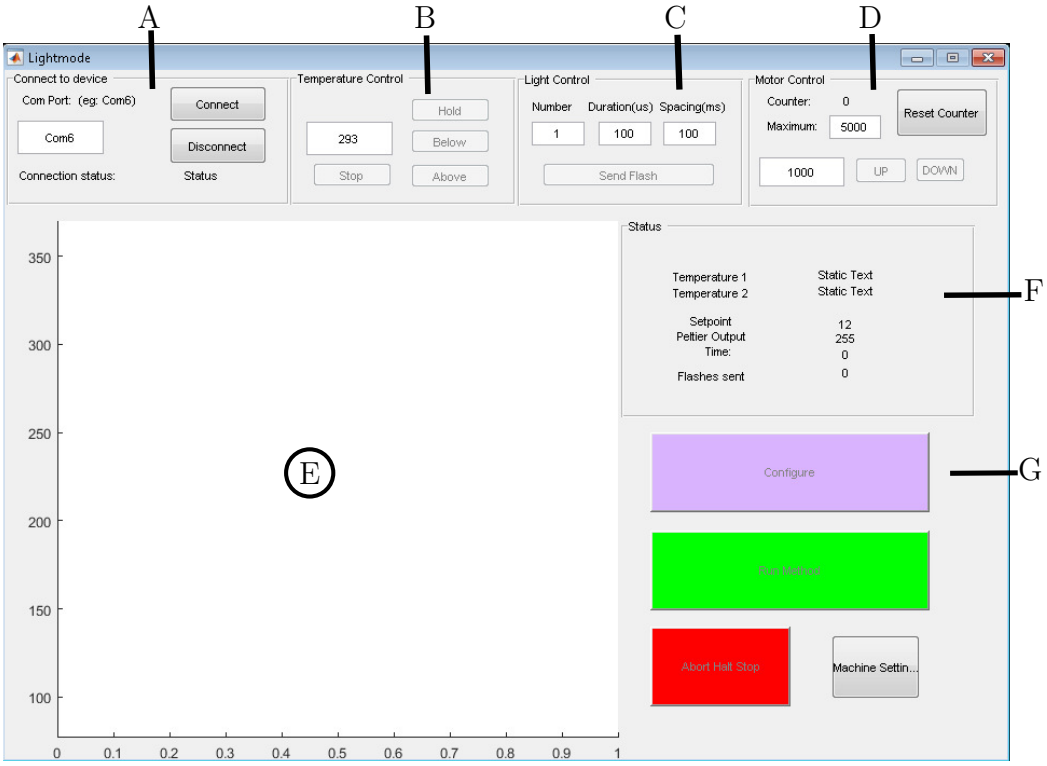

Figure 7.11: Screenshot of software main window. A: Connection box; B:Temperature control box; C:Light control box; D: Stepper motor control box; E: Monitoring window; F: Machine status report box; G: Start, Configure, Stop, and machine settings buttons.

the com port of the Tl machine can be specified and the connection to the machine established and cut. The temperature control box (B) allows to set the different temperature control modes. The temperature is entered in K. The light control box (C) is used to trigger the laser. The flash length parameter stems from the LED illumination setup and is currently not used. The Stepper motor control box (D) tracks the position of the moveable stage. As the machine does not know in which position the stage is when turned on, both the zero position and the maximum can be adjusted. When the counter reaches the specified maximum value, no further steps will be sent to the machine. To go further, the maximum needs to be adjusted or the counter reset. If steps beyond the zero position (negative steps counter) are sent, a warning message will be shown prior to executing the command. Whilst physical endstops prevent the stage from moving to far upward or downward, care should be taken when overriding the counter. Only when the counter is at zero can a thermoluminescence program be started. While the stepper motor is moving, the software is not responsive and the user should refrain from pushing any buttons until the temperature reading started.

The central graph (E) shows the temperature progression over time of both thermocouples, as well as the set point of the temperature control. The status display box (F) shows the measured the temperatures measured by both thermocouples, the temperature setpoint, the current Peltier output, the machine time, and the total amount of flashes sent to the machine since the software was started. Both E and F are updated every 500 ms. In the bottom right of the main window (G) are the “Configure”, “Run”, “Stop”, and “machine-settings” buttons. The “machine settings” button allows to alter the PID tuning of the Peltier-element. The big red stop button has no function and does nothing.

The purple “Configure” button opens the experiment configuration window (Figure 7.12). Here the specifics of a given experiment are defined. Every TL experiment constitutes two main phases. In the first phase the sample is dark adapted for a given amount of time and then illuminated. In the second phase the temperature is increased at a certain rate over time and the TL signal is recorded. This scheme

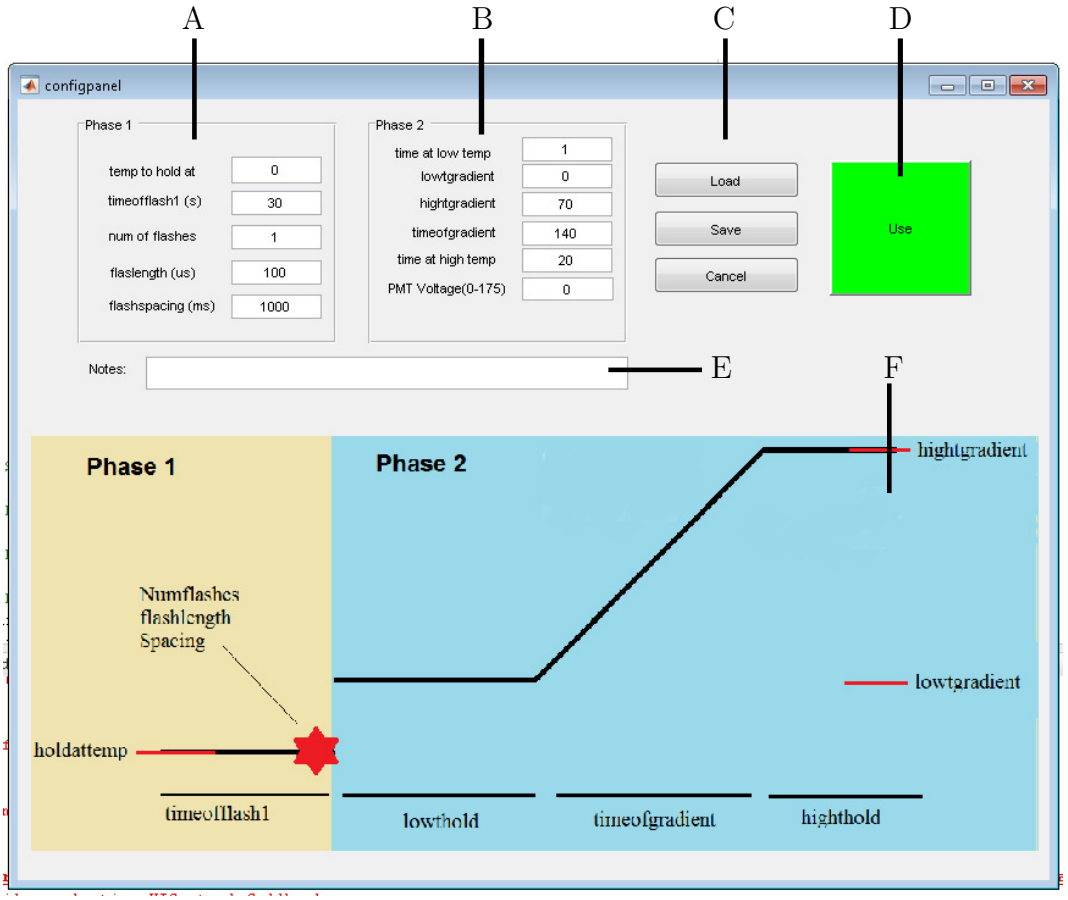

Figure 7.12: Experiment configuration window.

and the names of the parameters that can be set is depicted in the figure at the bottom of the experiment configuration window (F). In practice phase 1 (A) of this scheme is not used, as it is easier and more flexible to use the main control window for this phase of the experiment. To skip phase 1 it is sufficient to set the time of the first flash to zero. Phase 2 (B) is defined by setting the following six parameters: time at low temp: Time spent holding (heating and cooling) at low temperature. Typically this is set to one second; lowtgradient and hightgradient are the lower and upper boundaries of the temperature gradient. The "time of gradient" should be set, so that the desired heating rate (typically 0.5 Ks^{-1} or 0.33 Ks^{-1} is obtained. "Time at high temp" defines how long the experiment continues after the end of the gradient is reached. This typically is also set to one second. The PMT voltage is typically set to the maximum which is 185. Experiment parameters can be loaded from a predefined set or saved as templates (C). Pushing the "cancel" button lets the user return to the main window without configuring an experiment. When phase 1 is not used, the experiment data file of a successful experiment will not contain information about the sample treatment prior to the phase 2. It is therefore advised to enter any relevant information about the experiment in the notes field (E), which will be saved to the experiment file.

Pressing the use button closes the configuration window and opens a "save as" prompt. Here the name of the experiment and save folder need to be defined. If an already existing name is chosen, the user will be warned that this data will be overwritten and a cancel option is provided. Once the experiment is defined, the green "run" button in the main window becomes click-able which will start the defined experiment. After the experiment is finished, the configure window needs to be opened again before a new experiment can be run.

7.5 Stepwise Manual for TL Experiment

1. Turn on Computer, Laser, TL device x 2.

2. Start software, it takes a while. Blame Matlab.

3. Connect USB cable to computer.

4. Enter correct COM port (currently Com10).

5. Press “Connect” and wait for temperature reading to appear.

6. Check if both thermocouples are working fine, check if Peltier element can heat by setting a “hold” or “above” briefly above current temperature. Press “Stop” to stop temperature control.

7. Set correct PID tuning for experiment by clicking on “Machine settings” and entering 20,2,35.

8. Start laser, fire a few flashes (at least one!), see if they arrive. Cover the MiniDye with a cloth (most light pollution comes from here).

9. Drive nitrogen stage down and fill dewar with liquid nitrogen.

10. Configure experiment by clicking on ‘”Configure”, leave out Phase 1 by setting timeofflash1 to zero. Specify experiment details in the notes field. Set PMT voltage to 185 for maximum sensitivity. You can save the experiment as a template for future use by clicking “Save”, or load a previous one by clicking “Load”. Press “Use” and specify save folder and experiment name.

11. Load sample onto sample plate and put holder in machine.

12. Put dewar with liquid nitrogen on stage and move upwards until its close to heat exchanger. Reset counter.

13. Close door, set temperature to 298 K, click “above” and let sample dark adapt for a few minutes.

14. Start cooling by moving nitrogen up by about 3000 steps. Set “above” 278 K.

15. Type desired lowest temperature in temperature field (saves time after flashes).

16. When temperature arrives at 278 K send desired flashes, then click above to cool down further. If necessary move nitrogen up by a small distance (max. 1000 steps increments). Close Iris at exit port of laser to reduce background, when looking for very small signals.

17. When lower temperature value (bottom thermocouple) is 10 K below desired low temperature move motor control back to 0 to remove the liquid nitrogen.

18. When temperature reading arrives at desired low temperature press “Run method”.

19. Wait till method is finished. To abort close window.

20. Find initial analysis and data in folder specified when configuring the experiment.

21. Rinse and repeat. Wash sample plate at least three times with water and ethanol. Every few experiments, clean with 1% helma clean solution. Clean acrylic window with soft tissue with ethanol to prevent scratching.

22. Press disconnect before turning everything off and disconnect USB cable.

8 Appendix: Separate Publications

During the course of this PhD, further work was done that is not covered directly in this thesis. This work was excluded from the thesis because it was outside the topic or the scope of this thesis. Nevertheless this work contributed to two publications that are appended here for the readers reference.

The first paper is an opinion paper published in "Frontiers in Bioengineering and Biotechnology" which resulted out of a discussion group on the usefulness of biofuels. Contributions were made to the discussions as well as to drafting and editing of the manuscript. Reproduction of this article is covered under the creative commons licence.

The second paper was published in PNAS and deals with the effect of bicarbonate on the redox potential of Q_A. Here contributions were made by measuring and analysing the kinetics of Q_A reoxidation under a range of conditions using BBY's from spinach. Furthermore the antenna connectivity in this system was determined. Reproduction of this article here is allowed by the NAS licensing agreement.

frontiers in
BIOENGINEERING AND BIOTECHNOLOGY

OPINION ARTICLE
published: 18 March 2015
doi: 10.3389/fbioe.2015.00036

Photosynthetic constraints on fuel from microbes

Charles A. R. Cotton, Jeffrey S. Douglass, Sven De Causmaecker, Katharina Brinkert, Tanai Cardona, Andrea Fantuzzi, A. William Rutherford* and James W. Murray

Department of Life Sciences, Imperial College London, London, UK
**Correspondence: a.rutherford@imperial.ac.uk*

Edited by:
M. Kalim Akhtar, University of Edinburgh, UK

Reviewed by:
Shota Atsumi, University of California Davis, USA
Conrad Mullineaux, Queen Mary University of London, UK

Keywords: photosynthesis, photosynthetic efficiency, biofuel, algal biofuel, EROI, light harvesting, rubisco, chlorophyll

THE WORLD ENERGY PROBLEM AND THE BIOFUEL ENERGY PROBLEM

Oxygenic photosynthesis has been promoted as a system for fuel production on a global scale to replace fossil fuels. The fundamental requirement for this to be viable is that the energy output of the system must be greater than the energy input from fossil fuels. For biofuel production, this criterion is not always met. This issue is often dodged because life-cycle analyses are complex (and thus disputed) and future technological innovations can always be invoked. The second requirement is a sufficiently high rate of solar energy conversion to make the process feasible in terms of the time and space needed to produce fuel on a relevant scale. Both requirements are closely linked to the photosynthetic efficiency; i.e., the conversion efficiency of solar energy to organic material (sugar, biomass, hydrocarbons, etc.). Here, we discuss limitations on photosynthetic efficiency and approaches suggested to overcome them. We focus on biofuels produced by photosynthetic microbes as they are often considered the fuels of the future for their year-round cultivation, non-competition with food crops, higher reported photosynthetic yields, and the potential for genetic engineering to produce fuels directly (Brennan and Owende, 2010).

The energy investment required for biomass production (e.g., water, nutrients, fertilizers, stirring, bubbling, containment, harvesting, processing) cancels out some or all of the energy gained from sunlight (Slade and Bauen, 2013). This is described by the energy returned as a proportion of energy invested (EROI), and this factor is the key measure of energy sustainability in life-cycle analysis (Murphy and Hall, 2010). If the EROI is >1, the system produces a fuel with net solar energy content; if <1 it does not: it wastes fossil fuel (Hall et al., 2014). The energy investment in bioreactors, required to achieve the highest photosynthetic conversion efficiencies (Cuaresma et al., 2009), cancels out all of the gain in energy returned and reduces the EROI below 1 (Resurreccion et al., 2012). While EROI values are better for low-input open pond systems, they still lie between 0.4 and −1.1 in multiple life-cycle analyses (Zaimes and Khanna, 2013; also Resurreccion et al., 2012) [c.f. ~20 for oil and ~84 for hydroelectric (Hall et al., 2014)]. Furthermore, the energy required for processing biomass into liquid biofuel decreases the EROI.

Instead of producing biomass, photosynthetic microbes that continuously excrete biofuel or biofuel precursors have been genetically engineered (Nozzi et al., 2013). If the product can be easily isolated, and if the microbe diverts energy captured from the sun away from growth and into the product, this would have advantages over conventional approaches. Given the relative novelty and commercial interest in such approaches, independent life-cycle analyses are not yet available (Moheimani and McHenry, 2013); however, the intrinsic limitations of photosynthesis will still apply. The production of volatile fuels, the use of genetically modified strains, and the prevention of contamination would all seem to call for the use of closed photobioreactors, thus incurring a serious energy cost (Resurreccion et al., 2012; Slade and Bauen, 2013).

Scaling-up of the process in order to produce enough fuel to replace fossil fuels is a major problem, as energetic and material costs are not always linear. Serious challenges for scalability include water usage, nitrogen and phosphorus recovery, and a range of environmental and ecological issues (Clarens et al., 2010; Chisti, 2013; Benson et al., 2014). However, meeting both energy prerequisites (an EROI significantly >1 and a high rate of solar energy conversion) on a pilot scale seems advisable before scaling-up is considered.

The energetic prerequisites rely fundamentally on the efficiency of photosynthesis. Calculations for theoretical photosynthetic efficiency agree on a maximum value for solar energy to carbon–carbon bonds in glucose of around 13%, falling to around 5% of solar energy to biomass for C3 plants, considering photorespiratory and respiratory losses (Zhu et al., 2010). The highest efficiency reported for photosynthetic microbes under controlled lab conditions is 3% for light-to-biomass [Melis, 2009; also Cuaresma et al. (2009)]. Under growth conditions more relevant to industrial settings, the efficiency is stated to be significantly lower than this (Melis, 2009). Efforts are thus being made to find ways of improving photosynthesis itself.

ENGINEERING TO IMPROVE LIGHT COLLECTION

The first stage of photosynthesis is light-capture by pigments in the antenna complexes which deliver excitation energy to the chlorophylls of photochemical reaction centers (Croce and van Amerongen, 2014). Antenna pigments greatly outnumber the reaction center chlorophylls so that the reaction centers can obtain excitations from light over a much bigger surface area. Complex regulatory mechanisms, which

convert excess energy into heat when reaction centers become saturated, are activated at surprisingly low photon fluxes, resulting in the majority of absorbed photons being wasted.

In principle, reducing the antenna size should alleviate this problem by reducing saturation and the related shading problem (Nakajima and Ueda, 1997). In practice, some antennae mutants do show moderate improvement in photosynthetic growth [e.g., Mussgnug et al. (2007) and Kirst et al. (2014)]. This has only been demonstrated under a narrow range of growth conditions (high light, high cell density, low CO_2 concentration), and lower productivity is reported under other conditions [e.g., Page et al. (2012), Kirst et al. (2014), and Lea-Smith et al. (2014)].

Antennae truncation can improve photosynthetic yields under specific, controlled conditions. The improvement gained should be considered as moving, slightly, toward the 13% limit rather than extending that limit. The requirement for special growth conditions likely cancels these gains.

ENGINEERING TO IMPROVE PHOTOCHEMISTRY

Photosynthetic pigments absorb from 400 to 700 nm, less than half of the solar spectrum. Longer-wavelength pigments could be used to extend this range (Blankenship et al., 2011). Extending absorption out to 750 nm would result in an increase in the number of available photons by 19% (Chen and Blankenship, 2011) and, in principle, could allow a small increase in the theoretical 13% limit.

Organisms containing longer-wavelength chlorophylls *d* and *f* naturally occur (Chen et al., 2010; Gan et al., 2014). While chlorophyll *d* is involved in primary charge separation in both photosystem I and photosystem II (PSII) in *Acaryochloris marina* (Renger and Schlodder, 2008), it is not yet known if chlorophyll *f* plays a role in reaction center photochemistry. The energy of the 710 nm photon absorbed by chlorophyll *d* is 70 meV, less than that in the 680 nm photon (1.82 eV) absorbed by chlorophyll *a*. Given the stringent energy requirements for water oxidation, this is expected to result in an increase in the probability of back-reactions leading to singlet oxygen-induced damage (Rutherford et al., 2012). While this does not impact on the efficiency of growth under optimized conditions (Mielke et al., 2011), it may make PSII more susceptible to photodamage under variable light conditions. A 750 nm pigment in PSII would decrease the energy available by 170 meV with an even greater risk of back-reaction-mediated oxidative damage and associated metabolic costs. When photosynthesis using far-red pigments occurs in nature, it does so in restricted environments (Chen et al., 2010; Gan et al., 2014). In applications aimed at fuel production, more of the spectrum may be accessed but it would likely require tightly controlled growth conditions and thus cost energy.

ENGINEERING TO IMPROVE CARBON FIXATION

Ribulose 1,5-bisphosphate carboxylase/oxygenase (Rubisco) is the enzyme responsible for carbon fixation in the Calvin cycle. This enzyme is slow and inefficient (Savir et al., 2010). While there is a variety of different Rubiscos in nature (Tabita et al., 2008), there is a suggested trade-off between CO_2 affinity and carboxylation velocity, limited by structural or biochemical characteristics of the enzyme (Tcherkez et al., 2006; Savir et al., 2010). Recently, directed evolution of a cyanobacterial Rubisco produced a mutant with 2.9-fold improvement in activity with only a 9% loss in CO_2/O_2 specificity. *Synechocystis* sp. PCC 6803 (henceforth *Synechocystis*) expressing the improved Rubisco did not show growth improvements, instead producing 25% less Rubisco (Durão et al., 2015). This is consistent with the finding that altering Rubisco activity has little effect on the rate of photosynthesis in *Synechocystis* (Marcus et al., 2011). Results under conditions of high CO_2 are different (Atsumi et al., 2009).

Photorespiration is the set of biochemical pathways which starts with Rubisco oxygenation activity and recycles the product 2-phosphoglycolate. Photorespiration is considered an energetic cost. While reducing photorespiratory losses can yield large growth improvement in plants (Kebeish et al., 2007), current efforts to improve recovery of photorespiratory metabolites in cyanobacteria show no change in growth (Shih et al., 2014). This may be due to carbon-concentrating mechanisms in cyanobacteria which protect against high levels of O_2 around Rubisco, reducing photorespiration (Dou et al., 2008; Mangan and Brenner, 2014). Furthermore, the by-products of photorespiration are managed by three different pathways in *Synechocystis* (c.f. one in plants) (Eisenhut et al., 2008; Peterhansel and Maurino, 2011; Young et al., 2011).

Avoiding Rubisco using alternative aerobic carbon fixation cycles, such as the 3-hydroxypropionate bi-cycle (Zarzycki et al., 2009), or even newly designed pathways (Bar-Even et al., 2010; Erb, 2011), is being attempted to improve carbon fixation.

There is clearly scope for improvement in carbon fixation. Most approaches work within the 13% efficiency limit; however, alternative carbon fixation pathways may require less ATP, potentially extending this limit. Unlike in plants, it is hard to imagine a more effective carbon-concentrating and photorespiratory metabolism than that already found in cyanobacteria.

ENGINEERING TO INFLUENCE DOWNSTREAM METABOLIC PATHWAYS

Incorporating biofuel producing pathways into microbial photosynthesizers can be relatively straightforward. Alkanes are made naturally (Han et al., 1968) and strains producing detectable levels of ethanol (Dexter and Fu, 2009), acetone (Zhou et al., 2012), ethylene (Guerrero et al., 2012), isoprene (Lindberg et al., 2010) and 2,3-butanediol (Oliver et al., 2013) among others have been generated (Rosgaard et al., 2012; Nozzi et al., 2013).

In contrast, metabolic engineering to increase product yield is difficult, product-specific, and hard to rationalize when models of central metabolism are still being adjusted (Knoop et al., 2013). It is clear that some progress can be made; for example, isoprene producing strains have recently been improved 2.5-fold by co-expression of the mevalonic acid pathway (Bentley et al., 2014). Even so, standard metabolic engineering approaches such as removing storage pathways require careful attention in photosynthetic organisms (Van der Woude et al., 2014).

ENGINEERING SO IT WORKS: A HOLISTIC APPROACH TO A COMPLEX SYSTEM

Most efforts directed at improving photosynthetic efficiency focus on the individual components described in previous sections. In contrast, perhaps the most striking improvement on "natural" photosynthesis came from the optimization of source (light energy) versus sink (metabolic capacity). This takes into account the fact that the kinetics of both the light and dark reactions are inherently linked (Paul and Foyer, 2001).

The advantage of source/sink optimization was illustrated by the heterologous expression of the proton/sucrose symporter CscB in *Synechococcus elongatus*. Up to 36.1 mg l^{-1} h^{-1} of sucrose was exported, a record for direct photobiological production (Ducat et al., 2012). These strains also

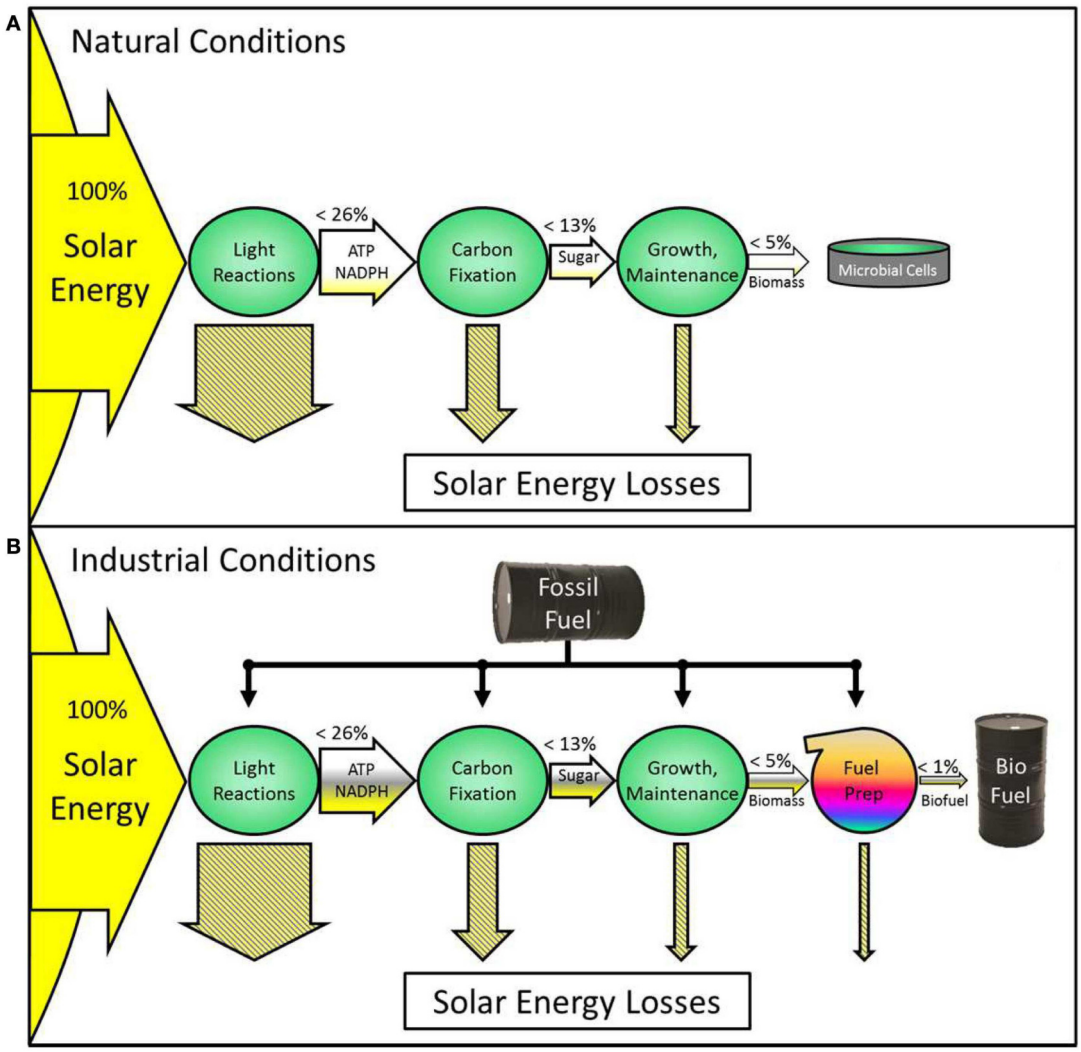

FIGURE 1 | This diagram illustrates energy flow through a photosynthetic system without fossil fuel energy input (A) and another using fossil fuels (B). Horizontal arrows represent the flow of energy through the system, with labels on the arrows showing the type of stored energy at each stage. Theoretical maximum percentages of solar energy retention are written above the arrows for each stage, with yellow fill indicating that achievable levels are lower. Hatched arrows represent solar energy losses. Green circles represent cellular processes. Energy losses in the light reactions include: (1) photons outside the chlorophyll absorbance range, (2) the energy in absorbed photons in excess of that corresponding to the first excited state of the reaction center, and (3) antennae saturation and shading effects; those incurred in the dark reactions include: (1) mismatched substrate stoichiometries (e.g., NADPH, ATP), (2) Rubisco oxygenation reactions, and (3) thermodynamic losses; those in growth include: (1) protein turnover and (2) respiratory losses. **(A)** Biomass grows naturally with no fossil fuel input. The percentage of solar energy converted into the final product is very low (small yellow gradient). **(B)** Fossil fuel is used to control conditions such as temperature, light, CO_2, sterility, mixing, and other factors. This system produces biofuel. The yield (arrow fill) is higher at each stage, partly due to an increased percentage of solar energy which is retained (yellow fill) and partly due to the energy from fossil fuel (gray fill). Synergistic interactions between engineered strains and controlled environments could increase the fossil-fuel-generated improvements to photosynthetic efficiency and the maximum energy retained. Such systems are only beneficial if the increase in yield is greater than the fossil fuel input. Currently, this condition is rarely met and generally ignored. Using energy from renewable sources such as hydro, photovoltaic, or wind instead of fossil fuels could make a similar conversion system sustainable.

showed increases in PSII activity, carbon fixation, and chlorophyll content under optimized conditions. The export of the photosynthetic sink (sucrose) is critical, suppressing photodamage by helping to maintain an oxidized electron transport chain. In addition, the sucrose biosynthetic pathway is endogenous to *S. elongatus* and does not place heavy demands on either ATP or NADPH.

The high-energy photoexcited states and highly reactive redox intermediates of the light reactions are heavily reliant on regulatory and protective mechanisms to prevent oxidative damage. Mismatches in the source/sink balance could, for example, result in the dark reactions being outrun by the light reactions causing photoinhibition. Specific changes to improve the light or dark reactions independently may be counterproductive if the balance of source to sink is perturbed. Sink-enhanced strains may be the material of choice for future attempts to improve specific aspects of photosynthesis (antenna, pigment optimization, electron transfer efficiency, CO_2 fixation, and down-stream metabolism).

CONCLUSION

At present, photosynthetic microbial biofuels are not viable in energy terms. This is related to intrinsic inefficiencies in photosynthesis, and thus research has been directed to improving photosynthesis. A brief survey indicates that most suggested modifications would be beneficial only under restricted culture conditions. Controlled growth in bioreactors may then be required but this will incur a significant energy cost, which at present is much bigger than the engineered efficiency gain (see **Figure 1**). Nevertheless, attempts to improve photosynthesis have not been wholly negative and it is suggested that "sink-maximized" strains should be used for engineering of targeted improvements in order to avoid metabolic congestion and mismatches at the interface between the dark and light reactions.

Given the energetic problems with "algal" biofuels, it may be better to use the technology to produce complex, high-value chemicals (including specialized aviation fuels or their precursors) rather than low-value products such as biomass and ethanol. This, however, becomes a manufacturing process rather than a means of capturing solar energy. The production of fuels made in this way might be economically or strategically viable, but with fossil fuels as the main energy input, this would clearly not be relevant to fossil fuel replacement. These processes could become a sustainable energy conversion and storage technology if alternative energy sources such as hydroelectric, wind, solar, geothermal were used to drive them.

ACKNOWLEDGMENTS

TC is supported by an Imperial College London Junior Research Fellowship. CC is supported by a BBSRC Scholarship. AR is supported by a Wolfson Merit Award from the Royal Society and BBSRC Grant number: BB/K002627/1. SDC is supported by an Imperial College Ph.D. Scholarship Scheme.

REFERENCES

Atsumi, S., Higashide, W., and Liao, J. C. (2009). Direct photosynthetic recycling of carbon dioxide to isobutyraldehyde. *Nat. Biotechnol.* 27, 1177–1180. doi:10.1038/nbt.1586

Bar-Even, A., Noor, E., Lewis, N. E., and Milo, R. (2010). Design and analysis of synthetic carbon fixation pathways. *Proc. Natl. Acad. Sci. U.S.A.* 107, 8889–8894. doi:10.1073/pnas.0907176107

Benson, D., Kerry, K., and Malin, G. (2014). Algal biofuels: impact significance and implications for EU multi-level governance. *J. Clean. Prod.* 72, 4–13. doi:10.1016/j.jclepro.2014.02.060

Bentley, F. K., Zurbriggen, A., and Melis, A. (2014). Heterologous expression of the mevalonic acid pathway in cyanobacteria enhances endogenous carbon partitioning to isoprene. *Mol. Plant.* 7, 71–86. doi:10.1093/mp/sst134

Blankenship, R. E., Tiede, D. M., Barber, J., Brudvig, G. W., Fleming, G., Ghirardi, M., et al. (2011). Comparing photosynthetic and photovoltaic efficiencies and recognizing the potential for improvement. *Science* 332, 805–809. doi:10.1126/science.1200165

Brennan, L., and Owende, P. (2010). Biofuels from microalgae-A review of technologies for production, processing, and extractions of biofuels and co-products. *Renew. Sustain. Energ. Rev.* 14, 557–577. doi:10.1016/j.rser.2009.10.009

Chen, M., and Blankenship, R. E. (2011). Expanding the solar spectrum used by photosynthesis. *Trends Plant Sci.* 16, 427–431. doi:10.1016/j.tplants.2011.03.011

Chen, M., Schliep, M., Willows, R. D., Cai, Z.-L., Neilan, B. A., and Scheer, H. (2010). A red-shifted chlorophyll. *Science* 329, 1318–1319. doi:10.1126/science.1191127

Chisti, Y. (2013). Constraints to commercialization of algal fuels. *J. Biotechnol.* 167, 201–214. doi:10.1016/j.jbiotec.2013.07.020

Clarens, A. F., Resurreccion, E. P., White, M. A., and Colosi, L. M. (2010). Environmental life cycle comparison of algae to other bioenergy feedstocks. *Environ. Sci. Technol.* 44, 1813–1819. doi:10.1021/es902838n

Croce, R., and van Amerongen, H. (2014). Natural strategies for photosynthetic light harvesting. *Nat. Chem. Biol.* 10, 492–501. doi:10.1038/nchembio.1555

Cuaresma, M., Janssen, M., Vílchez, C., and Wijffels, R. H. (2009). Productivity of *Chlorella sorokiniana* in a short light-path (SLP) panel photobioreactor under high irradiance. *Biotechnol. Bioeng.* 104, 352–359. doi:10.1002/bit.22394

Dexter, J., and Fu, P. (2009). Metabolic engineering of cyanobacteria for ethanol production. *Energy Environ. Sci.* 2, 857–864. doi:10.1039/b811937f

Dou, Z., Heinhorst, S., Williams, E. B., Murin, C. D., Shively, J. M., and Cannon, G. C. (2008). CO_2 fixation kinetics of *Halothiobacillus neapolitanus* mutant carboxysomes lacking carbonic anhydrase suggest the shell acts as a diffusional barrier for CO_2. *J. Biol. Chem.* 283, 10377–10384. doi:10.1074/jbc.M709285200

Ducat, D. C., Avelar-Rivas, J. A., Way, J. C., and Silver, P. A. (2012). Rerouting carbon flux to enhance photosynthetic productivity. *Appl. Environ. Microbiol.* 78, 2660–2668. doi:10.1128/AEM.07901-11

Durão, P., Aigner, H., Nagy, P., Mueller-Cajar, O., Hartl, F. U., and Hayer-Hartl, M. (2015). Opposing effects of folding and assembly chaperones on evolvability of Rubisco. *Nat. Chem. Biol.* 11, 148–155. doi:10.1038/nchembio.1715

Eisenhut, M., Ruth, W., Haimovich, M., Bauwe, H., Kaplan, A., and Hagemann, M. (2008). The photorespiratory glycolate metabolism is essential for cyanobacteria and might have been conveyed endosymbiontically to plants. *Proc. Natl. Acad. Sci. U.S.A.* 105, 17199–17204. doi:10.1073/pnas.0807043105

Erb, T. J. (2011). Carboxylases in natural and synthetic microbial pathways. *Appl. Environ. Microbiol.* 77, 8466–8477. doi:10.1128/AEM.05702-11

Gan, F., Zhang, S., Rockwell, N. C., Martin, S. S., Lagarias, J. C., and Bryant, D. A. (2014). Extensive remodeling of a cyanobacterial photosynthetic apparatus in far-red light. *Science* 345, 1312–1317. doi:10.1126/science.1256963

Guerrero, F., Carbonell, V., Cossu, M., Correddu, D., and Jones, P. R. (2012). Ethylene synthesis and regulated expression of recombinant protein in *Synechocystis* sp. PCC 6803. *PLoS ONE* 7:e50470. doi:10.1371/journal.pone.0050470

Hall, C. A. S., Lambert, J. G., and Balogh, S. B. (2014). EROI of different fuels and the implications for society. *Energy Policy* 64, 141–152. doi:10.1016/j.enpol.2013.05.049

Han, J., McCarthy, E. D., Hoeven, W. V., Calvin, M., and Bradley, W. H. (1968). Organic geochemical studies, II. A preliminary report on the distribution of aliphatic hydrocarbons in algae, in bacteria, and in a recent lake sediment. *Proc. Natl. Acad. Sci. U.S.A.* 59, 26–33. doi:10.1097/00006534-198004000-00042

Kebeish, R., Niessen, M., Thiruveedhi, K., Bari, R., Hirsch, H.-J., Rosenkranz, R., et al. (2007). Chloroplastic photorespiratory bypass increases photosynthesis and biomass production in *Arabidopsis thaliana*. *Nat. Biotechnol.* 25, 593–599. doi:10.1038/nbt1299

Kirst, H., Formighieri, C., and Melis, A. (2014). Maximizing photosynthetic efficiency and culture productivity in cyanobacteria upon minimizing

the phycobilisome light-harvesting antenna size. *Biochim. Biophys. Acta* 1837, 1653–1664. doi:10.1016/j.bbabio.2014.07.009

Knoop, H., Gründel, M., Zilliges, Y., Lehmann, R., Hoffmann, S., Lockau, W., et al. (2013). Flux balance analysis of cyanobacterial metabolism: the metabolic network of *Synechocystis* sp. PCC 6803. *PLoS Comput. Biol.* 9:e1003081. doi:10.1371/journal.pcbi.1003081

Lea-Smith, D. J., Bombelli, P., Dennis, J. S., Scott, S. A., Smith, A. G., and Howe, C. J. (2014). Phycobilisome-deficient strains of *Synechocystis* sp. PCC 6803 have reduced size and require carbon-limiting conditions to exhibit enhanced productivity. *Plant Physiol.* 165, 705–714. doi:10.1104/pp.114.237206

Lindberg, P., Park, S., and Melis, A. (2010). Engineering a platform for photosynthetic isoprene production in cyanobacteria, using *Synechocystis* as the model organism. *Metab. Eng.* 12, 70–79. doi:10.1016/j.ymben.2009.10.001

Mangan, N., and Brenner, M. (2014). Systems analysis of the CO_2 concentrating mechanism in cyanobacteria. *eLife* 3:e02043. doi:10.7554/eLife.02043

Marcus, Y., Altman-Gueta, H., Wolff, Y., and Gurevitz, M. (2011). Rubisco mutagenesis provides new insight into limitations on photosynthesis and growth in *Synechocystis* PCC6803. *J. Exp. Bot.* 62, 4173–4182. doi:10.1093/jxb/err116

Melis, A. (2009). Solar energy conversion efficiencies in photosynthesis: minimizing the chlorophyll antennae to maximize efficiency. *Plant Sci.* 177, 272–280. doi:10.1016/j.plantsci.2009.06.005

Mielke, S. P., Kiang, N. Y., Blankenship, R. E., Gunner, M. R., and Mauzerall, D. (2011). Efficiency of photosynthesis in a Chl *d*-utilizing cyanobacterium is comparable to or higher than that in Chl *a*-utilizing oxygenic species. *Biochim. Biophys. Acta* 1807, 1231–1236. doi:10.1016/j.bbabio.2011.06.007

Moheimani, N. R., and McHenry, M. P. (2013). Developments of five selected microalgae companies developing "closed" bioreactor biofuel production systems. *Int. J. Innov. Sustain. Dev.* 7, 367–386. doi:10.1504/IJISD.2013.057045

Murphy, D. J., and Hall, C. A. S. (2010). Year in review-EROI or energy return on (energy) invested. *Ann. N. Y. Acad. Sci.* 1185, 102–118. doi:10.1111/j.1749-6632.2009.05282.x

Mussgnug, J. H., Thomas-Hall, S., Rupprecht, J., Foo, A., Klassen, V., McDowall, A., et al. (2007). Engineering photosynthetic light capture: impacts on improved solar energy to biomass conversion. *Plant Biotechnol. J.* 5, 802–814. doi:10.1111/j.1467-7652.2007.00285.x

Nakajima, Y., and Ueda, R. (1997). Improvement of photosynthesis in dense microalgal suspension by reduction of light harvesting pigments. *J. Appl. Phycol.* 9, 503–510. doi:10.1023/A:1007920025419

Nozzi, N. E., Oliver, J. W. K., and Atsumi, S. (2013). Cyanobacteria as a platform for biofuel production. *Front. Bioeng. Biotechnol.* 1:7. doi:10.3389/fbioe.2013.00007

Oliver, J. W. K., Machado, I. M. P., Yoneda, H., and Atsumi, S. (2013). Cyanobacterial conversion of carbon dioxide to 2,3-butanediol. *Proc. Natl. Acad. Sci. U.S.A.* 110, 1249–1254. doi:10.1073/pnas.1213024110

Page, L. E., Liberton, M., and Pakrasi, H. B. (2012). Reduction of photoautotrophic productivity in the cyanobacterium *Synechocystis* sp. strain PCC 6803 by phycobilisome antenna truncation. *Appl. Environ. Microbiol.* 78, 6349–6351. doi:10.1128/AEM.00499-12

Paul, M. J., and Foyer, C. H. (2001). Sink regulation of photosynthesis. *J. Exp. Bot.* 52, 1383–1400. doi:10.1093/jexbot/52.360.1383

Peterhansel, C., and Maurino, V. G. (2011). Photorespiration redesigned. *Plant Physiol.* 155, 49–55. doi:10.1104/pp.110.165019

Renger, T., and Schlodder, E. (2008). The primary electron donor of photosystem II of the cyanobacterium *Acaryochloris marina* is a chlorophyll *d* and the water oxidation is driven by a chlorophyll *a*/chlorophyll *d* heterodimer. *J. Phys. Chem. B* 112, 7351–7354. doi:10.1021/jp801900e

Resurreccion, E. P., Colosi, L. M., White, M. A., and Clarens, A. F. (2012). Comparison of algae cultivation methods for bioenergy production using a combined life cycle assessment and life cycle costing approach. *Bioresour. Technol.* 126, 298–306. doi:10.1016/j.biortech.2012.09.038

Rosgaard, L., de Porcellinis, A. J., Jacobsen, J. H., Frigaard, N.-U., and Sakuragi, Y. (2012). Bioengineering of carbon fixation, biofuels, and biochemicals in cyanobacteria and plants. *J. Biotechnol.* 162, 134–147. doi:10.1016/j.jbiotec.2012.05.006

Rutherford, A. W., Osyczka, A., and Rappaport, F. (2012). Back-reactions, short-circuits, leaks and other energy wasteful reactions in biological electron transfer: redox tuning to survive life in O_2. *FEBS Lett.* 586, 603–616. doi:10.1016/j.febslet.2011.12.039

Savir, Y., Noor, E., Milo, R., and Tlusty, T. (2010). Cross-species analysis traces adaptation of Rubisco toward optimality in a low-dimensional landscape. *Proc. Natl. Acad. Sci. U.S.A.* 107, 3475–3480. doi:10.1073/pnas.0911663107

Shih, P. M., Zarzycki, J., Niyogi, K. K., and Kerfeld, C. A. (2014). Introduction of a synthetic CO_2-fixing photorespiratory bypass into a cyanobacterium. *J. Biol. Chem.* 289, 9493–9500. doi:10.1074/jbc.C113.543132

Slade, R., and Bauen, A. (2013). Micro-algae cultivation for biofuels: cost, energy balance, environmental impacts and future prospects. *Biomass Bioenergy* 53, 29–38. doi:10.1016/j.biombioe.2012.12.019

Tabita, F. R., Hanson, T. E., Satagopan, S., Witte, B. H., and Kreel, N. E. (2008). Phylogenetic and evolutionary relationships of RubisCO and the RubisCO-like proteins and the functional lessons provided by diverse molecular forms. *Philos. Trans. R. Soc. Lond. B Biol. Sci.* 363, 2629–2640. doi:10.1098/rstb.2008.0023

Tcherkez, G. G. B., Farquhar, G. D., and Andrews, T. J. (2006). Despite slow catalysis and confused substrate specificity, all ribulose bisphosphate carboxylases may be nearly perfectly optimized. *Proc. Natl. Acad. Sci. U.S.A.* 103, 7246–7251. doi:10.1073/pnas.0600605103

Van der Woude, A. D., Angermayr, S. A., Puthan Veetil, V., Osnato, A., and Hellingwerf, K. J. (2014). Carbon sink removal: increased photosynthetic production of lactic acid by *Synechocystis* sp. PCC6803 in a glycogen storage mutant. *J. Biotechnol.* 184, 100–102. doi:10.1016/j.jbiotec.2014.04.029

Young, J. D., Shastri, A. A., Stephanopoulos, G., and Morgan, J. A. (2011). Mapping photoautotrophic metabolism with isotopically nonstationary ^{13}C flux analysis. *Metab. Eng.* 13, 656–665. doi:10.1016/j.ymben.2011.08.002

Zaimes, G. G., and Khanna, V. (2013). Environmental sustainability of emerging algal biofuels: a comparative life cycle evaluation of algal biodiesel and renewable diesel. *Environ. Prog. Sustain. Energy* 32, 926–936. doi:10.1002/ep.11810

Zarzycki, J., Brecht, V., Müller, M., and Fuchs, G. (2009). Identifying the missing steps of the autotrophic 3-hydroxypropionate CO_2 fixation cycle in *Chloroflexus aurantiacus*. *Proc. Natl. Acad. Sci. U.S.A.* 106, 21317–21322. doi:10.1073/pnas.0908356106

Zhou, J., Zhang, H., Zhang, Y., Li, Y., and Ma, Y. (2012). Designing and creating a modularized synthetic pathway in cyanobacterium *Synechocystis* enables production of acetone from carbon dioxide. *Metab. Eng.* 14, 394–400. doi:10.1016/j.ymben.2012.03.005

Zhu, X.-G., Long, S. P., and Ort, D. R. (2010). Improving photosynthetic efficiency for greater yield. *Annu. Rev. Plant Biol.* 61, 235–261. doi:10.1146/annurev-arplant-042809-112206

Conflict of Interest Statement: The authors declare that this research was conducted in the absence of any commercial or financial relationships that could be construed as a potential conflict of interest.

Received: 29 January 2015; accepted: 04 March 2015; published online: 18 March 2015.

Citation: Cotton CAR, Douglass JS, De Causmaecker S, Brinkert K, Cardona T, Fantuzzi A, Rutherford AW and Murray JW (2015) Photosynthetic constraints on fuel from microbes. Front. Bioeng. Biotechnol. ***3****:36. doi: 10.3389/fbioe.2015.00036*

This article was submitted to Synthetic Biology, a section of the journal Frontiers in Bioengineering and Biotechnology.

Bicarbonate-induced redox tuning in Photosystem II for regulation and protection

Katharina Brinkert[a], Sven De Causmaecker[a], Anja Krieger-Liszkay[b], Andrea Fantuzzi[a,1], and A. William Rutherford[a,1]

[a]Department of Life Sciences, Imperial College London, London SW7 2AZ, United Kingdom; and [b]Institute for Integrative Biology of the Cell, Commissariat à l'Énergie Atomique, CNRS, Univ Paris-Sud, Université Paris-Saclay, F-91198 Gif-sur-Yvette cedex, France

Edited by Pierre A. Joliot, Institut de Biologie Physico-Chimique, Paris, France, and approved August 30, 2016 (received for review June 1, 2016)

The midpoint potential (E_m) of $Q_A/Q_A^{-\bullet}$, the one-electron acceptor quinone of Photosystem II (PSII), provides the thermodynamic reference for calibrating PSII bioenergetics. Uncertainty exists in the literature, with two values differing by ∼80 mV. Here, we have resolved this discrepancy by using spectroelectrochemistry on plant PSII-enriched membranes. Removal of bicarbonate (HCO_3^-) shifts the E_m from ∼−145 mV to −70 mV. The higher values reported earlier are attributed to the loss of HCO_3^- during the titrations (pH 6.5, stirred under argon gassing). These findings mean that HCO_3^- binds less strongly when $Q_A^{-\bullet}$ is present. Light-induced $Q_A^{-\bullet}$ formation triggered HCO_3^- loss as manifest by the slowed electron transfer and the upshift in the E_m of Q_A. HCO_3^--depleted PSII also showed diminished light-induced $^1O_2$ formation. This finding is consistent with a model in which the increase in the E_m of $Q_A/Q_A^{-\bullet}$ promotes safe, direct $P^{+\bullet}Q_A^{-\bullet}$ charge recombination at the expense of the damaging back-reaction route that involves chlorophyll triplet-mediated $^1O_2$ formation [Johnson GN, et al. (1995) *Biochim Biophys Acta* 1229:202–207]. These findings provide a redox tuning mechanism, in which the interdependence of the redox state of Q_A and the binding by HCO_3^- regulates and protects PSII. The potential for a sink (CO_2) to source (PSII) feedback mechanism is discussed.

photoinhibition | photosynthesis | CO_2 fixation | photoassembly | water oxidation

Photosystem II (PSII), the water/plastoquinone photooxidoreductase, is at the heart of the major energy cycle that powers the biosphere. Chlorophyll-based photochemistry drives charge separation followed by electron transfer reactions that result in the reduction of quinone on one side of the thylakoid membrane (Fig. 1) and the oxidation of water on the other. The photochemistry is intrinsically a one-photon/one-electron process, but the quinone reduction and water oxidation are two- and four-electron processes, respectively. As a result, both processes involve the accumulation of intermediates that are stabilized by the protein and by coupling to protonation reactions (1–3).

The electron acceptor side of PSII contains a nonheme ferrous iron (Fe^{2+}) that is flanked by the two quinones, Q_A and Q_B (Fig. 1) (reviewed in refs. 3 and 4). The Fe^{2+} is coordinated by four histidine residues, two from D1 and two from D2, and a bicarbonate ion (HCO_3^-) that provides a bidentate ligand (3–5). The HCO_3^- is thought to play a role in the Q_B protonation pathway (reviewed in refs. 3–5). Recent EPR (6) and computation chemistry studies (7) based on the highest-resolution X-ray crystallographic model (8) implicated HCO_3^- in the second of two protonation steps that are associated with Q_B reduction. Measurements of the dissociation constant of HCO_3^- (K_d = 40–80 μM), compared with estimates of the HCO_3^- concentration in the stroma (reviewed in ref. 9), led to the assumption that HCO_3^- remains bound under physiological conditions (10). Recently, however, it was reported that the HCO_3^- bound to PSII in *Chlamydomonas* can be displaced by acetate when present in the culture medium (11).

The redox potential of Q_A has been the subject of research for decades (12). The current detailed thermodynamic picture of PSII redox chemistry is based on estimates of energy differences between the electron transfer components, but these estimates rely on measurements of redox potentials to fix absolute values (1–3). The experimental redox potential of $Q_A/Q_A^{-\bullet}$ (12) provides the key reference value (1–3).

Krieger et al. (12) collated 29 reported values for the E_m of $Q_A/Q_A^{-\bullet}$ showing significant scatter. Much of the variation in the reported E_m values could be explained by the experimental demonstration that there were two E_m values for $Q_A/Q_A^{-\bullet}$, differing by ∼150 mV, depending on the nature of the PSII (12–14). The fully active enzyme showed an E_m value that was ∼150 mV lower than that in PSII lacking the Mn_4CaO_5 cluster. This shift was, in fact, due to the binding (or absence thereof) of the Ca^{2+} ion involved in water splitting, but because the Mn cluster provides the Ca binding site, the potential is indirectly determined by the presence of Mn cluster (12–14). Given the high valence state on the Mn cluster even in the lowest redox state of the water splitting cycle (15), it is not surprising that the use of chemical mediators, the role of which is to equilibrate the external redox potential with the cofactors, can lead to the reduction and consequent loss of the Mn cluster. Because loss of the Mn leads to loss of Ca^{2+} binding, then the high potential form of the $Q_A/Q_A^{-\bullet}$ couple is easily generated during the course of redox titrations, and this technical problem explained some of the scatter in the E_m values reported in the literature (12).

In a parallel study, Johnson et al. (13) showed that the high and low potential forms of Q_A had clear physiological relevance. PSII is assembled as a functional photochemical reaction center lacking the Mn_4CaO_5 cluster and consequently, unable to split water. It then undergoes a light-driven oxidative process by which the cluster is assembled (16), so-called photoactivation. The downshift in the redox potential of $Q_A/Q_A^{-\bullet}$ occurs during photoactivation (13). A rationale was given for this process, with two competing pathways for the decay $P^{+\bullet}Q_A^{-\bullet}$ by charge

Significance

The E_m of $Q_A/Q_A^{-\bullet}$ is the reference pegging the thermodynamics of Photosystem II (PSII) to an absolute value. This work resolves a long-standing discrepancy in the literature, removing this ambiguity at the heart of PSII bioenergetics. The discrepancy in the literature reflects the loss of bicarbonate in some titrations. This surprising finding shows that bicarbonate binding controls the E_m of $Q_A/Q_A^{-\bullet}$, and thus the redox state of Q_A influences the binding of bicarbonate. This process constitutes a previously unrecognized regulation of PSII: $Q_A^{-\bullet}$ triggers bicarbonate release, slowing electron transfer and tuning the potential of Q_A to protect PSII against photodamage. This work provides an explanation for the existence of bicarbonate in PSII, a mystery for more than half a century.

Author contributions: A.F. and A.W.R. designed research; K.B., S.D.C., A.K.-L., and A.F. performed research; K.B., S.D.C., A.K.-L., A.F., and A.W.R. analyzed data; and K.B., A.F., and A.W.R. wrote the paper.

The authors declare no conflict of interest.

This article is a PNAS Direct Submission.

[1]To whom correspondence may be addressed. Email: a.fantuzzi@imperial.ac.uk or a.rutherford@imperial.ac.uk.

This article contains supporting information online at www.pnas.org/lookup/suppl/doi:10.1073/pnas.1608862113/-/DCSupplemental.

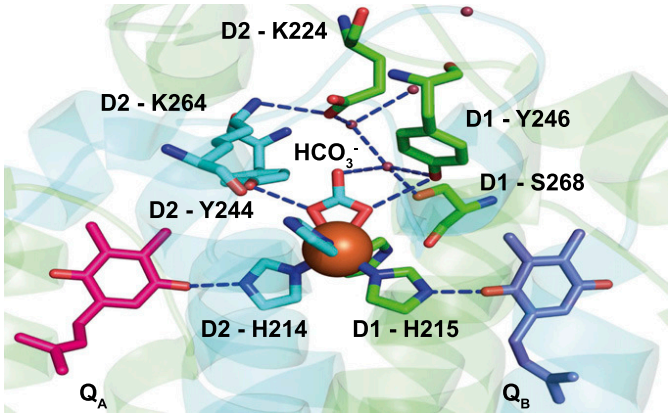

Fig. 1. Structure of PSII in the region of the quinones and the nonheme iron. The structure was made using Pymol based on Protein Data Bank ID code 3WU2 (8). It shows several relevant amino acids and the H-bond network, including several waters (red beads showing the oxygen atoms) near the HCO_3^- distal to the Fe^{2+} (rust red sphere). The upper surface of the protein is exposed to the aqueous phase on the stromal side of the membrane.

recombination (13): (*i*) a direct pathway in which $P^{+\bullet}Q_A^{-\bullet}$ recombines in a slow process involving the loss of energy to heat, and (*ii*) a back-reaction route forming $P^{+\bullet}Ph^{-\bullet}$, which recombines to form the reaction center chlorophyll triplet state, ^3P (17), in the majority of the centers. Chlorophyll triplets are relatively long-lived and very reactive with O_2 to generate $^1O_2$, a very toxic species. This concept of redox tuning controlling the competition between two main charge recombination routes in PSII (13) has dominated much of the subsequent thinking concerning photoinhibition and redox-based protective mechanisms (18–20).

Recently, Shibamoto et al. (21, 22) used an optically transparent thin-layer electrochemical cell to obtain data that confirmed the 150-mV redox difference with and without the Mn cluster, but they also showed that both values shifted to lower potentials by ∼80 mV compared with the earlier data (12). These titrations were done with a limited set of redox mediators that did not equilibrate with the Mn cluster. Subsequently, some evidence was published indicating that, when titrations were done with the same mediators, the lower potential values were obtained, whereas in the absence of mediators, the higher potential values similar to those by Krieger and coworkers (12–14) were obtained (23). However, low potential values were also recently reported without the use of mediators (24). Since then, the situation has remained unresolved, leaving a doubt about the correct potential and consequently, a serious ambiguity at the heart of PSII bioenergetics.

In this work, we have readdressed the discrepancy in the literature over the E_m of Q_A. We have used spectroelectrochemical titrations, and we have been able to reproduce the two conflicting sets of values. The key component that was not previously taken into account is the HCO_3^- ligand to the nonheme iron, which can be lost from PSII during the course of the titration. The data also indicate that this redox effect has physiological significance not only in forward electron transfer but also in controlling the back-reaction pathways and hence, photodamage. Overall, the data indicate the presence of an unexpected Q_A^--triggered, HCO_3^--mediated redox tuning mechanism, which regulates and protects PSII. This model provides a chemical mechanism rationalizing why HCO_3^-, an exchangeable ligand to the iron, is beneficial and thus, why it is present in PSII.

Results

Fig. 2*A*, circles shows redox titrations of plant PSII-enriched membranes at pH 6.5 with a $Q_A/Q_A^{-\bullet}$ $E_m = -144 \pm 2$ mV. This result is in good agreement with the value reported by Shibamoto et al. (21) for the same biological material and using a comparable spectroelectrochemical method. Fig. 2*B*, circles shows redox titrations of PSII membranes depleted of the Mn_4CaO_5 cluster. The resulting E_m for the $Q_A/Q_A^{-\bullet}$ couple is $E_m = -32 \pm 2$ mV. The Mn depletion-induced increase in potential is somewhat smaller than that reported earlier (12–14); however, both values are ∼80 mV lower than those reported originally in potentiometric titrations using the same material (12).

At pH values close to or below 6.35, the pK_a of bicarbonate (HCO_3^-) with carbonic acid (H_2CO_3), the CO_2 formed from its equilibrium with carbonic acid may be lost from solution, particularly when flushed with N_2 or Ar:

$$CO_2\uparrow + H_2O \leftrightarrow \underset{\text{carbonic acid}}{H_2CO_3} \overset{pK_{a1}\,6.35}{\longleftrightarrow} \underset{\text{bicarbonate}}{HCO_3^-} + H^+ \overset{pK_{a2}\,10.5}{\longleftrightarrow} \underset{\text{carbonate}}{CO_3^{2-}} + 2H^+. \quad [1]$$

It thus seemed possible that HCO_3^- could be lost under the conditions of the redox titration. We, therefore, tested if the removal of HCO_3^- could influence the E_m of $Q_A/Q_A^{-\bullet}$.

Redox titrations of $Q_A/Q_A^{-\bullet}$ were performed on HCO_3^--depleted, PSII-enriched membranes with (Fig. 2*A*, triangles) and without (Fig. 2*B*, triangles) the Mn_4CaO_5 cluster. The E_m values were both upshifted: $E_m = -70 \pm 2$ mV, a shift of +74 mV, for Mn-containing PSII and $E_m = +54 \pm 2$ mV, a shift of +86 mV, for the Mn-depleted PSII. The values obtained in HCO_3^--depleted PSII membranes are close to those obtained by Krieger and coworkers (12–14), indicating that HCO_3^- had been lost in these studies (*Discussion*). When HCO_3^- was added back to samples that had undergone the HCO_3^- depletion procedure, the lower potential E_m values were restored (*SI Appendix*, Fig. S1).

Fig. 2*C* shows that the HCO_3^- removal procedure used results in the typical HCO_3^- depletion-induced slowdown in the rate of

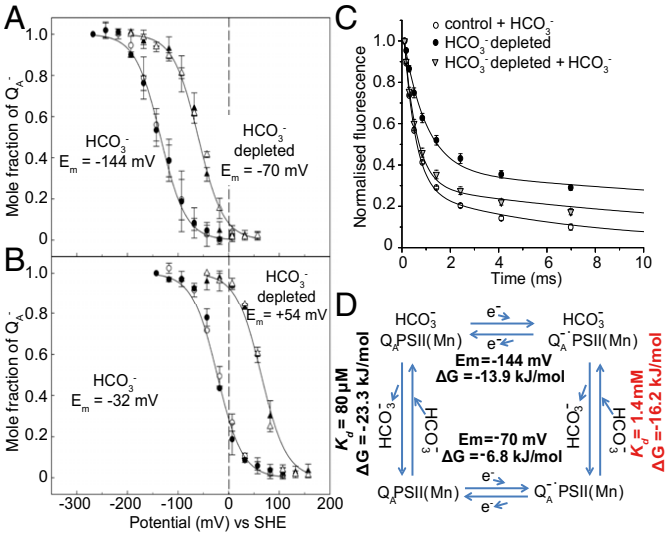

Fig. 2. Effects of bicarbonate depletion on PSII. *A* and *B* show redox titrations of $Q_A/Q_A^{-\bullet}$ monitoring fluorescence in (*A*) intact and (*B*) Mn-depleted PSII membranes in the presence (circles) and absence (triangles) of the HCO_3^-. The concentration of reduced Q_A was corrected for connectivity (*SI Appendix*). The data points were fitted to the Nernst equation with $n = 1$, with error bars indicating the SD of three independent titrations. Black symbols, oxidative titration; white symbols, reductive titration. *C* shows the influence of HCO_3^- depletion on the decay of flash-induced $Q_A^{-\bullet}$ measured as the decay of the variable fluorescence after the third flash given at 1 Hz. Untreated PSII with 1 mM HCO_3^- (circles), HCO_3^--depleted PSII (black symbols), and HCO_3^--depleted PSII with 1 mM HCO_3^- added back (triangles). Error bars are the SD of three independent measurements. *D* shows the relationship between HCO_3^- binding/dissociation and the redox state of Q_A in redox and energy terms. SHE, standard hydrogen electrode.

$Q_A^{-\bullet}$ oxidation as measured by the fluorescence decay seen after excitation by a flash of light (reviewed in ref. 5). Reversible changes in the kinetics were seen, closely matching those reported earlier (25, 26). When HCO_3^- depletion was accompanied by the addition of formate as a replacement ion, more marked changes were seen in the kinetics of $Q_A^{-\bullet}$ oxidation as measured by the fluorescence decay seen after a flash (Fig. 3*A*). This enhanced inhibition also agrees with the literature (25, 26). In contrast, formate has a significantly smaller effect on the E_m of $Q_A/Q_A^{-\bullet}$ (Fig. 3*B*). A positive shift in the E_m still occurred (Fig. 3*B*), but it was significantly smaller, being about one-half that seen with HCO_3^- [$E_{m(form)} \sim -95$ mV].

A shift of +74 mV in the E_m on dissociation of HCO_3^- (−74 mV on HCO_3^- binding) indicates that the binding of the HCO_3^- should become weaker when Q_A^- is present as shown in Fig. 2*D* based on the relationship in the following equation:

$$E_m^b = E_m^d + \frac{RT}{nF}\ln\left(\frac{K_d^{ox}}{K_d^{red}}\right), \qquad [2]$$

where $E_m{}^b$ and $E_m{}^d$ are the reduction potentials when the HCO_3^- is either bound or dissociated, respectively; K_d^{ox} is the HCO_3^- dissociation constant when Q_A is oxidized; and K_d^{red} is the HCO_3^- dissociation constant when Q_A is reduced.

This effect is confirmed in Fig. 3*C*, which shows the influence of a period of illumination on electron transfer from $Q_A^{-\bullet}$ to Q_B (or $Q_B^{-\bullet}$) as monitored by fluorescence decay after a flash. The characteristic slowdown in the rate of forward electron transfer from $Q_A^{-\bullet}$ associated with HCO_3^- removal is seen after the illumination of a sample in a low-HCO_3^- medium. This slowdown of $Q_A^{-\bullet}$ oxidation is reversed when HCO_3^- is added back to the medium.

Fig. 3*D* shows a redox titration experiment aimed at testing the prediction that $Q_A^{-\bullet}$ formation could result in HCO_3^- release. A sample without added HCO_3^- was poised at −58 mV, close to the E_m of the HCO_3^--depleted, Mn_4CaO_5-containing PSII. The red triangle in Fig. 3*D* shows the fluorescence level after 15 min at this potential. As expected, the fluorescence remained low, because no $Q_A^{-\bullet}$ was present at this potential in an HCO_3^--containing sample. The poising potential was then switched off, and the sample was allowed to relax in the dark for 10 min before being illuminated by 4 min of blue light to generate $Q_A^{-\bullet}$. After the illumination, the dark sample was again poised at −58 mV. The fluorescence level had increased to 50% of the maximum value (as shown by the arrow in Fig. 3*D*) [i.e., the level expected if HCO_3^- had been released (Fig. 2*A*)]. An abbreviated redox titration was then performed on the same sample, and a reversible redox transition was seen corresponding to the value obtained earlier for the HCO_3^--depleted PSII. In a control experiment, exactly the same procedure was carried out with a dark period given instead of the illumination and when repoised at −58 mV; the fluorescence level was the same as that recorded before the dark incubation. The experiment in Fig. 3*D* is an additional indication that illumination favors release of the HCO_3^-. The positive shift in the redox potential of $Q_A/Q_A^{-\bullet}$ is predicted to increase the energy gap between $P^{+\bullet}Q_A^{-\bullet}$ and $P^{+\bullet}Ph^{-\bullet}$ and thus, decrease back-reactions via the $P^{+\bullet}Ph^{-\bullet}$ and consequently, the formation of the reaction center triplet state and $^1O_2$ (13) as shown in Fig. 4*A*. Fig. 4*B* shows the effect of HCO_3^- depletion on light-induced $^1O_2$ generation monitored using EPR to detect an $^1O_2$-specific spin trap. The HCO_3^--depleted sample shows decreased levels of $^1O_2$ formation (<60%) compared with the controls (*SI Appendix*, Table S1), verifying the expectations of the model (13).

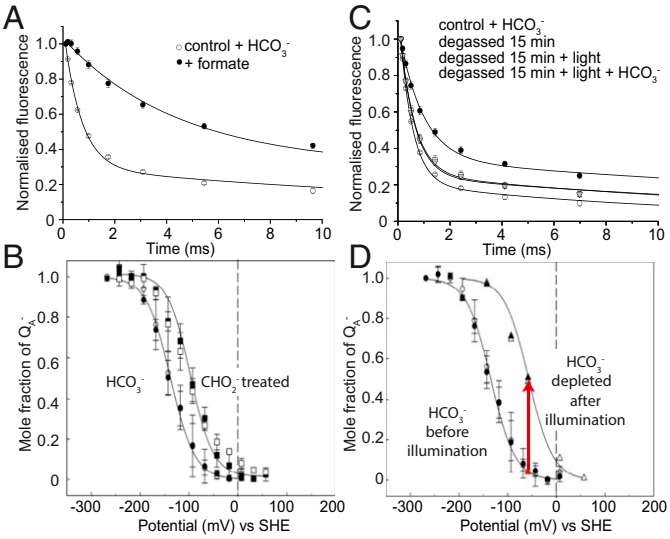

Fig. 3. Influence of formate and effect of preillumination on bicarbonate depletion. (*A*) Decay of flash-induced $Q_A^{-\bullet}$ as described in Fig. 2. HCO_3^--depleted PSII with 100 mM sodium formate present (black circles). Untreated PSII with 1 mM HCO_3^- (white circles). Error bars: SD of three measurements. (*B*) Redox titrations of $Q_A/Q_A^{-\bullet}$ in the presence of formate (squares) or HCO_3^- (circles) (from Fig. 2*A* and other details in *SI Appendix*). (*C*) Effect of preillumination on HCO_3^- depletion: $Q_A^{-\bullet}$ oxidation (i.e., fluorescence decay as in Fig. 2). Untreated PSII with 1 mM HCO_3^- (white circles), degassed PSII (i.e., Ar-bubbled for 15 min; white squares), degassed PSII and then illuminated (4 min, 590 nm, 350 μmol photons m^{-2} s^{-1}; black circles), and degassed PSII, illuminated, and then, 1 mM HCO_3^- added (triangles). (*D*) Effect of preillumination on HCO_3^- depletion: redox titrations of $Q_A/Q_A^{-\bullet}$ in intact PSII (triangles). The red triangle shows the level of fluorescence when a sample (in this case, it had been frozen and thawed once) was poised at −65 mV in the dark for 12 min. The sample was then illuminated (4 min, 620 nm, 273 μmol photons m^{-2} s^{-1}), dark-adapted (10 min), and poised again at −65 mV (8 min). The arrow shows the light-induced increase in fluorescence. A titration was then performed. The data are the average of two experiments, which gave similar results. A standard "dark titration" is also shown (data from Fig. 2). Black symbols, oxidative titration; white symbols, reductive titration. SHE, standard hydrogen electrode.

Discussion

***E_m* of $Q_A/Q_A^{-\bullet}$: Explaining the Discrepancy in the Literature.** Here, we show that removal of bicarbonate (HCO_3^-) from its site on the nonheme iron (Fe^{2+}) in PSII shifts the E_m of $Q_A/Q_A^{-\bullet}$ by ∼+74 mV. The E_m value obtained for PSII in the presence of the HCO_3^- (−144 mV) agrees with those in the work by Shibamoto et al. (21), which used a comparable spectroelectrochemical method (21, 22). Furthermore, the values obtained here without HCO_3^- correspond quite well to those reported in the potentiometric studies of Krieger and coworkers (12–14), strongly suggesting that the PSII used in those studies was HCO_3^--depleted. Comparing the two methods, we explain the loss of HCO_3^- in the latter work (12–14, 23) as follows: (*i*) the lack of mediators meant longer equilibration times; (*ii*) in the potentiometric method, the sample was stirred under a stream of Ar or N_2, whereas the sample in the thin-layer cell is not stirred, and there is little or no sample surface exposed to inert gas; and (*iii*) frozen and thawed samples were used, and these samples seem to lose the HCO_3^- more easily (*SI Appendix*).

Relevant to this argument is a report in which Allakhverdiev et al. (24) verified the values reported by Shibamoto et al. (22) but used the method by Krieger et al. (12). This finding, however, does not contradict the present explanation, because the work in ref. 24 was done at pH 7.0, well above the pK_a 6.35 of H_2CO_3/HCO_3^-, and this pH would significantly inhibit the loss of HCO_3^-. A comparison of the most relevant E_m values in the literature with these results is given in *SI Appendix*, Table S2.

These findings resolve the long-standing discrepancy and reveal another factor influencing the E_m of $Q_A/Q_A^{-\bullet}$, HCO_3^- binding. Overall, four valid values for the E_m values for $Q_A/Q_A^{-\bullet}$ have now been defined depending on the state of the PSII: with and without Ca^{2+} (and the rest of the Mn_4CaO_5 cluster) and with and without the HCO_3^- ligand to the nonheme iron.

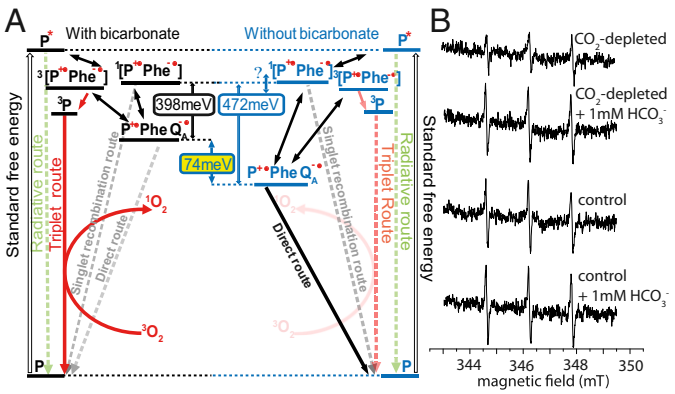

Fig. 4. Charge recombination pathways and singlet O_2 generation in PSII. (*A*) Energy scheme illustrating the outcomes of charge recombination pathways in PSII and the influence of bicarbonate release. The scheme shows the competition between two dominant routes (13): (1) the triplet route is favored when HCO_3^- is present and the energy gap between the $P^{+\bullet}PheQ_A^\bullet$ and $P^{+\bullet}Phe^{-\bullet}$ is small, and (2) the direct route is favored when HCO_3^- is not bound when the energy gap is bigger by ~74 mV as measured here. The question mark at the $P^{+\bullet}Phe^{-\bullet}$ energy indicates that this has not been measured for the HCO_3^--depleted PSII. The changes in standard free energy are not to scale. This scheme is simplified: for example, (*i*) it omits details of the first radical pair formation, and (*ii*) it does not specify which pigments are considered to be P, P*, ^3P, and P^+ (see 2 and 3). (*B*) Generation of $^1O_2$ in HCO_3^--depleted PSII (row 1), after addition of 1 mM $NaHCO_3$ (row 2), and in control samples (rows 3 and 4) measured by EPR using the spin probe TEMPD. Typical spectra are shown (additional data are in *SI Appendix*).

Table 1 shows the measured E_m values and those corrected for (*i*) "connectivity" of the PSII centers (27) (details are in *SI Appendix*) and (*ii*) both connectivity and the measurement temperature (15 °C) calculated based on the assumption that, for a small temperature range, the average dE/dT was 1 mV/K (28). The functional value at 25 °C of −145 mV can be used for anchoring bioenergetics schemes of PSII. The other three corrected values are also relevant, because they represent conditions that are likely to be encountered by PSII in vivo (e.g., during photoassembly of the Mn_4CaO_5 cluster, before repair when photoinhibited, and/or when $Q_A^{-\bullet}$ is long-lived).

Relevance to Donor-Side Effects of Bicarbonate. A role for HCO_3^- on the electron donor side of PSII has been suggested (5). However, its absence in the high-resolution crystal structures (8) confirmed the results of other studies (29, 30) that HCO_3^- was not bound to the electron donor side of PSII. A secondary nonbound donor-side role has not been ruled out, however (5). A role of HCO_3^- in photoassembly of the cluster has been suggested previously, and remains possible (5, 16). A role of HCO_3^-, enhancing proton removal from the site of water splitting, was recently reported (10), and it was suggested that this could represent a regulatory link between CO_2 and water splitting (10). The present work also shows a mechanism in which the CO_2 level can control PSII activity (see below). Future research will need to distinguish between these two mechanisms.

The "donor-side" studies of PSII are often based on the idea that the acceptor-side HCO_3^- has a single fixed binding constant for HCO_3^- bound to the Fe^{2+}, keeping it permanently bound to PSII under physiological conditions (10). These results change that premise, and thus it may be worthwhile reassessing some phenomena attributed to the donor side. (Additional discussion on donor-side effects on the E_m values of Q_A is provided in *SI Appendix*.)

Redox Effect of HCO_3^-: Significance on Charge Recombination. An HCO_3^--dependent shift in the E_m of $Q_A/Q_A^{-\bullet}$ has not been reported previously as far as we are aware (3–6). An effect of HCO_3^- removal on the E_m of $Q_A/Q_A^{-\bullet}$ was looked for but was not observed (31). There are two potential explanations for this: (*i*) formate was added to the sample to aid HCO_3^- depletion, and we show here that, when formate is present, the redox shift is much less marked; and (*ii*) the titrations reported (31) were not reversible, presumably because of the loss of the Mn cluster as shown subsequently (12–14).

Since the introduction of the concept of competing charge recombination routes to explain the influence of switching between high and low potential forms of Q_A in PSII (13), any changes in the energy gap between $P^{+\bullet}Ph^{-\bullet}$ and $P^{+\bullet}Q_A^{-\bullet}$ have been interpreted within this model as favoring or disfavoring back-reactions via the ^3P-mediated $^1O_2$ formation (18–20, 32). The HCO_3^- effect reported here can be interpreted in the same way. Loss of the HCO_3^- shifts the E_m by +74 mV, thus increasing the energy gap between the $P^{+\bullet}Ph^{-\bullet}$ and $P^{+\bullet}Q_A^{-\bullet}$ and making the back-reaction to $P^{+\bullet}Ph^{-\bullet}$ less likely, and consequently, less ^3P-mediated $^1O_2$ is expected to be formed (Fig. 4*A*). Here, we show that this prediction holds true (Fig. 4*B*). Thus, the loss of HCO_3^- is predicted to protect PSII from this kind of photodamaging reaction.

In the extensive literature on photoinhibition of PSII, there are some reports investigating the removal of HCO_3^-, and they show both positive and negative correlations with photoinhibition, depending on the conditions (33–35). Given the wide range of conditions used and the multiple mechanisms possible for damaging PSII, the contradictory observations are not too surprising. The mechanistic role of HCO_3^- and its correlation with diminished $^1O_2$ formation shown in this work will act as a starting point for future research aimed at assessing the physiological significance of this protective mechanism.

Effect of the Redox State of Q_A on the Binding of HCO_3^-. The +74-mV shift in the E_m of $Q_A/Q_A^{-\bullet}$ implies that the presence of $Q_A^{-\bullet}$ should diminish the binding affinity of HCO_3^-. The binding of HCO_3^- should be weaker by a factor of 10 for every 59-mV shift in the potential, according to Eq. **2**. In this case, then the +74-mV shift implies a weakening of the binding constant by a factor of ~17.9 (Fig. 2*D*). This weak binding would be predicted to result in loss of the bicarbonate when $Q_A^{-\bullet}$ is reduced, depending on the ambient concentration of HCO_3^-. Under the conditions of our experiment, illumination of the sample to maintain $Q_A^{-\bullet}$ reduced led to HCO_3^- loss as shown by the typical slowing of forward electron transfer from $Q_A^{-\bullet}$ (Fig. 2*C*) and characteristic shift in the E_m of $Q_A/Q_A^{-\bullet}$ (Fig. 2*D*). We duly interpret this as confirming that formation of $Q_A^{-\bullet}$ results in HCO_3^- release from the nonheme iron.

The influence of illumination on HCO_3^- binding has been investigated previously (36–39), but it has not been mentioned in recent work (3–5). In general, the observations made in this work that Q_A^- formation results in HCO_3^- release are consistent with the diverse observations in the literature (36–39). However, in the previous work, there was no suggestion made linking the redox state of Q_A and the binding of the HCO_3^-.

Table 1. Experimental and corrected Q_A/Q_A^- reduction potentials

Sample	Measured E_m	Corrected E_m	
		$E_{m\ (con)}$*	$E_{m\ (con,\ 25\ °C)}$†
PSII + HCO_3	−138 ± 2	−134 ± 2*	−144 ± 2†
PSII − HCO_3	−61 ± 2	−60 ± 2*	−70 ± 2†
−Mn PSII + HCO_3	−23 ± 2	−22 ± 2*	−32 ± 2†
−Mn PSII − HCO_3	+65 ± 2	+64 ± 2*	+54 ± 2†

*E_m corrected for the nonlinear behavior of chlorophyll fluorescence (connectivity) based on the excitation energy transfer in PSII dimer complexes (details are in *SI Appendix*).

†E_m corrected for the connectivity and the temperature difference between the experimental temperature (15 °C) and the standard conditions (25 °C) with an average dE/dT of −1 mV/K.

The nature of the interaction between the HCO_3^- and $Q_A^{-\bullet}$ could be (*i*) at least partially electrostatic, because the two anions are within 10 Å of each other, and (*ii*) electronic, transmitted through the Fe^{2+} to the D2-His214 ligand, weakening its H bond to Q_A (Fig. 1). It seems reasonable to expect that both mechanisms would lower the redox potential of $Q_A/Q_A^{-\bullet}$.

These findings are relevant to an earlier suggestion based on X-ray absorption studies that the bidentate carboxylic acid binding to the nonheme iron becomes transiently monodentate on $Q_A^{-\bullet}$ formation (40). That said, it also seems possible that the presence of an uncompensated anion on Q_A could make binding of the HCO_3^- anion less strong without the formation of a discrete monodentate intermediate. This point is worth investigating further to clarify the specific molecular mechanism.

When considering electrostatic and electronic effects, both formate and HCO_3^- have the same charge, and yet, formate has a much smaller effect. A possible explanation for this apparent anomaly is that HCO_3^- differs from formate and most other relevant carboxylic acids in that it can undergo an additional ionization, forming the CO_3^{2-} anion with a pK_a 10.3. Cox et al. (41) proposed that the presence of CO_3^{2-} rather than HCO_3^- as a ligand to the Fe^{2+} could explain the specific EPR signal arising from the semiquinone complex in PSII (6, 41). The lower pK_a needed to make the model feasible was attributed to an association between the HCO_3^- and a lysine, D2-K264 (41). Subsequently, with the availability of the high-resolution crystal structure (8), it was pointed out (7) that this lysine was, in fact, involved in an ion pair with a nearby glutamate, D1-E244 (Fig. 1). Nevertheless, we consider that the pK_a on HCO_3^- could still be significantly shifted by other factors: (*i*) binding to the Fe^{2+}, (*ii*) the presence of H bonds to HCO_3^- from the symmetrical tyrosine residues D2Y268 and D1Y246, and (*iii*) the distal O of the HCO_3^- being part of an extended H-bond network (Fig. 1), which could allow dynamic deprotonation and protonation reactions. We, thus, consider that CO_3^{2-} remains a valid candidate as the native ligand to the Fe^{2+}.

The light-induced loss of the HCO_3^-, shown here, occurred in a low-CO_2 environment. Our experiments were done at pH 6.5, which was chosen for the stability of the Mn cluster. The pK_a of HCO_3^-/carbonic acid is at pH 6.35, and therefore, at pH 6.5, the concentration of HCO_3^- present in the buffer was low (17.5 μM) and relatively easily lost by flushing with Ar or N_2. The question thus arises whether HCO_3^- loss will occur under physiological conditions where the pH is higher. The dissociation constant for HCO_3^- has been estimated to be 40–80 μM, whereas the concentration of HCO_3^- in the stroma at ∼pH 8 is estimated to be 220 μM (9, 42). Thus, it has been generally assumed that the HCO_3^- should be constantly bound to the site (10). A weakening of the HCO_3^- binding, with the estimated K_d increasing by ∼18 times (Fig. 2*D*), on formation of $Q_A^{-\bullet}$, as reported here, should allow dissociation of the bicarbonate even under physiological conditions. This conclusion needs to be verified experimentally. However, because it is known that, under physiological conditions, acetate is able to replace HCO_3^- in vivo (11), it seems very likely that the $Q_A^{-\bullet}$-dependent HCO_3^- exchange will occur under some physiological conditions. It is also worth examining the possibility that other natural ligands (e.g., glycolate, malate, and glycerate) in the stroma could replace HCO_3^- under some conditions.

Conclusions and Working Model. This study resolves the long-standing discrepancy concerning the E_m of $Q_A/Q_A^{-\bullet}$ (described in the Introduction and refs. 12 and 21) and thus, provides a firm basis for understanding the bioenergetics of PSII (Fig. 4*A*). It also shows that HCO_3^- binding to the nonheme iron has a significant influence on the redox potential of Q_A. Correspondingly, the redox state of Q_A influences HCO_3^- binding, with the $Q_A^{-\bullet}$ state favoring its dissociation. This work also provides a mechanistic explanation for the presence of HCO_3^- in PSII, and it rationalizes the long-studied bicarbonate effect in terms of an unexpected redox-based protective mechanism.

The principle aspects of this protective mechanism are described in what follows. Normal photosynthesis can lower the ambient concentration of CO_2 to the point when it becomes limiting, resulting in the overreduction of the electron transfer components and leading to the accumulation of $Q_A^{-\bullet}$ (43). From this work, the presence of $Q_A^{-\bullet}$ would be expected to result in weaker binding of HCO_3^- to the nonheme iron, and thus, HCO_3^- would be released. This HCO_3^- loss would not only slow down electron transfer to the plastoquinone pool (9, 42) (and thus, water splitting and O_2 formation), but importantly, it would also change the potential of $Q_A/Q_A^{-\bullet}$ to a more positive value (Fig. 4*A*). This higher potential increases the energy gap between $P^{+\bullet}Q_A^{-\bullet}$ and $P^{+\bullet}Ph^{-\bullet}$, favoring the harmless, direct recombination of $P^{+\bullet}Q_A^{-\bullet}$ over the back-reaction via $P^{+\bullet}Ph^{-\bullet}$ (13). This direct route is beneficial, because the back-reaction route forming $P^{+\bullet}Ph^{-\bullet}$ leads to formation of the chlorophyll triplet, ^3P, which reacts with O_2 to form the highly toxic reactive oxygen species $^1O_2$ (Fig. 4). When the CO_2 level returns to normal, which would be favored by the inhibition of PSII activity, linear electron transfer and CO_2 fixation would resume, reoxidizing the plastoquinol pool and $Q_A^{-\bullet}$. HCO_3^- would then rebind to the nonheme iron, returning the potential of the $Q_A/Q_A^{-\bullet}$ couple to its low potential form, restoring normal proton-coupled electron transfer between the quinones, and returning electron transfer out of PSII to normal rates.

This simplified model does not take into account the numerous processes that regulate electron transfer, CO_2 fixation, and photorespiration, but the basic idea is straightforward, intuitive, and consistent with the results here and in the literature (43). Also, the model as presented does not specify or require that CO_2, the true terminal electron acceptor, through its equilibrium with HCO_3^- regulates the function of PSII. Indeed, with the dissociation constants reported in the literature (40–80 μM), the HCO_3^- bound to PSII would be released when Q_A^- is present even under the normal (i.e., nonlimiting) concentrations of CO_2 in the stroma, where HCO_3^- is estimated to be 220 μM (9, 42). However, we have two doubts about this point. First, we doubt the validity of the 40–80 μM dissociation constant: our samples were maintained at pH 6.5 for long periods, the expected HCO_3^- concentration in our samples at equilibrium with atmospheric CO_2 should be 17 μM, and what we see is just a fractional loss of HCO_3^-. It thus seems likely that the K_d is lower than the current estimates. Second, the stroma can reach pH values higher than pH 8.0, leading to significant increases in HCO_3^- concentration. Given these two factors, it remains possible that the accumulation of $Q_A^{-\bullet}$ may result in HCO_3^- release only when the HCO_3^- concentration is low, potentially coinciding with CO_2-limiting conditions. If so, the mechanism could then represent a sink (CO_2) to source (PSII) regulation mechanism. To test this possibility, it is worth investigating the following: (*i*) the conditions in which this regulation mechanism actually occurs in vivo; (*ii*) the detailed chemical parameters that determine the mechanism, including a more accurate determination of the HCO_3^- K_d in a range of conditions; and (*iii*) the rate of binding and dissociation of HCO_3^- to determine how dynamic the mechanism can be. (*SI Appendix* has an example of published data that may be reinterpreted in light of the mechanism.)

The protective/regulation model also provides the explanation for the presence of HCO_3^- in PSII. Nonoxygenic Type II reaction centers lack HCO_3^- as a ligand to the nonheme iron. Instead, a glutamate provides a nonexchangeable but otherwise structurally similar bidendate ligand. It has been pointed out that these nonoxygenic Type II reaction centers do not undergo back-reactions from $P^{+\bullet}Q_A^{-\bullet}$ to $P^{+\bullet}BPh^{-\bullet}$ (where BPh is bacteriopheophytin), because they have a much bigger energy gap between these states than is present in functional PSII; therefore, this back-reaction does not need to be regulated in the same way as it does in PSII (18). It also seems reasonable to suppose that the nonoxygenic Type II reaction centers, with their cyclic electron transfer system, single reaction center, and low-O_2 environment, would need much less in terms of protective regulation compared with the situation

encountered by PSII in oxygenic photosynthesis. A protective role for HCO_3^- aimed at diminishing $^1O_2$ formation also implies that this type of regulation evolved in an O_2-containing environment, perhaps during the phase of PSII evolution when water could be split but still only inefficiently (44).

Materials and Methods

PSII-enriched membranes were prepared from spinach (45) with modifications shown in ref. 46. Mn depletion was done using NH_2OH (47). O_2 evolution was assayed with a Clark-type oxygen electrode (Oxylab; Hansatech) at 25 °C with 0.5 mM dichlorobenzoquinone/1 mM $K_3Fe(CN)_6$ using saturating red light (590-nm cutoff filter; 5,000 μE m^{-2} s^{-1}). The activity in the various preparations was 300–500 μmol O_2 mg chlorophyll^{-1} h^{-1}. HCO_3^- was depleted (48), and the PSII was stored on ice in the dark under Ar until use. If not indicated otherwise, the samples used for the spectroelectrochemical titrations were prepared and used on the same day. Formate treatment of PSII membranes was as described in ref. 48. Spectroelectrochemical redox titrations were performed as reported earlier (21, 22) with minor differences (details are in *SI Appendix*). The redox state of $Q_A^{\bullet}$ was monitored by measuring chlorophyll *a* fluorescence and corrected for connectivity (additional details are in *SI Appendix*). Singlet oxygen was trapped using the water soluble spin probe 2,2,6,6-tetramethyl-4-piperidone hydrochloride (TEMPD) (11) and measured with EPR (*SI Appendix*). Samples (10 μg chlorophyll mL^{-1}) were illuminated for 2 min with 500 μmol quanta m^{-2} s^{-1} red light (RG 630).

ACKNOWLEDGMENTS. We thank Fabrice Rappaport, Alain Boussac, Wolfgang Nitschke, James Murray, Jeff Douglass, Charles Cotton, and Peter Nixon for useful discussions. A.F. and A.W.R. thank Gino Bettati, Claudio Silingardi, and Mauro Fantuzzi for invaluable help with modifications to the instruments. This work was supported by Biotechnology and Biological Sciences Research Council Grant BB/K002627/1 and the Royal Society Wolfson Research Merit Award (to A.W.R.). K.B. was supported, in part, by a grant from The Heinrich Boll Foundation. S.D.C. was supported by an Imperial College Scholarship.

1. Dau H, Zaharieva I (2009) Principles, efficiency, and blueprint character of solar-energy conversion in photosynthetic water oxidation. *Acc Chem Res* 42(12):1861–1870.
2. Rappaport F, Diner BA (2008) Primary photochemistry and energetics leading to the oxidation of the Mn_4Ca cluster and to the evolution of molecular oxygen in Photosystem II. *Coord Chem Rev* 252:259–272.
3. Cardona T, Sedoud A, Cox N, Rutherford AW (2012) Charge separation in photosystem II: A comparative and evolutionary overview. *Biochim Biophys Acta* 1817(1):26–43.
4. Müh F, Glöckner C, Hellmich J, Zouni A (2012) Light-induced quinone reduction in photosystem II. *Biochim Biophys Acta* 1817(1):44–65.
5. Shevela D, Eaton-Rye JJ, Shen JR, Govindjee (2012) Photosystem II and the unique role of bicarbonate: A historical perspective. *Biochim Biophys Acta* 1817(8):1134–1151.
6. Sedoud A, et al. (2011) Effects of formate binding on the quinone-iron electron acceptor complex of photosystem II. *Biochim Biophys Acta* 1807(2):216–226.
7. Saito K, Rutherford AW, Ishikita H (2013) Mechanism of proton-coupled quinone reduction in Photosystem II. *Proc Natl Acad Sci USA* 110(3):954–959.
8. Umena Y, Kawakami K, Shen JR, Kamiya N (2011) Crystal structure of oxygen-evolving photosystem II at a resolution of 1.9 Å. *Nature* 473(7345):55–60.
9. Blubaugh DJ, Govindjee (1988) The molecular mechanism of the bicarbonate effect at the plastoquinone reductase site of photosynthesis. *Photosynth Res* 19(1-2):85–128.
10. Koroidov S, Shevela D, Shutova T, Samuelsson G, Messinger J (2014) Mobile hydrogen carbonate acts as proton acceptor in photosynthetic water oxidation. *Proc Natl Acad Sci USA* 111(17):6299–6304.
11. Roach T, Sedoud A, Krieger-Liszkay A (2013) Acetate in mixotrophic growth medium affects photosystem II in *Chlamydomonas reinhardtii* and protects against photoinhibition. *Biochim Biophys Acta* 1827(10):1183–1190.
12. Krieger A, Rutherford AW, Johnson GN (1995) On the determination of the redox midpoint potential of the primary quinone electron acceptor, Q_A, in Photosystem II. *Biochim Biophys Acta* 1229:193–201.
13. Johnson GN, Rutherford AW, Krieger A (1995) A change in the midpoint potential of Q_A in Photosystem II associated with photoacrtivation of oxygen evolution. *Biochim Biophys Acta* 1229:202–207.
14. Krieger A, Weis E, Demeter S (1993) Low-pH-induced Ca^{2+} ion release in the water-splitting system is accompanied by a shift in the midpoint redox potential of the primary quinone acceptor-Q_A. *Biochim Biophys Acta* 1144:411–418.
15. Krewald V, et al. (2015) Metal oxidation states in biological water splitting. *Chem Sci* 6:1676–1695.
16. Burnap RL (2004) D1 protein processing and Mn cluster assembly in light of the emerging Photosystem II structure. *Phys Chem Chem Phys* 6:4803–4809.
17. Rutherford AW, Paterson DR, Mullet JE (1981) A light-induced spin-polarized triplet detected by EPR in photosystem II reaction centers. *Biochim Biophys Acta* 635(2):205–214.
18. Rutherford AW, Osyczka A, Rappaport F (2012) Back-reactions, short-circuits, leaks and other energy wasteful reactions in biological electron transfer: Redox tuning to survive life in O(2). *FEBS Lett* 586(5):603–616.
19. Rappaport F, Guergova-Kuras M, Nixon PJ, Diner BA, Lavergne J (2002) Kinetics and pathways of charge recombination in photosystem II. *Biochemistry* 41(26):8518–8527.
20. Vass I, Cser K (2009) Janus-faced charge recombinations in photosystem II photoinhibition. *Trends Plant Sci* 14(4):200–205.
21. Shibamoto T, et al. (2010) Species-dependence of the redox potential of the primary quinone electron acceptor Q_A in photosystem II verified by spectroelectrochemistry. *FEBS Lett* 584(8):1526–1530.
22. Shibamoto T, Kato Y, Sugiura M, Watanabe T (2009) Redox potential of the primary plastoquinone electron acceptor Q(A) in photosystem II from Thermosynechococcus elongatus determined by spectroelectrochemistry. *Biochemistry* 48(45):10682–10684.
23. Ido K, et al. (2011) High and low potential forms of the Q_A quinone electron acceptor in Photosystem II of Thermosynechococcus elongatus and spinach. *J Photochem Photobiol B* 104(1-2):154–157.
24. Allakhverdiev SI, et al. (2011) Redox potentials of primary electron acceptor quinone molecule (Q_A)- and conserved energetics of photosystem II in cyanobacteria with chlorophyll a and chlorophyll d. *Proc Natl Acad Sci USA* 108(19):8054–8058.
25. Eaton-Rye JJ, Govindjee (1984) A study of the specific effect of bicarbonate on photosynthetic electron transport in the presence of methyl viologen. *Photobiochem Photobiophys* 8:279–288.
26. Jursinic P, Stemler A (1986) Correlation between the binding of formate and decreased rates of charge transfer through the photosystem II quinones. *Photochem Photobiol* 43:205–212.
27. Cuni A, Xiong L, Sayre R, Rappaport F, Lavergne F (2004) Modification of the pheophytin midpoint potential in Photosystem II: Modulation of the quantum yield of charge separation and of charge recombination pathways. *Phys Chem Chem Phys* 6:4825–4831.
28. Bratsch SJ (1989) Standard electrode potentials and temperature coefficients in water at 298.15 K. *J Phys Chem Ref Data* 18(1):1–22.
29. Shevela D, Su JH, Klimov V, Messinger J (2008) Hydrogencarbonate is not a tightly bound constituent of the water-oxidizing complex in photosystem II. *Biochim Biophys Acta* 1777(6):532–539.
30. Ulas G, Olack G, Brudvig GW (2008) Evidence against bicarbonate bound in the O_2-evolving complex of photosystem II. *Biochemistry* 47(10):3073–3075.
31. Vermaas WFJ, Govindjee (1982) Bicarbonate effects on chlorophyll-a fluorescence transients in the presence and the absence of diuron. *Biochim Biophys Acta* 680(2): 202–209.
32. Sugiura M, et al. (2014) Modification of the pheophytin redox potential in *Thermosynechococcus elongatus* Photosystem II with PsbA3 as D1. *Biochim Biophys Acta* 1837(1):139–148.
33. Sundby C, Mattsson M, Schiött T (1992) Effects of bicarbonate and oxygen concentration on photoinhibition of thylakoid membranes. *Photosynth Res* 34(2):263–270.
34. Demeter S, Janda T, Kovacs L, Mende D, Wiessner W (1995) Effects of *in vivo* CO_2-depletion on electron-transport and photoinhibition in the green-algae, *Chlamydobotrys-stellata* and *Chlamydomonas reinhardtii*. *Biochim Biophys Acta* 1229(2): 166–174.
35. Cheng HM, et al. (2008) Influence of CO_2 concentrating mechanism on photoinhibition in *Synechococcus* sp PCC7942 (Cyanophyceae). *Phycologia* 47:588–598.
36. Stemler A, Govindjee (1973) Bicarbonate ion as a critical factor in photosynthetic oxygen evolution. *Plant Physiol* 52(2):119–123.
37. Stemler A (1979) A dynamic interaction between the bicarbonate ligand and photosystem II reaction center complexes in chloroplasts. *Biochim Biophys Acta* 545(1): 36–45.
38. Stemler A, Murphy J (1983) Determination of the binding constant of $H^{14}CO_3^-$ to the photosystem II complex in maize chloroplasts - effects of inhibitors and light. *Photochem Photobiol* 38:701–707.
39. Vermaas WFJ, Van Rensen JJS (1981) Mechanism of bicarbonate action on photosynthetic electron transport in broken chloroplasts. *Biochim Biophys Acta* 636(2):168–174.
40. Chernev P, Zaharieva I, Dau H, Haumann M (2011) Carboxylate shifts steer interquinone electron transfer in photosynthesis. *J Biol Chem* 286(7):5368–5374.
41. Cox N, et al. (2009) The semiquinone-iron complex of photosystem II: Structural insights from ESR and theoretical simulation; evidence that the native ligand to the non-heme iron is carbonate. *Biophys J* 97(7):2024–2033.
42. Eaton-Rye JJ, Govindjee (1988) Electron transfer through the quinone acceptor complex of photosystem II in bicarbonate-depleted spinach thylakoid membranes as a function of actinic flash number and frequency. *Biochim Biophys Acta* 935: 237–247.
43. Holland SC, Kappell AD, Burnap RL (2015) Redox changes accompanying inorganic carbon limitation in *Synechocystis* sp. PCC 6803. *Biochim Biophys Acta* 1847(3):355–363.
44. Cardona T, Murray JW, Rutherford AW (2015) Origin and evolution of water oxidation before the last common ancestor of the cyanobacteria. *Mol Biol Evol* 32(5): 1310–1328.
45. Berthold DA, Babcock GT, Yocum CF (1981) A highly resolved oxygen-evolving photosystem-II preparation from spinach thylakoid membranes: Electron-paramagnetic-res and electron-transport properties. *FEBS Lett* 134:231–234.
46. Johnson GN, Boussac A, Rutherford AW (1994) The origin of 40-50°C thermoluminescence band in Photosystem-II. *Biochim Biophys Acta* 1184:85–92.
47. Renger G, Volker M, Weiss W (1984) Studies on the nature of the water-oxidizing enzyme. 1 The effect of trypsin on the system-II reaction pattern in inside-out thylakoids. *Biochim Biophys Acta* 766:582–591.
48. Shevela D, Klimov V, Messinger J (2007) Interactions of photosystem II with bicarbonate, formate and acetate. *Photosynth Res* 94(2-3):247–264.

NATURE PUBLISHING GROUP LICENSE TERMS AND CONDITIONS

Sep 25, 2017

This Agreement between Mr. Sven De Causmaecker ("You") and Nature Publishing Group ("Nature Publishing Group") consists of your license details and the terms and conditions provided by Nature Publishing Group and Copyright Clearance Center.

License Number	4167150059690
License date	Aug 13, 2017
Licensed Content Publisher	Nature Publishing Group
Licensed Content Publication	Nature
Licensed Content Title	Light-induced structural changes and the site of O=O bond formation in PSII caught by XFEL
Licensed Content Author	Michihiro Suga, Fusamichi Akita, Michihiro Sugahara, Minoru Kubo, Yoshiki Nakajima, Takanori Nakane
Licensed Content Date	Feb 20, 2017
Licensed Content Volume	543
Licensed Content Issue	7643
Type of Use	reuse in a dissertation / thesis
Requestor type	academic/educational
Format	print and electronic
Portion	figures/tables/illustrations
Number of figures/tables /illustrations	1
High-res required	no
Figures	Figure 3 Panel a and b
Author of this NPG article	no
Your reference number	
Title of your thesis / dissertation	Bioenergetic Studies on the Quinone Electron Acceptors of Photosystem II
Expected completion date	Sep 2017
Estimated size (number of pages)	200
Requestor Location	Mr. Sven De Causmaecker Imperial College London Exhibition Rd SEC London, London SW72AZ United Kingdom Attn: Mr. Sven De Causmaecker
Billing Type	Invoice
Billing Address	Mr. Sven De Causmaecker Imperial College London Exhibition Rd SEC London, United Kingdom SW72AZ Attn: Mr. Sven De Causmaecker
Total	**0.00 GBP**
Terms and Conditions	

Terms and Conditions for Permissions

Nature Publishing Group hereby grants you a non-exclusive license to reproduce this material for this purpose, and for no other use,subject to the conditions below:

ELSEVIER LICENSE
TERMS AND CONDITIONS

Sep 25, 2017

This Agreement between Mr. Sven De Causmaecker ("You") and Elsevier ("Elsevier") consists of your license details and the terms and conditions provided by Elsevier and Copyright Clearance Center.

License Number	4157600777917
License date	Jul 28, 2017
Licensed Content Publisher	Elsevier
Licensed Content Publication	Biochimica et Biophysica Acta (BBA) - Bioenergetics
Licensed Content Title	Identification of the reduced primary electron acceptor of Photosystem II as a bound semiquinone anion
Licensed Content Author	Hans J. Van Gorkom
Licensed Content Date	Jun 28, 1974
Licensed Content Volume	347
Licensed Content Issue	3
Licensed Content Pages	4
Start Page	439
End Page	442
Type of Use	reuse in a thesis/dissertation
Portion	figures/tables/illustrations
Number of figures/tables /illustrations	1
Format	both print and electronic
Are you the author of this Elsevier article?	No
Will you be translating?	No
Original figure numbers	Figure 2 main window
Title of your thesis/dissertation	Bioenergetic Studies on the Quinone Electron Acceptors of Photosystem II
Expected completion date	Sep 2017
Estimated size (number of pages)	200
Requestor Location	Mr. Sven De Causmaecker Imperial College London Exhibition Rd SEC London, London SW72AZ United Kingdom Attn: Mr. Sven De Causmaecker
Publisher Tax ID	GB 494 6272 12
Total	**0.00 EUR**
Terms and Conditions	

INTRODUCTION

1. The publisher for this copyrighted material is Elsevier. By clicking "accept" in connection with completing this licensing transaction, you agree that the following terms and conditions apply to this transaction (along with the Billing and Payment terms and conditions established by Copyright Clearance Center, Inc. ("CCC"), at the time that you opened your Rightslink account and that are available at any time at http://myaccount.copyright.com).

GENERAL TERMS

2. Elsevier hereby grants you permission to reproduce the aforementioned material subject to the terms and conditions